UNIVERSITÀ
DEGLI STUDI
FIRENZE

International Doctorate in Atomic and Molecular Photonics

Ciclo XXVIII

Coordinatore Prof. Roberto Righini

ATOM INTERFEROMETRY WITH FERMIONIC AND BOSONIC ISOTOPES OF STRONTIUM FOR PRECISION GRAVITY MEASUREMENTS AND TEST OF THE EQUIVALENCE PRINCIPLE

Settore Scientifico Disciplinare FIS/03

Dottorando
Tommaso Mazzoni

Tutor
Prof. Guglielmo M. Tino

Anni 2012/2015

Abstract

Atom interferometry is rapidly growing as a new tool for high precision gravity measurements, finding important applications in applied and fundamental physics, especially in quantum-level tests of general relativity. In this context, testing the Einstein Equivalence Principle with quantum systems is motivated by the aim of improving the limits reached by classical tests with macroscopic bodies, but mostly by the possibility to perform qualitatively new tests with "test masses" having well defined properties, in terms of spin, bosonic or fermionic nature, and proton-to-neutron ratio.

In this thesis, two experiments based on ultra-cold strontium atom interferometry are presented. In the first one, we performed an experimental comparison of the gravitational acceleration for two different strontium isotopes: one which has zero total spin, the boson ^{88}Sr, and one which has a half-integer spin, the fermion ^{87}Sr. Gravity acceleration was measured by means of a genuine quantum effect, namely, the coherent delocalization of matter waves in an optical lattice. The results set an upper limit of $\sim 10^{-7}$ for the Weak Equivalence Principle violation and for the existence of a possible spin-gravity coupling.

In a second experiment a new interferometric scheme with the ^{88}Sr isotope was developed with the purpose of setting the basis for a new generation of high precision gravimeters. We realized the first vertical Mach-Zehnder interferometer with ^{88}Sr atoms based on large-momentum-transfer Bragg pulses. This isotope has specific favorable characteristics: it has no nuclear spin so that in the ground state it is a scalar particle which is virtually insensitive to stray magnetic fields, and its small scattering length results in reduced decoherence due to cold collisions. These unique properties make this isotope of superior interest for the highest precision gravimetric devices. We demonstrated atomic diffraction by a laser standing wave of up to eight photon recoils and the realization of a gravimeter with a sensitivity $\delta g/g = 4 \times 10^{-8}$.

Contents

Chapter 1

Introduction

In the last twenty years, the incredibly fast development of a wide range of matter-wave interferometer devices opened new ways in high precision metrology of inertial forces, finding important applications both in fundamental and applied physics [1, 2]. In particular, thanks to its foreseen improvements, the role of neutral atom interferometry in gravity measurements is rapidly growing. Indeed, such devices have already demonstrated superior performances in measuring gravity acceleration [3–5], gravity gradients [6, 7], gravity curvatures [8] and rotations [9, 10]. Accurate and sensitive measurements of such effects have direct applications to inertial navigation [11] and underground prospecting. Atom interferometry has also advanced the field of precision determination of fundamental constants, such as the atomic fine structure constant α [12–14], and the Newtonian gravitational constant G [15–17].

Furthermore, atom interferometry is becoming a promising tool for fundamental quantum-level tests of general relativity, the present theory of gravity [18]. For example, searches for non-Newtonian gravitational potentials are motivated by string theory and the possibility of compact dimensions [19]. In this direction, experiments with multiple atom interferometers located at different distances from the Earth's center have been discussed [20, 21], and measurements of force at micrometer scales have been carried out and discussed [22–24]. Atom interferometer gyroscopes in low Earth orbit should be able to measure the geodetic effect as well as the Lense-Thirring rotation, a general relativity effect that causes a gyroscope to rotate relative to the fixed stars due to a massive rotating body being nearby. Both effects are objectives of future space borne atom interferometer missions [25]. Other exciting proposals prospects atom interferometry as sensors of gravitational waves [26–29].

Of major interest for the present dissertation are tests of the Einstein Equivalence Principle (EEP), which is at the heart of general relativity. Violations of the EEP

are expected in attempts to unify general relativity with the other fundamental interactions and in theoretical models for dark energy in cosmology [30, 31] as well as in extended theories of gravity [32]. From a phenomenological point of view, three aspects of the EEP can be tested [33]: the Weak Equivalence Principle (WEP), the Local Lorentz Invariance (LLI) and the Local Position Invariance (LPI). The WEP, which corresponds to the universality of free fall, goes back to Galileo Galilei's idea that the motion of a mass in a gravitational field is independent of its structure and composition. A direct test of the WEP is the comparison of the acceleration of two "test masses" of different composition. If the principle is violated, then the accelerations of different bodies would differ.

The best current constraints on the relative differential acceleration of two bodies are at the level of 10^{-13} and come from two methods: the study of the motion of moons and planets [34] and the use of torsion balances [35]. The interest of using atoms is not only to improve the limits reached by classical tests with macroscopic bodies, but mostly in the possibility to perform qualitatively new tests with probe masses having well defined properties, e.g., in terms of spin, bosonic or fermionic nature, and proton-to-neutron ratio. In recent years, experiments based on atom interferometry compared the fall in Earth's gravitational field of two Rb isotopes [36, 37] and Rb versus K [38] reaching a relative precision of about 10^{-7}. At the same level of precision is the experiment described in this thesis, which was published in Physical Review Letter [39]. More recently the best result so far of 10^{-8} was obtained with two Rb isotopes [40]. Tests of WEP were carried out in which the measurement of Earth's gravity acceleration with an atom interferometer was compared with the value provided by a classical gravimeter [3, 41]. A much higher precision will be achieved in future experiments with atom interferometers that are planned on the ground [21, 42] and in space [43, 44]. The possibility of tests with atom interferometry for matter versus antimatter has also been investigated [45, 46].

Possible spin-gravity coupling, torsion of space-time, and EEP violations have been the subject of extensive theoretical investigation (see, for example, refs. [47–53]). Experimental tests were performed based on macroscopic test masses [53, 54], atomic magnetometers [55, 56], and atomic clocks [57]. In ref. [36], a differential free fall measurement of atoms in two different hyperfine states was also performed. Possible differences in gravitational interaction for bosonic and fermionic particles were also discussed [58, 59] and efforts towards experimental tests with different atoms are under way [59, 60].

The initial aim of my thesis project was the realization of a test of Einstein Equivalence Principle and search for spin-gravity coupling effects with two isotopes of strontium atoms. We performed an experimental comparison of the gravitational interaction for a bosonic isotope of strontium (^{88}Sr) which has zero total spin with that of a fermionic isotope (^{87}Sr) which has a half-integer spin. This represented

the first test of the WEP, for quantum probe masses with deeply different internal characteristics. Indeed, they do not only undergo different statistics (one is a boson, one is a fermion), but one has a spin, while the other is a spin-less particle. This was also a favorable system to look for possible existence of spin-gravity coupling effects. Gravity acceleration was measured by means of a genuine quantum effect, namely, the coherent delocalization of matter waves in an optical lattice. To compare gravity acceleration for the two Sr isotopes, we confined atomic wave packets in a vertical off-resonant laser standing wave and induced a dynamical delocalization by amplitude modulation of the lattice potential at a frequency corresponding to a multiple of the Bloch frequency ω_B, which is directly related to the gravity acceleration g. In conclusion of our experiment, we obtained upper limits of $\sim 10^{-7}$ for pure inertial effects and for a possible spin-gravity coupling.

In order to dramatically improve the future tests of general relativity, new interferometric schemes have to be employed. Because of this reason, in the second part of my Ph.D. fellowship, I started to develop a new scheme with the bosonic ^{88}Sr based on large-momentum-transfer Bragg pulses. Indeed, important goals are increase of the sensitivity of these devices as well as the demonstration of interferometry with atomic species other than alkali-earth atoms, which are most commonly used. For some experiments, indeed, the possibility of choosing the atomic species with the right characteristics is crucial. In particular, for precision measurements there is a considerable interest in using alkaline-earth or alkaline-earth-like atoms, such as Ca, Sr or Yb [9, 39, 42, 61–63], that are already used for the most advanced optical atomic clocks [64–66].

Alkaline-earth atoms have several characteristics that make them particularly interesting in this context. Firstly, their zero electronic angular momentum in the $^1S_0$ ground state makes these atoms less sensitive than alkali atoms to perturbation due to magnetic fields. Furthermore, they offer more flexibility thanks to the presence of both dipole allowed transitions and narrow intercombination transitions that can be used for efficient multi-photon Bragg diffraction [67–69] and for single-photon atom interferometry schemes [62, 70]. Finally, resonance transitions from the ground state are in the blue/near-UV (e.g., 461 nm for Sr, 399 nm for Yb) resulting in a larger momentum transferred to the atoms for the same diffraction order compared to alkali-metal atoms and hence in a correspondingly higher potential sensitivity of the interferometers.

In addition to the general features of alkaline-earth-metal atoms listed above, the ^{88}Sr isotope has specific favorable characteristics: it has no nuclear spin so that in the ground state it is a scalar particle which is virtually insensitive to stray magnetic fields, and its small scattering length ($a = -2a_0$) results in reduced decoherence due to cold collisions. On the other hand, since strontium has no hyperfine structure in the ground state, the usual schemes based on Raman transitions cannot be employed to realize the beam splitters and the mirrors for an interferometer. Therefore, we

used Bragg diffraction which, acting only on the atom's external degrees of freedom, can split the atomic wave packet into two momentum states separated by a even number of photon recoils while maintaining the same electronic state. We have studied the Bragg diffraction by a 461 nm laser standing wave up to eight photon recoils and we realized a vertical Mach-Zehnder interferometer with up to 60 ms of free fall time, demonstrating its performance as a gravimeter with a sensitivity $\delta g/g = 4 \times 10^{-8}$. The results were published in Physical Review A [71].

This dissertation is organized as follows:

Chapter 2 introduces the theoretical aspects of the physics of ultra-cold atoms and optical lattice potentials, which are at the basis of the two experimental methods used. In particular, I will discuss the main tools for coherent control of atomic motion, namely Bragg diffraction and Bloch oscillations. I will also introduce the characteristics of the techniques for gravity measurements.

Chapter 3 presents a general overview of the experimental apparatus for ultra-cold strontium atom experiments, in our laboratory at LENS. I will briefly discuss the main characteristics of strontium isotopes and their potential for high precision measurements.

Chapter 4 presents the experiment on the test of Einstein Equivalence Principle and spin-gravity coupling. The specific details of the experimental setup as well as the measurement results are discussed.

Chapter 5 presents the large-momentum-transfer Bragg interferometer experiment. I will discuss the characteristics of the setup we used, and I will presents the results of the Bragg diffraction and the Mach-Zehnder interferometer, providing the current performances of the gravimeter and the evaluation of the main noise sources.

Chapter 2

Coherent control of atomic motion with optical lattices and applications to inertial sensors

2.1 Atoms in optical lattices

In the first part of this section an introduction to the main concepts and notations to describe the dynamics of an atom in a laser field will be presented. A semi-classical approach will be taken in order to easily separate and calculate the force contributions. While the internal degrees of freedom of the atom will be treated in a quantum description, the external degrees of freedom will be treated with the classical equations of motion. Two force contributions will emerge from this analysis and one of them, the dipole force, will be the first ingredient to describe the interaction between an atom and an optical lattice. We will also present the dressed-atom picture which gives a useful physical interpretation of the dipole force, and it will be used to describe the two-photon transitions in the later section.

In the second part of this section the Bloch theorem will be used to describe the motion of an atom in an optical lattice in terms of the band structure. We will present a formal description of the system in the tight-binding limit, which will be useful to describe the delocalization coupling induced by an amplitude modulation of the lattice, later in this chapter.

2.1.1 Atom-light interaction

In this section we will mainly follow the theory developed by Cohen-Tannoudji [72–74].

Two-level atom

Let's consider an ideal system composed by a single atom A with an internal structure composed of just two levels $|g\rangle$ and $|e\rangle$, separated by an energy $E_e - E_g = \hbar\omega_A$, where ω_A is the so called atomic frequency. In its external degrees of freedom the atom is described by the spatial $\mathbf{R}$ and momentum $\mathbf{P}$ coordinates of the center of mass, and by the electric dipole moment $\mathbf{d}$.

Let's also consider a monochromatic laser radiation with frequency ω_L that can be represented by the coherent field

$$\mathbf{E}_L(\mathbf{r}, t) = \epsilon(\mathbf{r})\mathcal{E}(\mathbf{r})\cos(\omega_L t + \phi(\mathbf{r})), \tag{2.1}$$

where $\epsilon(\mathbf{r})$, $\mathcal{E}(\mathbf{r})$ and $\phi(\mathbf{r})$ are respectively the polarization, amplitude and phase of the field in $\mathbf{r}$.

The atom A is coupled to the laser field and to the vacuum field which contains all the modes that initially are not occupied by any photon. The atom-laser coupling $\mathcal{V}_{AL}$ can be analyzed in terms of the fundamental process of absorption and stimulated emission of laser photon by the atom. The atom-vacuum coupling $\mathcal{V}_{AV}$ is responsible for spontaneous emission of photon from the excited state. It is characterized by the natural linewidth $\gamma = 1/\tau_r$, where τ_r is the radiative time of $|e\rangle$. The Hamiltonian of the total system can then be divided in four terms:

$$\mathcal{H} = \mathcal{H}_A + \mathcal{H}_V + \mathcal{V}_{AL} + \mathcal{V}_{AV}. \tag{2.2}$$

The atomic Hamiltonian $\mathcal{H}_A$ contains the kinetic energy of the center of mass and the internal energy (we take $E_g = 0$):

$$\mathcal{H}_A = \mathcal{H}_A^{ext} + \mathcal{H}_{tot}^{int} = \frac{\mathbf{P}^2}{2M} + \hbar\omega_A |e\rangle\langle e| . \tag{2.3}$$

The Hamiltonian of the quantum radiation field $\mathcal{H}_V$ is the summation over all the modes of the electromagnetic field:

$$\mathcal{H}_V = \sum_j \hbar\omega_j \left(a_j^\dagger a_j + \frac{1}{2}\right). \tag{2.4}$$

The atom-laser coupling is the scalar product between the electric dipole moment and the laser electric field $\mathbf{E}_L$ of eq. (2.1):

$$\mathcal{V}_{AL} = -\mathbf{d}\cdot\mathbf{E}_L(\mathbf{R}, t). \tag{2.5}$$

The atom-vacuum coupling is

$$\mathcal{V}_{AV} = -\mathbf{d}\cdot\mathbf{E}(\mathbf{R}) = -\mathbf{d}\cdot\sum_j \left(i\sqrt{\frac{\hbar\omega_j}{2\epsilon_0 L^3}}\epsilon_j a_j e^{i\mathbf{k}_j\cdot\mathbf{R}} + h.c.\right), \tag{2.6}$$

where $a_j^\dagger$ (a_j) is the creation (annihilation) operator of a photon of momentum $\hbar\mathbf{k}_j$, energy $\hbar\omega_j = \hbar c k_j$ and polarization ϵ_j, L^3 is the quantization volume, and ϵ_0 is the electric permittivity.

If the laser field is not far from resonance, such that the detuning $\delta = \omega_L - \omega_A$ is small, one can apply the *rotating wave approximation*. The off-resonance terms $e^{-i\omega_L t} |g\rangle \langle e|$ (and $h.c.$) can be neglected, leading to a simpler form for the coupling

$$\mathcal{V}_{AL} = \frac{\hbar\Omega_1(\mathbf{R})}{2} \left[e^{-i\phi(\mathbf{R})} e^{-i\omega_L t} |e\rangle \langle g| + h.c. \right], \tag{2.7}$$

where we have written the electric moment in its diagonal components $\mathbf{d} = \mathbf{d}_{eg} |e\rangle \langle g| + \mathbf{d}_{ge} |g\rangle \langle e|$) since the atom does not have a dipole moment when it is in an energy eigenstate, and we have introduced the Rabi frequency Ω_1 as

$$\hbar\Omega_1(\mathbf{R}) = -\mathcal{E}(\mathbf{R})\mathbf{d} \cdot \epsilon(\mathbf{R}). \tag{2.8}$$

The same approximation can be done for the off-resonance terms $a_j |g\rangle \langle e|$ (and $h.c.$) in $\mathcal{V}_{AV}$.

Optical Bloch equations and Heisenberg equations of motion

The evolution of the system can be initially separated in the internal and external degrees of freedom. The evolution of the internal atomic states can be obtained in a density matrix description by solving the equation

$$i\hbar\dot{\rho} = [\mathcal{H}, \rho], \tag{2.9}$$

where $\rho = |\psi\rangle \langle\psi|$ is the density matrix built on the internal states basis $|g\rangle$ and $|e\rangle$. The solution of eq. (2.9) leads to the optical Bloch equations

$$\begin{pmatrix} \dot{u} \\ \dot{v} \\ \dot{w} \end{pmatrix} = \begin{pmatrix} -\gamma/2 & \delta + \dot{\phi} & 0 \\ -(\delta + \dot{\phi}) & -\gamma/2 & -\Omega_1 \\ 0 & \Omega_1 & -\gamma \end{pmatrix} \begin{pmatrix} u \\ v \\ w \end{pmatrix} + \begin{pmatrix} 0 \\ 0 \\ -\Gamma/2 \end{pmatrix} \tag{2.10}$$

where Ω_1 and ϕ are function of $\mathbf{R}(t)$, and we have introduced the variables u, v and w that describe the correlations between the states $|g\rangle$ and $|e\rangle$ and the population imbalance, and are related to the density matrix by

$$u(t) = \mathrm{Re}\rho_{ge}(t) e^{-i\omega_L t - i\phi(\mathbf{R}(t))} \tag{2.11}$$

$$v(t) = \mathrm{Im}\rho_{ge}(t) e^{-i\omega_L t - i\phi(\mathbf{R}(t))} \tag{2.12}$$

$$w(t) = \tfrac{1}{2}[\rho_{ee}(t) - \rho_{gg}(t)]. \tag{2.13}$$

The steady-state solution for eq. (2.10) is given by

$$u = \frac{\delta}{\Omega_1}\frac{s}{1+s}, \quad v = \frac{\gamma}{2\Omega_1}\frac{s}{1+s}, \quad w = -\frac{1}{1+s}, \tag{2.14}$$

where

$$s(\mathbf{R}) = \frac{\Omega_1^2(\mathbf{R})/2}{\delta^2 + \gamma^2/4} \tag{2.15}$$

is called saturation parameter. The $s = 1$ condition defines the saturation intensity $I_s = c\epsilon_0 E_L^2(\mathbf{R})/2$.

The dynamics of the center of mass of A can be studied with the Heisenberg equations for $\mathbf{R}$ and $\mathbf{P}$:

$$\dot{\mathbf{R}} = \frac{1}{i\hbar}[\mathbf{R}, \mathcal{H}] = \frac{\partial \mathcal{H}}{\partial \mathbf{P}} = \frac{\mathbf{P}}{M}, \tag{2.16}$$

$$\begin{aligned}\dot{\mathbf{P}} = M\ddot{\mathbf{R}} &= \frac{1}{i\hbar}[\mathbf{P}, \mathcal{H}] = -\frac{\partial \mathcal{H}}{\partial \mathbf{R}} \\ &= -\nabla \mathcal{V}_{AL}(\mathbf{R}) - \nabla \mathcal{V}_{AV}(\mathbf{R}) = \mathbf{F}(\mathbf{R}),\end{aligned} \tag{2.17}$$

where eq. (2.16) represents the center of mass velocity and eq. (2.17) represents the force operator $\mathbf{F}(\mathbf{R})$. Therefore, the equation of motion for the mean value of $\mathbf{R}$ calculated over the atomic wave functions is

$$M\left\langle \ddot{\mathbf{R}} \right\rangle = -\left\langle \nabla \mathcal{V}_{AL}(\mathbf{R}) + \nabla \mathcal{V}_{AV}(\mathbf{R}) \right\rangle. \tag{2.18}$$

The expectation value of $\mathbf{R}$ gives the position $\mathbf{r}$ of the center of the atomic wave packet, so $M\left\langle \mathrm{d}^2\mathbf{R}/\mathrm{d}t^2 \right\rangle = M\ddot{\mathbf{r}}$.

Semi-classical approximation and force contributions

Let's consider the initial time $t = 0$, at which the external atomic state is described by a wave function $\psi(\mathbf{r})$ centered on $\mathbf{r} = \langle \mathbf{R}(0) \rangle$ with a width $\Delta R(0)$. In the same way, the momentum has a mean value $\mathbf{p} = \langle \mathbf{P}(0) \rangle$ and a width $\Delta P(0)$, related to the position by an indetermination relation

$$\Delta R(0) \Delta P(0) \geq \hbar. \tag{2.19}$$

We can consider the force exerted on the atomic wave packet as semi-classical, i.e. with a very small fluctuation around its mean value, if two conditions are fulfilled. Firstly, the position spread $\Delta R(0)$ must be smaller than the spatial scale of variation of the laser field ($\lambda_L = 2\pi/k_L$):

$$\Delta R(0) \ll \lambda_L \quad \Leftrightarrow \quad k_L \Delta R(0) \ll 1. \tag{2.20}$$

Secondly, the velocity spread must be smaller enough to allow the corresponding spread of Doppler shift $k_L \Delta v(0)$ to be negligible respect to γ:

$$\frac{k_L \Delta P(0)}{M} \ll \gamma. \tag{2.21}$$

The eqs. (2.20) and (2.21) describe the localization of the wave packet. Multiplying both sides of the equations and using eq. (2.19) we get the compatibility condition with the Heisenberg indetermination relation

$$\frac{\hbar k_L^2}{M} \ll \gamma \quad \Leftrightarrow \quad E_r \ll \hbar\gamma, \tag{2.22}$$

where $E_r = \hbar^2 k_L^2 / 2M$ is the recoil energy of an atom when it absorbs or emits a photon. The corresponding recoil velocity is $v_r = \hbar k_L / M$.

In the semi-classical limit, the existence of two different time scales for the internal and external degrees of freedom is also necessary. In fact, the time scale for the internal degrees of freedom is related to the spontaneous emission $T_{int} = \tau_r = 1/\gamma$, while the time scale for the external degrees of freedom depends on the damping of the atomic velocity so that $T_{ext} = \hbar / E_r$. Equation (2.22) leads to the condition $T_{ext} \gg T_{int}$.

The localization conditions of eqs. (2.20) and (2.21) permit substitution of the position operator with its medium value $\langle \mathbf{R} \rangle = \mathbf{r}$. Therefore, the eq. (2.18) becomes

$$M \ddot{\mathbf{r}}_A = \sum_j \left\langle d_j \right\rangle \left[\nabla E_j \right]_{\mathbf{r},t}. \tag{2.23}$$

Because $T_{ext} \gg T_{int}$, we can uncouple the internal and external degrees of freedom, so that for an atom initially at rest $\mathbf{r} = \mathbf{0}$ we can use the stationary solutions (2.14) for $\langle \mathbf{d} \rangle$ which is calculated with the density matrix ρ:

$$\langle \mathbf{d} \rangle = \mathbf{d}(\rho_{ge} + \rho_{eg}) = \mathbf{d}[u \cos(\omega_L t + \phi(\mathbf{R})) - v \sin(\omega_L t + \phi(\mathbf{R}))]. \tag{2.24}$$

Therefore, using the definition of Rabi frequency (2.8) and the saturation parameter (2.15), we can get a final expression for the mean force

$$\mathbf{F}(\mathbf{r}) = -\hbar \left[\frac{\nabla \Omega_1(\mathbf{r})}{\Omega_1(\mathbf{r})} \delta + \frac{\gamma}{2} \nabla \phi(\mathbf{r}) \right] \frac{s(\mathbf{r})}{1 + s(\mathbf{r})} \tag{2.25}$$

which is the sum of two contributions, one proportional to the Rabi frequency gradient and one proportional to the phase gradient. They describe, respectively, the reactive and dissipative response of the atom to the laser excitation.

The dissipative term is also called radiation pressure force, or scattering force, since it originates from the absorption-spontaneous emission cycles. In fact, if the

laser field is approximated as a plane wave with a wave vector $\mathbf{k}_L$, the phase of the field is $\phi(\mathbf{r}) = -\mathbf{k}_L \cdot \mathbf{r}$, so that $\nabla\phi|_{r=0} = -\mathbf{k}_L$ and the dissipative term can be written in the form

$$\mathbf{F}_{\text{diss}} = \hbar\mathbf{k}_L \frac{\gamma}{2} \frac{s}{1 + s + (2\delta/\gamma)^2} \equiv \hbar\mathbf{k}_L \Gamma_s, \tag{2.26}$$

where we have introduced the rate Γ_s of photon momentum transfer to the atom. As a function of the detuning δ, $\mathbf{F}_{\text{diss}}$ is a Lorentz function centered on $\delta = 0$, which is expected for a dissipative process. The radiation pressure force is the main ingredient for standard laser cooling techniques.

The reactive term is the one responsible for the dipole interaction, and is the main ingredient for describing the dynamics of an atom in an optical lattice. We will discuss this term in more detail in the following section.

2.1.2 Dipole force

The reactive component of the force (2.25), also called dipole force $\mathbf{F}_{\text{dip}}$, is proportional to the gradient of the intensity through the Rabi frequency Ω_1. For a laser plane wave, in which the amplitude and polarization are independent of position, $\nabla\Omega_1$ vanishes, so that $\mathbf{F}_{\text{dip}} = \mathbf{0}$. The dipole force is present only in a superposition of plane waves, and since it is associated to the reactive response of the force, it cannot involve absorption of energy. These two properties suggest that the dipole force is associated to the redistribution of photons between the plane waves forming the laser field, via absorption and stimulated emission processes. The atom will not absorb energy during such a redistribution because all the plane waves have the same ω_L, however, since the momentum of the photons associated to the plane waves is different, there will be a net momentum transfer to the atom.

A more explicit form of $\mathbf{F}_{\text{dip}}$ can be written using the definition of the saturation parameter s defined by eq. (2.15):

$$\mathbf{F}_{\text{dip}} = -\frac{\hbar\delta}{4} \frac{\nabla\Omega_1^2}{\delta^2 + \gamma^2/4 + \Omega_1^2/2}. \tag{2.27}$$

In function of the detuning δ, the dipole force varies as a Lorentzian dispersion function, as expected for a reactive process. For red detuning ($\delta < 0$) the dipole force pushes the atoms towards the higher intensity regions, while for blue detuning ($\delta > 0$) the opposite holds true.

The conservative nature of the dipole force is clear when we write it in function of the potential

$$U(\mathbf{r}) = \frac{\hbar\delta}{2} \ln\left[1 + \frac{\Omega_1^2(\mathbf{r})/2}{\delta^2 + (\gamma^2/4)}\right], \tag{2.28}$$

so that $\mathbf{F}_{\text{dip}} = -\nabla U(\mathbf{r})$. While the dipole force is zero on resonance ($\mathbf{F}_{\text{dip}} = 0$ for $\delta = 0$), it dominates the radiation pressure force for large detunings ($|\delta| \gg \gamma$). In the limit of low intensity ($s \ll 1$) the potential can be approximated as

$$U(\mathbf{r}) \sim \hbar\Omega_1^2(\mathbf{r})/4\delta = \frac{\hbar\gamma^2}{8\delta} s(\mathbf{r}), \tag{2.29}$$

which takes the form of the *a.c. Stark effect* [75]. On the other hand, the scattering rate Γ_s defined in eq. (2.26) can be approximated as

$$\Gamma_s = \frac{\hbar\gamma^3}{8\delta^2} s. \tag{2.30}$$

The ratio between the two energy scales is proportional to the detuning

$$U/\hbar\Gamma_s \sim \delta/\gamma. \tag{2.31}$$

Therefore, to realize a dipole trap one typically requires a large detuning and a large intensity to keep the scattering rate, which is responsible for the decoherence, as small as possible for a fixed trapping depth. In the limit of large detuning, the rotating wave approximation cannot be applied, so the expression of the potential and the scattering rate have to be corrected [76]:

$$U(\mathbf{r}) = \frac{\hbar\Omega_1^2(\mathbf{r})}{4} \left(\frac{1}{\omega_L - \omega_A} - \frac{1}{\omega_L + \omega_A} \right), \tag{2.32}$$

$$\Gamma_s(\mathbf{r}) = U(\mathbf{r}) \frac{\gamma}{\hbar} \left(\frac{\omega_L}{\omega_A} \right)^3 \left(\frac{1}{\omega_L - \omega_A} - \frac{1}{\omega_L + \omega_A} \right), \tag{2.33}$$

while the considerations done up to now still hold.

Focused-beam traps

Let us now consider the more realistic case of far off-resonance laser beam with a Gaussian profile propagating along the z direction. The spatial intensity distribution of a Gaussian beam with power P is

$$I(r, z) = \frac{2P}{\pi w^2(z)} \exp\left(-\frac{2r^2}{w(z)} \right), \tag{2.34}$$

where r is the radial direction and $w(z)$ is the $1/e^2$ radius:

$$w(z) = w_0 \sqrt{1 + \left(\frac{z}{z_R} \right)^2}. \tag{2.35}$$

Here, w_0 is the beam waist and $z_R = \pi w_0^2/\lambda_L$ is the Rayleigh length. One can derive the trapping potential by using the intensity profile in the eq. (2.32). Since the Rayleigh length is larger than the beam waist, the potential in the radial direction is much steeper than in the axial direction.

If the thermal energy of the atomic sample $k_B T$ (where k_B is Boltzmann constant) is smaller than the potential depth U_0, the extension of the atomic cloud is radially small compared to the waist and axially small respect to the Rayleigh length. In this condition, the optical potential can be approximated as a harmonic trap with two frequencies ω_z and ω_r:

$$U(r,z) \simeq -U_0 \left[1 - 2\left(\frac{z}{z_R}\right)^2 - 2\left(\frac{r}{w_0}\right)^2 \right]. \tag{2.36}$$

The corresponding trapping frequencies for the radial and the axial direction are $\omega_r = (4U_0/Mw_0^2)^{1/2}$ and $\omega_z = (4U_0/Mz_R^2)^{1/2}$ respectively.

It is important to remark that for a focused beam the typical trapping potential along the beam axis is not enough to compensate for the gravitational force, while the strong radial confinement can minimize the perturbation effect of gravity. For this reason such traps are usually aligned in the horizontal plane. As we will see in the next section, a standing-wave trap can overcome this issue.

Dressed-atom picture

As we observed in the previous section, the semi-classical approximation leads to expressions for the force components which are average values of the atomic internal operators and field operators taken at the center of the atomic wave packet $\mathbf{r}$. In this approach, the atom-field interaction was represented in terms of the atomic eigenstates. Another useful approach for the physical interpretation of the dipole force is the dressed-atom picture [77–79], in which all or part of the coupled atom-field system is solved exactly and the resultant atom-field eigenstates are used as the basis for further calculations.

In absence of coupling, the energy levels of the total system (atom + laser modes) are labeled by two quantum numbers: e, g for the atom and n for the number of photons in the laser mode of frequency ω_L. The eigenstates are divided in manifolds $\mathcal{E}_n$ separated by the energy $\hbar\omega_L$, consisting of the two states $|g, n+1\rangle$ and $|e, n\rangle$.

If we write the atomic Hamiltonian (2.3) in terms of the lowering and rising operators $b = |g\rangle\langle e|$ and $b^\dagger = |e\rangle\langle g|$, and the atom-laser coupling $\mathcal{V}_{AL}$ of eq. (2.5) in the semi-classical approximation, the dressed-atom Hamiltonian at position $\mathbf{r}$ is

$$\mathcal{H}_{DA}(\mathbf{r}) = \hbar(\omega_L - \delta)b^\dagger b + \hbar\omega_L a^\dagger a - [\mathbf{d}\cdot\mathcal{E}_L(\mathbf{r})b^\dagger a + \mathbf{d}\cdot\mathcal{E}_L^*(\mathbf{r})ba^\dagger] \tag{2.37}$$

in which we haven't written the interaction $\mathcal{V}_{AV}$ of eq. (2.6) because in the dressed-atom basis it is null, and also note that since this treatment is done at a given position r, we omitted the kinetic energy in $\mathcal{H}_A$.

The atom-laser coupling connects only the two states of a given manifold, i.e. transitions between g and e with the absorption of one laser photon:

$$\langle e, n| \mathcal{V}_{AL} |g, n+1\rangle = -\sqrt{n+1}\, \mathbf{d} \cdot \mathcal{E}_L(\mathbf{r}) \equiv \tfrac{\hbar}{2}\Omega_1(\mathbf{r}) e^{i\phi(\mathbf{r})}. \tag{2.38}$$

Therefore, the Rabi frequency $\Omega_1(\mathbf{r})$ actually depends on the number of photons in the manifold, but we will neglect this dependence supposing that the laser field is initially excited in a coherent state with a Poisson distribution for n, for which the width Δn is very small compared with the average number of photons. Under this approximation, the eigenvalues of $\mathcal{H}_{DA}$ for the manifold $\mathcal{E}_n$ are

$$\begin{aligned} E_{1n}(\mathbf{r}) &= (n+1)\hbar\omega_L - \tfrac{\hbar}{2}\delta + \tfrac{\hbar}{2}\Omega_{DA}(\mathbf{r}), \\ E_{2n}(\mathbf{r}) &= (n+1)\hbar\omega_L - \tfrac{\hbar}{2}\delta - \tfrac{\hbar}{2}\Omega_{DA}(\mathbf{r}), \end{aligned} \tag{2.39}$$

where $\Omega_{DA}(\mathbf{r}) = \sqrt{\Omega_1^2(\mathbf{r}) + \delta^2}$. The corresponding eigenstates (dressed states) are $|1, n; \mathbf{r}\rangle$ and $|2, n; \mathbf{r}\rangle$, linear combinations of the uncoupled states $|g, n+1\rangle$ and $|e, n\rangle$:

$$\begin{aligned} |1, n; \mathbf{r}\rangle &= +e^{i\phi(\mathbf{r})/2} \cos\theta(\mathbf{r}) |e, n\rangle + e^{-i\phi(\mathbf{r})/2} \sin\theta(\mathbf{r}) |g, n+1\rangle, \\ |2, n; \mathbf{r}\rangle &= -e^{i\phi(\mathbf{r})/2} \sin\theta(\mathbf{r}) |e, n\rangle + e^{-i\phi(\mathbf{r})/2} \cos\theta(\mathbf{r}) |g, n+1\rangle, \end{aligned} \tag{2.40}$$

where the angle $\theta(\mathbf{r})$ is defined as $\cos(2\theta(\mathbf{r})) = -\delta/\Omega_{DA}(\mathbf{r})$ and $\sin(2\theta(\mathbf{r})) = -\Omega_1(\mathbf{r})/\Omega_{DA}(\mathbf{r})$. The energy diagram for the dressed-atom states is depicted in fig. 2.1.

In an inhomogeneous laser beam (as is the case for a Gaussian beam), the eigenstates will vary with the position $\mathbf{r}$ (fig. 2.1c). Outside of the beam, the dressed levels coincide with the bare ones, split by $\hbar\delta$ in the manifold. Inside the beam each dressed state is a linear superposition of the bare states with an energy splitting of $\hbar\Omega_{DA}(\mathbf{r})$ larger than $\hbar\delta$. This result is just another expression for the a.c. Stark shift.

For an atom initially at rest ($\mathbf{r} = \mathbf{0}$) the mean value of the dipole force can be written in the dressed atom base as

$$\mathbf{F}_{\text{dip}} = \tfrac{\hbar}{2}\nabla\Omega_{DA}(\rho_{22} - \rho_{11}), \tag{2.41}$$

where ρ_{11} and ρ_{22} are the steady-state density matrix element describing the populations of $|1, n; \mathbf{r}\rangle$ and $|2, n; \mathbf{r}\rangle$. It can be shown that the steady-state solution for these populations are [79]

$$\rho_{11}(\mathbf{r}) = \frac{\sin^4\theta(\mathbf{r})}{\sin^4\theta(\mathbf{r}) + \cos^4\theta(\mathbf{r})}, \quad \rho_{22}(\mathbf{r}) = \frac{\cos^4\theta(\mathbf{r})}{\sin^4\theta(\mathbf{r}) + \cos^4\theta(\mathbf{r})}. \tag{2.42}$$

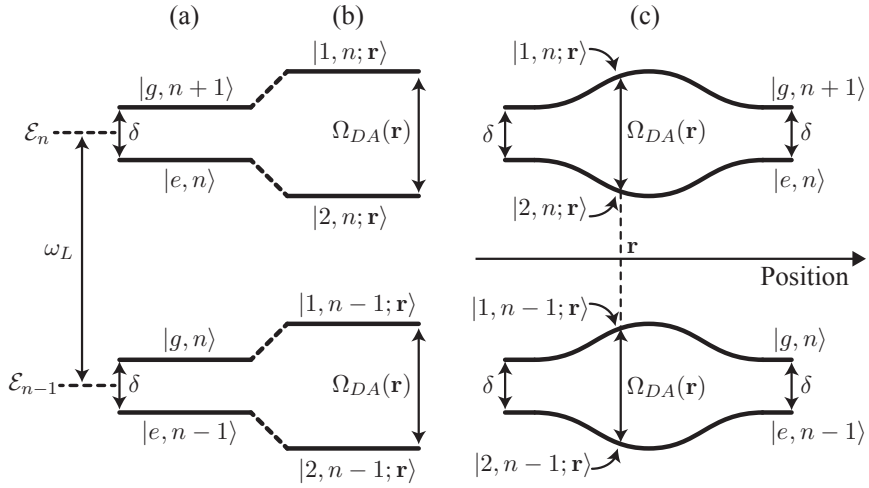

Figure 2.1: Dressed-atom energy diagram. (a) Energy manifolds without coupling. (b) In presence of a position-dependent coupling the energy of each manifold splits by $\Omega_{DA}(\mathbf{r})$. (c) Energy splitting as a function of the position for a Gaussian laser beam. Outside the beam the energy levels connect with the uncoupled states of (a).

Therefore, the mean dipole force becomes

$$\mathbf{F}_{\text{dip}} = -\hbar\delta \frac{\Omega_{DA}}{\Omega_1^2 + 2\delta^2} \nabla\Omega_{DA} = -\nabla \left[\frac{\hbar\delta}{2} \ln\left(1 + \frac{\Omega_1^2}{2\delta^2}\right)\right], \tag{2.43}$$

which is the same expression as eq. (2.28) derived from the Optical Bloch equations in the limit $\delta \gg \gamma$.

The dressed-atom approach gives a simple interpretation of the dependence of $\mathbf{F}_{\text{dip}}$ on the sign of the detuning. If $\delta > 0$ the levels 1 are those that coincide with $|g, n+1\rangle$ outside the laser beam. They are less contaminated by $|e, n\rangle$ than levels 2 so less spontaneous emission occurs from levels 1 than from levels 2. It follows that the levels 1 are more populated than levels 2. The resulting force from levels 1 is then dominant, and the atom is pushed out of the high-intensity regions. For $\delta < 0$ the opposite is true: levels 2 are more populated and the atom is attracted in the high-intensity regions.

2.1.3 Optical lattices

As we have discussed in the previous section, a dipole trapping potential is present just in presence of plane waves superposition, and the case of a Gaussian beam was analyzed. Let's now consider the superposition of two counter-propagating plane waves with wave vector $\pm\mathbf{k}_L$ along the z direction, polarization along x and same

amplitude $\mathcal{E}_0$

$$\begin{aligned}\mathbf{E}(z,t) &= \epsilon_x \mathcal{E}_0 \cos(\omega_L t - k_L z) + \epsilon_x \mathcal{E}_0 \cos(\omega_L t + k_L z) \\ &= 2\epsilon_x \mathcal{E}_0 \cos k_L z \cos \omega_L t = 2\epsilon_x \mathcal{E}(z) \cos \omega_L t,\end{aligned} \tag{2.44}$$

which has a position dependent amplitude $\mathcal{E}(z)$, and an average intensity

$$I(z) = 4I_0 \cos^2 (k_L z), \tag{2.45}$$

where I_0 is the single-beam intensity. In the limit of large detuning the potential can be written using eq. (2.29)

$$U(z) = \frac{U_0}{2} \cos^2(2k_L z), \quad \text{where} \quad U_0 = -\frac{\hbar\gamma^2}{2\delta} s \tag{2.46}$$

is the potential depth. The result is a standing-wave with an intensity profile pattern with a periodicity of $\lambda_L/2$, and it is also called one-dimensional optical lattice. For $\delta > 0$ the atoms will be trapped in the minima of the light intensity pattern, while for $\delta < 0$ they will be trapped in the maxima. Around its minima, the potential (2.46) can be approximated as a harmonic oscillator with a trapping frequency $\omega_{latt} = k_L \sqrt{4U_0/M}$. It can also be extended to the case of two counter-propagating Gaussian beams, so using eq. (2.36)

$$U(r,z) \simeq -\frac{U_0}{2} \cos^2 (2k_L z) \left[1 - 2\left(\frac{z}{z_R}\right)^2 - 2\left(\frac{r}{w_0}\right)^2\right]. \tag{2.47}$$

which has a potential depth four times larger along the z direction with respect to the single beam, and a new axial trapping frequency $\omega_{z'} = \sqrt{\omega_z^2 + \omega_{latt}^2} \simeq \omega_{latt}$. This leads to a strong confinement in the lattice nodes (or antinodes), which is able to compensate for the gravity force once the lattice is aligned along the vertical direction.

Bloch theorem and band structure

The Hamiltonian of an atom in a 1D optical lattice, once we neglect the radial contribution in the potential of eq. (2.47), is simply given by

$$\mathcal{H} = \frac{p^2}{2M} - \hbar \frac{U_0}{2} (1 + \cos 2k_L z). \tag{2.48}$$

The solutions of this periodic Hamiltonian can be derived by the well known theorem formulated by Bloch in the context of solid-state physics [80] (extensive dissertations can be found in refs. [81, 82]).

The Hamiltonian is invariant under translations of multiples of the distance $d = \lambda_L/2$, i.e. it commutates with the translation operator

$$T_d = \exp\left(i\frac{dp}{\hbar}\right). \tag{2.49}$$

Therefore, the solutions of the Hamiltonian are the eigenstates $|q, j\rangle$ and eigenvalues $E_j(q)$ of T_d, that can be labeled by a discrete band index j and a continuous quasimomentum q. The corresponding eigenfunctions are

$$\psi_{q,j}(z) = \langle z|q, j\rangle = e^{iqz}u_{q,j}(z), \tag{2.50}$$

where $u_{j,q}(z)$ are functions with the same spatial periodicity d of the lattice. The eigenstates $|q, j\rangle$ are called *Bloch states*. The phase is always defined modulo 2π, so the quasimomentum q is defined modulo $2\pi/d = 2k_L$. The Bloch states and their eigenvalues $E_j(q)$ are conventionally represented in the first Brillouin zone $q \in]-k_L, +k_L]$. For each j, the set of energy levels specified by $E_j(q)$ is called an *energy band*. Figure 2.2 shows the first three energy bands for the case of the free particle and for two different lattice depths U_0. The energies are numerically calculated with the Kronig-Penny model [83].

Even if in many ways the quasimomentum q is a natural extension of the momentum p to the case of periodic potential, one can not consider it as a momentum on its own. Only in the presence of an external field does the dynamical significance of q emerge. Up to now q has to be considered solely as a quantum number

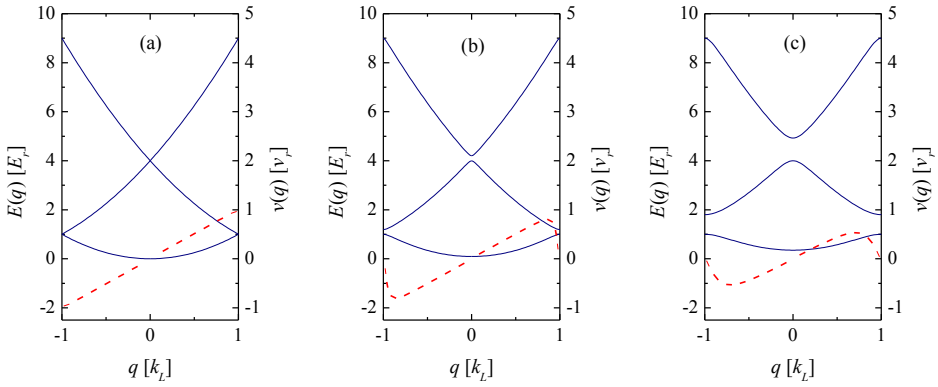

Figure 2.2: The first three energy bands $E_j(q)$ numerically calculated with the Kronig-Penny model [83] (solid blue line) and the group velocity $v(q)$ for the lowest band (red dashed line), in the case of: (a) free particle, (b) weak-binding limit $U_0 = E_r$, (c) tight-binding limit $U_0 = 5E_r$. In presence of a periodic structure a gap opens at the edges $q = \pm k_L$ of the Brillouin zone.

characteristic of the translational symmetry of the lattice, just as the momentum p is a quantum number for the full translational symmetry of a free particle.

It can be shown [81] that a wave packet in a level specified by the band index j and quasimomentum q has a group velocity

$$v_j(q) = \frac{1}{\hbar}\nabla_q E_j(q). \tag{2.51}$$

This means that there are stationary levels for which, despite the interaction with the lattice, the particle moves forever without any degradation of its mean velocity. The group velocity for the lowest band is reported in fig. 2.2 for three different lattice depths U_0.

In general, the solution for the eigenvalues $E_j(q)$ needs to be numerically calculated from the Hamiltonian (2.48). There are two limits for which the eigenvalues can be analytically calculated: the weak-binding limit and the tight-binding limit.

In the tight-binding limit (fig. 2.2c) the lattice depth is high enough to localize the particle in the lattice sites. The spatial extension of the wave packet reduces to less than $\lambda_L/2$, so its momentum is larger than $2\hbar k_L$ and its kinetic energy is larger than $4E_r$. This means that the lattice depth has to be $U_0 \gg 4E_r$. In this limit, the eigenvalues $E_j(q)$ are mostly dependent (for low j) on the band index j and not on the quasimomentum q.

In the weak-binding limit $U_0 \ll E_r$ (fig. 2.2b), the optical lattice is a small perturbation to the free particle. In this limit, the eigenstates of the system are the momentum eigenstates of the free particle and the lattice couples these states only at the edges of the Brillouin zone, for which $q \simeq \pm k_L$. This means that the coupled momentum eigenstates of the free particle are $|p_0\rangle$ and $|p_0 + 2\hbar k_L\rangle$, where p_0 is the initial momentum of the particle. This represents a *Bragg transition* and it will be discussed widely in the next sections.

Tight-binding model and Bloch tunneling

We will now focus on the tight-binding limit, which will give us an interesting description of the quantum transport properties in a lattice.

The Bloch theorem tell us that we can write the Bloch states $|q, j\rangle$ as a superposition of plane waves $\left|\Phi_{n,j}\right\rangle$, with $n \in \mathbb{Z}$ indexing the n-site position

$$|q, j\rangle = \sum_n e^{indq} \left|\Phi_{n,j}\right\rangle, \tag{2.52}$$

where $\left|\Phi_{n,j}\right\rangle$ form a discrete set of states, called *Wannier states* [84]. The inverse relation of eq. (2.52) is

$$\left|\Phi_{n,j}\right\rangle = \int_{BZ} e^{-indq} \, |q, j\rangle \, \mathrm{d}q, \tag{2.53}$$

where the integration is extended over the first Brillouin zone. Since the Bloch states are orthogonal with a normalization $\langle q', j|q, j\rangle = \delta(q' - q)$, the Wannier states also form an orthogonal base, with normalization $\left\langle \Phi_{n',j}|\Phi_{n,j} \right\rangle = \delta_{n',n}$. This means that they have a finite spatial extension. Substituting the Bloch theorem (2.49) into eq. (2.1.3) shows that $T_d \left|\Phi_{n,j}\right\rangle = \left|\Phi_{n+1,j}\right\rangle$, so that $\left|\Phi_{n,j}\right\rangle$ is related to $\left|\Phi_{0,j}\right\rangle$ by a translation of n sites.

Let's now assume that the atomic sample is cold enough so that only the lowest band of the potential is populated, allowing us to neglect the band index j. In the tight-binding limit, the lowest state of the atom in one potential well is only coupled to its nearest neighbors. We can then assume that the Wannier state $|\Phi_n\rangle$ is mainly located within a single site at position $x_n = nd$. The Hamiltonian for such a system is

$$\mathcal{H} = -\frac{J}{4} \sum_n |\Phi_{n+1}\rangle \langle \Phi_n| + h.c. \tag{2.54}$$

where J is the tunneling energy, and depends on the potential depth U_0. The eigenvalues of the Hamiltonian calculated on the Bloch states base set $|q\rangle$ gives the energy spectrum for the lowest band

$$E(q) = -\frac{J}{2} \cos(dq). \tag{2.55}$$

It can be seen in fig. 2.2c that as the depth of the lattice increases, the first energy band and its corresponding mean velocity can be better approximated by a sinusoidal function.

As an easy application of the tight-binding model, we will evaluate the coherent spreading of an atomic wave packet which is tunneling between the lattice sites [85]. Let's consider the initially localized state in the well $x_0 = 0$, $|\psi(t = 0)\rangle = |\Phi_0\rangle$, with a Gaussian spatial extension $\Delta x(0)$ and with wave vector q. The average position moves according to the group velocity of eq. (2.51) where the dispersion relation is (2.55):

$$\langle x(t)\rangle = v(q)t = \frac{Jt}{4\hbar} \sin(dq), \tag{2.56}$$

and the width of the wave packet, in the limit of $\Delta x(0) \gg \lambda_L$, expands according to

$$\langle \Delta x(t)\rangle^2 = \Delta x^2(0) \left[1 + \frac{J^2 t^2}{32\hbar^2 \Delta x^4(0)} \left(1 + \cos(dq)\right)\right]. \tag{2.57}$$

As anticipated, because of the Bloch tunneling, the wave packet propagates indefinitely without any change in its mean velocity. Importantly, we notice that for

particular values of $q = \pm k_L/2$ the wave packet moves without spreading. This provides an efficient mechanism to coherently manipulate atoms in optical lattices.

Later in this chapter, the tight-binding model will be used to describe the delocalization coupling induced by an amplitude modulation of the lattice.

2.2 Traveling optical lattices

In the previous section we discussed the interaction and dynamics of an atom trapped in a steady optical lattice, realized by superposing two laser fields with the same frequency ω_L and opposite wave vector k_L. If we set different frequencies for the two beams we obtain a traveling standing wave. We will see that the main phenomena arising from such a system are two-photon transitions. If the difference in frequency changes linearly with time, the lattice is accelerated and Bloch oscillations take place. The same phenomenon happens when an external force, such as the gravity force, is applied to a steady lattice.

2.2.1 Two-photon transitions: Bragg diffraction

Let's consider two counter-propagating laser beams with slightly different frequencies $\Delta\omega = \omega_1 - \omega_2 \ll \delta \ll \omega_1, \omega_2 \sim \omega_L$. The resulting field, according to eq. (2.44), is a traveling standing wave

$$\mathbf{E}(z,t) = 2\epsilon_x \mathcal{E}_0 \cos(k_L(z - vt)) \cos \omega_L t, \tag{2.58}$$

where v is the propagation velocity

$$v = \frac{\Delta\omega}{2k_L}. \tag{2.59}$$

This velocity corresponds to the velocity of the reference frame in which the two waves have the same frequency due to the opposing Doppler shift.

In presence of a traveling optical lattice, an atom will be able to absorb a photon at ω_1 from one beam and undergo stimulated emission of a photon at ω_2 into the other beam. This is a resonant process called *Bragg diffraction*. During the simultaneous absorption and re-emission of a photon, the lattice will transfer a net momentum to the atom $\hbar(k_1 + k_2) \sim 2\hbar k_L$. The intermediate state in which the atom has absorbed one photon is out of resonance, so the spontaneous emission is strongly suppressed.

The resonance condition results from the conservation of energy and momentum

$$\tfrac{1}{2}Mv_i^2 + \hbar\omega_1 = \tfrac{1}{2}Mv_f^2 + \hbar\omega_2, \tag{2.60}$$

$$M\mathbf{v}_i + \hbar\mathbf{k}_1 = M\mathbf{v}_f + \hbar\mathbf{k}_2, \tag{2.61}$$

where $\mathbf{v}_i$ and $\mathbf{v}_f$ are the initial and final velocity of the atom, and we have considered an arbitrary direction for the input velocity and the wave vectors of the two waves. The resonance condition for the frequency difference is

$$\Delta\omega = (\mathbf{k_1} - \mathbf{k}_2) \cdot \left(\mathbf{v}_i + \frac{\hbar}{2M}(\mathbf{k}_1 - \mathbf{k}_2)\right) \tag{2.62}$$

which contains two terms: the Doppler shift and the energy recoil. In the counter-propagating configuration ($\mathbf{k}_1 \sim -\mathbf{k}_2$), to be on resonance with an atom at rest ($\mathbf{v}_i = \mathbf{0}$) the lasers need to be shifted by four times the recoil energy

$$\hbar\Delta\omega = 4E_r = 4\hbar\omega_r, \tag{2.63}$$

where we have introduced the recoil frequency

$$\omega_r = \frac{\hbar k_L^2}{2M}. \tag{2.64}$$

The situation we described is the simplest one. The frequency difference can be increased to induce higher-order resonances in which more pairs of photon can simultaneously transfer momentum to the atom. For an atom initially at rest, the interaction with the traveling standing wave can transfer $2n$-photon momenta to the atom, so that discrete momentum states $\left|p = 2n\hbar k_L, E = 4n^2E_r\right\rangle$ on the momentum-energy parabola of the free particle can be occupied. If the atom is initially occupying one of these states, let's say the $\left|p = 2m\hbar k_L, E = 4m^2E_r\right\rangle$ state, the resonance condition for an n-order Bragg diffraction to the state $\left|p = 2(m+n)\hbar k_L, E = 4(m+n)^2E_r\right\rangle$ is

$$n\Delta\omega = 4n(2m+n)\omega_r. \tag{2.65}$$

Figure 2.3 depicts a 2nd order Bragg transition in the momentum-energy plot.

Viewing Bragg scattering as a two-photon transition from the initial ground state to the final ground state with a momentum difference of $2\hbar k_L$ shows the close connection with a Raman transition between two internal hyperfine states of the ground state manifold, each with its own external momentum state. The main difference resides in the fact that because of the change in the internal state, Raman transitions can not transfer more than two-photon recoils at the time. Another change in the internal state is required to transfer momentum in the same direction. On the other hand, Bragg transitions can transfer, in principle, an infinite number of photon momenta during the same interaction. We will explain how this is limited experimentally in the following chapters.

Since the atom always remains in the same internal state during this process, the coupling between all the possible momentum states has to be taken into account. To calculate the transition probabilities and coupling between different momentum states, one can use the dressed-atom picture we have introduced in section 2.1.2.

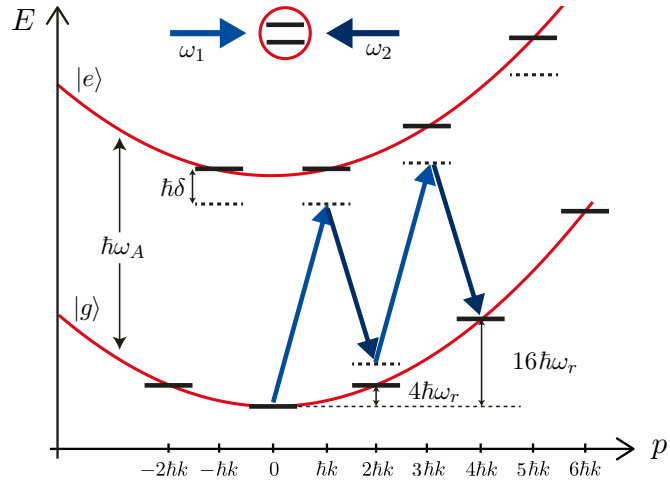

Figure 2.3: Second-order Bragg diffraction represented in the momentum-energy plot. The two-level atom interacts with two counter-propagating waves with a frequency difference $\Delta\omega = \omega_1 - \omega_2 \ll \delta$ tuned on resonance with a 4-photon transition. The atom receives a kick $\Delta p = 4\hbar k_L$.

Hamiltonian of Bragg transitions

In the dressed-atom picture, the Hamiltonian of a two-level atom in presence of two electromagnetic fields with amplitude $\mathcal{E}_L$ and frequencies ω_1 and ω_2 takes a form analogous to the one of eq. (2.37)

$$\mathcal{H} = \frac{p^2}{2m} + \hbar\omega_0 b^\dagger b + \hbar\omega_1 a_1^\dagger a_1 + \hbar\omega_2 a_2^\dagger a_2 - [\mathbf{d}\cdot\mathcal{E}_L(b^\dagger a_1 + b a_2^\dagger) + h.c.] \quad (2.66)$$

where in this case $a_1^\dagger a_1$ and $a_2^\dagger a_2$ are the number operators for photons of energy ω_1 and ω_2 respectively. The eigenstates of the system are $|i, \mathbf{p}, N_1, N_2\rangle$, where $i = g, e$ is the internal state, were $\mathbf{p}$ is the momentum of the atom and N_l is the number of photons in the mode $l = 1, 2$.

The interaction operator is composed of two terms $\mathcal{V}_{AL} = \mathcal{V}_1 + \mathcal{V}_2$, both products of the dipole operator and the photon field operator. The dipole operator $\mathbf{d}$ couples the two atomic states $|g\rangle$ and $|e\rangle$, while the number operators $a_1^\dagger a_1$ and $a_2^\dagger a_2$ are responsible for the coupling between the two modes of the field. The photon field 1 will couple the states $|g, \mathbf{p}, N_1, N_2\rangle$ and $|e, \mathbf{p} - \hbar\mathbf{k}_1, N_1 + 1, N_2\rangle$, so we can define the Rabi frequency for the field 1 as:

$$\langle g, \mathbf{p}, N_1, N_2|\,\mathcal{V}_1\,|e, \mathbf{p} - \hbar\mathbf{k}_1, N_1 + 1, N_2\rangle = \hbar\Omega_1/2, \quad (2.67)$$

where we have not taken into account the spatial dependence of the electric field, so the phase term is constant and it will be neglected. In the same way we can

define the Rabi frequency Ω_2. In typical conditions, $\Delta\omega$ is in the order of kHz while the $\Omega_1 \simeq \Omega_2$ are in the MHz range and the detuning δ in the GHz range. It is then possible to neglect the contribution from the excited states. The only difference between the initial and final state will be the kinetic energy. We can define a two-photon Rabi frequency

$$\Omega = \frac{\Omega_1 \Omega_2}{2\delta} \simeq \frac{\Omega_1^2}{2\delta} \tag{2.68}$$

that couples the state $|g, \mathbf{p}, N_1, N_2\rangle$ to the states $|g, \mathbf{p} + 2\hbar\mathbf{k}_L, N_1 - 1, N_2 + 1\rangle$ and $|g, \mathbf{p} + 2\hbar\mathbf{k}_L, N_1 + 1, N_2 - 1\rangle$.

Since the atom always remains in its internal ground state, we have to also consider the coupling to states in which two photons were absorbed and two photons were re-emitted and so on. This means that $|g,\mathbf{p}+2\hbar\mathbf{k}_L,N_1+1,N_2-1\rangle$ will be coupled to $|g,\mathbf{p}+4\hbar\mathbf{k}_L,N_1+2,N_2-2\rangle$, which is coupled to $|g,\mathbf{p}+6\hbar\mathbf{k}_L,N_1+3,N_2-3\rangle$, and so on. Therefore, we have to consider an infinite number of states labeled by the integer number n:

$$|\mathbf{p}, n\rangle = |g, \mathbf{p} + 2n\hbar\mathbf{k}_L, N_1 + n, N_2 - n\rangle\,. \tag{2.69}$$

If the initial state has a definite momentum $\mathbf{p}$, it will remain in the basis of the $|\mathbf{p}, n\rangle$ states. In the simplest approach, we can apply perturbation theory [86] of the first order in the interaction coupling $\mathcal{V}_{AL}$. Thus, the Hamiltonian can be written in the basis $|\mathbf{p}, n\rangle$ and takes the matrix form [87]

$$\mathcal{H} = \hbar \begin{pmatrix} \ddots & \kappa & 0 & \cdots & 0 & \cdots & 0 \\ \kappa & q_{-n} & \kappa & \ddots & \vdots & & \vdots \\ 0 & \kappa & \ddots & \kappa & 0 & & 0 \\ \vdots & \ddots & \kappa & q_0 & \kappa & \ddots & \vdots \\ 0 & \cdots & 0 & \kappa & \ddots & \kappa & 0 \\ \vdots & & \vdots & \ddots & \kappa & q_n & \kappa \\ 0 & \cdots & 0 & \cdots & 0 & \kappa & \ddots \end{pmatrix} \tag{2.70}$$

where $\hbar q_n = (\mathbf{p} + 2n\hbar\mathbf{k}_L)^2/2M + n\hbar\Delta\omega + \hbar\Omega$ contains the light shift $\hbar\Omega$, and $\hbar\kappa = \hbar\Omega/2$ is the effective coupling between states separated by $2\hbar\mathbf{k}_L$. We notice that momenta differing from the resonant momentum $\mathbf{p} = 2n\hbar\mathbf{k}_L$ lead to a Doppler shift $\mathbf{k}\cdot\mathbf{v} = \mathbf{p}\cdot 2n\mathbf{k}_L/M$ which acts as a detuning. This shows that only a momentum class around the resonance is diffracted, while the diffraction of other momentum classes is suppressed. This phenomenon is known as velocity selectivity [88, 89] and can be used to create atomic samples with a narrower momentum distribution.

If we introduce the interaction time between a traveling standing-wave and the atom, we can induce Rabi oscillations between momentum states. This process forms the basis of the matter wave optics used in free-falling atom interferometry. The time dependence of Bragg transitions will be discussed later in this chapter.

Steady lattice interpretation

We will now try to give an interpretation of a steady lattice in terms of the model we just described. If we consider the spatial dependence of the electric field, we need to include a phase term in the effective coupling operator $\mathcal{V}_{AL}$ responsible for transitions from the state $|\mathbf{p}\rangle$ to the states $|\mathbf{p} + 2n\hbar\mathbf{k}_L\rangle$ and $|\mathbf{p} - 2n\hbar\mathbf{k}_L\rangle$:

$$\mathcal{V}_{AL} = \frac{\hbar\Omega}{2}\left(e^{i2k_Lz} + e^{-i2k_Lz}\right). \tag{2.71}$$

In the semi-classical limit of a high number of photons, we can consider the classical electromagnetic field. The Hamiltonian (2.66) in the case $\omega_1 = \omega_2$ becomes

$$\mathcal{H} = \frac{p^2}{2M} - \hbar\frac{\Omega}{4}\left(1 + \cos 2k_Lz\right) \tag{2.72}$$

which is the classical expression for the Hamiltonian of an atom in an optical lattice, like the one in eq. (2.48). By comparison, we see that $\Omega = U_0/2$, where U_0 is the lattice depth.

Let's now consider the band structure picture of the lattice in the weak-binding limit. In section 2.1.3 we touched on the fact that the atom can be considered a free particle and the lattice only couples the momentum eigenstates at the edges of the Brillouin zone, let's say $q - 2k_L$ and q. In this case, the Hamiltonian (2.70) can be simply written in a 2×2 form

$$\mathcal{H} = \hbar\begin{pmatrix} q - 2k_L & \kappa \\ \kappa & q \end{pmatrix} \tag{2.73}$$

that can be easily diagonalized. The energies are significantly different from the one of a free particle when $|q - k_L| \leq \kappa$. The energy gap between the first and the second band is then $2\hbar\kappa = \hbar\Omega$. As a result, we can interpret the coupling between momentum eigenstates at the edges of the Brillouin zone as first-order Bragg transitions.

2.2.2 Accelerated optical lattices: Bloch oscillations

If we now consider the possibility to tune the frequency difference $\Delta\omega(t)$ between the two waves linearly in time, the resulting field will be an accelerated standing wave in the laboratory frame. On the other hand, in the frame of the lattice, the atom will experience a constant inertial force in addition to the effect of the periodic potential.

If $\Delta\omega(t)$ is swept, we impose an acceleration on the lattice

$$a = \frac{\mathrm{d}v}{\mathrm{d}t} = \frac{1}{2k_L}\frac{\mathrm{d}\Delta\omega}{\mathrm{d}t}, \tag{2.74}$$

where we have used the expression of v in eq. (2.59) for the propagation velocity of the lattice. In this case the Hamiltonian can be expressed as

$$\mathcal{H}_{lab} = \frac{p^2}{2M} - \frac{U_0}{2}\cos\left[2k_L(z - z(t))\right], \text{ where } \quad z(t) = \int_0^t \frac{\Delta\omega(t')}{2k_L}\mathrm{d}t'. \tag{2.75}$$

In the case of a linear frequency sweep, $z(t) = \frac{1}{2}at^2 + v_0 t$, where a is the acceleration of eq. (2.74) and v_0 is related to the frequency difference at $t = 0$.

In the non-inertial reference frame which is co-moving with the accelerated standing wave the Hamiltonian is time independent

$$\mathcal{H}_{acc} = \frac{p^2}{2M} - \frac{U_0}{2}\cos(2k_L z) + Maz, \tag{2.76}$$

where we have applied a unitary transformation $U(t)$ that is responsible for a translation in position space $\alpha(t) = \frac{1}{2}at^2 - v_0 t$ and a translation in momentum space $\beta(t) = m(at - v0)$. As we can see from eq. (2.76), in the non-inertial reference frame an inertial force appears:

$$F = Ma = \frac{M}{2k_L}\frac{\mathrm{d}\Delta\omega}{\mathrm{d}t}. \tag{2.77}$$

Therefore, there are two analogous situations: an accelerated lattice realized by sweeping the frequency difference, and a steady-lattice in presence of a constant external force. Both lead to the same phenomenon: Bloch oscillations.

Bloch oscillations in a lattice with an external force

Bloch oscillations were first studied by Zener in the scenario of an electron moving in a crystal in which a constant electric field is applied [90, 91], and then studied theoretically and experimentally in the context atomic physics [92–96]. The problem can be generalized for the case of an atom in an optical lattice subject to an external force, that in our case would be the gravitational force.

Let's consider the Hamiltonian (2.76). The presence of the external force $F = Ma$ breaks the translational symmetry due to the $d = \lambda_L/2$ periodicity of the potential. However, it is still possible to calculate the evolution of the translation operator T_d of eq. (2.49), in order to obtain the evolution of the quasimomentum q:

$$-i\hbar\dot{T}_d = [\mathcal{H}, T_d] = [-Fz, T_d] = FdT_d. \tag{2.78}$$

Therefore, the eigenstates of the Hamiltonian are always Bloch states

$$\psi_{q,j}(z) = e^{iq(t)z}u_j(z,t) \tag{2.79}$$

with a time-dependent quasimomentum $q(t) = q(0) + Ft/\hbar$. Since the quasimomentum has a periodicity of $2k_L$, $q(t)$ will evolve linearly in time and it will acquire the initial value $q(0)$ again after a period

$$\tau_B = \frac{2\hbar k_L}{Ma} \tag{2.80}$$

called *Bloch period*, corresponding to obtain the time required to a full scan of the first Brillouin zone. At the edge of the energy band, the lattice transfers two photon momenta ($2\hbar k_L$) to the atom, i.e. a first-order Bragg transition occurs.

The mean velocity $\langle v\rangle_j\,(q(t))$ of the atom in the state $|j, q(t)\rangle$ is given by the group velocity of eq. (2.51). Since q evolves linearly in time, $\langle v\rangle_j\,(q(t))$ is an oscillatory saw-tooth function with zero mean value. This oscillatory motion takes the name of *Bloch oscillation*.

Here we also want to introduce the *Bloch frequency* of these oscillations

$$\omega_B = \frac{1}{\tau_B} = \frac{Ma}{2\hbar k_L} \tag{2.81}$$

that would be the actual observable in our experiment.

Bloch oscillations as adiabatic passage between momentum states

Let's consider an atom initially at rest in a steady-lattice. In the Bragg transition description, if we change the difference in frequency $\Delta\omega$ we should expect a first-order Bragg transition whenever the energy difference between two adjacent momentum states in the energy-momentum parabola match $\Delta\omega$. According to eq. (2.65), this kind of transition occurs when

$$\Delta\omega = 4(2m+1)\omega_r, \tag{2.82}$$

where m labels the initial momentum state, i.e. $|p = 2m\hbar k_L\rangle \rightarrow |p = 2(m+1)\hbar k_L\rangle$. Therefore, every time $\Delta\omega$ increases by $8\omega_r$, the atom momentum increase by a factor of $2\hbar k_L$.

If the lattice is uniformly accelerated in the laboratory frame, the frequency difference changes linearly $\dot{\Delta\omega}(t) = 2k_L at$ (see eq. (2.74)). Therefore, the time required for the atom to undergo a resonant Bragg transition is

$$t = \frac{8\omega_r}{\dot{\Delta\omega}} = \frac{2\hbar k_L}{Ma} \tag{2.83}$$

which is exactly the Bloch period (2.80) for the inertial force $F = m\dot{\Delta\omega}/2k_L$. The Bloch oscillations in an accelerated optical lattice can be used to coherently accelerate atoms in the laboratory frame.

For this process to be efficient, the frequency sweep has to be done adiabatically. This criterion comes directly from the adiabatic rapid passage techniques developed in nuclear physics [97]. The adiabatic condition is fulfilled when

$$\dot{\Delta\omega} \ll \Omega^2 \ll (8\omega_r)^2, \tag{2.84}$$

where the first condition is equivalent to avoiding inter-band transition in the band-structure model, while the second is equivalent to the weak-binding limit condition and allows for the transitions to be sequential, so that only two momentum states can be considered at a time.

To better understand the adiabatic passage, let's have a look at the dressed-atom picture we have introduced in the description of Bragg diffraction (see sec. 2.2.1). In absence of coupling Ω, an atom with initial zero momentum will evolve in the space subtended by the states $|m\rangle = |2m\hbar k_L, N_1 - m, N_2 + m\rangle$, with an energy

$$E_m(\Delta\omega) = 4m^2 E_r + N_1\hbar\omega_1 + N_2\hbar\omega_2 - m\hbar\Delta\omega. \tag{2.85}$$

The effect of a weak coupling ($\Omega \ll 4E_r$) is appreciable only when the states $|m\rangle$ are degenerate. For an atom initially preprepared in the $|0\rangle$ state, the system adiabatically follows the evolution of the eigenstates, when the frequency difference $\Delta\omega$ is increased, leading to subsequent momentum changes of $2\hbar k_L$. This corresponds to Bloch oscillations in the fundamental band. Intuitively we can say that in order for the atom to remain in the first band, the speed of change in frequency has to be small enough to prevent the atom from crossing the energy gap $\hbar\Omega$. The larger the gap, the faster the sweep $\dot{\Delta\omega}$ can be.

This phenomenon was studied rigorously by Zener [90] and Landau independently [98]. They found that the probability for a particle in an accelerated lattice to tunnel between the fundamental energy band and the first excited band has an exponential decay, that can be expressed as a function of a critical acceleration a_c

$$P \propto \exp(-a_c/a). \tag{2.86}$$

This probability represents the *Landau-Zener tunneling* rate. The critical acceleration is proportional to the square of the band gap, which in the limit of weak-binding

is proportional to the lattice depth U_0:

$$\frac{a_c}{a} = \frac{\pi\Omega^2}{2\dot{\Delta\omega}} = \frac{\pi}{64}\frac{U_0}{E_r}. \tag{2.87}$$

For a typical atomic physics experiment, the lattice depth is $U_0 \sim 5E_r$, and with $a = g$ gravity acceleration, $a_c \sim 10^2$ m/s^2. Therefore, the losses per oscillation due to gravity are on the order of 10^{-12}. This result confirms Bloch oscillations as a very efficient tool to coherently accelerate atoms. Furthermore, as long as the atoms initially occupy the first band, i.e. if their momentum spread is smaller than $2\hbar k_L$, the efficiency of the process is independent of the initial velocity. This is an important difference between Bloch oscillations and Bragg diffraction, as we will see later in this chapter.

Wannier-Stark states and Wannier-Stark ladder

Bloch oscillations can also be described in terms of the Wannier-Stark states $\left|\Psi_{n,j}\right\rangle$, which are stationary states localized in the lattice site n in the jth band [99]. The presence of the potential $-Fz$ breaks the translational symmetry, and the energy of different sites is mismatched to produce a ladder, called a *Wannier-Stark ladder*:

$$E_{n,j} = \bar{E}_j - Fdn = \bar{E}_j - n\hbar\omega_B, \tag{2.88}$$

where $\bar{E}_j$ is the mean energy of the jth band, and ω_B is the Bloch frequency defined in eq. (2.81). The Bloch tunneling is then suppressed and Wannier-Stark localization occurs. In reality, the energies are not perfectly discrete, but have a Lorentzian shape because of a finite lifetime due to the Landau-Zener tunneling [100].

The tight-binding Hamiltonian (2.54) in the Wannier states basis (see sec. 2.1.3) in presence of an external force is given by

$$\mathcal{H} = \sum_n (\bar{E}_j - n\hbar\omega_B)\left|\Phi_{n,j}\right\rangle\left\langle\Phi_{n,j}\right| - \frac{J_j}{4}\sum_n \left|\Phi_{n+1,j}\right\rangle\left\langle\Phi_{n,j}\right| + h.c. \tag{2.89}$$

This Hamiltonian can be diagonalized in the Wannier-Stark states basis

$$\left|\Psi_{n,j}\right\rangle = \sum_m \mathcal{J}_{m-n}\left(\frac{J_j}{2\hbar\omega_B}\right)\left|\Phi_{m,j}\right\rangle, \tag{2.90}$$

where $\mathcal{J}_n(z)$ are the Bessel functions of the first kind. The corresponding eigenvalues form the energy ladder of eq. (2.88). Because the Bessel functions are exponentially small for $|n| > |z|$, the Wannier-Stark states are localized in the nth lattice site. The localization length is $1/d$ for $dF > J_j$, and $\sim J_j/dF$ for $dF < J_j$ [101]. From now on, we will consider the strong localization regime ($dF < J_j$) in which the Landau-Zener tunneling is strongly suppressed and the single-band approximation can be used.

2.3 Coherent delocalization in a driven optical lattice

In this section we will introduce a driving of the optical potential, in the form of a time-dependent modulation. We will see how the driving can be used to coherently control the quantum motion of the atoms in a lattice. This system can be a powerful tool for precision force measurements. We will show how this is applied in the case of a vertical optical lattice, where the external force is the gravity force. Although the considerations we will do can also be applied in the case of a phase modulation [102–104], we will just focus on the amplitude-modulation driving [105, 106], since it is the technique used in the present work.

2.3.1 Amplitude-modulated optical lattice

Let's consider an atom in a periodic potential subject to an external force, as we considered in sec. 2.2.2. We can add an amplitude-modulation driving (fig. 2.4) to the lattice in the form

$$U(z,t) = \frac{U_0}{2}\cos(2k_L z)\left[1 + \alpha\sin\left(\omega_M t - \phi\right)\right], \tag{2.91}$$

where α, ω_M and ϕ are respectively the depth, the frequency and the phase of the modulation. The Hamiltonian governing the system becomes

$$\mathcal{H}_{AM}(p,z,t) = \frac{p^2}{2M} - U(z,t) + Fz. \tag{2.92}$$

We will show that in the present system a resonant tunneling mechanism induces a coherent delocalization of the matter wave. The resonance occurs when the atoms absorb or emit energy quanta $\hbar\omega_M$ resonant with the ℓth harmonic of the Bloch frequency ω_B, tunneling to lattice sites separated by ℓ. Since we are interested in the resonant process, we will just consider near-resonance modulation frequencies $\omega_M \simeq \ell\omega_B$. Moreover, we will consider the Landau-Zener tunneling negligible, i.e. the strong localization regime we discussed in sec. 2.2.2. Under this condition we can drop the band index j, and consider the atomic dynamics confined always in the initial lattice band.

The Hamiltonian (2.92) can be expressed in the Wannier-Stark states basis $|\Psi_n\rangle$ defined in eq. (2.90) and in the tight-binding form:

$$\mathcal{H}_{AM} = -\sum_n n\hbar\omega_B|\Psi_n\rangle\langle\Psi_n| + \sum_n\left(\frac{\alpha U_0}{2}C_\ell^{AM}\sin(\omega_M t-\phi)|\Psi_{n+\ell}\rangle\langle\Psi_n| + h.c.\right) \tag{2.93}$$

where the coefficients $C_\ell^{AM} = \langle\Psi_{n+\ell}|\cos(2k_L z)|\Psi_n\rangle$ represent the overlap integrals between resonantly coupled $|\Psi_n\rangle$ states. If we consider the quasi-resonant situation

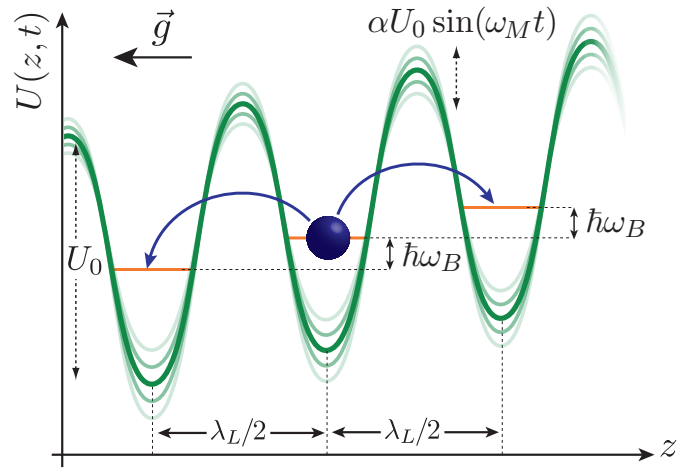

Figure 2.4: Intra-band coherent delocalization induced by an amplitude-modulation driving of the optical lattice. The intensity is modulated in time by a sinusoid at frequency ω_M and relative amplitude α. The site-to-site tunneling occurs when ω_M matches the energy separation between two adjacent Wannier-Stark states, i.e. $\hbar\omega_M = \ell\hbar\omega_B$. Here the energy separation is induced by the gravitational force.

$\delta_M = \omega_M - \ell\omega_B \sim 0$, it is possible to neglect the fast-oscillating terms by moving to the rotating frame through the operator

$$U_{RF} = \exp\left(-i \sum_n n\frac{\omega_M}{\ell} t \, |\Psi_n\rangle \langle\Psi_n|\right), \tag{2.94}$$

The Hamiltonian (2.93) under the rotating-wave approximation acquire a time-independent form:

$$\mathcal{H}_{AM} = \sum_n \left[n\frac{\hbar\delta_M}{\ell} \, |\Psi_n\rangle \langle\Psi_n| + \left(e^{i(\pi/2-\phi)} \frac{J_\ell^{AM}}{2} \, |\Psi_{n+\ell}\rangle \langle\Psi_n| + h.c. \right) \right], \tag{2.95}$$

where the terms $\exp[i(\pi/2 - \phi)]J_\ell^{AM}$ represent the tunneling rates, which can be tailored by the lattice depth α and phase ϕ:

$$J_\ell^{AM} = \frac{\alpha U_0}{2} \langle\Psi_{n+\ell}| \cos(2k_L z) \, |\Psi_n\rangle \, . \tag{2.96}$$

In real space, this site-to-site tunneling can be viewed as a two-photon Bragg process between neighboring Wannier-Stark states excited by the amplitude modulation which brings sidebands $\omega_L \pm \omega_M$ to the original lattice [107]. It can be demonstrated [108] that the stationary states on resonance are delocalized Bloch states moving with an effective energy dispersion

$$E(q) = J_\ell^{AM} \sin(q\ell d - \phi). \tag{2.97}$$

2.3.2 Transport dynamics in real space: Resonant tunneling

The Hamiltonian (2.95) contains two terms: a localizing term proportional to the detuning δ_M and a delocalizing term proportional to the tunneling rate J_ℓ^{AM} which couples states separated by ℓ sites. For $\delta_M \neq 0$, the translational symmetry is broken and the Hamiltonian is similar to the one of a static lattice in presence of an effective external force $F_\delta = \hbar\delta_M/\ell d$ (see eq. (2.89)). In this regime the dynamics is governed by Bloch oscillations with a period $2\pi/\delta_M$. When the system is on resonance, a coherent delocalization of the wave packet takes place, which spreads ballistically according to the dispersion relation of eq. (2.97).

The eigenstates of the Hamiltonian can be written in terms of the Wannier-Stark states basis of eq. (2.98) for the force F_δ with a phase factor due to the phase ϕ of the modulation:

$$|\psi_n(\delta_M)\rangle = \sum_m e^{im(\pi/2-\phi)} \mathcal{J}_{-m}\left(\frac{J_\ell^{AM}}{F_\delta d}\right)|\Psi_{n+m\ell}\rangle\,. \tag{2.98}$$

Therefore, the eigenstates of the driven Hamiltonian are always Wannier-Stark states localized on the lattice site n, and they form a ladder of energies

$$E_n(\delta_M) = \frac{n\hbar\delta_M}{\ell}. \tag{2.99}$$

If the amplitude modulation is applied for a time t_M, we can write the evolution operator in the $|\psi_n(\delta_M)\rangle$ states basis and in the rotating frame:

$$U_{RF}(t_M) = \exp\left(-i\sum_n n\frac{\delta_M}{\ell}t_M\,|\psi_n(\delta_M)\rangle\langle\psi_n(\delta_M)|\right), \tag{2.100}$$

which, applied to the initial state $|\Psi_n(t=0)\rangle$, leads to the time-evolved state

$$|\Psi_n(t_M)\rangle = e^{-in\delta_M t_M/\ell}\sum_m e^{-im\frac{\delta_M t_M}{2+\phi}}\mathcal{J}_m\left[\frac{J_\ell^{AM}t_M}{\hbar}\mathrm{sinc}\left(\frac{\delta_M t_M}{2}\right)\right]|\Psi_{n+m\ell}\rangle \tag{2.101}$$

where the sinc function is defined as $\mathrm{sinc}(x) = \sin(x)/x$.

We can compute the broadening of the time-evolved wave packet initially localized on the nth site by evaluating the square of the shifted spatial operator:

$$\sigma_n^2(t_M) \equiv \langle\Psi_n(t_M)|\,(z-nd)^2\,|\Psi_n(t_M)\rangle \sim v_\ell^2 t_M^2\,\mathrm{sinc}\left(\frac{\delta_M}{\Gamma_F}\right) \tag{2.102}$$

which is the asymptotic ballistic expansion, valid for large t_M, and where we introduced the speed of the broadening at resonance

$$v_\ell = \frac{1}{\hbar}\frac{\ell d\left|J_\ell^{AM}\right|}{\sqrt{2}} \tag{2.103}$$

and the Fourier-limited linewidth of the resonance spectrum

$$\Gamma_F = 2\pi \times \frac{1}{\pi t_M}. \tag{2.104}$$

In a real experiment, one does not measure the extent of an atomic wave packet, but the size of a thermal cloud which has a Gaussian distribution with initial finite size σ_0. The actual observable would be the convolution between the variance of eq. (2.103) and the atomic cloud's size:

$$\sigma(t_M) = \sqrt{\sigma_0^2 + v_\ell^2 t_M^2 \operatorname{sinc}\left(\frac{\omega_M - \ell\omega_B}{\Gamma}\right)} \tag{2.105}$$

which represents a series of resonances centered at every ℓth harmonic of the Bloch frequency ω_B, with a linewidth Γ that can generally be larger than the Fourier-limited one.

It is worth to say that it's possible to evaluate the exact position of the resonances without making any approximation on the Hamiltonian (2.92) and generalizing to an arbitrary modulation function $f(t)$ with period $2\pi/\omega_M$. This analysis can be done taking advantage of the space and time symmetries and exploiting the Floquet theory [109]. As result [106], in case of amplitude modulation, the positions of the resonances remain unchanged, while in the case of phase modulation the resonances could be shifted by a non zero average value of the effective force due to the driving. In conclusion, for precise force measurements we have chosen an amplitude modulation driving, which is insensitive to the presence of spurious harmonics and subharmonics of ω_M.

2.3.3 Effects of decoherence

Since the resonant tunneling and Bloch oscillations are coherent quantum processes, one has to take into account possible decoherence effects. Typical decoherence mechanisms are spontaneous emission, cold atom interactions [96], random recoils by lattice photons [110] and environmental scattering by incoherent photons or background gas.

It is worth to stress that even if in most applications (such as the precision measurements of this work) decoherences are negative phenomena, they can be of interest on their own. Indeed, the conventional conductivity in solid crystals is possible only in presence of some decoherence induced by scattering with impurities. Without any relaxation process, under the effect of an electric field, electrons would undergo Bloch oscillations without any real conduction.

Since in the present discussion we are interested in the effects of the decoherence, and not in the specific physical mechanism from which the decoherence is originated,

we can just consider a general coupling between the system under study and the environment, which can be constituted by atomic collisions or scattering with random photons. In both cases, the effect of the decoherence can be schematized by the collapse of the atomic wave packet into one single lattice site. This localization process, known as *sequential tunneling*, inhibits the coherent coupling among the adjacent Wannier-Stark states, induced by the amplitude modulation.

To investigate the interaction between the system and an environment the approach based on the single-particle Schrödinger equation is not valid, and the dynamics should be described by a density matrix ρ. The evolution of ρ can be obtained by solving the stochastic Liouville equation [111, 112], where a localization operator is introduced

$$\dot{\rho} = \frac{1}{i\hbar}\left[\mathcal{H}_{AM}, \rho\right] + \sum_m \left(2L_m\rho L_m^\dagger - L_m^\dagger L_m\rho - L_m^\dagger L_m\rho\right). \tag{2.106}$$

Here, $\mathcal{H}_{AM}$ is the Hamiltonian (2.92) governing the coherent transport, and L_m are the projections of the recoil operator (*Lindblad operator*), responsible for a certain relaxation process one wants to take into account. In the Wannier states basis $|\Phi_m\rangle$ (see sec. 2.1.3) and in the tight-binding approximation, L_m take the form of a localizing term in the site m:

$$L_m = \sqrt{\gamma_D}\,|\Phi_m\rangle\langle\Phi_m|, \tag{2.107}$$

where γ_D represents the rate of collapse of the atomic wave function. By substituting the Lindblad operators in the Liouville eq. (2.106) one obtains

$$\dot{\rho} = \frac{1}{i\hbar}\left[\mathcal{H}_{AM}, \rho\right] - 2\gamma_D(\rho - \mathcal{D}), \tag{2.108}$$

where $\mathcal{D} = \sum_m \rho_{mm}\,|m\rangle\langle m|$ is the diagonal part of the density matrix. This equation shows that the off-diagonal terms of the density matrix, which are the *coherences*, relax to zero at the rate γ_D, while the diagonal terms, which are the *populations*, are not affected by the decoherence mechanism. The off-diagonal term cause a sequential tunneling, which in momentum space leads to a decay of the Bloch oscillations

$$\langle p(t)\rangle = p_0 e^{-\gamma_D t}\sin(\omega_B t), \tag{2.109}$$

where the amplitude p_0 in absence of decoherence is damped at a rate γ_D. In real space, the sequential tunneling asymptotically leads to a diffusive spreading of the atom ensemble

$$\sigma^2(t) \sim Dt, \quad \text{where} \quad D = \left(\frac{p_0}{M}\right)^2 \frac{\gamma_D}{\omega_B^2 + \gamma_D^2} \tag{2.110}$$

represents a diffusion constant. Note that since $\omega_B \propto F$, the external force tends to suppress the diffusion. Therefore, the conductivity of a system goes to zero when the frequency of Bloch oscillations is larger than the decoherence rate.

Since we are interested in the resonance spectrum, we note that a numerical integration of the Liouville equation leads to Lorentzian line-shape, with γ_D approximately the linewidth of the spectrum [108]. The presence of a decoherence process will result in a broadening of the Fourier-limited linewidth defined in eq. (2.104), by an additive quantity γ_D, which is the inverse of the coherence time of the system.

2.3.4 Bloch frequency based dynamometer

The measurement of the atomic wave packet broadening as a function of the amplitude-modulation frequency of the lattice potential allows reconstruction of the resonance spectrum given by eq. (2.105). The spectroscopy of the Wannier-Stark resonant tunneling profile permits determination of the potential energy between nearest neighboring sites, i.e. $\hbar\omega_B$. Interrogation of the atoms to higher harmonics of the modulated potential allows a precise determination of the local force F through the definition of the Bloch frequency

$$\omega_B = \frac{F\lambda_L}{2\hbar}. \tag{2.111}$$

The presented system is a dynamometer which works at the micrometer scale. Such a device finds interesting applications, spanning from measurements of the Casimir-Polder force [22, 23, 113, 114] to possible violation of Newtonian gravity [19].

Aside from the potential of short-distance measurements, this technique has already demonstrated very high performances in the measurement of gravitational forces. With the bosonic ^{88}Sr isotope, gravity acceleration $g = F_g/M_{Sr}$ was measured with a relative uncertainty of 10^{-7}, by interrogating the atomic sample at the sixth harmonic of the Bloch frequency [41].

2.4 Atom optics with Bragg pulses

In section 2.2.1 we have discussed the main characteristics of Bragg transitions in a time-independent description. In this section, we will see how Bragg pulses are responsible for the time evolution of the atom's momentum. By choosing a proper interaction time it is possible to produce atom-optical components such as "mirrors" and "beam splitters", essential for the realization of an atom interferometer.

Contrary to Raman transitions, for which the internal state entanglement with the external degrees of freedom makes the system a real two-level problem, in Bragg

transitions there is always a coupling between unwanted momentum states, leading to losses. We will see how to take into account such losses and possible reduction solutions. We will also discuss the importance of the atom's initial momentum distribution in the realization of efficient atom-optical elements.

2.4.1 Rabi oscillations between momentum states

As we have already seen in sec. 2.2.1, the Hamiltonian describing the interaction between an atom and a traveling standing wave (formed by two beams with opposite wave vector $|k_1| \sim |k_2| = k_L$) can be written in terms of the single-photon Rabi frequency Ω_0. For now, we consider a mono-energetic wave packet, with a δ-momentum distribution. In the frame rotating at frequency ω_L:

$$\mathcal{H} = \frac{p^2}{2M} - \hbar\delta \left|e\right\rangle\left\langle e\right| + \hbar\Omega_0 \cos(k_L z) \left(\left|e\right\rangle\left\langle g\right| + h.c.\right). \tag{2.112}$$

Here we are interested in solving the evolution of the system, so we consider a time-dependent atomic wave function $|\psi(t)\rangle = e(z,t)\,|e\rangle + g(z,t)\,|g\rangle$. By solving the Schrödinger equation $i\hbar|\dot{\psi}\rangle = \mathcal{H}\,|\psi\rangle$ we obtain two coupled differential equations for the coefficients $e(z,t)$ and $g(z,t)$. Since we are in the case of a far-detuned lattice ($\delta \gg \Omega_0, \omega_r$), we can adiabatically eliminate the excited state, so that we remain with just a single differential equation:

$$i\hbar\dot{g}(z,t) = -\frac{\hbar^2}{2M}\frac{\partial^2 g(z,t)}{\partial z^2} + \frac{\hbar\Omega_0^2}{\delta}\cos^2(k_L z) g(z,t), \tag{2.113}$$

where we can recognize that the coupling with the potential is mediated by the two-photon Rabi frequency $\Omega = \Omega_0^2/2\delta$ we have introduced in sec. 2.2.1.

For constant Ω_0 we can apply the method of separation of variables and look for a solution in the form $g(z,t) = g_t(t)g_z(z)$. Thus, we can divide eq. (2.113) into two coupled spatial and temporal equations

$$ig_t' - \omega_t g_t = 0, \tag{2.114}$$

$$-\tfrac{\hbar}{2M} g_z'' + 2\Omega\cos^2(k_L z) g_z - \omega_t g_z = 0, \tag{2.115}$$

where ω_t is the separation constant. Equation (2.115) is a Mathieu equation for which exact solutions exist and are known as Mathieu functions [115, 116].

Since eq. (2.113) contains the periodic potential, which is invariant under translation of an integer multiple of $1/k_L$, we can apply the Bloch theorem (see sec. 2.1.3) and separate the spatial dependence in $g(z,t)$ in terms of eigenfunctions of constant quasimomentum $g(z,t) = \sum_m g_m(t)\exp(imk_L z)$. The integer-index m in this context refers to the state of momentum $m\hbar k_L$ which lies on the momentum-energy parabola we have discussed in sec. 2.2.1. The Mathieu equation (2.113)

becomes

$$i\hbar\sum_m \dot{g}_m e^{imk_L z} = \hbar\sum_m \left[\left(\omega_r m^2+\Omega\right)g_m+\frac{\Omega}{2}(g_{m+2}+g_{m-2})\right]e^{imk_L z} \tag{2.116}$$

where we have made use of the definition of recoil frequency ω_r in eq. (2.64), and trigonometric relation $\cos^2(k_L z) = \frac{1}{2} + \frac{1}{4}(e^{2ik_L z} + e^{-2ik_L z})$ which is responsible for the presence of the g_{m+2} and g_{m-2} terms. The Mathieu eq. (2.116) holds for all m only if

$$i\hbar\dot{g}_m = \hbar\left(\omega_r m^2 + \Omega\right) g_m + \frac{1}{2}\hbar\Omega\left(g_{m+2} + g_{m-2}\right). \tag{2.117}$$

As we can see this equation only couples either even or odd momentum states.

At this point we can distinguish between two different regimes: the Raman-Nath regime, which occurs for short interaction times; and the Bragg regime, in the case of long interaction times. While in the Raman-Nath regime many momentum states are populated, in the Bragg regime just the initial and the final states are occupied.

Although, atom interferometer experiments were proposed and realized in the Raman-Nath regime to obtain a multi-mode beam splitter [117–120], we are more interested in a pure Bragg diffraction [121] where just two momentum states are populated and a clear description of the atomic phase is expected. On the other hand, the Bragg regime requires a very long interaction time, which is typically not feasible in real experiments. In the intermediate regime, known as quasi-Bragg regime, mainly two states are populated, but the coupling with the other states is also taken into account. Useful results can be obtained by numerical computation, but some solutions can be also obtained analytically. We will follow the analysis in ref. [122] which also provides strategies to minimize the unwanted losses.

Raman-Nath regime

In the case of very short interaction times ($t \ll 1/\sqrt{\Omega\omega_r}$), the kinetic energy can be neglected in eq. (2.117), resulting in

$$i\hbar\dot{g}_m = \tfrac{1}{2}\hbar\Omega\left(g_{m+2} + g_{m-2}\right). \tag{2.118}$$

Since this equation only couples states separated by an even number of momenta $\hbar k_L$, we restrict attention to the states $2m$, for which the solution is expressed by the Bessel functions:

$$g_{2m}(t) = (-i)^m \mathcal{J}_m(\Omega t). \tag{2.119}$$

Therefore, the transition probability from the state $g_0 = 1$ at $t = 0$ to the state with momentum $2m\hbar k_L$ is $P_{2m}(t) = \mathcal{J}_m^2(\Omega t)$. This means that in this regime more

than two momentum states are populated at time, even if the occupation probability would not be the same for every m.

In atomic physics, the Raman-Nath regime is a special case of the Kapitza-Dirac effect [123–127], which is the diffraction of a collimated atomic beam by an optical standing-wave. It can be shown [128] that the dispersion of the optical wave vector in a focused beam, which is responsible for the multiple-order diffraction, is analogous to the short pulse time situation. Intuitively, thinking in the Fourier-transform domain, a short pulse in time will correspond to a wide frequency spectrum, the components of which can excite a larger number of momentum states.

Bragg regime: pure π and $\pi/2$ pulses

In the Bragg regime the kinetic energy in eq. (2.117) is not negligible. Let's consider the initial situation in which only the momentum state $-n\hbar k$ is populated, therefore $g_{-n} = 1$ and $g_m = 0$ for $m \neq -n$. Equation (2.117) tell us that there is an infinite number of coupled equations between states separated by an even number $2l$ with $l \in \mathbb{Z}$:

$$i\hbar\dot{g}_{\pm n+2l} = 4l(l \pm n)\hbar\omega_r g_{\pm n+2l} + \tfrac{1}{2}\hbar\Omega(g_{\pm n+2l+2} + g_{\pm n+2l-2}) \tag{2.120}$$

where, for simplicity, we have removed a constant offset $n^2\hbar\omega_r + \hbar\Omega$ from the energy scale. If the process is sufficiently slow, the energy conservation will favor the transition $-n \to n$. This allows an adiabatic elimination of the intermediate state ($0 < l < n$) for which

$$\left|4l^2 - 4nl\right| \hbar\omega_r \gg \hbar\Omega. \tag{2.121}$$

Under this condition we can assume that the lth equation is always in equilibrium with $\dot{g}_{-n+2l} \sim 0$, so for example

$$g_{-n+2} = -\frac{1}{8}\hbar\Omega\frac{1}{(nl - l^2)\hbar\omega_r}g_{-n}. \tag{2.122}$$

We can eliminate all the $n - 1$ intermediate states by defining an effective Rabi frequency for the $-n \to n$ transition

$$\Omega_{\text{eff}} = \frac{\Omega^n}{(8\omega_r)^{n-1}}\prod_{l=1}^{n-1}\frac{1}{nl - l^2} = \frac{\Omega^n}{(8\omega_r)^{n-1}}\frac{1}{(n-1)!^2}. \tag{2.123}$$

The same expression was first found by Giltner *et. al.* [129] using simple considerations on the detuning of the intermediate states. The remaining equations are

$$i\hbar\dot{g}_{-n} = \tfrac{1}{2}\hbar\Omega_{\text{eff}}g_n, \qquad i\hbar\dot{g}_n = \tfrac{1}{2}\hbar\Omega_{\text{eff}}g_{-n} \tag{2.124}$$

which can be easily solved

$$g_{-n}(t) = \cos\left(\tfrac{1}{2}\Omega_{\text{eff}}t\right), \qquad g_n(t) = -i\sin\left(\tfrac{1}{2}\Omega_{\text{eff}}t\right). \tag{2.125}$$

Thus, the system oscillates between the momentum states separated by $2n\hbar k_L$ in a manner analogous to the Rabi oscillations of atomic population between two resonantly coupled states. Rabi oscillation for the two Bragg coupled states is known as Pendellösung and was first observed for X-rays on a crystal [130]. The integer number n represents the order of Bragg diffraction that we have introduced in sec. 2.2.1.

If the argument $\Omega_{\text{eff}}t$ of the trigonometric functions in eq. (2.125) is equal to π (a π-*pulse*), the population will be completely transfered from the initial state $-n$ to the state n; if $\Omega_{\text{eff}}t = \pi/2$ (a $\pi/2$-*pulse*), the population will be equally divided in the two momentum states. These pulses correspond respectively to a *mirror* and a *beam splitter* in the atom optics context, and they will be the main ingredient for atom interferometry.

The adiabatic elimination we did is justified by the (2.121) condition, and set a limit to the two-photon Rabi frequency $\Omega \ll 4(1-n)\omega_r$, which can be inserted in eq. (2.123) to get the general condition

$$\Omega_{\text{eff}} \ll \frac{8(n-1)^n\omega_r}{2^n(n-1)!^2}. \tag{2.126}$$

This expression sets a lower bound for the interaction time needed in order to have a pure n-order Bragg diffraction. The intermediate regime between Raman-Nath and Bragg is known as quasi-Bragg regime.

2.4.2 Quasi-Bragg regime: Losses and pulse shaping

In the quasi-Bragg regime the adiabatic approximation is not valid and the losses in unwanted momentum states are not zero. Exact numerical solutions can be obtained by a Mathieu equation approach [122]. The results are consistent with a numerical integration of the coupled differential eqs. (2.120). Figure 2.5 shows the numerical simulation of the output population for a $-3\hbar k_L \rightarrow +3\hbar k_L$ transition with $\Omega = 3\omega_r$. This simulation considers an interaction coupling $\Omega = 3\omega_r$ starting from $t = 0$, an initial population $g_{-3}(0) = 1$, and includes 5 outer states ($0 < |l| < n + 5$) in the integration.

Severed things can be discussed looking at the result. For instance, the effective Rabi frequency Ω_{eff} of eq. (2.123), found in the adiabatic approximation (i.e. in absence of losses), is in good agreement with the frequency of oscillations extrapolated from a sinusoidal fit function. This remains true as long as $|g_{m\neq\pm n}|^2 \ll |g_{\pm n}|^2$. Therefore, Ω_{eff} can also be used in the quasi-Bragg regime.

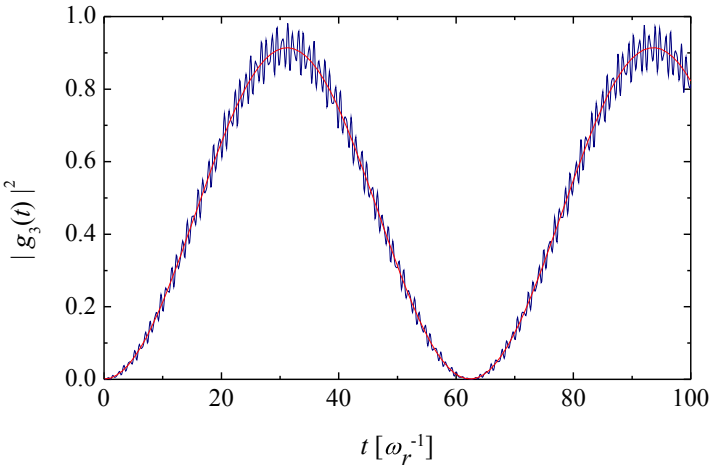

Figure 2.5: Numerical simulation of the output population for a third-order Bragg transition: $-3\hbar k_L \rightarrow +3\hbar k_L$, with $\Omega = 3\omega_r$. The red curve is a sinusoidal fit with frequency $\Omega_{\text{fit}} = 1.05 \times \Omega_{\text{eff}}$.

Secondly, we observe a fast oscillations around the mean Rabi oscillation. The frequency is large compared to Ω_{eff} and depends on the pulse amplitude. To observe such fast oscillation a very precise timing and amplitude control of the system is required. Most of the time one observes just the mean value, which can lead to an effective π-pulse efficiency smaller than one (91.3% in the figure).

An approximate, but useful way to algebraically calculate the losses contribution, is an expansion of the adiabatic method we used in the previous section. Let's first consider a generic pulse amplitude shape, i.e. we suppose the two-photon Rabi frequency $\Omega(t)$ to be time-dependent. Equations (2.125) for the population evolution in the adiabatic approximation become

$$g_{-n}^{(1)}(t) = \cos\left(\frac{1}{2}\int_{-\infty}^{t}\Omega_{\text{eff}}(t')\mathrm{d}t'\right), \quad g_{n}^{(1)}(t) = -i\sin\left(\frac{1}{2}\int_{-\infty}^{t}\Omega_{\text{eff}}(t')\mathrm{d}t'\right), \tag{2.127}$$

where the label $^{(1)}$ stands for the first-order adiabatic approximation, in which just the initial and final states are populated. The corrections to the population can be calculated as an expansion

$$g_m = g_m^{(1)} + g_m^{(2)} + g_m^{(3)} + \ldots \tag{2.128}$$

where the second order, for example, is calculated by inserting $g_{\pm n}^{(1)}$ in the differential

eqs. (2.120). We obtain equations for the states next to the initial and final states:

$$\begin{aligned} i\dot{g}_{-n\pm2}(t) &= 4(1\mp n)\omega_r g_{-n\pm2}(t) + \frac{1}{2}\Omega(t)\cos\left(\frac{1}{2}\int_{-\infty}^{t}\Omega_{\text{eff}}(t')\mathrm{d}t'\right), \\ i\dot{g}_{n\pm2}(t) &= 4(1\pm n)\omega_r g_{n\pm2}(t) - \frac{i}{2}\Omega(t)\sin\left(\frac{1}{2}\int_{-\infty}^{t}\Omega_{\text{eff}}(t')\mathrm{d}t'\right). \end{aligned} \tag{2.129}$$

These are states for which $g^{(2)} \neq 0$. To get the third order terms $g^{(3)}$ we can iterate the process by inserting $g^{(2)}_{\pm n\pm2}$ in (2.120), and so on for the next orders. Solutions for these inhomogeneous differential equations can be obtained by standards methods, such as Green's functions [131].

With this method we can calculate the losses and the relative phase shift up to the desired order. Let's say we are interested to the second-order correction. The losses L in the $-n \to n$ transition come from the neighboring states

$$L^{(2)} = |g_{-n-2}|^2 + |g_{-n+2}|^2 + |g_{n-2}|^2 + |g_{n+2}|^2 \tag{2.130}$$

and an upper limit to the losses-induced phase shift can be evaluated as $|\Delta\phi| \leqslant \sqrt{L}$ [122]. This method can be applied to an arbitrary pulse shape to calculate losses and phase shift. We will consider the simplest square pulse, experimentally used for a long time in Raman interferometry, and a smooth-envelope pulse, namely a Gaussian pulse.

Square pulses

In the case of a square pulse, $\Omega(t) = \bar{\Omega}$ for $0 < t < T$ and zero otherwise where T is the duration of the pulse. In the second-order approximation, the integrals in eq. (2.129) are easy to solve, and we obtain the populations of the neighboring states

$$g_{-n\pm2} = \frac{\bar{\Omega}}{\omega_r}\frac{1}{8(1\mp n)}, \quad g_{n\pm2} = i\frac{\bar{\Omega}}{\omega_r}\frac{1}{8(1\pm n)}e^{4i(1\pm n)\omega_r T}. \tag{2.131}$$

So the total losses, according to eq. (2.130), are

$$L^{(2)} = \frac{1}{16}\frac{\bar{\Omega}^2}{\omega_r^2}\frac{n^2+1}{(n^2-1)^2}. \tag{2.132}$$

This equation is a good prediction for the real case, where no approximation is applied. For example, in the case where $n = 3$ and $\bar{\Omega} = 3\omega_r$ the losses are $L = 8.8\%$, in agreement with the efficiency found for the numerical simulation in fig. 2.5.

Since real experiments requires much smaller losses, this would mean reducing the Rabi frequency $\bar{\Omega}$ to a level for which the practical implementation is not

possible. For example, if we want to keep losses below the 10^{-4} level, as required for high-precision interferometry, the π-pulse time would be of the order of $\tau_\pi \equiv \pi/\Omega_{\text{eff}} \sim 10$ s.

Smooth pulses exhibit much smaller losses and phase shifts for a given pulse duration. We will see that Gaussian envelopes are a good solution.

Gaussian pulses

A Gaussian pulse envelope can be written in the form

$$\Omega(t) = \bar{\Omega} e^{-t^2/2\sigma^2}. \tag{2.133}$$

We will refer to the pulse duration as the width σ. The corresponding effective Rabi frequency (2.123) becomes

$$\Omega_{\text{eff}}(t) = \bar{\Omega}^n \left(\frac{1}{8\omega_r}\right)^{n-1} \frac{1}{(n-1)!^2} e^{-nt^2/2\sigma^2}. \tag{2.134}$$

The correction calculations in the case of a Gaussian envelope are much harder because they involve complicated integrals, and moreover higher correction orders in general would be needed. If we considered losses smaller than the 10^{-2} level, the second-order corrections are enough [122] and lead to

$$L^{(2)} \simeq 4(0.5\bar{\Omega}\sigma)^2 \exp\left[-16(1-n)^2\sigma^2\omega_r^2/(1.6n^{1/3})\right] \tag{2.135}$$

which decreases very rapidly with σ. Therefore, high effective Rabi frequency can be used and very small losses can be obtained. Indeed, to have losses below 10^{-10}, which are small enough to be neglected with respect to other technical errors, the π-pulse duration has to be $\sigma_\pi/\omega_r > 1.5n^{1/6}/(n-1)$ which is feasible in real experiments. For comparison with the square envelope situation we discussed, for $n = 3$ we can reach losses below 10^{-10} with $\sigma_\pi > 1/\omega_r \sim 10$ μs.

As a more detailed example, in fig. 2.6 we show a numerical simulation of the population evolution for a 3rd order Bragg diffraction in the case of a Gaussian envelope. We use $\bar{\Omega} = 20\omega_r$ and we consider 5 outer states in the computation. The Gaussian was truncated at 6σ. The population at the input and output states, as well as the nearest neighboring states are shown. For a pulse duration $\sigma \lesssim 0.3\omega_r^{-1}$, the population is transfered from the initial state $-3\hbar k$ to the output state $+3\hbar k_L$ as well as the nearest neighboring states. The system is in the Raman-Nath regime. When the pulse becomes longer, the system evolves in the quasi-Bragg regime and the losses decrease rapidly, becoming negligible after a time $\sim 0.8\omega_r^{-1}$ in which the system performs Pendellosöung oscillations as in the Bragg regime.

A proper optimization of the Rabi frequency $\bar{\Omega}$ can lead to π-pulse efficiency very close to 100%. The practical losses will then be dominated by issues such

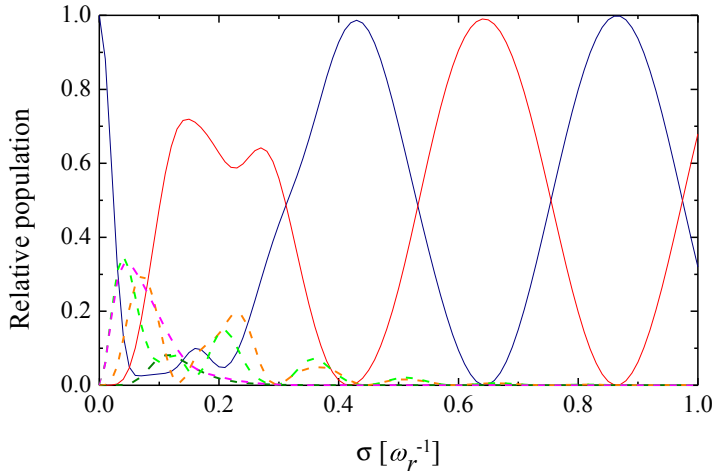

Figure 2.6: Numerical simulation of the population evolution for a 3rd order Bragg diffraction and a Gaussian pulse with $\bar{\Omega} = 20\omega_r$. The blue and red curve are the input $|g_{-n}|^2$ and output $|g_n|^2$ state populations respectively. The dashed lines correspond to the next neighboring states $|g_{\pm n\pm 2}|^2$ population.

as single-photon excitation, finite laser power, finite size and temperature of the atomic cloud, wave-front distortions.

In particular we will see that Bragg pulses are highly velocity selective, and more so as the diffraction order is increased. This leads to a dependence of the population transfer on the multi-photon detuning $\Delta\omega$. To minimize this dependence, other pulse solutions have been developed, such as composite-pulse techniques [132, 133] or adiabatic-rapid-passage pulses [134].

2.4.3 Velocity selectivity of Bragg pulses and the importance of momentum distribution

Let's now relax the mono-energetic condition we introduced at the beginning of this section. We consider the realistic situation of an atomic momentum distribution $\rho(p)$ [135]. The wave packet would be a superposition of momentum states $|\Psi(t)\rangle = \int \rho(p) \left|\psi_p(t)\right\rangle \mathrm{d}p$, where $\rho(p)$ is normalized separately from $\left|\psi_p(t)\right\rangle$ so that $\int |\rho(p)|^2 \,\mathrm{d}p = 1$.

In sec. 2.2.1, we noticed that momenta deviating from the resonance condition act as a detuning δ_p because of the Doppler shift. Therefore, the atomic wave function can be written as

$$|\Psi(t)\rangle = \sum_m \int g_m(\delta_p, t) e^{i(m+\delta_p)kz} \mathrm{d}\delta_p, \tag{2.136}$$

where δ_p has been chosen as adimensional detuning from the resonant state $|m\hbar k\rangle$. Because of the same consideration, the Mathieu equations (2.117) that govern the evolution of the system become

$$i\hbar\dot{g}_m = \hbar\left[\omega_r(m+\delta_p)^2 + \Omega\right] g_m + \hbar\frac{\Omega}{2}\left(g_{m+2} + g_{m-2}\right). \tag{2.137}$$

The population evolution can be obtained by numerically solving these differential equations, with the initial condition that the atoms occupy the state n with a Gaussian distribution of width σ_p:

$$\rho(\delta_p) = \left(2\pi\sigma_p^2\right)^{-1/2} \exp\left[-(\delta_p - n)^2/(2\sigma_p^2)\right]. \tag{2.138}$$

To point out the main effects of a Bragg pulse interacting with a finite momentum distribution, we consider the simple case were the initial population is distributed in the $n = -1$ state. Figure 2.7 shows the result of the numerical simulation for the case of an initial δ-distribution (a) and for an initial Gaussian distribution of width $\sigma_p = 1\hbar k_L$ (b). We again consider a Gaussian pulse with $\bar{\Omega} = 3\omega_r$ and we keep 5 outer states in the calculation.

Two effects are clear by comparing the mono-energetic situation with the finite momentum distribution. At short times the losses into the neighboring states increase, larger is the initial momentum width σ_p. This can be interpreted by realizing that the tails of the Gaussian centered on the $-n$ states are closer to the states $-n-2, -n+2$, and therefore the effective coupling would be increased.

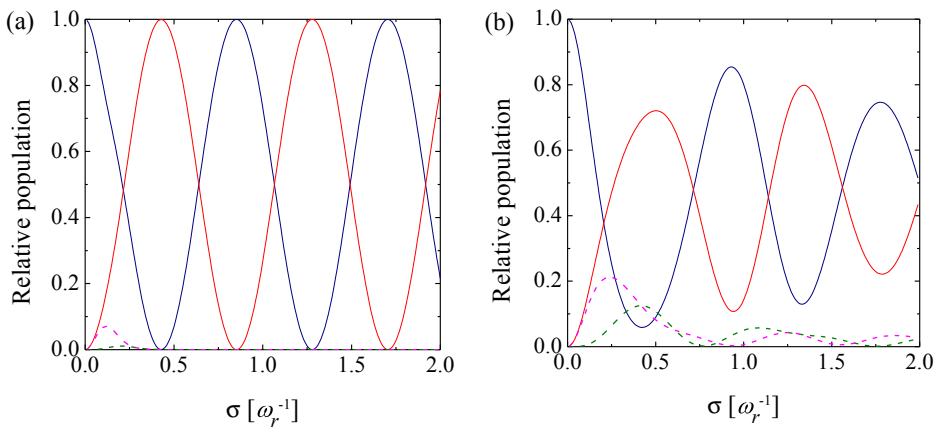

Figure 2.7: Numerical simulation of the population evolution for a 1st-order Bragg transition $-\hbar k_L \rightarrow +\hbar k_L$ in the case of an initial δ-momentum distribution (a) and for a Gaussian distribution of width $\sigma_p = 1\hbar k_L$ (b). The blue (red) curve is the population in $n = -1$ $(+1)$ state, while the dashed curves are the losses in $n = -3, +3$. Here $\bar{\Omega} = 3\omega_r$.

At longer times ($\sigma > \omega_r^{-1}$ in the figure) the losses become negligible, but a damping of the two-state oscillation is observable. The damping is due to the velocity selectivity of the Bragg transition, caused by the Doppler shift [89]. The longer the interaction time, the narrower the resonance condition would be, resulting in an exponential decay of the transfer efficiency. The resonant condition is Fourier-limited by the interaction time. This result shows that, in order to increase the Bragg pulses efficiency, it is better to start with a narrow momentum distribution, for which the losses and the damping effects are smaller.

On the other hand, it turns out that such pulses can be used to prepare an atomic sample with arbitrary narrow momentum distribution, by tuning the interaction time. We notice that this process does not increase the number of atoms in a given velocity class, and is therefore not a cooling technique.

Finally, Bragg pulses can be used for momentum distribution analysis with sub-recoil resolution, by resolving the Doppler width of the Bragg transition itself. This technique, called *Bragg spectroscopy* [136], is a powerful tool for momentum distribution measurements and is commonly used in situations where time-of-flight techniques can be limited in resolution, such as with Bose-Einstein condensates [137, 138].

A systematic numerical simulation of the π-pulse efficiency carried out by Szigeti *et al.* [135] demonstrates the importance of a narrow initial momentum distribution to produce a large-momentum-transfer atom-optical element. In their analysis it emerges that the π-pulse efficiency does not depend strongly on the order n as long as Ω can be arbitrarily increased, i.e. if no constraints are placed on the available optical power. In a realistic scenario, the optical power is limited, so it is only possible to increase Ω by reducing the detuning δ from the excited internal state. This has the consequence of increasing the losses due to resonant scattering, whose probability is expressed by eq. (2.30).

In conclusion, placing constraints on the available optical power and on the maximum acceptable losses due to resonant scattering leads to very strong constraints on the starting momentum distribution width, especially when one wants to move to higher Bragg orders.

2.5 Free-falling Mach-Zehnder atom interferometer with Bragg pulses

In general, an interference process occurs when a (matter-)wave is split in a coherent superposition of two states along two paths and it is recombined after a certain free-evolution time T. The accumulated phase between the two paths leads to an interference pattern at the recombiner. At the output channels of the interferometer, we have a complementary probability to find the wave in one of the two states. The

probability oscillates periodically as a function of the total phase difference $\Delta\Phi$.

In this section we will describe the theoretical concept of a Mach-Zehnder atom interferometer between momentum states, realized by a sequence of three $\pi/2 - \pi - \pi/2$ Bragg pulses, which split, reflect and recombine the wave-packet. In the presence of a gravity field, the atom will fall along the geodesics of the field during the free-evolution time, and the accumulated phase shift between the two arms will depend on the gravity acceleration g.

Another important interferometric scheme, that will not be presented in this discussion, is the Ramsey-Bordé interferometer [139–142], which is constituted by a sequence of four $\pi/2$-pulses. This scheme is sensitive to the recoil frequency ω_r and for this reason is used for the determination of the fine constant α [13, 14, 143].

2.5.1 Phase shift calculation

For instance, let's consider the atom interferometer represented in fig. 2.8 in a time-space diagram. The classical paths with and without the presence of the gravitational field are both shown. We define the effective wave vector $k_{\text{eff}} = 2n\hbar k_L$ of the nth order Bragg transition, which transfer atoms from the initial state $|p_0\rangle$ to the final state $|p_0 + 2n\hbar k_L\rangle$. The transition probability depends on the pulse area $\Omega_{\text{eff}}\tau$ (see sec. 2.4.1) and can be adjusted to realize a mirror (π) or a beam splitter ($\pi/2$).

The total phase difference between the upper path ACB and the lower path ADB

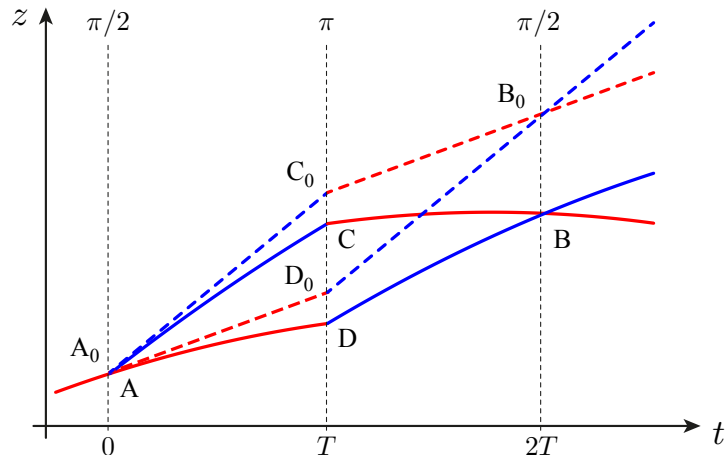

Figure 2.8: Time-space diagram of a Mach-Zehnder interferometer, in presence of a gravitational field (solid lines) and without gravity (dashed lines). The red (blue) paths correspond to momentum states $|p_0\rangle$ ($|p_0 + 2n\hbar k_L\rangle$).

can be divided into three terms

$$\Delta\Phi = \Delta\phi_{\text{path}} + \Delta\phi_{\text{light}} + \Delta\phi_{\text{sep}}. \tag{2.139}$$

The first term is responsible for the free evolution between the pulses and can be calculated with the classical action. The second term comes from the phase imparted by the Bragg pulses at the atom position. The last term originates from the difference in the initial position of the interfering wave packets, and it is typically negligible because the wave packets are overlapped.

A commonly used method to calculate the phase shift of an atom interferometer takes advantage of the path integral description of quantum mechanics [144]. This formalism is very useful since it reduces the analysis to a calculation of integrals along classical paths. This approach was first used to calculate the phase shift of an atom interferometer by Kasevich and Chu [145]. Similar approaches [141, 146] and extensions of the method [147, 148] were developed for Raman pulse interferometers, in which different paths also correspond to a different atomic internal state. The theory can be easily extended to Bragg pulse interferometers, in which the paths are just labeled by a different momentum state.

The action is defined as the integral of the Lagrangian $\mathcal{L}(z, \dot{z})$ over the path $z(t)$ connecting two points $z_A = z(t_A)$ and $z_B = z(t_A)$:

$$S = \int_{t_A}^{t_B} \mathcal{L}\left[z(t), \dot{z}(t)\right] \mathrm{d}t. \tag{2.140}$$

According to the principle of stationary action, we define the classical path Γ_{cl}, for which the action is extremal, so that $S_{\text{cl}} \equiv S_{\text{cl}}(z_B t_B, z_A t_A)$ is just function of the endpoints of the path.

In presence of a uniform gravitational potential the Lagrangian is $\mathcal{L} = \frac{M}{2}\dot{z}^2 - Mgz$. The classical action is found by integrating $\mathcal{L}$ along the classical path, derived from the Euler-Lagrange equations:

$$S_{\text{cl}} = \frac{M}{2}\frac{(z_B - z_A)^2}{t_B - t_A} - \frac{Mg}{2}(z_B + z_A)(t_B - t_A) - \frac{Mg^2}{24}(t_B - t_A)^3. \tag{2.141}$$

The phase difference $\Delta\phi_{\text{path}}$ can be calculated as the difference of the classical action between the two paths:

$$\begin{aligned} \hbar\Delta\phi_{\text{path}} &= S_{\text{cl}}^{\text{AC}} + S_{\text{cl}}^{\text{CB}} - \left(S_{\text{cl}}^{\text{AD}} + S_{\text{cl}}^{\text{DB}}\right) \\ &= \tfrac{M}{T}\left(z_C - z_D\right)\left(z_C + z_D - z_A - z_B - gT^2\right) \end{aligned} \tag{2.142}$$

where we have set $t_B - t_A = 2T$. With a simple geometrical comparison (fig. 2.8), we can see that the parabolic trajectories are related to the straight-line paths by:

$$z_A = z_{A_0}, \quad z_C = z_{C_0} - gT^2/2, \quad z_D = z_{D_0} - gT^2/2, \quad z_B = z_{B_0} - 2gT^2. \tag{2.143}$$

Therefore, we find that the second term in eq. (2.142) is zero:

$$z_C + z_D - z_A - z_B - gT^2 = z_{C_0} + z_{D_0} - z_{A_0} - z_{B_0} = 0 \tag{2.144}$$

because the straight-line trajectories enclose a parallelogram. This means that the phase shift in a free-falling Mach-Zehnder interferometer rises only from the phase imprinting of the laser pulses and not from the free evolution of the two paths. This is true only if we consider a uniform gravity field, or in general for a Lagrangian linear in z. If we account for gravity gradients, which introduce terms proportional to z^2 or higher order terms, the contribution to the phase shift is not null and can be calculated [148]. For typical working parameters gravity gradients can be neglected, since the largest contributions come from the Earth's gravity gradient, on the order of 3×10^{-9} g/cm.

The phase difference due to the interaction with the light pulses can be calculated as the phase difference accumulated in the upper and lower paths

$$\Delta\phi_{\text{light}} = \sum_{\text{ACB}} \phi_i - \sum_{\text{ADB}} \phi_j. \tag{2.145}$$

Since the atom remains always in the same internal state during Bragg transitions, the calculation of the phases ϕ_i is simple. The interaction with a pulse in the time-space position $z_i t_i$ will be responsible for a phase shift

$$\phi_i = \pm \left(k_{\text{eff}} z_i - \omega_{\text{eff}} t_i - \phi_{\text{eff}}\right) \tag{2.146}$$

where the sign is positive for the transitions $|p\rangle \rightarrow |p + 2n\hbar k_L\rangle$ and negative for the opposite, and $\phi_{\text{eff}} = n(\phi_1 - \phi_2)$ is the phase difference between the two optical beams. Adding the phase contributions of the three pulses in the upper and in the lower path, we find the final phase difference

$$\begin{aligned} \Delta\Phi = \Delta\phi_{\text{light}} &= k_{\text{eff}} T^2 g + (\phi_{\text{I}}^{\text{eff}} - 2\phi_{\text{II}}^{\text{eff}} + \phi_{\text{III}}^{\text{eff}}) \\ &= 2nk_L T^2 g + n(\phi_{\text{I}} - 2\phi_{\text{II}} + \phi_{\text{III}}) \end{aligned} \tag{2.147}$$

which is independent with respect to the position, so we label the optical phases ϕ_{I}, ϕ_{II} and ϕ_{III} for the pulses at $t = 0, T$ and $2T$ respectively.

This result can be generalized to a variety of inertial effects arising from different forces. For example, this scheme can be used to measure rotations through the Sagnac effect [10, 149].

2.5.2 Gravimeter based on large-area Bragg interferometry

In eq. (2.147), the factor $k_{\text{eff}} T^2$ represents the space-time area of the interferometer. It is easy to see that in order to increase the sensitivity of a gravity acceleration

measurement we need to increase the the space-time area. This can be done by increasing the free evolution time T or by increasing the effective wave vector of the multi-photon transition.

The simplest solution to increase the time T is to drop the cold atomic cloud from a trap and detect the output states as far as possible from the trapping position, in order to exploit the separation of the arms in free fall for longer time. Another solution is to launch the atoms upward in a fountain in order to double the free evolution time available before the detection [3, 150]. A typical way to launch atoms is based on a moving optical molasses [150, 151], but launching with an accelerated optical lattice is also possible, as explained in sec. 2.2.2, and by using a sequence of high-efficiency π-pulses, as demonstrated in this work. Other more expensive possibilities rely on the operation of the interferometer in a micro-gravity environment, such as dropping towers [152], parabolic flights [153, 154] and orbital space missions [155].

To increase the effective momentum separation between the interferometer arms we need to increase k_{eff}. This can be done by reducing the wavelength of the laser used for the Bragg pulses and by increasing the diffraction order n. Dipole allowed transitions in alkaline-earth atoms are in the blue/near-UV region of the optical spectrum (461 nm for Sr and 399 nm for Yb) resulting in a net momentum transfer to the atoms which is ~ 2 times larger than the momentum imparted by infrared/red transition on more commonly used alkali atoms with the same diffraction order. At the same time, exploiting high order Bragg transitions can linearly increase the interferometer area. Large-momentum-transfer with single Bragg pulses was demonstrated up to 10th order for Cs atoms [122]. Other possibilities have also been investigated to increase the interferometer area. Multi-pulse schemes [156] have been developed and a total momentum splitting of $102\hbar k_L$ [157] was demonstrated. A combination of Bragg pulses and Bloch oscillations can be used to accelerate one of the arm of the interferometer [158–160] or to increase the interferometer time by letting the two arms evolve in a steady lattice [161].

Chapter 3

Apparatus for ultra-cold strontium atom experiments

3.1 Strontium atoms for precision measurements

Strontium is an alkaline-earth metal atom with atomic number $Z = 38$. As all the elements in the second column of the periodic table, it has two valence electrons. We can find four stable isotopes in nature, that can be laser cooled and trapped starting from the same solid sample. The main characteristics of these isotopes are reported in table 3.1.

All of the isotopes, except ^{87}Sr, are bosons with zero nuclear spin. Their level structure is the same, the only difference comes from the isotopic shift. ^{87}Sr is the only fermion, with a nuclear spin $I = 9/2$ and therefore it has a hyperfine structure. Because of the presence of two valence electrons, the energetic ground state does not present any electronic angular momentum. Therefore the bosons have a zero total magnetic moment in their ground state, making these isotopes insensitive to

Isotope	Atomic mass [162, 163]	Abundance (%) [164]	Nuclear spin	Scattering length (a_0) [165, 166]
^{84}Sr	83.913425(3)	0.56(1)	0	122.76(9)
^{86}Sr	85.909260731(9)	9.86(1)	0	798(12)
^{87}Sr	86.908877497(9)	7.00(1)	9/2	97.37(7)
^{88}Sr	87.905612257(10)	82.58(1)	0	−2.00(27)

Table 3.1: Properties of stable strontium isotopes. For completeness we report here the nuclear magnetic moment of ^{87}Sr $\mu = -1.0936030(13)\mu_N$ [167].

external magnetic fields. This is a precious characteristic for implementation in high precision measurement experiments, where the control of the spurious magnetic fields is a real technical issue. On the other hand, the fermion has a magnetic moment that arises only from the nuclear spin, i.e. about 2000 times smaller with respect to alkali atoms.

Among the known elements, ^{88}Sr possesses the unique characteristic of an almost vanishing scattering length. This property has important consequences. For instance, a cold ensemble of ^{88}Sr can be considered as a system of non interacting particles, so it can be described in terms of a single-particle Hamiltonian. Another important consequence is the absence of decoherence among the external degrees of freedom because of the absence of cold collisions. This feature is the reason why long-lived Bloch oscillations in a vertical optical lattice could be observed for up to 17 s with a transfer of more than 10000 photon recoils [24, 41]. For alkali atoms (as well as all others) this lifetime is drastically reduced [92, 168, 169], unless polarized fermions in a single Zeeman sublevel are used [170], or by exploiting Feshbach resonances [171, 172] which imply the use of strong magnetic fields typically not desirable in precision measurement experiments. As a counterpart, such a small scattering length does not facilitate evaporative cooling. This is the reason why Bose-Einstein condensation was first obtained for the less abundant ^{84}Sr isotope [173], which has a more suitable scattering length. ^{88}Sr has only been condensed subsequently through sympathetic cooling [174].

Another interesting feature of strontium isotopes is the presence of narrow optical transitions. Such resonances can be used to produce ultra-cold thermal samples down to the recoil limit, and allow for the implementation of fast optical cooling schemes toward quantum degeneracy [175]. Ultra-narrow optical transitions also allow the development of the most stable and accurate optical clocks [176].

For all these reasons strontium atoms were demonstrated to be very good candidates for precision measurements. In this work, we will focus our attention to the boson ^{88}Sr and the fermion ^{87}Sr, because the difference of their quantum properties are of special interest in Einstein Equivalence Principle tests. Particularly, in addition to following different statistics, one is a spin-less atom and the other has a half-integer spin.

3.2 Laser cooling and trapping of strontium atoms

The cooling technique we use to cool and trap strontium atoms relies on the dissipative term of the light-atom interaction discussed in sec. 2.1.1 and expressed by eq. (2.26), also called the *radiation pressure force*. When the transition is saturated ($s \gg 1$) the force exerted on the atoms is maximum $F_{\max} = \hbar k_L \gamma/2$, and is limited by the linewidth of the transition γ. Broad transitions are more efficient

in slowing and cooling a large amount of velocity classes in a short time.

On the other hand, the upper state lifetime limits the minimum temperature reachable in an optical molasses [177, 178] to the so called *Doppler temperature* (when the detuning is set to be $\delta = -\gamma/2$):

$$k_B T_D = \hbar\gamma/2 \tag{3.1}$$

which is due to the balance between the viscous force of the molasses and the discrete and random nature of the momentum exchange between atoms and light. A more fundamental limit can be found in such system and is called the *recoil temperature* [179], which depends on the recoil energy:

$$k_B T_r = \hbar^2 k_L^2/m = 2E_r. \tag{3.2}$$

This temperature limit comes from the fact that, due to the exchange of momentum quanta, the final indetermination on the velocity can not be smaller than of the one which corresponds to the emission of a single photon, i.e. the recoil velocity $v_r = \hbar k_L/M$.

A full dissertation about the laser cooling techniques based on the radiation pressure force can be found in refs. [180, 181].

In this section we will describe the optical characteristics of the two strontium isotopes that we aim to use in our experiments, and the procedure we adopted to produce samples at 1 μK temperature. We will first describe the boson case, which has a simpler structure, and then we will introduce the modification we need to adopt to trap the fermion.

3.2.1 Optical transitions for cooling of ^{88}Sr

The presence of two valence electrons results in strontium having an energy level structure similar to that of helium. Depending on the reciprocal orientation of the two spins we can distinguish two distinct series of levels: triplet states (for parallel spins) and singlet states (for anti-parallel spins). The levels can be described by the Russell-Saunders coupling [182] because the electrostatic interaction is much larger than the spin-orbit one. Therefore, the states are denoted by three quantum numbers in the form $^{2S+1}L_J$, where S is the total spin, L is the total orbital angular momentum and $J = L + S$. According to Hund's rule, the ground state is the one with smaller total angular momentum, i.e. $5s^2\,{}^1S_0$. In fig. 3.1 the lowest energy levels are shown, together with the transitions of interest for the cooling procedure.

The selection rules for the electric dipole transitions in the Russell-Saunders coupling forbid transitions between singlet and triplet states ($\Delta S = 0$). The presence of spin-orbit coupling breaks this rule, leading to the presence of narrow intercombination transitions.

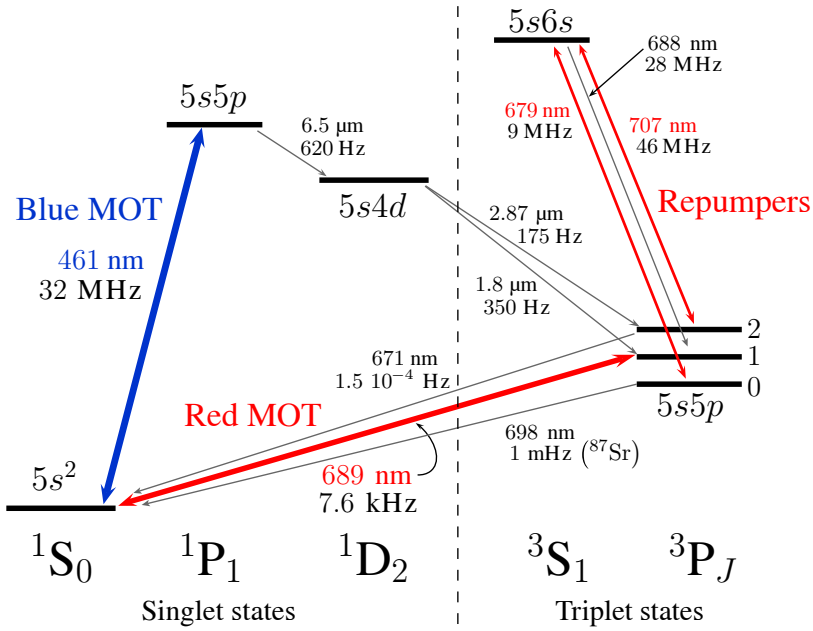

Figure 3.1: Grotrian diagram of the lowest ^{88}Sr levels, and the transitions of interest for cooling. The states are represented in the Russell-Sunders notation $^{2S+1}L_J$ and are divided between singlet ($S = 0$) and triplet states ($S = 1$). For each level we indicate the valence electron configuration, the wavelength and the natural linewidth γ are indicated for each transition.

The first excited state in the singlet series is the $5s5p\,^1P_1$ state, with angular momentum $J = 1$. The transition from the ground state $5s^2\,^1S_0$–$5s5p\,^1P_1$ has a wavelength of 461 nm and a natural linewidth of 32 MHz, so it can be used for efficient slowing of a thermal beam and for Doppler cooling in a magneto-optical trap (MOT). Because of the color of this transition, we refer to this trapping stage as the "blue MOT".

The level scheme composed by the ground state $5s^2\,^1S_0$ and the excited state $5s5p\,^1P_1$ is not a "closed" system. The state $5s5p\,^1P_1$, in addition to decaying to the ground state, also has a finite probability to decay to the $5s4d\,^1D_2$ state. From this state the atoms decay to the fine structure sublevel of the first excited triplet state: $5s5p\,^3P_1$ e $5s5p\,^3P_2$. The $5s5p\,^3P_1$ state can rapidly decay ($\tau = 1/\gamma = 0.13$ ms) to the ground state, while the $5s5p\,^3P_2$ state only decays to the ground state after a very long time ($\tau \sim 2$ h). The resulting effect is that, during the cooling cycle, many atoms are trapped in this metastable state and become transparent to the radiation pressure force.

A few possibilities can be adopted to close the blue MOT cycle. In our experiment we make use of two repumping transitions: the $5s5p\,^3P_2$–$5s6s\,^3S_1$

	λ	γ	ω_r	T_D	T_r	I_s
$^1S_0$–$^1P_1$	461 nm	32 MHz	11 kHz	770 μK	1.03 μK	43 mW/cm^2
$^1S_0$–$^3P_1$	689 nm	7.6 kHz	4.8 kHz	180 nK	460 nK	3 μW/cm^2

Table 3.2: Important parameters for the two cooling transitions of ^{88}Sr, based on the definitions introduced in the previous section.

transition at 707 nm and the $5s5p\,^3P_0$–$5s6s\,^3S_1$ transition at 679 nm. The first one allows pumping to $5s6s\,^3S_1$, from which the atoms can rapidly decay to $5s5p\,^3P_1$, which in turn decay to the ground state. This would be enough to close the cycle, except that the pumped state $5s6s\,^3S_1$ can also decay to $5s5p\,^3P_0$, which is the ultra-metastable "clock" state. From here, the transition to the ground state is totally forbidden for ^{88}Sr and only slightly permitted for the ^{87}Sr with a lifetime of several hours. For this reason we need a beam at 679 nm to repump atoms away from the clock state to close the cycle.

According to the Doppler cooling theory, the final temperature in a broadband MOT is limited by the linewidth of the transition. The 461 nm transition with a linewidth of 32 MHz limits the temperature of the blue MOT to the mK range. To further cool the atoms we use a second MOT stage on the intercombination transition $5s^2\,^1S_0$–$5s5p\,^3P_1$ at 689 nm. Thanks to its narrow linewidth ($\gamma = 7.6$ kHz) the Doppler temperature lies below the recoil temperature, and the sample can be cooled below 1 μK. This second stage is called the "red MOT".

Because of no ambiguity with the Russell-Saunders notation for the transitions of interest, we will omit the full valence electronic configuration, from now on. The important parameters for the two cooling transitions are reported in table 3.2.

3.2.2 ^{88}Sr cooling and trapping procedure

Slowing the atomic beam

The atomic source is composed of a collimated atomic beam produced by an oven heated to about $T \sim 400$ °C. The corresponding mean longitudinal velocity is $v = \sqrt{3k_BT/M} \sim 350$ m/s. Since the capture velocity of the first MOT stage is about 50 m/s, we need to slow down the atomic beam to velocities about one order of magnitude smaller. This is done with a Zeeman slower [183] operating on the $^1S_0$–$^1P_1$ transition, which can exert a maximum acceleration $a_{\max} \sim 10^6$ m/s^2, about five order of magnitude larger than gravity acceleration. For a typical working intensity of $s \sim 1$ and a detuning $\delta \sim -300$ MHz, the maximum acceleration is $a \sim a_{\max}/2$. Therefore, the distance needed to slow an atom with initial velocity $v = 350$ m/s is $L = v^2/2a \sim 30$ cm. The Zeeman slower is composed of a 30 cm long solenoid with conical section and a red detuned beam with circular polarization

propagating in opposite direction with respect to the atomic beam. The magnetic field produced by the solenoid is inhomogeneous and is chosen to compensate the Zeeman sublevels shift due to the Doppler effect of the moving atoms along the entire path. By properly setting the profile of the magnetic field, it is possible to slow all the velocity classes down to a desired final velocity, in our case 50 m/s.

The blue MOT

The atomic beam slowed in the Zeeman slower reaches the main vacuum chamber and it is trapped in a magneto-optical trap operating on the ${}^1S_0$–${}^1P_1$ broad transition. As sketched in fig. 3.2(a), the MOT is composed of three pairs of counter-propagating laser beams with opposite circular polarizations crossing at the zero of a quadrupole magnetic field produced by two coils in an anti-Helmholtz configuration (the current flows in opposite directions). The presence of the magnetic gradient creates a disequilibrium between the pairs of forces acting in opposite directions, as a function of position with respect to the zero of the field.

The operation of a 1D MOT is summarized in fig. 3.2(b). For a transition $J = 0 \rightarrow J = 1$, the Zeeman sublevels m_J of the excited state are split by the gradient of the magnetic field, approximately liner near the zero $B(z) = bz$. The energetic shift $\Delta E = g_J m_J \mu_B b z$ has a different sign for the states $m_J = \pm 1$. If the laser beams are red detuned with respect to resonance, the beam propagating from right to left and σ^- polarized, which couples the ground state with the $m_J = -1$, will

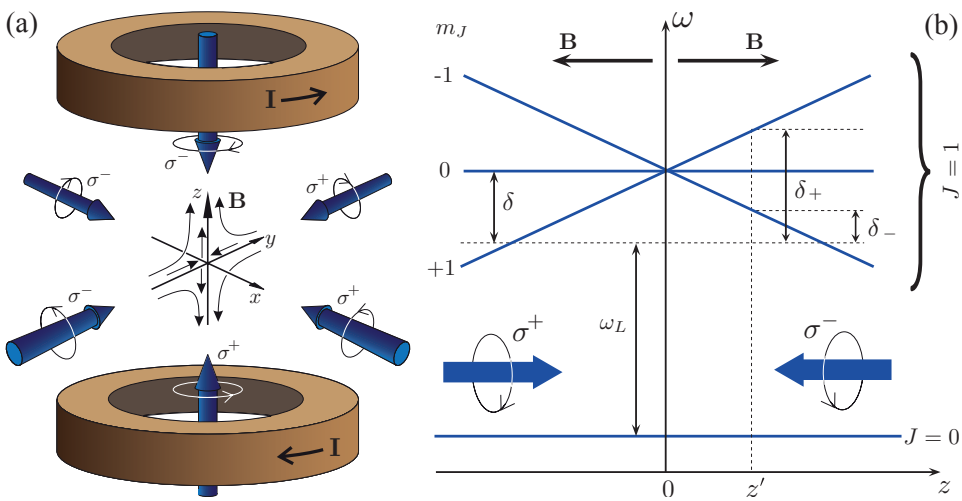

Figure 3.2: Schematic picture of the MOT operation. (a) The trap is composed of three pairs of orthogonal counter-propagating laser beam crossing the zero of a quadrupole field produced by two coils in anti-Helmholtz configuration. (b) One dimensional operation of the MOT.

interact more favorably with atoms in the positive z direction. On the other hand, the beam propagating from left and σ^+ polarized will push atoms in the negative z direction. Averaging between many cycles of absorption and spontaneous emission, the optical pumping will redistribute atoms among the magnetic sublevels and the resulting force for each beam can be written as the radiation pressure force (2.26) where the detuning has a dependence on velocity and position:

$$F_{\text{diss}}^{\sigma^\pm} = \hbar k_L \frac{\gamma}{2} \frac{s}{1 + s + (2\delta_\mp/\gamma)^2}, \quad \text{where} \quad \delta_\mp = \delta \mp k_L v \mp \beta z. \tag{3.3}$$

The total force $F_{\text{MOT}} = F_{\text{diss}}^{\sigma^+}(\delta_-) - F_{\text{diss}}^{\sigma^-}(\delta_+)$ acting on the atom is a dispersive force in velocity and position, able to cool and trap. The description can be easily extended in three dimensions, taking into account the fact that due to the asymmetry of the anti-Helmholtz configuration, the gradient along coils axis is twice the one in the radial direction: $b_x = b_y = -b_z/2$. The resulting trapping geometry is not a sphere, but an ellipsoid.

The blue MOT falls within the broadband MOT class, for which $\gamma \gg \omega_r$. The recoil frequency defines the energy scale that distinguish cooling processes obtained on broad or narrow transitions. For the blue MOT $\gamma/\omega_r \sim 3 \times 10^3$, so the linewidth, or more generally, the power broadened linewidth $\gamma_P = \gamma\sqrt{1+s}$, is the natural energy scale. In this regime the dynamics of the system can be described by a semi-classical theory that leads to the Doppler cooling, in which the recoil photon is more a conceptual tool than a real key object of the system dynamics. Moreover, gravity force is negligible since its ratio with the maximum force exerted by the radiation pressure is

$$\frac{Mg}{F_{\text{max}}} = \frac{2Mg}{\hbar k_L \gamma} \sim 10^{-5}. \tag{3.4}$$

In our experiment the configuration of the blue MOT is the following: each beam has a diameter of about 2 cm and operates close to saturation $s \sim 1$. The magnetic gradient is set to be about $b = 550$ G, which guarantees a capture velocity of 50 m/s, required to catch the maximum possible flux coming from the Zeeman slower. The detuning is experimentally optimized to $\delta = -30$ MHz to get the largest number of atoms trapped at the lowest temperature. With a time-of-flight (TOF) technique we estimate a temperature of about 1 mK at the end of the blue MOT.

The two repumping radiations at 707 nm and 679 nm are coupled and sent towards the MOT position, allowing an increase of about 40 times the number of trapped atoms. With this system we can prepare a cold sample of about 10^8 atoms in 1 s. Further cooling is obtained in a second MOT stage operating on the intercombination transition at 689 nm.

The red MOT

The red MOT transition at 689 nm, unlike the blue transition used in the first cooling stage, has a linewidth comparable to the recoil frequency $\gamma/\omega_r = 1.6$. The narrow transition allows the system to evolve in a different regime, where the semi-classical approach does not hold anymore, and different cooling properties emerge [184, 185]. For instance, gravity plays a key role in this kind of regime. Indeed, the maximum force exerted by the radiation pressure is just enough to compensate for the gravitational force: $F_{\max}/Mg \sim 16$.

The saturation intensity for the ${}^1S_0$–${}^3P_1$ transition is rather small ($I_s = 3\ \mu\mathrm{W/cm^2}$) with respect to the available optical power for the red MOT beams delivered by a laser diode. For a 2 cm diameter and a power of 5 mW per beam, we can have an intensity larger than 2000 I_s. The saturation parameter s (which sets the power broadened linewidth γ_P) and the detuning δ determine the dynamics in the red MOT. Depending on their relative size with respect to the recoil frequency, we can distinguish three regimes [186].

When the red MOT beams are switched on, their optical spectrum is broadened by modulating the radio frequency in an acusto-optical modulator (AOM). This is done in order to increase the capture velocity to cover the wide range of velocity classes coming from the blue MOT. A modulation of 8 MHz generates about 400 sidebands with an intensity of about $5I_s$ per tooth. After the blue beams are switched off, the magnetic gradient is suddenly decreased and then slowly ramped up to 0.6 G/cm in 50 ms, in order to maintain an adiabatic condition on the deceleration [187]. This procedure is called the "broadband red MOT", and allows us to recapture about 30% of the atoms.

After 200 ms of cooling in the broadband phase, the modulation is switched off and all the power is sent to the carrier to broaden the resonance by power. This situation corresponds to the regime $\delta \gg \gamma_p \gg \nu_r$, in which the leading energy scale is given by γ_P, and the dynamics can be described by a semi-classical approach in the same way as for the broadband transition MOT. Here gravity is negligible and the thermodynamics can be described by Doppler theory. The power is then slowly decreased and the detuning is ramped down to approach resonance. The system evolves in the regime $\delta < \gamma_p \gg \nu_r$, in which the dynamics of the trap becomes a damped oscillator. When the intensity and the detuning are reduced so that $\gamma_p = \gamma \sim \nu_r$, the system is in a quantum mechanical regime. Here gravity can not be neglected, and the thermodynamics are fully dominated by the photon recoil. Temperature close to the recoil limit can be reached.

Figure 3.3 summarizes the main aspects of the red MOT. The overall force acting on the atom along the vertical direction (the radiation pressure force and the gravity force $F_{\mathrm{MOT}} - Mg$) and the respective potential energy (in temperature units) for two different limits are plotted in fig. 3.3(a). The blue line corresponds to

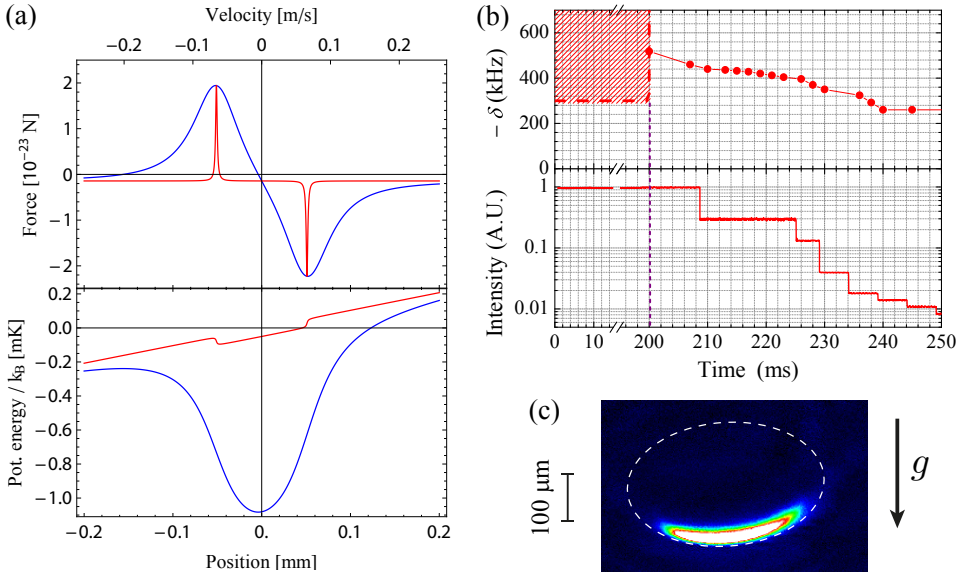

Figure 3.3: Red MOT operation. (a) Overall vertical force and potential of the red MOT in two different regimes: (blue line) $\gamma_p \gg \nu_r$, (red line) $\gamma_p \sim \nu_r$. (b) Experimental parameters of the red MOT beams. For up to 200 ms the frequency is modulated at 8 MHz, then is switched to single frequency and ramped towards resonance while the intensity is reduced. (c) Absorption image of the final red MOT.

the first regime, in which the power broadened linewidth dominates the dynamics, and the gravity force is a negligible contribution to the potential. The red line corresponds to the case $\gamma_P \sim \omega_r$. The force effectively acts as a barrier only in specific positions that depend on the detuning and magnetic gradient. In three dimensions, because of the asymmetry of the gradient, this barrier has an ellipsoid shape (see frame c). In this regime gravity tilt of the potential is not negligible and atoms will be collected at the energy minimum which lies below the zero of the magnetic field. In fig. 3.3(b) the experimental intensity and frequency ramp of the red MOT is shown. The broadband phase is 200 ms long and then a ramp is applied in single-frequency operation for 50 ms to cool the sample towards the recoil limit. An absorption image of the final sample is shown in fig. 3.3(c). The measured temperature in TOF is about 1.2 μK, and the number of atoms about 5×10^6. The spatial dimensions along the radial and vertical direction are 300 μm and 50 μm full width at half maximum (FWHM), respectively.

3.2.3 Hyperfine structure of ^{87}Sr

The presence of a non-zero nuclear spin $I = 9/2$ in ^{87}Sr gives rise to a hyperfine structure. Each level $^{2S+1}L_J$ is split into sublevels defined by the quantum number $F = I + J$. For $J < I$, as in the transitions of interest, each $^{2S+1}L_J$ state will contain $2J + 1$ hyperfine levels.

Taking into account the magnetic dipole and the electric quadrupole interactions (higher order terms contribution is 10^8 times smaller) the energy correction is [182]

$$\Delta E_{\text{hyp}} = \frac{1}{2}\mathcal{A}K + \frac{1}{4}\mathcal{B}\left[\frac{3K(K+1) - 4I(I+1)J(J+1)}{2I(2I-1)J(2J-1)}\right] \tag{3.5}$$

where $\mathcal{A}$ and $\mathcal{B}$ are the interaction constants for magnetic dipole and the electric quadrupole respectively, and $K = F(F+1) - I(I+1) - J(J+1)$. Each of these levels is composed by $2m_F + 1$ Zeeman sublevels, which can be split (neglecting the nuclear factor g_I) in presence of a magnetic field B by $\Delta E_{Zee} \simeq g_F m_F \mu_B B$, where the Landé factor is given by

$$g_F = \frac{F(F+1) + J(J+1)I(I+1)}{2F(F+1)}. \tag{3.6}$$

State	F	g_F	$\mathcal{A}$ (MHz)	$\mathcal{B}$ (MHz)
$^1S_0$	9/2	0	0	0
$^1P_1$	7/2	−2/9	−3.4(4) [188]	39(4) [188]
	9/2	4/99		
	11/2	2/11		
$^3P_0$	9/2	0	0	0
$^3P_1$	7/2	−1/3	−260.084(2) [189]	−35.658(6) [189]
	9/2	2/33		
	11/2	3/11		
$^3P_2$	5/2	−6/7	−212.765 [190]	67.34 [190]
	7/2	−1/7		
	9/2	2/11		
	11/2	51/143		
	13/2	6/13		
$^3S_1$	7/2	−4/9	−542.0(1) [191]	−0.1(5) [191]
	9/2	8/99		
	11/2	4/11		

Table 3.3: Hyperfine constants and Landé factors for the states of interest of ^{87}Sr. The Landé factor of ^{1}S$_0$ and ^{3}P$_0$ is determined by the nuclear g_I factor ($\sim 2 \times 10^{-3}$).

Table 3.3 summarizes the $\mathcal{A}$, $\mathcal{B}$ and g_F values for the levels of interest. Figure 3.4 shows the level structure and the transitions of interest for trapping and cooling of ^{87}Sr. The energy shifts with respect to the ^{88}Sr are reported, also taking into account the isotopic shift.

The $^1P_1$ state presents three hyperfine states $F = 7/2$, $9/2$ and $11/2$, each one consisting of $2m_F + 1$ sublevels. For an efficient trapping into a MOT, we operate on the transition with $\Delta F = +1$, which has a higher transition probability and a larger pressure force accordingly. Therefore, the blue MOT transition is $^1S_0(F = 9/2)$–$^1P_1(F = 11/2)$. Since $\mathcal{A}$ and $\mathcal{B}$ are on the order of γ, the hyperfine structure of $^1P_1$ cannot be resolved, leading to undesired excitations of the $F = 9/2$ and $11/2$ states. Another complication is the wide hyperfine structure of the repumping levels $^3P_2$ and $^3S_1$, which are divided into five and three F levels respectively.

The state $^3P_1$ is also divided into three states $F = 7/2$, $9/2$ and $11/2$, but the coupling constants are much larger and the linewidth much smaller. Therefore in the second MOT stage, the transitions between different hyperfine states are totally independent. The main cooling transition is $^1S_0(F = 9/2)$–$^3P_1(F = 11/2)$. Unfortunately, because the g_F factor of the ground state is much smaller than the excited state, the coupling between the Zeeman sublevels is strongly unbalanced.

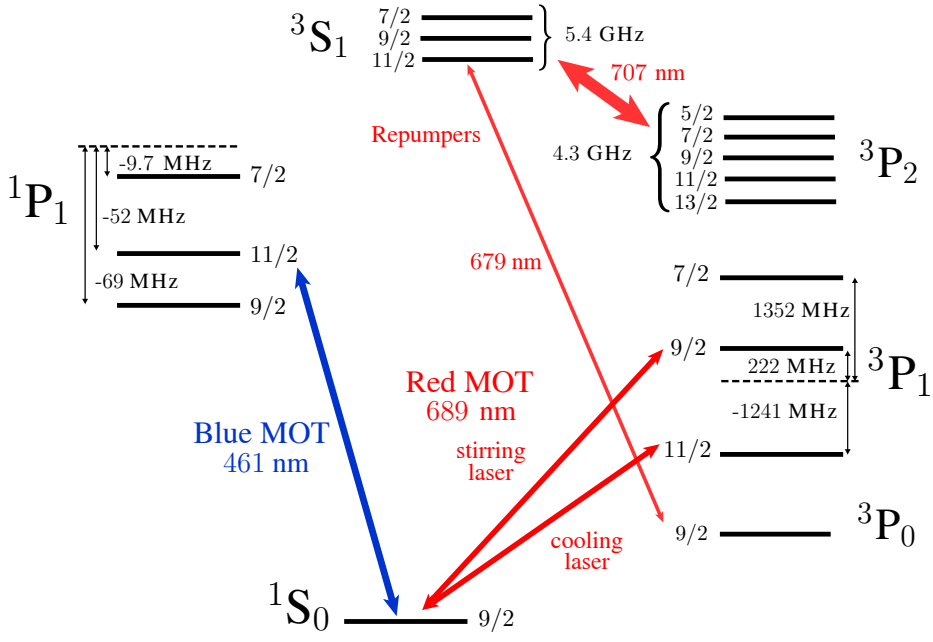

Figure 3.4: Hyperfine structure and transitions of interest for cooling and trapping of ^{87}Sr. The shifts are given with respect to ^{88}Sr, including the isotopic shift. For the states involved in the repumping process, the overall broadening is given.

As we will see in the next section, an additional laser has to be used in order to make the red MOT work.

3.2.4 ^{87}Sr cooling and trapping procedure

The blue MOT

A limiting factor in the fermion trapping is its pure natural abundance. As shown in table 3.1, the probability to find ^{87}Sr atoms in solid strontium is just 7%, against 83% of ^{88}Sr. Therefore, the atomic flux ϕ_f from the oven will be $7/83 \simeq 9\%$ of the ^{88}Sr flux. Because the loading flux is linear with ϕ_f, the number of ^{87}Sr atoms loaded in the MOT cannot be expected to exceed 9% of the ^{88}Sr atoms.

As we have already mentioned, because the hyperfine splitting is small compared to γ, operating the blue MOT on the $^1S_0(F = 9/2)$–$^1P_1(F = 11/2)$ transition leads to some losses in the $F = 9/2$ and 11/2 states. The main issue causing this is the wide hyperfine structure of the repumping levels $^3P_2$ and $^3S_1$, which requires an expedient. The state $^3P_2$ has five hyperfine sublevels separated by about 4.3 GHz. All of them are populated by the decay of $^1D_2$, and they need to be repumped to $^3S_1$, which in turn is divided into three levels separated by about 5.4 GHz. Instead of using different lasers to address all these hyperfine states, we simply sweep the frequency of the 707 nm laser [192]. By choosing the right modulation parameters it is possible to cover all the frequency range containing the hyperfine transitions $^3P_2(F)$–$^3S_1(F')$. Despite the laser not being single mode during a sweep cycle, by modulating the piezoelectric and the current it is possible to significantly increase the number of trapped atoms. The parameters are adjusted in order to maximize this number, and for normal operation we observe ten times more atoms with respect to single-frequency operation.

On the other hand, modulating the 679 nm laser is not necessary. The state $^3P_0$ has just one hyperfine state $F = 9/2$, therefore it is sufficient to tune the laser on the $^3P_2(F = 9/2)$–$^3S_1(F = 11/2)$ transition. In this way, all the atoms decaying from $^3S_1(F)$ to $^3P_2$ are transfered back into the cycle by the 707 nm laser. With this expedient we can trap about 3×10^6 atoms in 3 s in the blue MOT.

The red MOT

While for alkaline atoms the presence of a hyperfine structure does not significantly complicate the MOT operation, for alkali-earth atom the presence of a $J = 0(F)$ ground state leads to a remarkable complication because of the different Landé factors with respect to the $F+1$ excited state. To understand this point, let us consider a MOT operating on a $F \rightarrow F + 1$ transition, such as the $F = 9/2 \rightarrow F = 11/2$ for

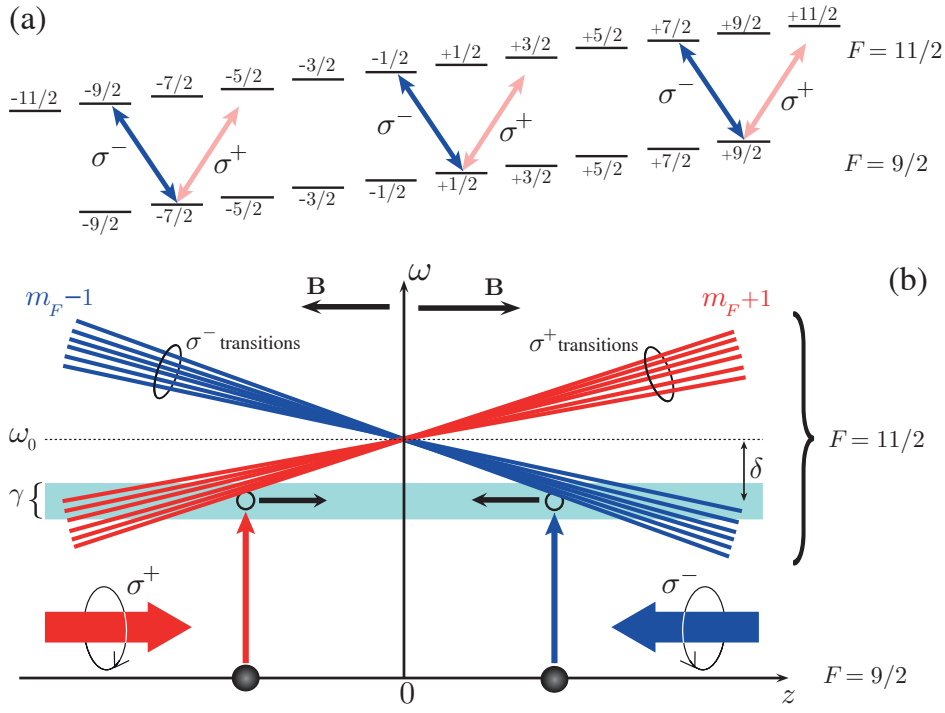

Figure 3.5: Operation of a 1D MOT working on the $F = 9/2 \rightarrow F = 11/2$ transition with $g_g \sim g_e$. (a) For a given fixed position ($z > 0$ for example), the Zeeman shift is almost the same in the ground and in the excited state. Atoms interact with σ^- regardless of which m_F state is occupied. (b) MOT operation depending on the position. For an atom in a certain m_F of the ground state, the blue (red) lines represents the $m_F + 1$ ($m_F - 1$) Zeeman sublevels shifted by $B(z) = bz$.

strontium. The Zeeman splitting due to a MOT magnetic field $B(z) = bz$ is

$$\hbar\Delta\omega = \left[(m_F \pm 1)g_e - m_F g_g\right] \mu_B b z, \tag{3.7}$$

where g_g and g_e are the Landé factors for the ground states m_F and the excited states $m_F \pm 1$ respectively. Figure 3.5 shows the schematic operation of an alkali atom MOT working on a $F = 9/2 \rightarrow F = 11/2$ transition. Alkali atoms, due to a ground state with $J \neq 0$, have $g_e \sim g_g$. Therefore, the splitting (3.7) makes the resonance frequency for a certain polarization independent on the populated sublevel of the ground state, as shown in fig. 3.5(a). The two counter-propagating laser beams with $\delta < 0$ and opposite circular polarizations exert the same force (despite small differences due to the slightly different slopes) regardless of which m_F state is populated. An atom moving in the $z < 0$ ($z > 0$) region will always have higher probability to absorb a photon from σ^- (σ^+) beam, receiving a kick towards the trap center (fig. 3.5b).

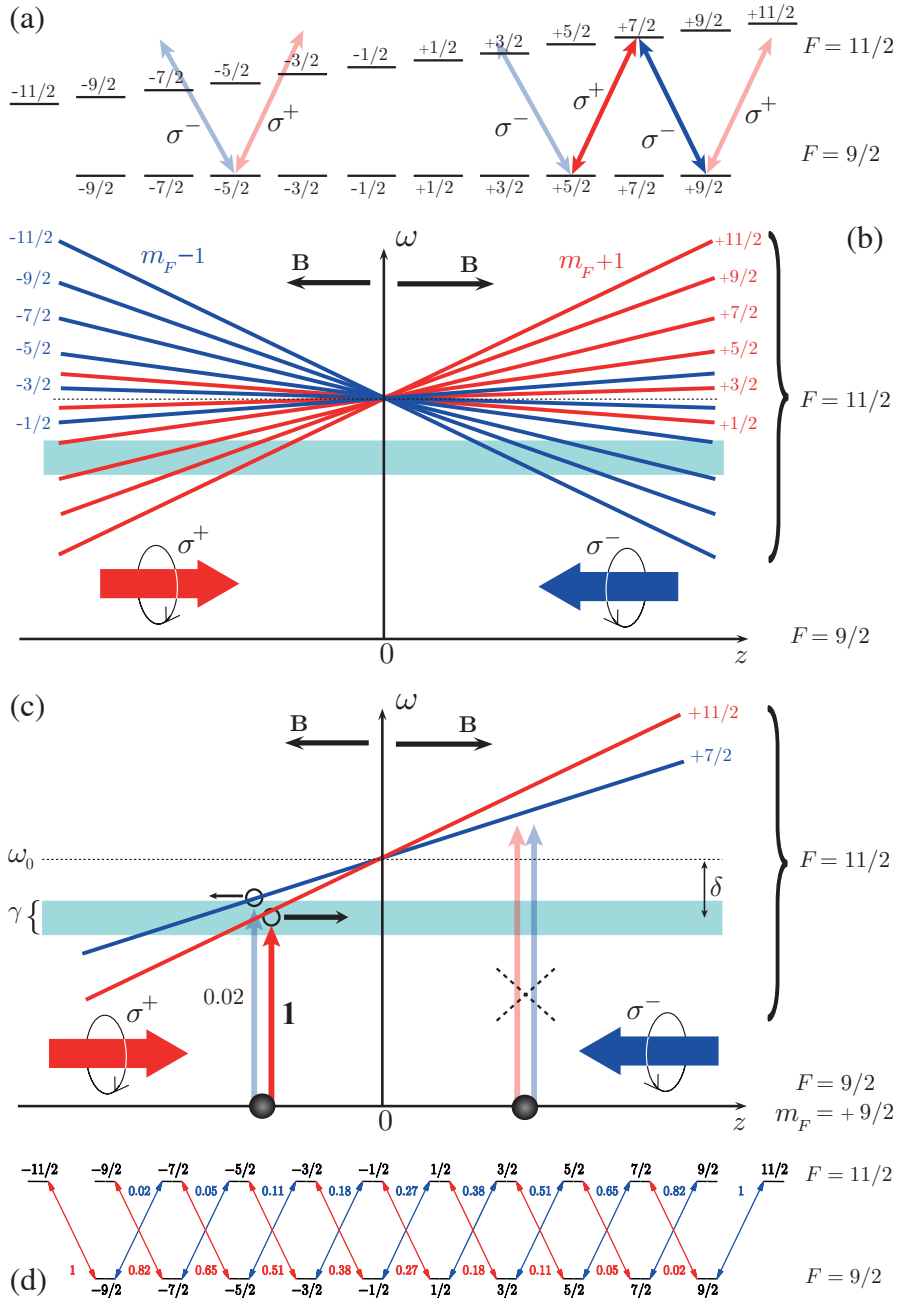

Figure 3.6: MOT operation on the $F = 9/2 \rightarrow F = 11/2$ transition with $g_e \gg g_g$. (a) For a given position, the atoms can only interact with σ^-, with σ^+, or neither of the two, depending on the occupied m_F state. (b) Depending on the position, for some m_F, δ can even change sign. (c) MOT operation for an atom in the $m_F = +9/2$ of the ground state. The Clebsch-Gordan asymmetry allows the atom to interact with the radiation in $z < 0$, but not in $z > 0$. (d) Square modulus of C-G coefficients.

For alkali-earth atoms, which have $g_g \ll g_e$, the situation is quite different. As shown in fig. 3.6(a), because of the degeneracy of the Zeeman sublevels in the ground state, in a given position $z > 0$ ($z < 0$) some m_F states have a higher probability to absorb σ^- (σ^+) photons, others will interact with σ^+ (σ^-) photons, while the rest will not interact with either beam. The probability for an atom to absorb photons from one beam or another does not only depend on the m_F state, but also on the atomic position z. Looking at the slope of the excited sublevels as a function of the position (fig. 3.6 b), one sees that the transition probabilities strongly depend on the m_F state, in same cases even an inversion of the sign of the Zeeman shift in the two sides of the trap occurs.

Let's see how the strong dependence of a given m_F state on the position obstructs the formation of a restoring force. In fig. 3.6(c) we consider an atom occupying $m_F = +9/2$ in the ground state. It can interact only with the excited $m_F = 11/2$ and 7/2, depending on the polarization. Because of the small g_g, the sign of the Zeeman shift will be the same for these two levels (see eq. 3.7). If we assume the atom is in $z < 0$, in principle it can absorb photons from both beams. However, the unbalanced Clebsch-Gordan coefficients [86] for this *stretched* states favor the transition σ^+ pushing towards the center of the trap. In general, as we can see by looking at the ratios of the Clebsch-Gordan coefficients for the pair transitions (fig. 3.6 d), the probability of absorbing a photon from the restoring beam is higher for stretched states, i.e. with larger $|m_F|$. This difference in transition probability between $\sigma^\pm$ lights can be used, instead of the resonance condition for the Zeeman shift, to create a restoring force [193]. The other important consequence is the fact that if the atom in $m_F = +9/2(-9/2)$ is in $z > 0(z < 0)$, it cannot be on resonance with any light and is free to leave the trap. Summarizing, only stretched states can be pushed by the radiation pressure force, but just in one side of the trap.

In the case of broad transitions, such as ${}^1S_0$–${}^1P_1$ in the blue MOT, the fast optical pumping rapidly randomizes the population between the sublevels. The stretched states are alternately populated and an average restoring force toward the center of the trap is obtained. On the other hand, in the case of narrow transitions, such as ${}^1S_0$–${}^3P_1$ in the red MOT, the atoms remain on resonance with the trapping beam for only a few cycles, so the population can not be efficiently redistributed among the Zeeman sublevels. This effect limits the ^{87}Sr MOT lifetime, which is about ten times smaller than the ^{88}Sr one.

To overcome this issue, by increasing the optical pumping efficiency towards the stretched states, we realize a MOT operating on two intercombination transitions [194]. In addition to a laser working on the ${}^1S_0(F = 9/2)$–${}^3P_1(F = 11/2)$ transition (called "cooling" or "trapping" laser because its the one that exerts the force), we introduce a second laser working on the ${}^1S_0(F = 9/2)$–${}^3P_1(F = 9/2)$ transition, with the same detuning $\delta < 0$ and polarization for each beam. The ${}^3P_1(F = 9/2)$ state has a Landé factor 4.5 times smaller than the ${}^3P_1(F = 11/2)$ state, so the

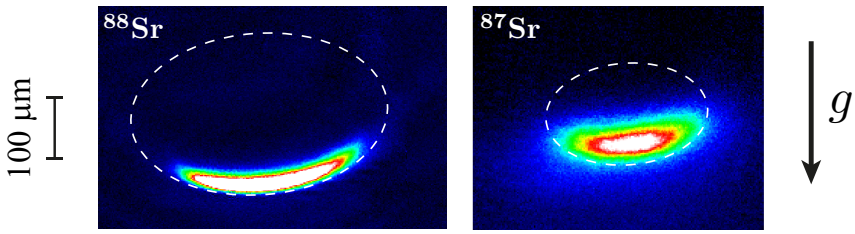

Figure 3.7: Comparison between the ^{88}Sr and ^{87}Sr final red MOT.

Zeeman splitting for the excited state is closer than the ground state one. Therefore, it remains on resonance for longer in an inhomogeneous magnetic field. A laser tuned to the $^1S_0(F = 9/2)$–$^3P_1(F = 9/2)$ transition allows a much more efficient pumping in a larger area, resulting in a rapid occupation of the stretched states. Because of this effect, this laser is called the "stirring" laser.

By using this technique, the red MOT can work in a similar way as the one for ^{88}Sr. The broadband phase, as well as the single-frequency ramp, is applied to both lasers. The result is a very efficient red MOT cooling. With this method we can produce a red MOT sample of about 3×10^5 at a temperature of 1.4 μK. Figure 3.7 shows an absorption imaging of the final ^{87}Sr red MOT, compared to the ^{88}Sr one. We keep the trap slightly tighter by tuning the lasers closer to resonance (δ = 220 kHz, instead of 260 kHz used for ^{88}Sr). The result is a hotter sample, but the number of atoms is almost doubled in this way.

3.3 Experimental apparatus

The vacuum system and the main components for the production of an ultra-cold strontium gas used for the experiments of this work are sketched in fig. 3.8.

3.3.1 Atomic source

The source consists of an atomic beam produced by a compact in-vacuum oven [195] containing about 5 g of solid strontium (99% purity). In comparison to a vapor cell, atomic beams allow cleaner systems, uncoupling the high-pressure part (the oven) from the MOT cell. Moreover, with the use of a Zeeman slower it is possible to obtain high loading fluxes into the cold trap. With alkali-earth atoms, the use of an oven is almost compulsory because of the low vapor pressure. Reasonable atomic beam fluxes require the solid sample to be heated to hundreds of degrees Celsius.

The oven consists of a stainless-steel reservoir with internal length and diameter of 34 mm and 10 mm respectively, filled with strontium, electrically heated by

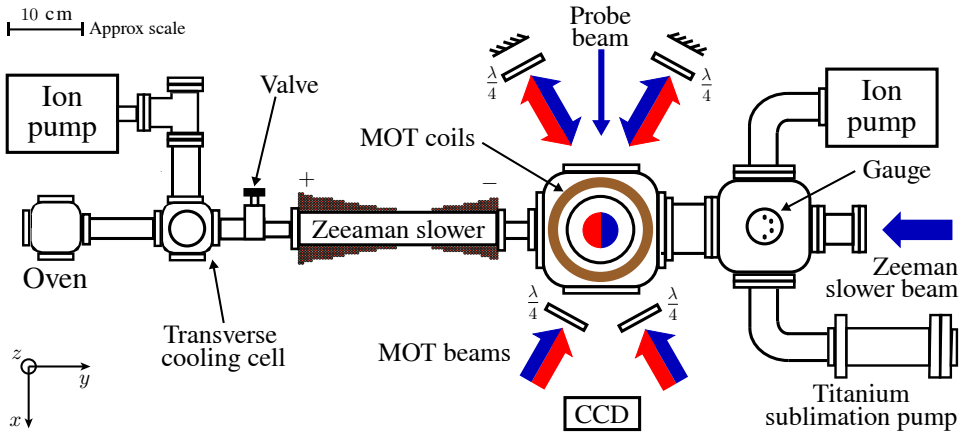

Figure 3.8: Schematic top view of the experimental apparatus.

a tantalum wire. The reservoir is secured to a standard DN40CF flange, and the thermal contact is reduced by steatite split bushes, which have very low thermal conductivity. The output of the reservoir terminates in a nozzle filled with about 120 stainless-steel capillaries 8 cm long, with internal diameter of 100 μm for beam collimation. The oven is located in vacuum into a standard DN40CF cube, facing the Zeeman slower tube. The vacuum environment isolates the oven from thermal conduction. Additional heating is due to blackbody radiation, for which a 1 mm thick aluminum cylinder provides shielding. The thermal isolation guarantees high efficiency with low power consumption (about 15 W at 440 °C). We typically heat the oven to about 430 °C. By means of transverse spectroscopy we have estimated a ^{88}Sr atomic flux of about 2×10^{11} atoms/s at this temperature.

3.3.2 Vacuum system

The direction of the atomic beam is adjustable by a bellow that connects the oven cube to another DN40CF cube with four optical accesses. Through this cell we performed transverse spectroscopy for the atomic beam characterization, but in principle it can be used to realize transverse cooling [196] for further beam collimation. A 20 l/s ion pump is attached to the cube, providing a residual pressure of about 10^{-8} mbar in the oven region. After the cube, a mechanical valve allows the atomic beam flux to be stopped without turning the oven off. After the valve, the oven vacuum and the MOT cell vacuum are connected through a tight nozzle in order to get a significant differential pressure between the “dirty” and the “clean” part of the apparatus. Opposite to the oven position, the optical access for the Zeeman slower beam is placed on a DN63CF cube. Because strontium reacts highly with silicates a sapphire window was chosen, to avoid coating of the Zeeman slower

optical access. A pressure gauge, a 40 l/s ion pump and a titanium sublimation pump are attached on the cube. To increase the effective pump speed, the cube is connected to the MOT cell via a 10 cm long DN63CF nipple. The residual pressure measured by the gauge is 7×10^{-10} mbar.

3.3.3 Zeeman slower

The Zeeman slower consists of a tube with length $L = 30$ cm, around which two tapered coils are wound. The magnetic profile produced by the solenoid, which allows the compensation of the Doppler shift during the slowing, follows the equation $B(y) = B_0\sqrt{1 - y/L} + B_{\text{bias}}$, where the offset B_{bias} is proportional to the detuning δ. We have chosen to work with a red detuned beam with σ^- polarization [197]. In this configuration the magnetic profile needs to pass from positive to negative, leading to the following advantages: the magnetic field has a lower maximum absolute value, which requires less current, and the magnetic field goes drastically to zero at the output, allowing a better definition of the output velocity distribution because the atoms will suddenly be out of resonance. We have chosen a detuning of $\delta = -480$ MHz, which is far enough from resonance to not affect the atoms trapped in the MOT. By choosing this value we need to set a maximum field $B_0 \simeq 550$ G in order to slow down atoms with a starting velocity up to 400 m/s. In practice the solenoid is divided into two parts, with opposing independent current control in order to arbitrary set the input capture velocity and the output velocity for best loading of the MOT.

3.3.4 MOT cell and coils

The MOT cell is constituted by a custom DN63CF cube, connected to the Zeeman slower on one side and to the pumps on the opposite side. Large windows (10 cm diameter) with a broad visible anti-reflection coating are located on the other four apertures. The windows are sealed by indium wire. The three MOT beams at 461 nm and 698 nm are overlapped with dichroic mirrors. Two horizontal MOT beams access the cell with a relative angle of 60°, while the vertical beam accesses from the lower window (tilted a few degrees with respect to the vertical direction to allow optical access for the lattice beams). The beam polarization is made circular by three quarter-wave plates ($\lambda/4$) placed just before the cell. The beams are retro-reflected and the polarization is rotated by three additional $\lambda/4$-plates.

The anti-Helmholtz coils have the axis oriented along the vertical direction. The magnetic gradient at the center of the cell is $b_z = 4.2$ Gm^{-1}A^{-1}. The coil current is remotely controlled by an analog power supply and a MOSFET, which has a response time of about 1 ms.

Because the 689 nm transition is so narrow, the red MOT is highly sensitive to

spurious magnetic fields. Relatively small magnetic fields can take the cooling laser out of resonance. For example, the Earth's magnetic field (~ 0.5 G) is responsible for a Zeeman shift of about 1 MHz, much larger than the natural linewidth $\gamma = 7.6$ kHz. Therefore, we compensate for the offset magnetic fields by means of three pairs of coils in Helmholtz configuration, which are oriented along orthogonal directions and controlled by three independent current supplies.

3.3.5 Robust breadboard tower

To increase the stability of the experimental optical setup, we implemented a robust breadboard system originally designed by Andrea Alberti. The system consists of two 50×120 cm custom breadboards (Kinetic System), placed one on top of the other and mounted around the vacuum system as shown in fig. 3.9. The two breadboards were made with a 5 cm thick honeycomb structure and a special geometry to fit the experimental setup. The lower breadboard has a squared hole on the long side in order to fit around the MOT cell. It is held 12 cm above the main optical table so that the top surface is 5 cm lower with respect to the MOT center, which is the correct height for our standard optic mounts. The top breadboard is held 30 cm above the lower one and has a hole of 10 cm diameter right on top the MOT cell window for vertical optical access. Both breadboards have mounting holes on both sides, so we used the lower parts to anchor the MOT coils, cables and fluorescence detection systems, in order to free space for other optics. Each breadboard is held by four extruded aluminum rods with a 9×9 cm cross section.

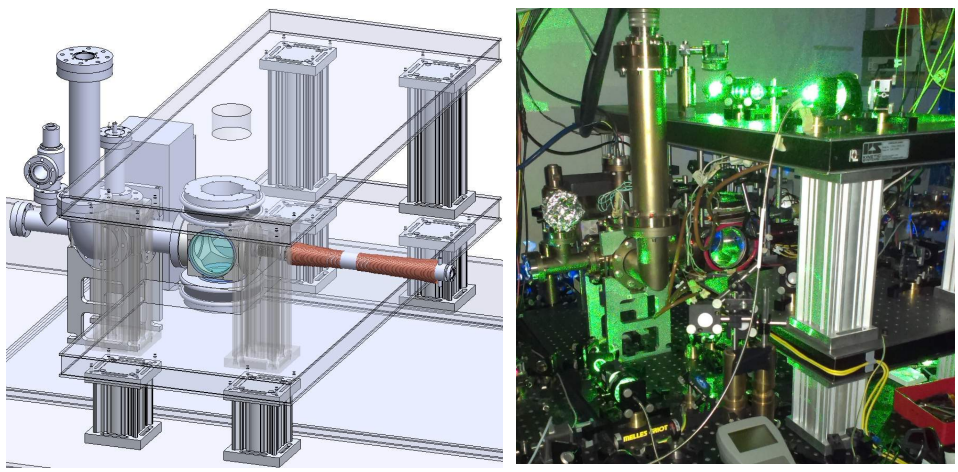

Figure 3.9: Robust breadboard tower drawing (left) and picture (right). Two vibration isolation breadboards are mounted around the vacuum system in order to increase the stability of the experiment in terms of long term drift and vibration isolation.

The lower breadboard hosts the MOT mirrors and the probe beam shaping optics. On the top breadboard we mounted optics for the optical lattice and a vibration isolation platform for the Bragg retro-reflection mirror that, as we will see, is the main limit in our free-falling interferometric measurements.

3.3.6 Atom detection systems

The number of atoms in the blue MOT is monitored by an avalanche photodiode, which measures the fluorescence due to the interaction with the MOT beams.

In the red MOT and in the lattice, the main characteristics of the atomic cloud (position, dimensions, density, temperature) can be studied by a standard absorption imaging technique on a CCD camera. The probe beam is a laser beam at 461 nm tuned on-resonance with respect to the ${}^1S_0$–${}^1P_1$ transition of the respective isotope. The beam comes from a polarization-maintaining fiber and arrives at the lower suspended breadboard with a power of $\sim 500\ \mu$W. It is expanded to a waist diameter of about 5 mm FWHM, and it enters the MOT cell from the x direction (see fig. 3.8). The absorption image is focused by a lens onto a 8×8 mm CCD camera (Andor Luca R), with a 8 μm pixel size. The focal length was chosen in order to have a magnification of about 1.7, and the camera was placed on the focal plane. This system is mainly used for resonant tunneling measurements, where a knowledge of the *in situ* spatial distribution is required.

We also count on fluorescence detection for high resolution momentum measurements in TOF, especially useful for free-falling interferometry. After the probe fiber, we placed a flipping mirror in order to switch easily between absorption imaging and fluorescence schemes. When the mirror is flipped, the beam is lowered 3 cm by a periscope and is expanded and compressed respectively in the horizontal and vertical direction by two cylindrical lens telescopes. The final beam size is about 5 mm and 200 μm diameter FWHM in the horizontal and vertical direction respectively. The beam enters the MOT cell from the x direction 3 cm lower with respect to the MOT position, close to the lower edge of the cell's window. This configuration allows the maximum TOF possible before the atoms touch the bottom of the cell. The aspect ratio we chose needs to guarantee interaction with the expanding cloud along the horizontal direction and to have the maximum vertical resolution as possible (limited by the diffraction limit of a beam at 461 nm). The fluorescence signal is collected by a gated photo-multiplier (H11526). Immediately after the cell, the beam is retro-reflected in order to compensate for the pushing of the probe beam. This allows an increase of the fluorescence signal by approximately one order of magnitude.

3.4 Laser systems

The $^1S_0$–$^1P_1$ transition at 461 nm is used for the first MOT stage, the Zeeman slower, the probe system and for the Bragg beams. Because of the high saturation intensity $I_s = 42$ mW/cm^2, high power laser sources are required for an efficient cooling. For this application a frequency-doubled diode laser system was developed [198] and later improved on [199] in our labs. This type of homemade system was optimized to deliver about 200 mW in the blue, just enough to get a decent cooling process. To have more power available, we also tested and implemented a slave-injected blue diode laser system which can deliver up to 120 mW. Because high-order Bragg transitions require as much power as possible (see sec. 2.4), we built a second dedicated frequency-doubled laser system.

The $^1S_0$–$^3P_1$ transition at 689 nm requires much less driving power to achieve efficient cooling, because the saturation intensity is about three orders of magnitude smaller. This remains true even if we need to broaden the spectrum in the first red MOT trapping stage (see sec. 3.2.2). Therefore, a master-slave diode laser system was developed for the production of all the red frequencies. However, because of the narrow linewidth we need a sub-kHz laser, which requires a high finesse cavity. In the ^{87}Sr configuration, the stirring light can be easily produced by shifting the ^{88}Sr light with an acousto-optical modulator (AOM), since the $F = 9/2 \rightarrow F = 9/2$ transition is 222 MHz away from the ^{88}Sr transition. For the $F = 9/2 \rightarrow F = 11/2$ trapping transition, which is 1.2 GHz away, we use a second ECDL locked to the master with a frequency-offset optical phase-locked-loop (OPLL).

The two repumping lasers at 707 nm and 679 nm are homemade extended-cavity diode lasers (ECDL) in Littrow configuration. They deliver about 30 mW each after optical isolators (OI). They are combined in a polarizing beam splitter (PBS), expanded in a telescope to ~ 2 cm waist diameter FWHM and sent through the MOT cell and retro-reflected. The frequency can be finely controlled with a piezoelectric transducer (PZT) mounted on the grating. As discussed in sec. 3.2.4, the frequency of the 707 nm repumper is modulated in order to cover the hyperfine structure of the $^3P_2$ and $^3S_1$ states, by sweeping the PZT and the diode current.

Finally, we are using a commercial Verdi-V6, which delivers up to 6 W at 532 nm, for the far-off-resonance optical lattice. The "green" optical lattice and the Bragg laser setups will be describe in detail in the next chapters, since their characteristics are directly involved in the experiments we performed.

3.4.1 Cooling blue laser system

Master laser

The master source is an ECDL at 922 nm in the Littrow configuration. The infrared light is amplified by a tapered amplifier (TA) and frequency doubled in a non-linear

crystal. The coupling efficiency into the crystal is enhanced with a bow-tie cavity.

The ECDL delivers ~ 35 mW with a 110 mA driving current with a linewidth of about 500 kHz. After passing through an OI the light is amplified to about 930 mW by the TA chip, driven at 2.65 A. A second OI is placed after the TA in order to suppress optical feedback from the cavity. The 922 nm radiation is frequency doubled in a 25 mm long periodically-polled $KTiOP_4$ crystal (PPKTP) [200]. This kind of crystal is made up of a periodic structure of KTP layers with alternate birefringence axis orientation. The periodicity is a multiple of the working wavelength. The resulting doubling condition is the *quasi-pase matching* [201], for which the phase-matching of the momentum is obtained by an additional contribution coming form the periodic structure. Our crystal has a poling period of 5 μm, so the matching temperature is around 25 °C. The faces are anti-reflection coated ($R < 0.2\%$).

The crystal is placed in a bow-tie cavity. The input and output couplers are plano-convex mirrors with 100 mm curvature radius, with an input reflectivity of 88.5%. The cavity is closed by two plane mirrors with high-reflection coating for 461 nm (99.5%) and high-transmission for 922 nm (97.5%). The cavity has a free spectral range (FSR) of 650 MHz. In optimal operating conditions the doubling efficiency is about 25% and the laser produce 220 mW at 461 nm. The cavity is kept on resonance with a Pound-Drever-Hall locking scheme. The ECDL current is modulated at 10 MHz and the error signal is obtained by demodulating the infrared light signal reflected by the cavity and collected on a photodiode (PD). The error signal is fed to a fast PZT mounted on one of the cavity plane mirrors via a proportional-integral-derivative servo (PID), and part of the signal is sent directly to a current modulation circuit in the diode current driver. The cavity and the master infrared laser are enclosed in an aluminum box placed on a rubber sheet for passive vibration and acoustic isolation. The box also protects the system from dust deposition on the cavity mirrors, which has a strong negative effect on the doubling efficiency. The entire system is also placed on a separated air-floating optical table.

Most of the blue light is transmitted through a window and is sent via a polarization-maintaining (PM) fiber to the optical table where the vacuum system is mounted. A small reflection from the first window surface is used for the production of the probe beam and the reflection from the second face is used for the spectroscopy beam. On the vacuum system table, the blue light is split by two PBS. The majority is used for the production of the MOT beam (~ 60 mW). A second beam is used to inject a slave diode laser for the production of the Zeeman slower beam. A third beam is used for beat-note stabilization of the Bragg laser. The optical scheme of the cooling blue laser system is shown in fig. 3.10(a).

The blue laser is stabilized on the $^1S_0$–$^1P_1$ transition. The error signal comes from saturation-absorption spectroscopy of strontium gas, produced in a 30 cm long heat pipe at 350 °C. The error signal is produced by phase modulating the

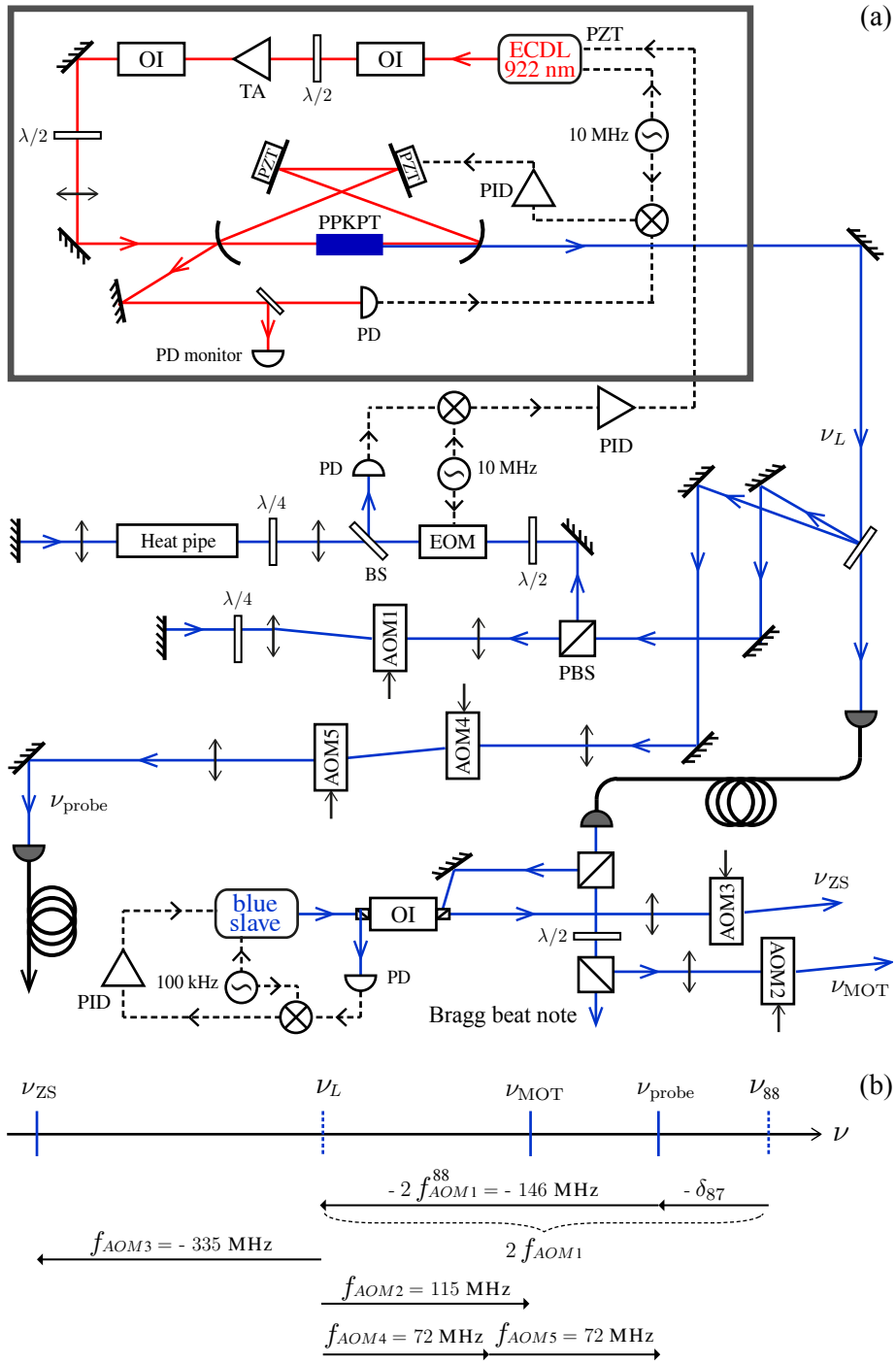

Figure 3.10: Cooling blue laser system. (a) Optical and locking scheme. (b) Frequency production scheme. See the text for details.

blue light at 10 MHz with an electro-optical modulator (EOM) and demodulating the spectroscopy signal with a mixer. The error signal is fed to the ECDL PZT via a PID servo. Because the isotopic shift of ^{87}Sr $F = 9/2 \rightarrow F = 11/2$ transition is just 52 MHz, the blue laser is tuned to the respective isotopic cooling resonance by simply shifting the frequency with an AOM.

Slave diode laser

To increase the available power for the blue cooling process, we implemented a blue diode slave (Nichia NDB4216E). The diode can deliver up to 120 mW at 461 nm, operating in a strong multi-mode regime. It can be injected by the master light with about 3.5 mW, but it cannot remain locked for more than few minutes. To solve this issue, we implemented an active frequency stabilization for the injection.

The diode light is collimated, then shaped by an anamorphic prism pair and passes through an optical isolator. We inject the master cooling radiation from the output polarizer of the OI. The diode's current is modulated at 100 kHz and its intensity noise is measured by a PD, which monitors a small reflection from the input polarizer of the OI. The signal is demodulated by a low-frequency lock-in amplifier and the output voltage gives the phase relationship between the induced amplitude noise and the current driving signal, which can be used as a correction. The error signal is integrated by a PID and sent to the current driver of the diode. The injection is monitored by a scanning Fabry-Perot cavity with 5 GHz FSR. The locked injection can typically work continuously, and it relocks automatically if the master laser is unlocked and relocked. With this system we produce an extra 100 mW which is used for the Zeeman slower beam.

Blue frequency production

All the specific frequencies for the blue cooling and imaging are generated through the use of AOMs. The scheme for frequency production is summarized in fig. 3.10(b). From now on we will indicate with ν the optical frequencies and f the radio frequencies used to drive the AOMs, where the sign of f depends on the diffraction order.

For instance, the AOM1 for the isotopic shift control is placed in the spectroscopy locking loop, and is mounted in a double-pass configuration in order to uncouple the beam direction from the frequency shift. Therefore the laser frequency is $\nu_L = \nu_{88} - 2f_{\mathrm{AOM1}}$, where ν_{88} is the optical frequency of the $^1S_0$–$^1P_1$ transition of ^{88}Sr. The AOM1 is controlled by a direct digital synthesizer (DDS) that allows a fast frequency switch between the two isotopes, so that $f_{\mathrm{AOM1}} = f^{88}_{\mathrm{AOM1}} + \delta_{87}/2$, where $\delta_{87}/2$ is zero for the ^{88}Sr trapping configuration and -52 MHz for ^{87}Sr. Because AOM1 has a maximum efficiency around 80 MHz, we chose to work at

$f_{\mathrm{AOM1}} = -72.8$ MHz for ^{88}Sr and -96.8 MHz for ^{87}Sr.

On the vacuum apparatus table, the MOT beam frequency is generated with a single-pass AOM, so that $\nu_{\mathrm{MOT}} = \nu_L + f_{\mathrm{AOM2}}$. Since the optimal frequency for trapping strontium is found experimentally to be at a detuning $\delta \simeq -30$ MHz, we set $f_{\mathrm{AOM2}} = 115$ MHz. The Zeeman slower beam comes from the slave blue diode injection-locked to the master at a frequency ν_L. It is shifted by a single-pass AOM, so that $\nu_{\mathrm{ZS}} = \nu_L + f_{\mathrm{AOM3}}$. As we discussed in sec. 3.3.3, according to the magnetic field profile and the capture velocity we select a detuning $\delta = -480$ MHz, so $f_{\mathrm{AOM3}} = -335$ MHz. The probe beam frequency is produced directly on the laser table by two AOMs in series, so that $\nu_{\mathrm{probe}} = \nu_L + f_{\mathrm{AOM4}} + f_{\mathrm{AOM5}}$. Because the probe beam has to be on resonance, $f_{\mathrm{AOM4}} = f_{\mathrm{AOM5}} = 72$ MHz.

All the AOMs (except for the spectroscopy one) also act as fast shutters. Since the probe beam is on resonance, it is especially important to prevent it from reaching the atoms after the blue MOT is switched off. This is the reason why the probe frequency is produced by two separate AOMs. In this way the residual light coming from the zero order is reduced. We also installed fast mechanical shutters ($\sim$ 1 ms response time) after the probe fiber and on the MOT and Zeeman slower beams, in order to completely block the light.

3.4.2 Red laser system

Master laser

The master laser is an ECDL at 689 nm in the Littrow configuration. The diffraction grating is mounted on a PZT and the cavity has a FSR = 1.5 GHz. The laser provides around 4.5 mW out from an OI, and thanks to the optical feedback from the extended cavity, the linewidth is reduced to about 220 kHz, mainly limited by low frequency acoustic noise. To further reduce the linewidth, we stabilize the ECDL to a high finesse external cavity by means of a Pound-Drever-Hall locking scheme. The cavity consists of two high-reflective mirrors ($R = 99.95\%$) glued onto a quartz support with low thermal expansion coefficient, at a distance of 10.2 cm which correspond to a FSR = 1.5 GHz. The estimated cavity finesse is $\mathcal{F} = \pi\sqrt{R}/(1-R) \sim 7800$, therefore the linewidth of the resonant modes is about FSR/$\mathcal{F} \sim 190$ kHz. The cavity is placed under vacuum ($\sim 10^{-8}$ mbar) and fixed by a rubber support onto the optical table to reduce vibration noise.

To lock the laser to the cavity resonance, the phase of the optical field is modulated at 10 MHz by an EOM and the error signal is obtained by demodulating the signal from a PD that collects the light from the cavity reflection. The error signal has a slope of 3.4 MHz/V and a signal-to-noise ratio (SNR) of 200 over 3 MHz bandwidth. The feedback acts on three different channels: the PZT of the extended cavity with 2 kHz bandwidth, the current supply of the diode laser with

50 kHz bandwidth and directly on the diode with 3 MHz bandwidth. The SNR should be enough to get 1 Hz linewidth, but it is actually limited by the residual acoustic and vibrational noise coupled to the cavity itself. From the integrated noise measured on a second high finesse cavity, a 20 Hz linewidth was estimated [198], more than enough for recoil-limited cooling.

To compensate for the thermal drift of the cavity ($\sim$ 20 MHz/h), we lock it to the ^{88}Sr atomic transition. The error signal is obtained by saturation-absorption spectroscopy in a heat pipe at 400 °C. The pump beam is shifted by an 80 MHz AOM and frequency modulated at 100 kHz. The error signal is obtained by demodulating the probe signal measured by an amplified low-noise PD. The error signal is fed to the cavity PZT via a PID servo.

Figure 3.11(a) shows the scheme for the whole red laser system. The remaining light coming from the zero order of AOM1 is used for the beat note stabilization of a second ECDL, named "master2". The light from the two masters is sent via PM fibers to the vacuum system table, where they inject slave diodes, which increase the available optical power .

Secondary phase-locked mater laser

While the frequency for the stirring laser can be obtained just by shifting the ^{88}Sr cooling frequency with an AOM, the trapping frequency for the ^{87}Sr is about 1.2 GHz away. We use a separated ECDL source (master2) offset locked to the master1 by an optical phase-locked-loop.

The master2 has the same diode and ECDL configuration as master1. Its output beam is superposed to a pick-off beam from master1 on an uncoated window and light is measured by a PD with 2 GHz bandwidth. The optical beat note produces an amplitude modulation at the frequency difference $f_a = \nu_{L2} - \nu_{L1}$. This signal is mixed down by an RF synthesizer with frequency $f_{\text{synt}} \simeq 1.2$ GHz, so that we find a signal out of the mixer with frequency $f_b = f_a - f_{sint}$. The phase and frequency are compared to a reference signal at 70 MHz by a digital phase and frequency detector (PFD) which has a linear response over 4π. The PFD gives a voltage signal which is proportional to the phase difference between the measured beat note and the reference signal, and it can be used to lock master2 to the frequency $\nu_{L2} = \nu_{L1} + f_{\text{synt}} + 70$ MHz (paying attention to the correct signs).

The PFD we used (designed at LENS) provides two outputs, one with kHz bandwidth (LF) and one with MHz bandwidth (HF). The HF signal is further filtered by a passive high-pass filter to cut DC and feed to the diode's current driver. The LF signal is integrated by a PID servo and sent to the extended cavity PZT. When the loop is closed the frequency is stabilized with an offset given by f_{synt}, and the linewidth is reduced from an initial 600 kHz of the ECDL to a few Hz (fig. 3.12).

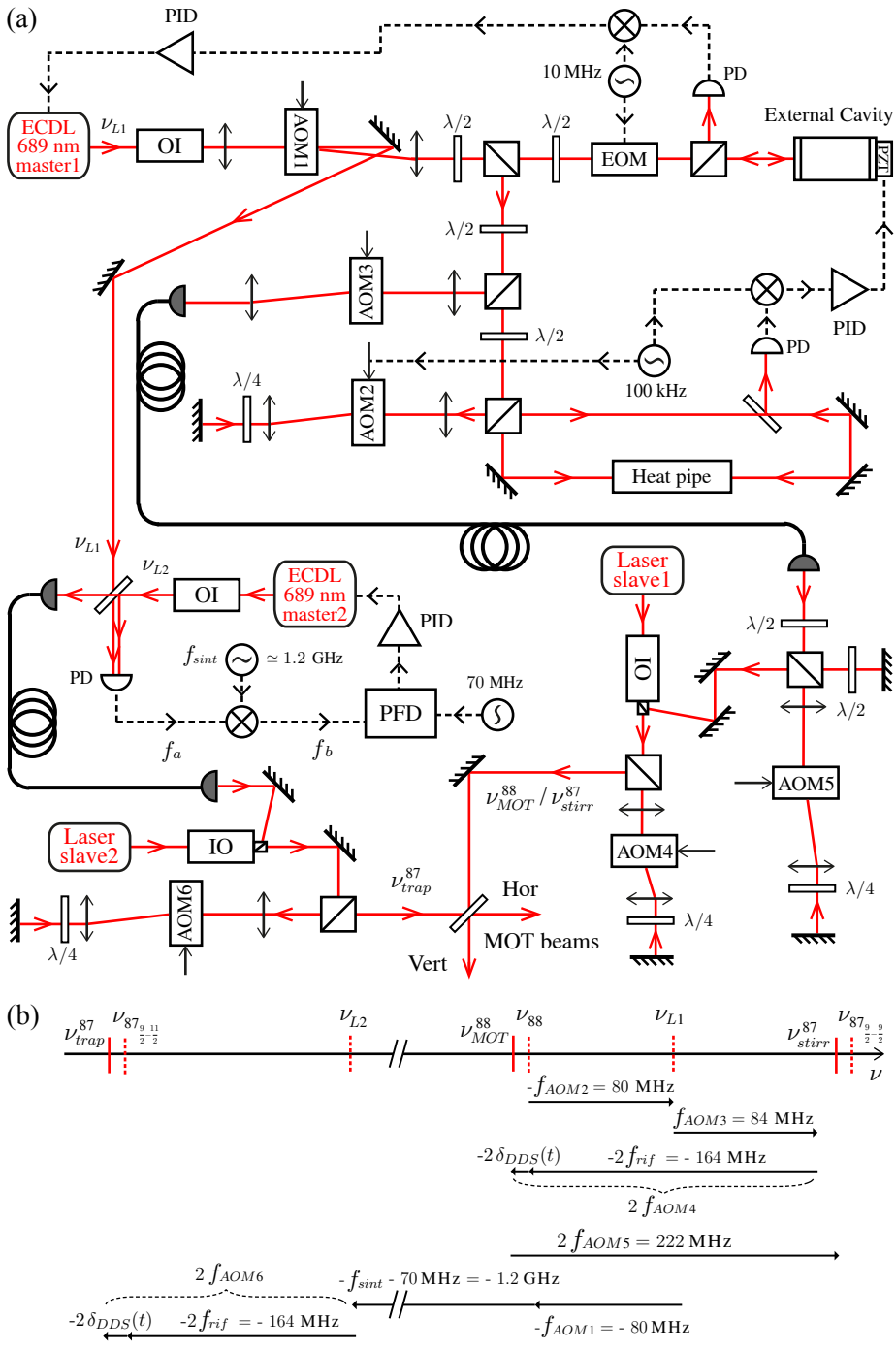

Figure 3.11: Red laser system. (a) Optical and locking scheme. (b) Frequency production scheme. See the text for details.

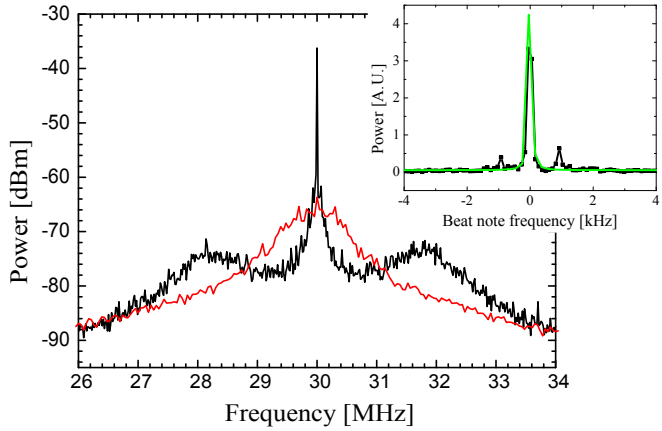

Figure 3.12: Beat note between the two ECDL master lasers, in-loop (black curve) and out-of-loop (red curve). The linewidth is reduced by more then four orders of magnitude. The top graph is a magnification of the in-loop beat note. A Lorentzian fit (green curve) gives a width of 45 Hz, limited by the resolution bandwidth (100 Hz) of our spectrum analyzer.

Red frequency production

The scheme for frequency production is summarized in fig. 3.11(b). Once it is locked to the ^{88}Sr $^1S_0$–$^3P_1$ transition, master1's frequency is determined by the frequency of the in-loop AOM2 which modulates the pump beam for the spectroscopy, so that $\nu_{L1} = \nu_{88} - f_{\mathrm{AOM2}}$. After passing through AOM3, master1's light is sent to the vacuum system table for optical amplification and distribution. The ^{88}Sr MOT beams comes from slave1, which is directly injected by the light coming from master1 and shifted by the double-pass AOM4, so that $\nu^{88}_{\mathrm{MOT}} = \nu_{L1} + f_{\mathrm{AOM3}} + 2f_{\mathrm{AOM4}}$. The AOM4 signal comes from a computer controlled DDS, and is used for the production of the red MOT broadband phase and single-frequency ramp. The AOM4 frequency can be written as $f_{\mathrm{AOM4}} = -(f_{\mathrm{ref}} + \delta_{\mathrm{DDS}}(t))$, where $f_{\mathrm{ref}} = 82.1$ MHz is a reference signal and $\delta_{\mathrm{DDS}}(t)$ is the tunable part. The AOM2 and AOM3 frequencies are chosen in order to have the optical detuning close to resonance except for the $\delta_{\mathrm{DDS}}(t)$ term, so that $-f_{\mathrm{AOM2}} + f_{\mathrm{AOM3}} - 2f_{\mathrm{ref}} = 0$. Therefore, we have set $f_{\mathrm{AOM2}} = -80.6$ MHz and $f_{\mathrm{AOM3}} = 83.6$ MHz.

For ^{87}Sr cooling, we can use the slave1 as stirring laser by compensating for the 222 MHz isotopic shift of the $F = 9/2 \rightarrow F' = 9/2$ transition. By properly tuning two $\lambda/2$-plates we can change the optical path of the injection beam in order to make it double-pass trough AOM5. We set $f_{\mathrm{AOM5}} = -110.8$ MHz to make salve1 work as the ^{87}Sr stirring laser.

The ^{87}Sr trapping frequency is determined by master2, which is offset locked to master1. Here we need to consider the contribution coming from the in-loop

AOM1, because the beam used for the beat note is taken from the zero order. The light is sent to the vacuum system table via a PM fiber, and after double-pass AOM6 it injects slave2. Therefore, the optical frequency for the trapping beam is $\nu_{\text{trap}}^{87} = \nu_{L2} - f_{\text{AOM1}} + 2f_{\text{AOM6}}$, where ν_{L2} is the frequency of master2 as described in the previous section. AOM6 is controlled by a second DDS which produces a broadband phase and a frequency ramp similar to AOM4, but optimized for ^{87}Sr cooling. f_{AOM1} was originally set to 80.8 MHz, and the remaining frequency shift needed to compensate for the isotopic difference is given by f_{sint}.

The stirring and the trapping lasers are combined in a 50:50 beam splitter, which also acts as splitter for the horizontal and vertical MOT beams. This configuration is particularly favorable for the red MOT which requires more power on the vertical beams, because of the asymmetric structure of the trap, combined with the presence of the gravity field. After the beam splitter we end up with 7 mW and 10 mW per beam for the stirring and trapping respectively. The horizontal beam is then equally separated in a PBS, and each beam is combined for the three directions with the blue MOT beams in three dichroic mirrors.

Chapter 4

Test of Einstein Equivalence Principle for 0-spin and half-integer-spin isotopes of strontium in a driven optical lattice

In this chapter I will present an experimental comparison of the gravitational interaction for a bosonic isotope of strontium (^{88}Sr) which has zero total spin with that of a fermionic isotope (^{87}Sr) which has a half-integer spin. This represents a test of the Weak Equivalence Principle (WEP), also known as universality of the free fall, for probe masses with deeply different quantum composition. Indeed, they do not only undergo different statistics (one is a boson, one is a fermion), but one has spin while the other is a spin-less particle. This is also a favorable system to explore for the possible existence of spin-gravity coupling effects.

4.1 Sr isotope system for fundamental gravity tests

Gravity acceleration was measured by means of a genuine quantum effect, namely, the coherent delocalization of matter waves in an optical lattice (see sec. 2.3 for the full description of the theory). To compare gravity acceleration for the two strontium isotopes, we confined atomic wave packets in a vertical off-resonant optical standing wave and induced a dynamic delocalization by amplitude modulation of the lattice potential (fig. 4.1). The principle of the technique lies in the induced resonant

tunneling at harmonics of the Bloch frequency, which, in presence of the gravity force, takes the form

$$\omega_B = 2\pi \times \frac{F_g \lambda_L}{2h}, \tag{4.1}$$

where F_g is the projection of the gravitational force on the atomic wave packet along the lattice direction, h is the Planck constant and λ_L the wavelength of the laser used for the lattice.

In order to account for anomalous accelerations and spin-dependent gravitational mass, the gravitational potential can be expressed as

$$V_{g,A} = (1 + \beta_A + kS_z)M_A g z, \tag{4.2}$$

where M_A is the rest mass of the atom, β_A is the anomalous acceleration generated by a nonzero difference between gravitational and inertial mass due to a coupling with a field with non-metric interaction with gravity [46, 202, 203], k is a model-dependent spin-gravity coupling strength, and S_z is the projection of the atomic spin along the direction of gravity. The coupling term k can be interpreted as the amplitude of a finite-range mass-spin interaction [53, and references therein], as a quantum-gravity property of the matter wave field [204], or as a gravitational mass tensor with a spin-dependent component in the standard model extension [205].

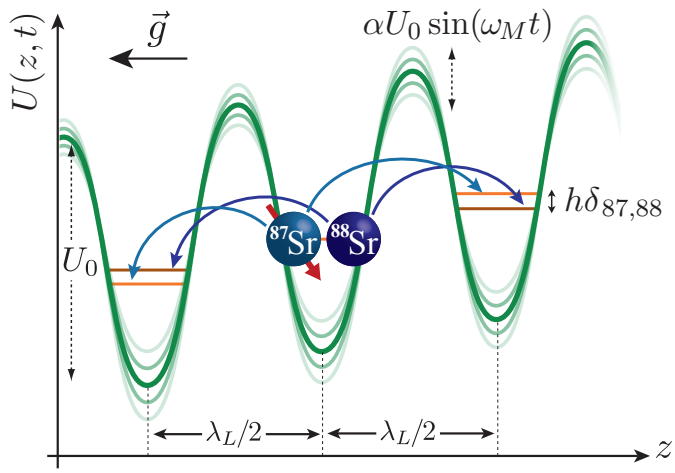

Figure 4.1: Experimental configuration to test the equivalence principle with two strontium isotopes. The two isotopes are alternately laser cooled and trapped in a vertical optical lattice. Intraband coherent delocalization of atomic wave packets is induced by means of amplitude modulation of the optical lattice potential: the difference between the resonant modulation frequencies of the two atomic species $\delta_{87,88} = \omega_{B,87} - \omega_{B,88}$ depends only on their mass ratio and the WEP violation parameter η.

The Bloch frequency corresponds to the site-to-site energy difference induced by the gravitational force, and, according to the WEP, the frequency difference $\delta_{87,88}$ for the two isotopes must depend only on the atomic mass ratio $R_{88,87} = M_{88}/M_{87}$ which is known with a relative uncertainty of 1.5×10^{-10} [163]. A measurement or limit on the fractional difference in acceleration between two bodies is represented by the well known *Eötvös ratio*, given in our case by

$$\eta \equiv 2\frac{a_{88} - a_{87}}{a_{88} + a_{87}} = 2\frac{\omega_{B,88} - R_{88,87}\omega_{B,87}}{\omega_{B,88} + R_{88,87}\omega_{B,87}}, \tag{4.3}$$

where $a_i = 2\hbar\omega_{B,i}/M_i\lambda_L$ ($i = 87, 88$) are the measured vertical accelerations for the two isotopes. Thus, experimental limits on η place limits on the WEP violation due to probe masses with different quantum internal composition.

4.2 A far off-resonance vertical optical lattice for gravity measurements

In this section I will describe the experimental setup for gravitational force measurements with strontium atoms trapped in a driven vertical optical lattice.

The Bloch frequency measurement sensitivity increases with the interaction time, therefore we need the atoms to be kept in the lattice for as longer a time as possible. In order to avoid resonant scattering-induced losses, we decided to operate with a far-detuned high power laser. We chose a wavelength $\lambda_L = 532$ nm for which many high-power sources are available and which has a detuning from the ${}^1S_0$–${}^1P_1$ transition $\delta \sim 2.7 \times 10^6\gamma$. With an easily reachable laser power of 500 mW per beam and a radius of 300 μm, we can have an intensity of 3.5×10^5 W/cm^2 that guarantees a lattice depth $U_0 = 6E_r$ and a residual scattering rate of about 0.03 Hz, according to eq.(2.30). The Bloch frequency and period for the 88 and 87 strontium isotopes in a 532 nm optical lattice are

$$\begin{aligned} \omega_{B,88} &\approx 2\pi \times 574\,\text{Hz}, \quad & \tau_{B,88} &\approx 1.74\,\text{ms}, \\ \omega_{B,87} &\approx 2\pi \times 568\,\text{Hz}, \quad & \tau_{B,87} &\approx 1.76\,\text{ms}. \end{aligned} \tag{4.4}$$

4.2.1 Lattice laser setup

A schematic view of the lattice laser setup is shown in fig. 4.2. The lattice laser source is a commercial single-mode frequency-doubled Nd:YVO_4 laser (Coherent Verdi-V6) delivering up to 6 W at 532 nm. The main output of the laser is split equally between two paths. They pass through two independent 100 MHz AOMs for frequency and amplitude control of the lattice beams and are injected into two single-mode polarization-maintaining fibers. One of the outputs is sent upwards from the

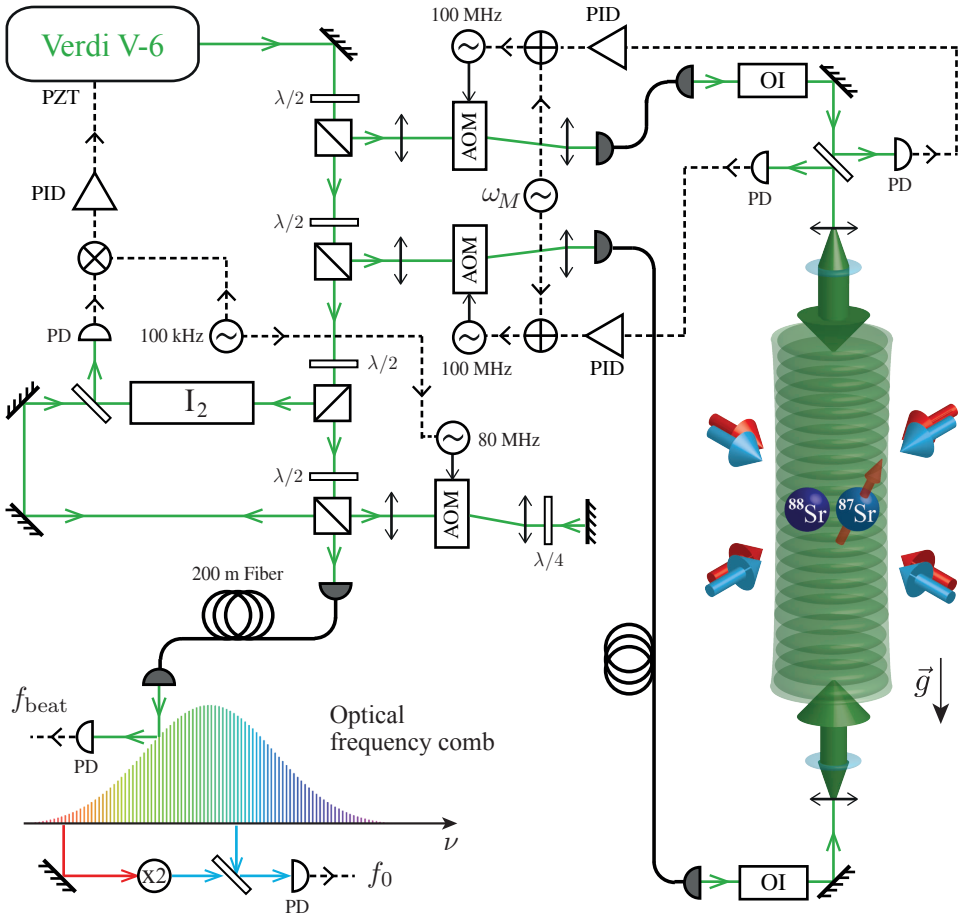

Figure 4.2: Lattice laser optical setup. The lattice is realized by superposing two counter-propagating beams coming from opposite fibers, whose amplitudes are stabilized to a voltage reference and modulated at a frequency ω_M. The lattice frequency is locked to a hyperfine transition of molecular iodine and is measured by an optical frequency comb.

lower cell window, and the other is sent downwards from the top. Both fibers are protected by optical isolators, and the beams are expanded by two telescopes in order to have the same waist when they reach the atoms, about 300 μm. For typical power levels of 500 mW per beam, the lattice depth is about $U_0 = 6E_r$, thus the trap frequencies are 7 kHz and 17 Hz along the longitudinal and radial directions, according to the expression obtained in sec. 2.1.2 and sec. 2.1.3. The intensity of the beams is monitored after the fibers by two independent photodiodes which collect light from the reflections on the same optical window placed after the optical isolator of the lower beam. These signals are used to stabilize the lattice potential

U_0.

Even though lattice verticality is not a necessary condition for differential gravity measurements, we aligned the beams along the direction of g with 1 mrad precision, in order to maximize the sensitivity to gravity acceleration. By interposing a large glass container filled with water on top of the vacuum cell, we verified the verticality of the upwards-directed beam by looking at a reflection from the water surface at a distance of 2 m. The downwards-directed beam was then aligned on top the other by maximizing the transmission through the opposite fiber.

Since the determination of g is directly related to the lattice wavelength λ_L through the Bloch frequency, a high precision measurement of λ_L is required for an absolute measurement of the gravitational acceleration. Indeed, previous results obtained with the same technique demonstrated a limit on the measurement accuracy of 2×10^{-7} due to the instability of the lattice wavelength [106]. For differential gravity measurements it is important that the frequency is stable between consecutive isotopes measurements; lattice frequency control is thus important. For this reason we use a new version of the Verdi model which enables direct frequency stabilization by a piezoelectric transducer mounted on the doubling cavity. We use a saturated absorption spectroscopy signal from a rotational line of molecular iodine to lock the laser, and at the same time we monitor the single-mode operation with a Fabry-Perot cavity. Finally, we can measure the absolute lattice frequency by means of a self-referenced Ti:sapphire optical frequency comb [206].

4.2.2 Controlling the lattice amplitude

The lattice beams' intensity is stabilized by a servo control system, which also allows the necessary amplitude modulation at frequency ω_M and depth α to induce resonant tunneling of atomic wave packets in the optical lattice. The intensity is stabilized by acting on the RF levels that drive the AOMs. The error signals for the two beams are obtained independently by comparing the photodiode signals with two stable voltage references. The stabilization avoids slow drift of the lattice depth that could arise from misalignment of the fiber injections and suppresses acoustic vibration-induced amplitude noise. In the range of acoustic frequencies, from tens of Hz to several kHz, amplitude noise could lead to heating of the atoms by exciting vibrational frequencies of the lattice [207].

Figure 4.3 shows typical power spectral densities (PSD) of the relative intensity noise of the lattice beams. The free running laser spectrum (red line) is compared to the condition after moving the water cooling chiller into a separate room (green curve). With this expedient the noise in the kHz region, due to the vibrations on the optical table induced by the water flow in the cooling baseplate, is reduced by one order of magnitude. With the servo feedback loop (blue line) the noise up to 10 kHz is reduced by two orders of magnitude. A residual 50 Hz modulation and

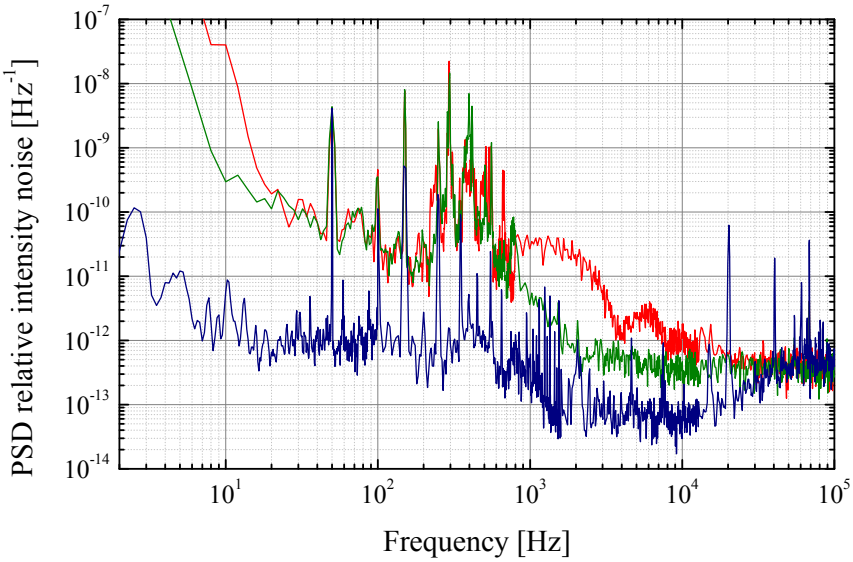

Figure 4.3: Power spectral densities of the lattice laser relative intensity noise for free running laser (red line), with water cooling chiller placed in a separate room (green line), with active feedback (blue line).

the servo bump at 80 kHz are also visible.

The servo control allows also to apply the amplitude-modulation driving signal, which is referenced, as many other relevant frequencies, to a primary rubidium standard stabilized on long term to a GPS signal. The servo control has a finite linear response of about 20% around the working point, thus we need to limit the modulation depth in order to avoid higher harmonics of the modulation frequency, which may lead to decoherence in the resonant tunneling process. By looking at the PSD of the modulated intensity signal we reduced the higher harmonic content below the floor level, i.e. about 120 dB of attenuation.

4.2.3 Controlling the lattice frequency

The laser Verdi-V6 we used for the experiment is a new version recently developed, with two PZTs mounted on two cavity mirrors, allowing tunability and stabilization of the laser frequency. We found couple of issues in this new version, therefore we had to pay special care to its daily operation.

We implemented a saturated absorption spectroscopy scheme on a molecular iodine cell, which has a wide range of rovibrational lines around 532 nm. The laser working point is not stable day-to-day, and we observed jumps in frequency of several GHz. Luckily, by tuning the PZT which has a sensitivity of 64 MHz/V and an overall dynamic range of 6.4 GHz, it is always possible to find one of the

iodine lines. By modulating the frequency of the pump beam at 100 kHz and demodulating it with a lock-in amplifier, we can use the error signal coming from one of the hyperfine transitions of the rotational lines to lock the laser by feedback to the PZT.

Figure 4.4 shows a saturated absorption spectroscopy signal with the related error signals of the hyperfine transitions. The cavity mirror was scanned across almost the entire PZT range, thus three rotational lines are visible. The frequency was calibrated by monitoring the laser wavelength with a commercial wavemeter with a resolution of 100 MHz. Each line contains at least one strong hyperfine transition to which we can lock the laser. By comparison with the reported iodine spectroscopy measurements in literature [208, 209] we were able to identify each line, and in some cases also each hyperfine component [210]. Depending on the laser working condition, we also observed other lines, such as the 1122 and 1123, which are 150 GHz away.

By means of a Ti:Sapphire femtosecond frequency comb we can measure the absolute frequency of the lattice and characterize its stability [211]. Part of the light from the lattice laser is sent to a laboratory in the Physics Department with a 200 m long fiber and it is superimposed to the radiation of the frequency comb. The beat note with the closest tooth of the comb is monitored by a fast photodiode.

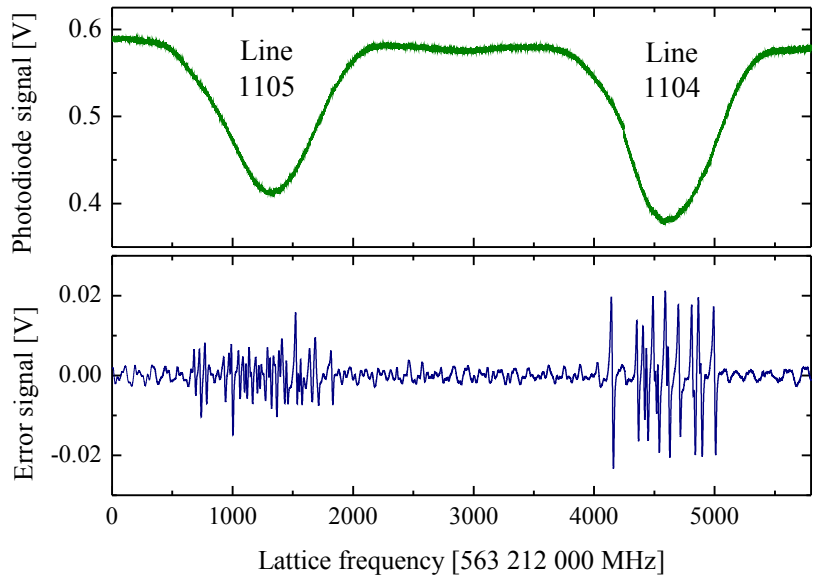

Figure 4.4: Saturated absorption spectroscopy of molecular iodine with the related error signals of the hyperfine transitions. The cavity mirror was scanned across almost the entire PZT range, thus three rotational lines are visible. Each line contains at least one strong hyperfine transition to which we can lock the laser.

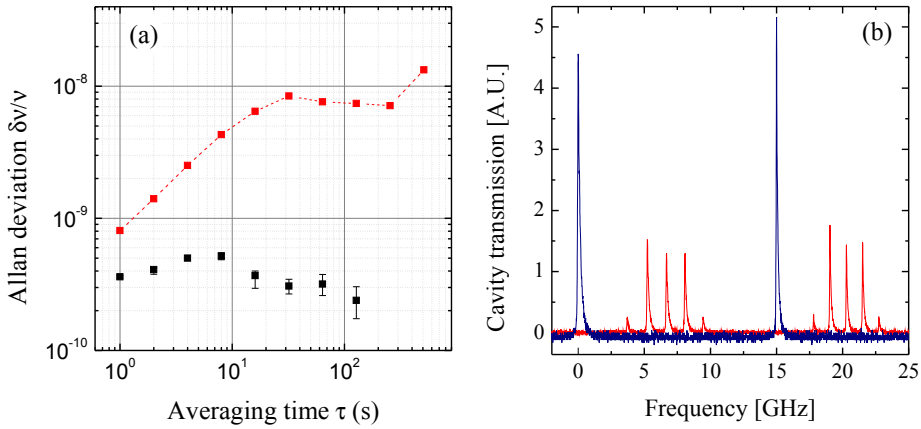

Figure 4.5: (a) Allan deviation of the relative frequency uncertainties of the lattice measured with the optical frequency comb, by locking to the spectroscopy signal (black data), and free running (red data). (b) Fabry-Perot cavity transmission of the lattice laser light for single-mode (blue line) and multi-mode (red line) operations.

The repetition rate f_{rep} of the comb is stabilized by locking the beat note on a RF synthesizer and the offset frequency f_0 is stabilized with a self-referenced technique, namely an $f - 2f$ interferometer. The absolute value of the lattice frequency is given by $f = nf_{\text{rep}} \pm f_0 \pm f_{\text{beat}}$, where n is the number of the closest tooth, which is determined by a wavemeter with a resolution of 100 MHz. By continuously counting f_{beat} we can measure the lattice frequency with MHz accuracy within a few seconds of integration and we can characterize its stability. Figure 4.5(a) shows the Allan deviation for the relative uncertainty of the lattice frequency when the laser is free running and when it is locked to a hyperfine transition of the iodine.

By looking at the beat note with the comb we also observed an unexpected multi-mode operation of the Verdi. We studied this behavior by constantly monitoring the laser radiation in a Fabry-Perot cavity with 15 GHz FSR. We discovered that the multi-mode operation depends on the voltage of the cavity PZT. Figure 4.5(b) shows typical spectra for the single-mode and multi-mode operations. We managed to always perform the experiment in single-mode operation by tuning the PZT in proper range. After the experiment the Verdi was fixed by the manufacturer.

4.2.4 Trapping atoms in the lattice

After the cooling process in the red MOT, the atoms are adiabatically loaded into the optical lattice. The lattice intensity is ramped up, starting 500 μs before switching off the red MOT, and it reaches the maximum value in 100 μs. The adiabatic loading mitigates the population of higher bands, suppressing the heating by the

lattice [107]. The adiabatic condition is fulfilled for loading times longer than the inter-band energy separation, according to the equation [212]

$$|\langle q, j| \frac{\partial \mathcal{H}}{\partial t} |q, 1\rangle| \ll \frac{(E_j(q) - E_1(q)))^2}{\hbar}, \tag{4.5}$$

where $|q, j\rangle$ is the Bloch state in the band j with quasi-momentum q and $E_j(q)$ is the energy of the j-band. Even a for small potential depth $U_0 \ll E_r$, the energy gap between the first two bands at the center of the band ($q \sim 0$) is $U_0 \sim 4E_r$ (see sec. 2.1.3). A rough estimation for the adiabatic loading condition is therefore

$$\frac{\mathrm{d}}{\mathrm{d}t} \frac{U_0(t)}{E_r} \ll 16 \frac{E_r}{\hbar}. \tag{4.6}$$

For our typical potential depth this condition is satisfied when the intensity is ramped up over a time longer than 20 μs and it is still one order of magnitude smaller than the Bloch period. In the case of ^{87}Sr, the loading produces an unpolarized trapped sample.

Because of the finite momentum distribution of the atomic sample, higher bands can still be populated, leading to losses via Landau-Zener tunneling (see sec. 2.2.2). Such losses are more important for higher bands respect to the fundamental one, because of the smaller energy gap. The fraction of population between the second

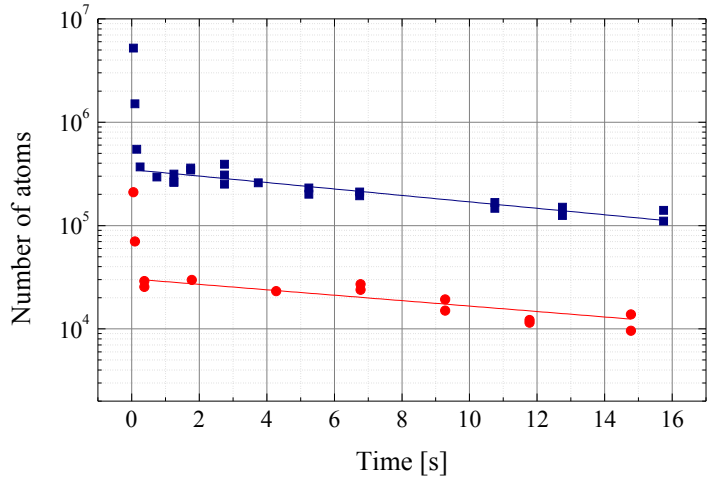

Figure 4.6: Lattice lifetime for ^{88}Sr (blue squares) and ^{87}Sr (red circles). The number of atoms decay exponentially with two different time scales. In the first 100 ms the hot atoms are lost by evaporation, after which the lifetime is limited to about 15 s by the background gas collisions. The solid lines are exponential least-squares fits which give $\tau_{88} = 14(2)$ s and $\tau_{87} = 16(3)$ s.

and the first band can be derived by the Maxwell-Boltzmann distribution and written in terms of the energy gap ΔE_G between the two bands:

$$\frac{N_2}{N_1} \sim \exp\left(-\frac{\Delta E_G}{k_B T}\right). \tag{4.7}$$

For moderate lattice depths ($U_0 \ll 16E_r$) the band gap can be approximated as $\Delta E_G \simeq U_0/2$, which can be demonstrated by a first order perturbation approach [81]. For our typical potential depth $U_0 = 6E_r$, this implies $N_2 \sim 0.3N_1$. Such a fraction of atoms is expected to be lost at a rate of the Bloch frequency. The residual losses come form the radial confinement which is poorer than the lattice confinement along the vertical direction. The combination of this phenomena leads to a strong evaporation of the hotter atoms in the first 100 ms. Figure 4.6 shows the typical lattice lifetime for ^{88}Sr and ^{87}Sr. Two time scales are clearly visible. An initial fast evaporation reduces the number of atoms by an approximate factor of 10. After around 100 ms the populations decay with a time constant of about 15 s, which is mainly limited by the collisions with the background gas.

In order to increase the number of trapped atoms, we implemented a further cooling step inside the lattice. After the atoms are adiabatically loaded, the MOT magnetic field is switched off, but the red MOT lasers are kept on for 5 ms. The resulting system is an optical molasses acting on an atomic cloud confined in the conservative optical trap. In this system a lower temperature can be obtained because density-dependent heating is reduced [213]. Since the red MOT transition is very narrow, the light shift due to the high power lattice laser has to be taken

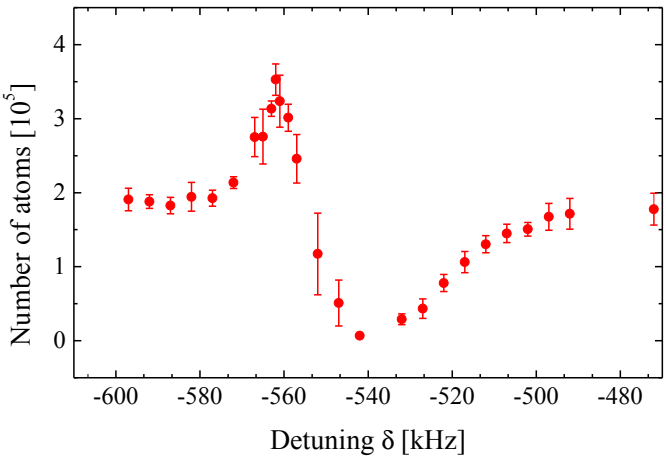

Figure 4.7: Molasses cooling stage in lattice. The number of ^{88}Sr atoms trapped in the lattice after 100 ms as a function of the frequency of a 5 ms red MOT beams stage. The resonance is shifted because of the lattice light shift.

into account. We have optimized the red molasses stage in the lattice by tuning the frequency and intensity and looking at the number of atoms trapped after the evaporation time (100 ms). The result for ^{88}Sr is shown in fig. 4.7. The number of trapped atoms is plotted versus the red MOT frequency detuning with respect to the estimated unperturbed resonance. A dispersive behavior is centered at about 500 kHz because of the lattice light shift. For higher frequencies the effective radiation crosses the resonance and goes to the blue, thus the atoms are lost. An increase of a factor of 1.5 can be obtained by tuning the laser to the red. The same parameters applied to ^{87}Sr lead to similar results.

4.3 Bloch frequency measurements

4.3.1 Resonant tunneling spectra

A few milliseconds after the lattice loading, an amplitude-modulation (AM) burst of frequency ω_M is applied for a time t_M. As described in sec. 2.3, the modulation induces a coherent delocalization of the atomic wave packets, arising from intra-band transitions among Wannier-Stark levels. This is a resonant process occurring at $\omega_M = \ell\omega_B$. The phenomenon can be observed by monitoring the atomic distribution width *in situ*. Figure 4.8 shows some absorption imaging pictures for atoms in the lattice with and without the resonant modulation. The cloud's σ-width is obtained by a Gaussian least-squares fit of the integrated profile. The dependence of the atomic distribution width as a function of the modulation frequency is expressed by eq. (2.105) (repeated here as a quick reference):

$$\sigma_z(\omega_M) = \sqrt{\sigma_0^2 + v_\ell^2 t_M^2 \,\mathrm{sinc}\left(\frac{\omega_M - \ell\omega_B}{\Gamma}\right)}, \tag{4.8}$$

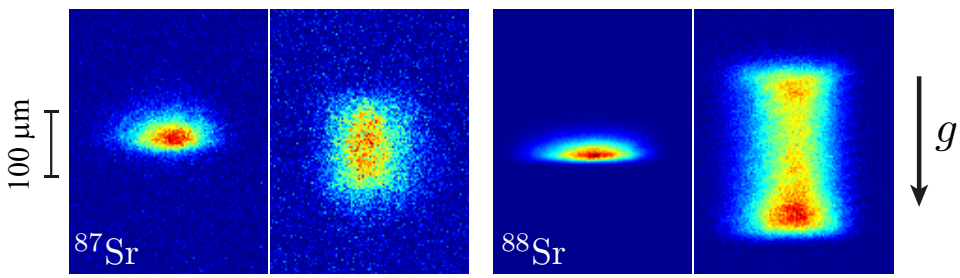

Figure 4.8: *In situ* absorption images of the ^{87}Sr and ^{88}Sr atomic samples confined in the optical lattice with and without resonant modulation. The induced coherent delocalization leads to a spatial broadening of the atomic sample along the lattice axis.

where σ_0 is the initial size of the cloud, v_ℓ is the speed of the broadening at resonance expressed by eq. (2.103) and Γ is the resonance linewidth.

Figure 4.9 shows typical resonant tunneling spectra for ^{88}Sr and ^{87}Sr used for the differential gravity measurements. The AM burst was applied for $t_M = 12$ s and 8 s at the $\ell = 2$ and $\ell = 1$ harmonics of ω_B respectively for both isotopes. The modulation depth α is tuned to maximize the signal-to-noise ratio of each spectrum while keeping the higher modulation harmonics at a low level, as discussed in sec. 4.2.2. By sweeping the modulation frequency ω_M we can obtain a full resonance spectrum. The recording time for consecutive resonance spectra of the two isotopes is about 1 h. The central frequency is obtained by a least-squares fit of the data with eq. (4.8), with σ_0, v_ℓ, ω_B and Γ as free parameters. A single measurement leads to a resolution of 5×10^{-7} for $\omega_{B,88}$ and 1.6×10^{-6} for $\omega_{B,87}$. The uncertainty is calculated as the standard error of the fit for each resonance profile. The difference in precision between the two isotopes is due to the reduced signal-to-noise ratio in the absorption profile for ^{87}Sr, caused by the smaller natural

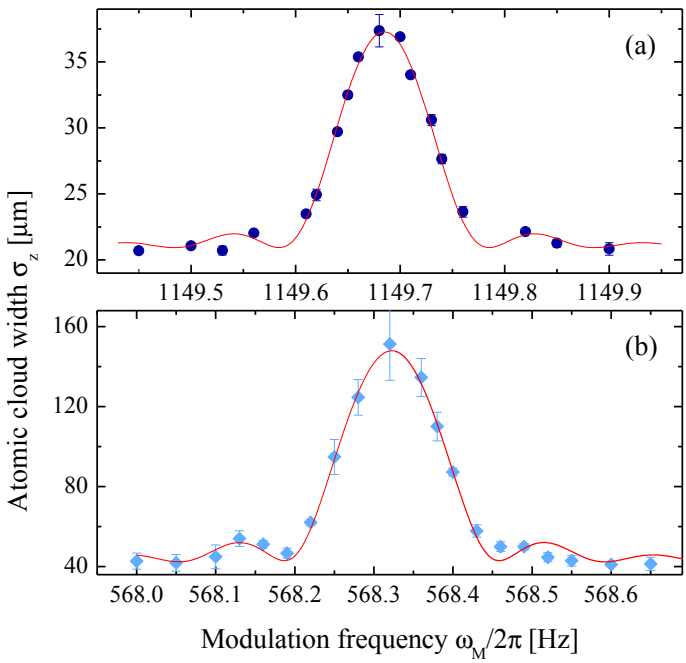

Figure 4.9: Typical amplitude modulation spectra and the corresponding least-squares best-fit function (solid line) for (a) ^{88}Sr ($t_M = 12$ s, $\ell = 2$) and (b) ^{87}Sr ($t_M = 8$ s, $\ell = 1$) atoms. Both the lattice frequency and the lattice beam intensities were kept constant for each pair of measurements, while the modulation depth α was tuned to maximize the signal-to-noise ratio of each spectrum. The error bars are the statistical errors over at least three consecutive measurements.

abundance of this isotope as well as the presence of the 10-level hyperfine manifold which yields a higher Doppler temperature and a smaller (about a factor of 2) absorption cross section due to optical pumping in the imaging process.

4.3.2 Sensitivity of Bloch frequency measurements

In general, the precision which is attainable in the measurement of forces by this technique is related to the quality factor $Q = \ell\omega_B/\Gamma$ of the resonances, as well as the signal-to-noise ratio. As long as the width of the resonance is Fourier-limited, Γ does not depend on ℓ, but only on the modulation time t_M, as discussed in sec. 2.3. This fact is significant because it allows the quality factor of the resonances Q to be improved, and therefore to an increase in the sensitivity of the measurement by a factor ℓ. In the case of Fourier-limited resonance, the ω_B sensitivity to spatial width fluctuations $\Delta\sigma$ can be written as [106]:

$$\Delta\omega_B = 2\pi \times \frac{3}{\pi t_M^2 v_\ell \ell}\Delta\sigma, \tag{4.9}$$

which is derived from a power expansion of eq. (4.1) and then by applying a first-order propagation of uncertainty theory.

The delocalization slows down (v_ℓ decreases) by increasing ℓ due to the reduction of the tunneling rate with increasing separation between the initial and final Wannier-Stark states. Since we have a constraint on the maximum modulation depth that we can apply without introducing higher harmonics of the modulation frequency, the driving at larger ℓ leads to smaller signal-to-noise ratio of the resonance. Because of this reason, we preferred to modulate the lattice at lower harmonics of the Bloch frequency and increase the interrogation time t_M instead. In absence of decoherence mechanisms, or at least for small decoherence effects, the resonance linewidth depends mainly on t_M. Therefore, the sensitivity to the determination of the center of the resonance increases quadratically with t_M, as we can see by looking at eq. (4.9). The modulation time is limited by the lifetime of the lattice, which limits the number of atoms participating in the tunneling and the final optical density at the detection.

Decoherence mechanisms which induce broadening of the resonance may reduce the quality factor. An important mechanism of decoherence is the scattering with photons of the lattice. By keeping a relatively small potential depth, photon scattering produces mainly losses instead of decoherence. As already mentioned, the absence of cold collisions for ^{88}Sr do not introduce broadening of the resonance, while for an unpolarized sample of ^{87}Sr, cold collisions between different spins states can give rise to a broadening of the resonance.

The signal-to-noise ratio depends on multiple factors. Firstly, the main contribution comes from the fluctuations of the initial atomic cloud size, due to the intensity

and frequency instabilities of the red cooling laser. We estimate a contribution of 70% of the statistical error coming from this term. Secondly, the intensity fluctuation of the lattice laser affects the tunneling rate. For a residual intensity fluctuation of 1% coming from the polarization fluctuations out of the fibers, the tunneling rate varies by 1-2%. Additionally, the system is sensitive to acoustic and seismic vibrations of the optical system in the frequency region which corresponds to the resonant frequencies $\ell\omega_B/2\pi$. The noise spectral density has to be integrated around these resonances over a range $\Gamma/2\pi$, but since the system is usually modulated for a time of the order of 10 s, there is a cut-off frequency of about 0.1 Hz. Above this frequency the vibrations are filtered out, except for the resonances which we have just considered. A further factor that affects the final sensitivity is the detection noise of the CCD system. When the optical density is $\lesssim 1$, an overestimation of the cloud width may occur. Finally, the atomic losses due to the finite lifetime in the lattice limit the sensitivity, by directly reducing the signal-to-noise ratio which is proportional to $\sqrt{N}$, where N is the number of atoms participating in the signal.

Since in these differential measurements we are limited by the signal-to-noise ratio of ^{87}Sr imaging, we did not push the ^{88}Sr measurements to the limit of our system, which was already demonstrated to work for modulation at $\ell = 6$ and $t_M = 12$ s [106]. With ^{88}Sr, this technique also demonstrated a relative precision of $\Delta g/g = 2 \times 10^{-7}$ in gravity acceleration measurements [41].

4.3.3 Active frequency lock to the Bloch frequency

We also developed a new technique to further improve the Bloch frequency sensitivity. The idea comes from optical atomic clocks [214, 215], in which one similarly wants to precisely determine the center of a resonance. In those cases the resonance is a narrow transition between two internal atomic states, one of which is highly metastable. In the present case, the resonance is a transition between Wannier-Stark levels of the tilted lattice. The idea is the following: instead of scanning the full resonance spectrum and extracting the center value from a fit of the data, it is possible to lock the local oscillator by interrogating the two sides of the fringe and thus continuously count the central value. In an optical clock the local oscillator is the clock laser, in our case it is the AM frequency synthesizer.

The experimental procedure we used is sketched in fig. 4.10. The local oscillator (LO) frequency f_M is digitally modulated in order to consecutively interrogate the two sides of the resonant tunneling spectrum. Subsequent demodulation is achieved by computing the difference of the two consecutive measurements of σ_z, which yields an odd-symmetry error signal suitable for locking. If the LO is initially tuned to a frequency f_M close to the Bloch frequency harmonic we want to measure, a first cycle interrogates the cloud with an AM burst at a $f_M - \Delta f$, recording a coherent broadening $\sigma_z(f_M - \Delta f)$. A second cycle interrogates the other side of

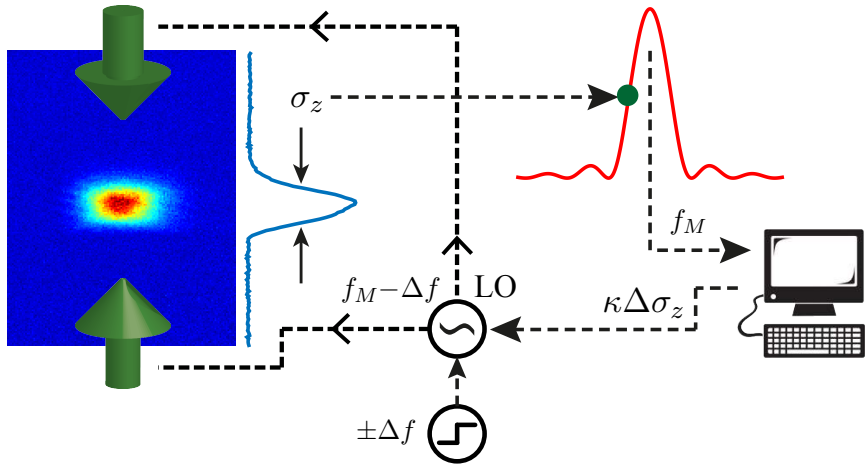

Figure 4.10: Operation principle of the active frequency lock to the Bloch frequency. The AM LO frequency is tuned to alternately interrogate the two sides of the resonance. The central value is recorded and a correction is applied to keep the LO on top of the fringe.

the fringe at an AM frequency $f_M + \Delta f$. While a third cycle begins, a computer program computes the demodulation by calculating the difference

$$\Delta\sigma_z = \sigma_z(f_M + \Delta f) - \sigma_z(f_M - \Delta f) \tag{4.10}$$

and it applies a correction to the central frequency value:

$$f_{M,n} = f_{M,n-1} + \kappa\Delta\sigma_z, \tag{4.11}$$

where n is the number of consecutive measurements, and κ is a weighting factor to be optimized, determined by the slope of the error signal. With this system, just two experimental cycles are needed to extract a measurement of the Bloch frequency. By counting f_M, the statistical uncertainty on ω_B can by rapidly integrated down.

Error signal

By scanning the central frequency f_M with a fixed modulation step Δf, it is possible to record a full error signal. The slope around the center determines the sensitivity to the broadening as a function of the modulation frequency, and is called the *resolution slope*.

Figure 4.11 shows typical error signals obtained with different modulation steps for a ^{88}Sr broadening resonance with $t_M = 10$ s, $\ell = 2$ and $\alpha = 6\%$. We used $\Delta f = 60$ mHz (red squares), 40 mHz (green diamonds), 80 mHz (blue circles). The solid lines are linear fits to the data around the center. A comparison between

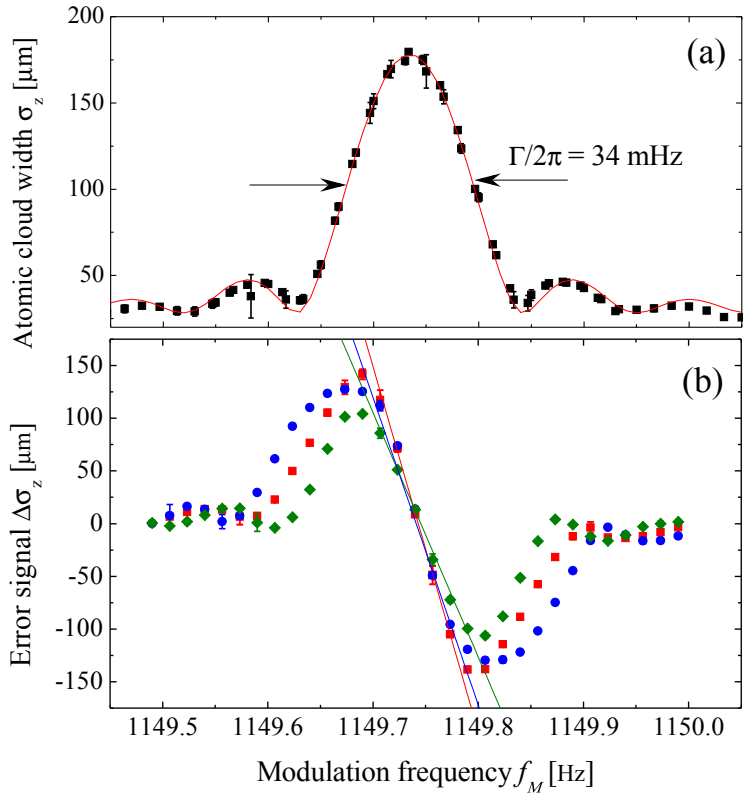

(a)

Figure 4.11: (a) Fourier-limited resonance for ^{88}Sr with $t_M = 10$ s, $\ell = 2$ and $\alpha = 6\%$. (b) Typical resonant tunneling error signals obtained by modulating the central frequency f_M with different modulation steps $\Delta f = 60$ mHz (red squares), 40 mHz (green diamonds), 80 mHz (blue circles). The solid lines are linear fits to the data around the center. The best slope is obtained for $\Delta f \simeq 2\Gamma/2\pi$.

the width of the resonance obtained by the fit of (a), which is Fourier-limited, and the slopes of the error signals, suggests that the best slope is obtained for $\Delta f \simeq 2\Gamma/2\pi$. For the case in the figure, the best slope is $\kappa = 0.6$ mHz/μm, obtained for $\Delta f = 60$ mHz.

Feedback to the AM frequency generator

Once we have chosen the resolution slope κ, the locking is achieved by correcting the central modulation frequency f_M every two consecutive cycles, as expressed by eq. (4.11). In general we can also apply a proportional and integral gain in the form

$$f_{M,n} = f_{M,n-1} + G_P \kappa \Delta\sigma_{z,n-1} + G_I \Delta\Sigma_{n-1}, \tag{4.12}$$

where G_P and G_I are dimensionless gains and $\Delta\Sigma_n$ is calculated as the instantaneous weighted average of the corrections:

$$\Delta\Sigma_n = \frac{1}{n}\sum_{m}^{n} \Delta\sigma_{z,m}. \tag{4.13}$$

In order to test the effectiveness of the locking system we run the same measurements with different locking parameters. The results are shown in fig. 4.12. If we start slightly out of resonance (about 50 mHz in the figure), the feedback brings the central frequency of the LO to resonance after few oscillations. When the resolution slope κ is optimized, a proportional gain larger then $G_P > 1$ leads to forced oscillations around the mean value. While the integral gain has some advantages when we start to acquire data far from resonance, it has just the effect of slowing the convergence, when we are close. This makes sense if one notices that the acquisition cycle time is much longer then the variations on the Bloch frequency that occur during a measurement set. Because of these reasons we typically lock the LO with $G_P = 1$ and $G_I \simeq 0$.

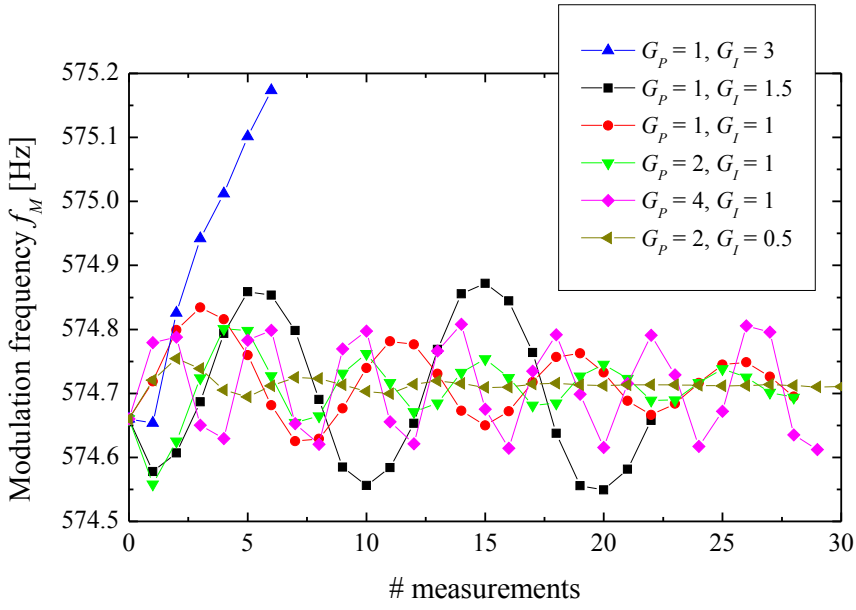

Figure 4.12: Active frequency lock to the Bloch frequency. The modulation frequency f_M is recorded after every two experimental cycles and the feedback is applied. Different gains were used. The lines are just a visual guide.

4.3.4 Sensitivity of the frequency locking technique

The sensitivity of the Bloch frequency measurements can be characterized by its Allan deviation [216]. This is a powerful tool to analyze the stability of an oscillator and to discriminate between different noise sources. The Allan variance $\sigma_y^2(\tau)$ is defined as one half of the time average of the squares of the differences between successive readings of the frequency deviation sampled over the sampling period. Mathematically:

$$\sigma_y^2(\tau) = \frac{1}{N-1}\sum_{k=1}^{N-1}\frac{1}{2}(\bar{y}_{k+1} - \bar{y}_k)^2, \tag{4.14}$$

where τ is the averaging time in which N measurements of the frequency f_M are sampled and $\bar{y}_k$ is the kth fractional frequency average in the interval τ:

$$\bar{y}_k(\tau) = \frac{1}{\omega_B \tau}\int_{t_k-\tau}^{t_k}\omega(t)\mathrm{d}t, \tag{4.15}$$

where t is the time over a single acquisition, and goes from 0 to T_c. In our case, since we need two cycles to record a frequency measurement, T_c is twice the single experimental cycle time, and $\tau = NT_c$. The Allan deviation is defined as the square-root of the Allan variance.

In presence of white noise only, the Allan variance of an oscillator which is locked to a resonance fringe with quality factor Q and signal-to-noise ratio SNR can be expressed in a simple form:

$$\sigma_y(\tau) \sim \frac{1}{Q}\frac{1}{\mathrm{SNR}}\sqrt{\frac{T_c}{\tau}}. \tag{4.16}$$

This definition suggests that with the same resonance parameters and the same noise sources discussed in sec. 4.3.1, the precision of a Bloch frequency measurement can be improved by averaging for a long time τ and by reducing the cycle time T_c.

In a typical measurement set, the ^{88}Sr and ^{87}Sr Bloch frequency are measured alternately. The single experimental cycle requires $T_{\mathrm{MOT}} + T_{\mathrm{AM}}$, where T_{MOT} is the loading time of the MOT and T_{AM} is the modulation time in the lattice. Typical values for the two isotopes are $T_{\mathrm{MOT}} = 3$ s, $T_{\mathrm{AM}} = 10$ s for ^{88}Sr and $T_{\mathrm{MOT}} = 7$ s $T_{\mathrm{AM}} = 6.8$ s for ^{87}Sr. Therefore, the overall cycle times are $T_c \sim 27$ s and ~ 29 s.

The Bloch frequency ω_B is determined by recording the f_M time series for about 700 s and taking the mean value of the time series. Figure 4.13 shows the Allan deviation of a set of 101 recorded values of f_M for ^{88}Sr and a set of 42 values for ^{87}Sr. In both cases the Allan deviation scales as $\tau^{-1/2}$ (as expected for white noise) with sensitivities at 1 s of $\sigma_{\omega_{B,88}} = 1.5 \times 10^{-6}\omega_{B,88}$ and $\sigma_{\omega_{B,87}} = 9.8 \times 10^{-6}\omega_{B,87}$, respectively.

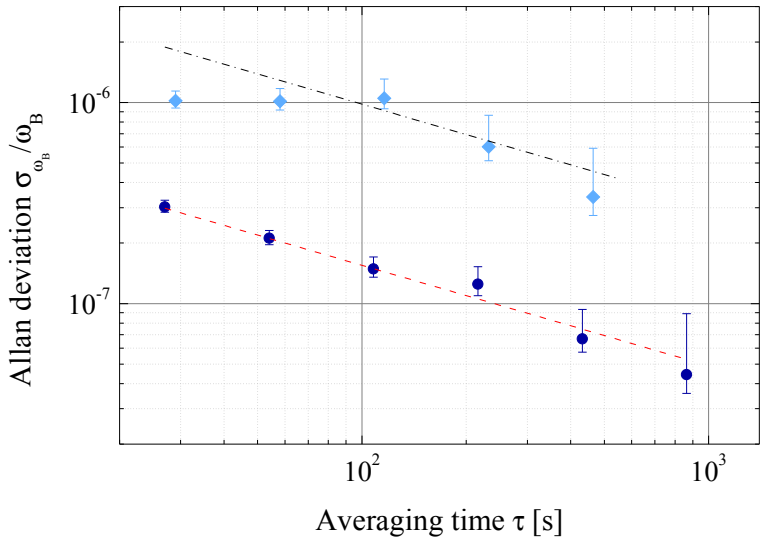

Figure 4.13: Allan deviations of the Bloch frequency measurements for ^{88}Sr (circles) and ^{87}Sr (diamonds) and their corresponding $\tau^{-1/2}$ asymptotic behavior (lines) obtained by frequency locking the AM frequency generator to the coherent delocalization resonance.

This new method allowed us to improve the sensitivity in the determination of the Bloch frequency (and gravity acceleration) by more than one order of magnitude with respect to the resonant tunneling spectra technique (see sec. 4.3.1) and to previous published results for ^{88}Sr [41]. In the same time required for the acquisition of a spectrum (about 30 min), we achieved a precision of 5×10^{-8} for ^{88}Sr, while for ^{87}Sr we obtained a precision of 4×10^{-7}. A comparison of the Allan deviation of the measured Bloch frequency with the Allan deviation of the red MOT size fluctuations projected into Bloch frequency fluctuations through eq. (4.9) shows that the main noise source comes from the red MOT size with a contribution of about 70%. The difference in precision between the two isotopes, in addition to what we have discussed in sec. 4.3.1, is also due to the slightly higher cycle time.

The ^{88}Sr result also represents the state-of-the-art in compact and local gravimeters when compared to the Rb interferometer based on Bloch oscillation pulses realized in Paris [217].

4.4 Test of the Weak Equivalence Principle

4.4.1 Differential force measurements: the Eötvös ratio

Each pair of Bloch frequency measurements obtained with the resonant tunneling spectra and with the frequency lock techniques were used to determine the Eötvös ratio defined by eq. (4.3). The data were recorded in $N = 68$ measurement sessions, spread over 9 months. Figure 4.14 shows the experimental results for η, their average value, and the comparison with the null value predicted by general relativity. Each point η_i is determined with its own error σ_i given by the quadratic sum of the statistical error and the uncertainty on the systematic effects.

The final result for the WEP violation parameter is

$$\eta = (0.2 \pm 1.6) \times 10^{-7}, \tag{4.17}$$

where the uncertainty corresponds to the standard deviation of the weighted mean $\sigma_{\bar{\eta}}$ corrected by the reduced chi-square:

$$\Delta\eta = \sigma_{\bar{\eta}} \frac{\chi}{\sqrt{N-1}}, \tag{4.18}$$

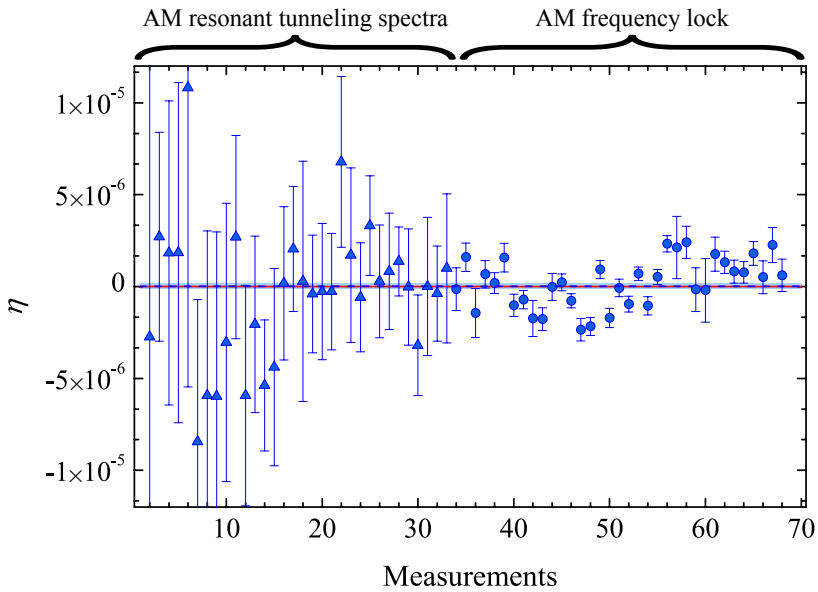

Figure 4.14: Summary of the measurements of the η parameter by AM resonant tunneling spectra (triangles) and by AM frequency lock (circles). The final weighted mean (blue dashed line) is compared with the null value expected from WEP (red line).

where $\sigma_{\bar{\eta}} = \sqrt{1/\sum_i^N \bar{\sigma}_i^2}$, and $\chi^2 = \sum_i^N (\eta_i - \bar{\eta})^2 / \bar{\sigma}_i^2$, which results in $\chi^2/(N-1) = 2.78$.

In the case of unpolarized ^{87}Sr atoms, the mean contribution of kS_z in the potential of eq. (4.2) is zero and $\eta = \beta_{88} - \beta_{87}$. This result can be interpreted in terms of the WEP violation parameters for the fundamental constituents of the two atoms, according to different parameterizations [46, 202, 218]. The parametrization in ref. [202] is particularly useful for comparing the result of this work with previous and older experimental tests because β_{88} and β_{87} are a function of the test mass nuclear structure and of the proton, neutron and electron gravitational anomalies β^w, where $w = \{p, n, e\}$. The observable WEP violation parameter η can be written in terms of linear combinations of the free particle β^w as

$$\eta = 10^{-3} \times \left[5.01\beta^{e+p-n} + 0.15(\beta^p + \beta^{\bar{p}}) + O(10^{-2})\right]. \tag{4.19}$$

In our experiment β^{e+p-n} is the most sensitive parameter, which can be bound by the η result as $\beta^{e+p-n} < 3.4 \times 10^{-5}$, i.e. three orders of magnitude bigger with respect to the existing bound [202], while the difference with measurements of η employing classical test masses is six orders of magnitude.

A more general violation of the EP related to spin concerns the fundamental nature of matter fields in quantum mechanics, which can be bosonic or fermionic. According to ref. [58], it is possible that the cosmological gravitational field generated by fermionic matter and bosonic matter has different strengths. This phenomenon can be parametrized by stating that the gravitational constant G is different for bosonic and fermionic matter. If this is true, this clearly breaks the universality of gravitation and thus the EP. Our result sets a 10^{-7} direct bound on the boson-to-fermion gravitational constant ratio $f_{BF} \equiv G_B/G_F$ from being different from 1.

4.4.2 Systematic corrections

The Bloch frequency measurements are affected by few systematic errors, which in our differential measurement, largely cancel and can be neglected at the present level of accuracy. Systematic error sources in common between the two isotopes measurements are: misalignment of the lattice beams, lattice frequency calibration, gravity gradients, and Gouy phase shift [219].

Lattice light shift

The main contribution to the systematic error in local gravity measurements with trapped neutral atoms arises from the space-dependent lattice depth $U_0(z)$ due to the local intensity gradient of the two interfering Gaussian beams. Since the Bloch

frequency measurement is a force measurement, we are actually sensitive to the effective driving force

$$F = -\partial_z V(z) = \partial_z [U_0(z) - Mgz]. \tag{4.20}$$

Therefore, the Bloch frequency of each isotope will contain an additional term proportional to the light gradient and weighted by their individual mass. Since we are interested only in the effect of the gravity acceleration upon ω_B, the differential acceleration due to the residual intensity gradient must be removed from the ratio given in eq. (4.3). Thus, the correction has been calculated to be

$$\Delta\eta_U = \frac{R_{88,87} - 1}{(\omega_{B,88} + R_{88,87}\omega_{B,87})/2} \frac{\partial_z U_0}{2\hbar k_L}, \tag{4.21}$$

where we have assumed that the difference in the trapping potential due to the dynamic polarizability of the two isotopes is negligible [220], so that $\partial_z U_0 = \partial_z U_{0,88} = \partial_z U_{0,87}$. The expression of the correction in eq. (4.21) is given by the product of the shift of $\omega_{B,88}$ induced by the lattice beam gradient $\Delta\omega_U = \partial_z U_0/2\hbar k_L$ and a weight factor $R_{88,87} - 1 \sim 10^{-2}$, divided by the mean Bloch frequency $(\omega_{B,88} + R_{88,87}\omega_{B,87})/2$. The physical interpretation of eq. (4.21) is that the acceleration due to the two-photon scattering process producing the confinement in the optical lattice has a reduced effect on the differential measurement but does not cancel out. This technical issue affects any EP tests employing an optical lattice [221].

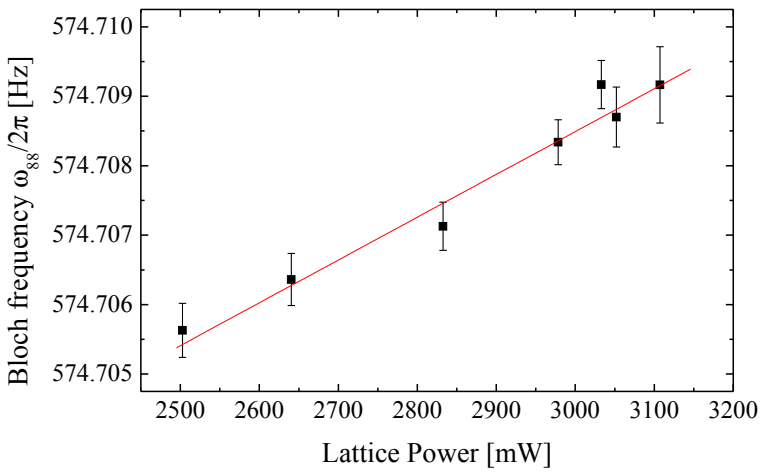

Figure 4.15: Determination of the light shift of the ^{88}Sr Bloch frequency due to the intensity gradient. $\omega_{B,88}$ was measured as a function of the total power on the atoms. The slope $\Delta\omega_U$ extrapolated from the linear fit is used to calculate the systematic correction.

A precise calibration of the acceleration due to the intensity gradient was done by measuring $\omega_{B,88}$ by means of the frequency lock technique. Repeated measurements of $\omega_{B,88}$ were performed with a stabilized lattice frequency as a function of the total lattice power

$$P = P_1 + P_2 + 2\epsilon\sqrt{P_1 P_2}, \tag{4.22}$$

where P_1 and P_2 is the power sent to the atoms per beam and ϵ is a geometrical correction factor due to the mismatch of the width of the two beams of order of unity. The results are shown in fig. 4.15. The resulting Bloch frequency shift $\Delta\omega_U = (\partial\omega_B/\partial P)P = (6.16 \pm 0.56) \times 10^{-6} \times P$ Hz/mW was obtained from the slope of a linear fit to the data. The corresponding correction is $\Delta\eta \sim 3.6 \times 10^{-7}$ for typical operating conditions.

Magnetic field gradients

The effect of magnetic field gradients in the differential Bloch frequency measurements was carefully studied. Residual magnetic field gradients $b = \partial B/\partial z$ were estimated by precise calibration of the ^{88}Sr red MOT vertical position dynamics to be less than 140 $\mu\mathrm{T} \cdot \mathrm{m}^{-1}$.

In general, the Bloch frequency measurement is sensitive to magnetic field gradients through the Zeeman effect. The position dependent Zeeman shift can be seen as a potential for which there is a corresponding effective force

$$F_{\mathrm{Zeem}}(m_F, b) = \partial_z U_{\mathrm{Zeem}}(z) = \frac{m_F}{F} g_I \mu_N b, \tag{4.23}$$

where m_F are the hyperfine spin components of the projection of the total angular momentum F, g_I is the nuclear Landé factor, μ_N is the nuclear Bohr magneton and $b = \partial_z B$ the external magnetic field gradient.

While ^{88}Sr is insensitive to magnetic field gradients at this level of precision because of its null total magnetic moment, the sensitivity of the ^{87}Sr isotope depends on the average spin projection $\langle m_F \rangle$. This was estimated by measuring $\omega_{B,87}$ while applying the magnetic field gradient with the MOT coils during the amplitude modulation in the lattice, up to 210 $\mathrm{mT} \cdot \mathrm{m}^{-1}$. Typical resonant tunneling spectra are shown in fig. 4.16(a) for a modulation time $t_M = 7.8$ s and $\ell = 1$.

Considering a homogeneous population of the magnetic sublevels, the presence of a magnetic gradient just removes the degeneracy of the 10 Bloch frequency resonances for each m_F. The resulting overall spectrum is a 10-component resonant broadening function of eq. (4.8):

$$\sigma(\omega_B) = \frac{1}{10}\sum_{m_F}\sqrt{\sigma_0^2 + v_\ell^2 t_M^2 \,\mathrm{sinc}^2\left[\left(\omega_M - \ell\left(\omega_B + \frac{\lambda_L}{2\hbar}F_{\mathrm{Zeem}}(m_F, b)\right)\right)/\Gamma\right]}. \tag{4.24}$$

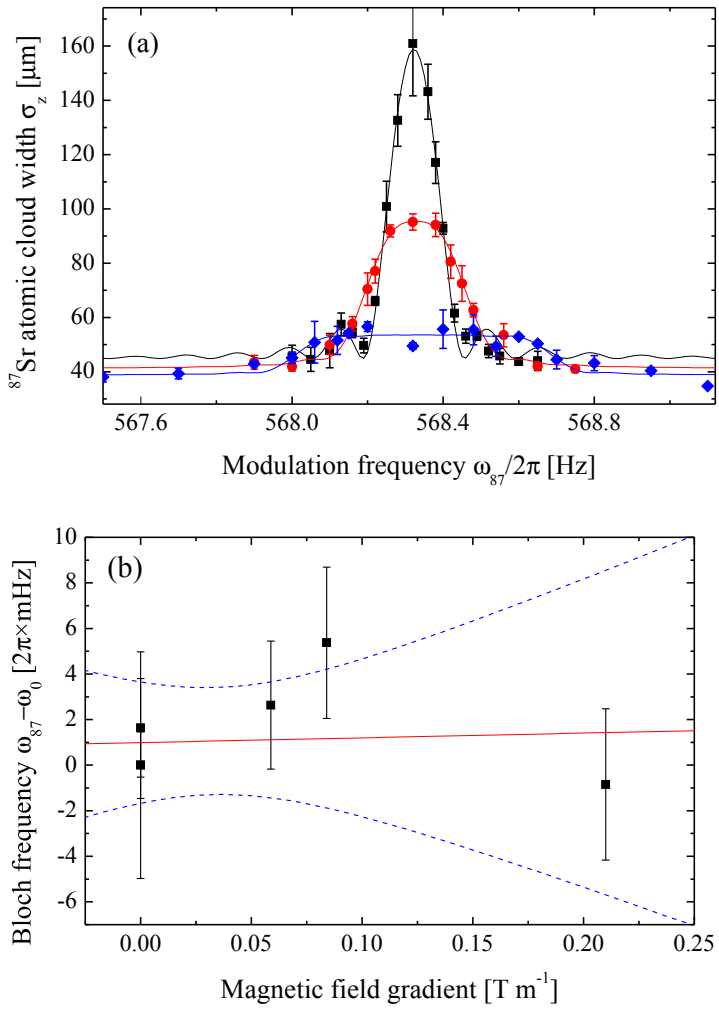

Figure 4.16: ^{87}Sr Bloch frequency sensitivity to magnetic field gradients. (a) Resonant tunneling spectra for different applied magnetic field gradients with the MOT coils: $b = 0$ (black squares), 84 mT · m^{-1} (red circles), 210 mT · m^{-1} (blue diamonds). The solid lines are least-squares fit to the data with eq. (4.24). (b) Central Bloch frequency values normalized to the unperturbed resonances. The red line is a linear fit to the data, the dashed blue lines are the mean prediction bands.

For Γ Fourier-limited (41 mHz for the data shown in figure), the width of each resonance component is much larger than the achievable Bloch frequency splitting with the MOT coils. Therefore, we can not resolve the Bloch frequency components and we just observe a broadening.

Figure 4.16(b) shows the measured central Bloch frequency values normalized to the unperturbed resonances. The red line is a linear fit to the data, the dashed

Effect	Correction	Uncertainty
Lattice light shift	3.6	0.3
Magnetic field gradient	0.001	0.01
Tides	0.16	0.01
Lattice frequency	0	0.05

Table 4.1: Uncertainty budget concerning the WEP violation parameter η. Correction values and uncertainties depend on the experimental conditions. Typical values are given in units of 10^{-7}.

blue lines are the mean prediction bands. The resulting sensitivity to magnetic field gradients is $\partial\omega_{B,87}/\partial b = 2\pi \times (2 \pm 15)$ mHz/(T $\cdot$ m^{-1}), which is consistent with a null effect at the level of 10^{-9} for our typical residual magnetic field gradient.

Other systematics and final budget

For every set of Bloch frequency measurements we considered the effect of tidal forces, which leads to a peak-to-peak variation at our site of the order of 2×10^{-6} m/s^2, i.e. a contribution of 10^{-7} to ω_B, on time scales of the order of 6 h. Since the measurements for the two isotopes were carried out in succession for a total time interval of 1 h, the maximum contribution from tides on the differential measurements that we could observe is 1.6×10^{-8} (typically is on the order of few parts in 10^{-9}).

As discussed in sec. 4.3.3, the frequency of the lattice is stabilized during a differential Bloch frequency measurement and the lattice frequency is measured with MHz precision, leading to a residual uncertainty contribution lower than 10^{-8} on η.

The total systematic uncertainty is thus dominated by the intensity gradient uncertainty at the level of 3×10^{-8}. Table 4.1 summarizes the important systematic corrections and uncertainty contributions.

4.5 Test of spin-gravity coupling violation

In presence of a gravitational potential of the form expressed by eq. (4.2), the ^{87}Sr hyperfine sublevels will experience a force due to the spin-gravity coupling:

$$F_{SG} = \partial_z V_{SG,87} = k I_z M_{87} g. \tag{4.25}$$

The effect of such a force is analogous to the one due to an external magnetic field gradient, discussed in the previous section. Each ^{87}Sr spin component I_z will feel different gravitational forces due to different spin-coupling kI_z, resulting in a

broadening of the resonant tunneling spectra. Because a Fourier-limited linewidth of the broadening resonance is expected in absence of decoherence mechanisms, a comparison between the measured linewidth and the Fourier one can be used to set a limit on the spin-gravity violation.

We analyzed a set of ^{87}Sr resonant tunneling spectra used for the determination of η. The residual deviations $\Delta\Gamma$ of the measured linewidth Γ from the Fourier linewidth, after removing systematic broadening effects, are shown in fig. 4.17.

A residual magnetic field gradient $|b| \leq 140\ \mu\mathrm{T}\cdot\mathrm{m}^{-1}$ may broaden the linewidth via the Zeeman effect of $\Delta\Gamma_b \leq 0.57$ mHz and we assume this value to be a systematic uncertainty on $\Delta\Gamma$. A second systematic broadening and uncertainty arises from atom-atom collisions. Since our fermions are unpolarized, they are distinguishable particles in quantum mechanics and undergo s-wave scattering. For an estimated density $n_{87} = 3.5(8)\times10^{15}\ \mathrm{m}^{-3}$, the estimated broadening is 2.4(6) mHz. Therefore, the measured residual broadening is $\Delta\Gamma = -0.4 \pm 0.5(\mathrm{stat}) \pm 0.8(\mathrm{syst})$ mHz.

The Bloch frequency separation between the extreme spin components $m_F = \pm 9/2$ can be seen as a broadening of the resonance for $\Delta\Gamma = 2 \times 9/2 \times k\ell\omega_{B,87}$, resulting in a spin-gravity coupling strength

$$k = (0.5 \pm 1.1) \times 10^{-7}. \tag{4.26}$$

Since the nucleus of ^{87}Sr has nine valence neutrons, this result also sets a limit of 10^{-7} for anomalous acceleration and spin-gravity coupling for the neutron either as a difference in the gravitational mass depending on the spin direction, which was

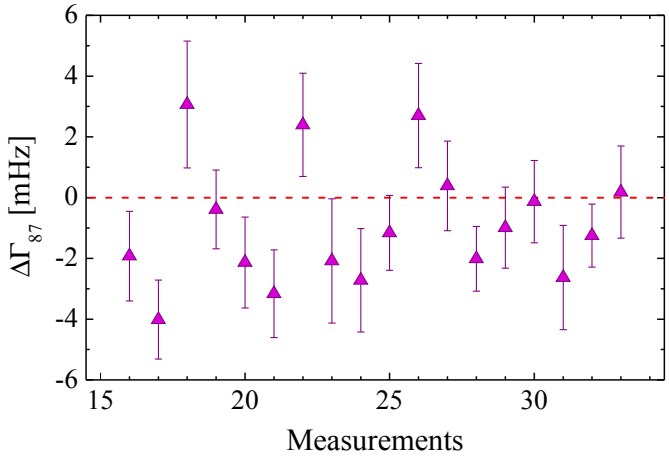

Figure 4.17: Measurements of the resonance linewidth broadening $\Delta\Gamma$ for ^{87}Sr. The displacement with respect to the Fourier linewidth ($\Delta\Gamma = 0$, red dashed line) sets a limit on spin-gravity coupling violation.

previously limited at 10^{-23} [55], or as a coupling to a finite-range Leitner-Okubo-Hari Dass interaction, which was limited to less than 10 at 30 mm by means of torsion balances with spin-polarized masses [53] and never with quantum matter.

Chapter 5

Large-momentum-transfer Bragg interferometer with ^{88}Sr atoms

In this chapter I will present the experimental realization of the first Mach-Zehnder interferometer with strontium atoms based on large-momentum-transfer Bragg transitions. The experimental setup used to produce Bragg pulses will be described, and the result of using such pulses for manipulation of ^{88}Sr atoms will be discussed. I will show how the control of efficient atom-optical components allows the realization of a highly sensitive gravimeter. Finally, I will present the current performances of such a device and an analysis of the main noise sources.

5.1 Bragg transitions for strontium atoms

5.1.1 Bragg laser setup

The laser source for the Bragg beams is a dedicated frequency-doubled diode laser at 461 nm, similar to the one used for the first cooling stage (see sec. 3.4.1). Indeed, we need as much power as possible to drive high-order Bragg transitions, therefore a dedicated high power source is almost compulsory. We reproduced the master cooling source in terms of mechanics and fundamental components (diode, tapered amplifier, cavity mirrors, crystal). In optimal conditions, the laser delivers 235 mW in the blue. Figure 5.1 shows the scheme of the Bragg laser setup.

The Bragg laser is frequency locked to the master cooling laser by an offset phase-locked-loop, in a similar way as we do for the red cooling lasers (see sec. 3.4.2). A small part of the laser light ($\sim$ 5 mW) is split by a PBS and combined with the master cooling laser light by another PBS; we project the polarizations on the same axis by using a third PBS at 45° with respect to the first one and we let them beat on

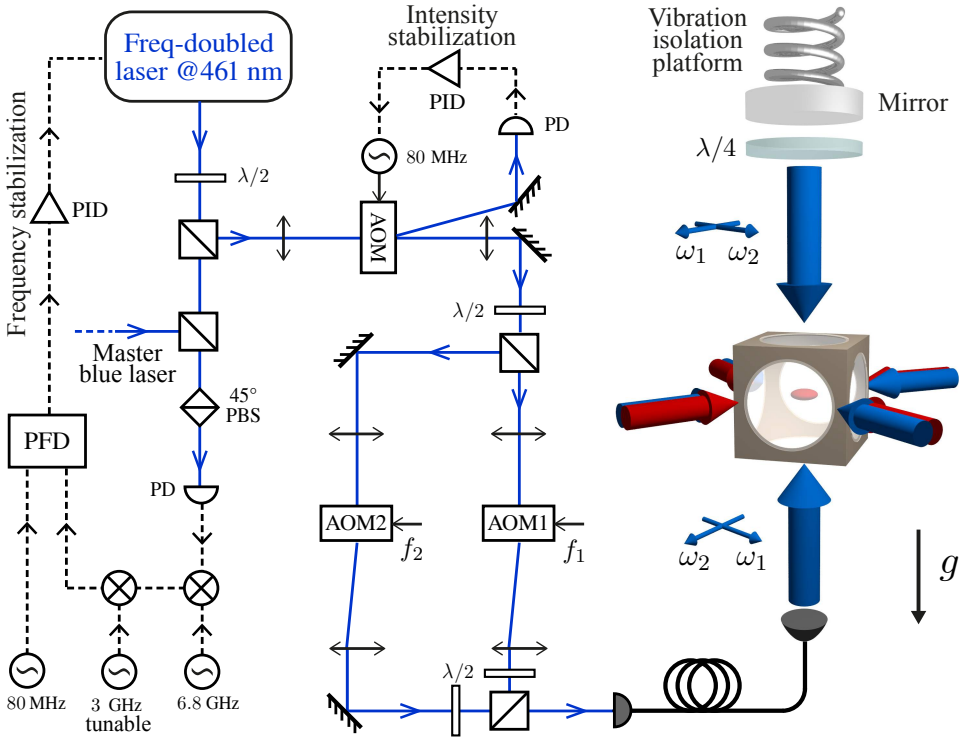

Figure 5.1: Optical scheme of the Bragg laser setup. The source is a frequency-doubled infrared laser delivering more than 200 mW at 461 nm. It is offset locked to the master blue laser by an OPLL. The intensity is actively stabilized by an AOM. The two frequencies for the Bragg pulses are controlled by two independent AOMs and combined with orthogonal polarizations in a PM fiber. They are sent upwards into the MOT cell, reflected by a suspended mirror and the polarizations are rotated 90° by a $\lambda/4$-plate.

a fast PD with 9 GHz bandwidth. The signal is mixed down by two RF generators: one delivers a fixed 6.8 GHz signal, and another is a tunable 3 GHz generator. The mixed signal is sent to a digital PFD and its phase is compared to an 80 MHz reference signal. The error signal is integrated by a PID servo and used to correct the frequency of the 922 nm master laser. By playing with the down-mixing frequency chain we are able to stabilize the Bragg laser in a range of detuning 2-8 GHz with respect to the $^1S_0$–$^1P_1$ transition.

The main Bragg laser beam passes through an AOM for active intensity stabilization. The AOM is driven by a low amplitude 80 MHz signal, which only diffracts a small fraction of the light (~ 1 mW) into the first order. The zero order is used for the Bragg beams production, while the first order is collected by a PD and used for the intensity stabilization. The PD's signal is compared to a stable

voltage reference. The difference signal is integrated by a PID servo and is used as correction for the AOM RF driver with 100 kHz bandwidth.

The undiffracted beam is split equally by a PBS and sent to two independent AOMs, which are used for frequency control and shaping of the Bragg pulses. The two beams, with frequencies ω_1 and ω_2, are then recombined in a PBS with mutual orthogonal polarizations and injected into a PM fiber. The whole laser is enclosed in an aluminum box, while the rest of the optical path, which is in free-space, is placed under a 2 mm thick, dense plastic box. The fiber output is collimated at a $1/e^2$ intensity radius of $r = 2.5$ mm and sent vertically upwards to the atomic sample. The light is then retro-reflected by a 2" mirror suspended on a vibration isolation platform (MinusK 25BM-4), placed on top of the upper breadboard. A quarter-wave plate is placed before the retro-reflection mirror to rotate the polarization of the returning light by 90°. The verticality of the beam is verified at 1 mrad level by retro-reflecting it on a water surface. The residual vibrations and tilt coupled to the retro-reflecting mirror are monitored by a triaxial accelerometer (Episensor ES-T) and a precision tiltmeter (Applied Geomechanics Tuff Tilt 420) placed on top of the vibration-isolation platform. The platform is enclosed in an acoustic isolation box.

5.1.2 Justification of the experimental configuration choices and consequences

The experimental configuration we chose is an attempt to reduce the phase noise of the optical system as much as possible. Indeed, as we will see, one of the main limitation to the interferometric phase sensitivity comes from the relative phase noise of the two Bragg beams.

A collinear configuration of the Bragg beams, in which the path difference is only due to the optical interferometer in which the AOMs are enclosed, is the most robust configuration we came up with. While a two fiber configuration in which the two beams are counter-propagating and sent to the atomic system independently from the top and from the bottom is conceptually simpler, it has the disadvantage of maximizing the path length difference. This configuration is incredibly sensitive to phase noise fluctuations, especially due to the fibers whose effective path length has a strong dependence on the environment temperature. Because the relative phase noise in the single-fiber configuration comes from the optical interferometer, it must be isolated as much as possible from vibration and acoustic noise. For this reason we enclosed the the interferometer in a box. An analysis of the residual noise is given in sec. 5.5.3.

To further reduce the phase noise one can completely eliminate the optical path difference by driving a single AOM with two frequencies. Unfortunately this configuration leads to a problem. To understand the issue let's consider this last situation, in which the AOM is driven by a frequency component f and a time-

varying component $f+\delta+\alpha t$, where δ is the frequency difference necessary to drive Bragg transitions for an atom at rest and α is a chirping that is needed to compensate for the Doppler shift of the falling atom. The beam coming out of the fiber consists of two co-propagating frequency components with same polarization, while the Bragg pulses need to be formed by two counter-propagating beams. For this reason the beam needs to be reflected after it passes through the cell. During a pulse, the atoms will then see four optical lattices made by all the possible combinations of frequency pairs, as sketched in fig. 5.2. An n-order Bragg resonance condition given by eq. (2.62) can be written for an atom that is fallen for a time t as

$$\hbar\Delta\omega = k_{\text{eff}}(-gt) + \hbar\delta_n, \tag{5.1}$$

where the two-photon wave vector $k_{\text{eff}} = k_1 + k_2 = 4\pi/\lambda_L$ is directed along g and its sign defines the direction of the diffraction, and $\delta_n = nk_{\text{eff}}^2/2M$ is the resonant detuning for an atom at rest.

Let us first consider the opposite pairs of beams with same frequencies (fig. 5.2a). They correspond to steady lattices in the laboratory frame, but they are seen as traveling standing waves by the falling atoms. Therefore, Bragg transitions can occur when the following resonance conditions are satisfied:

$$\hbar[f - (f)] = 0 = -k_{\text{eff}}gt + \hbar\delta_n, \tag{5.2}$$

$$\hbar[f + \delta + \alpha t - (f + \delta + \alpha t)] = 0 = +k_{\text{eff}}gt + \hbar\delta_n. \tag{5.3}$$

This means that a Bragg transition may occur if the Bragg pulse is applied at a time $t = \hbar\delta_n/k_{\text{eff}}g$. This situation can be seen as a Bragg transition in a steady

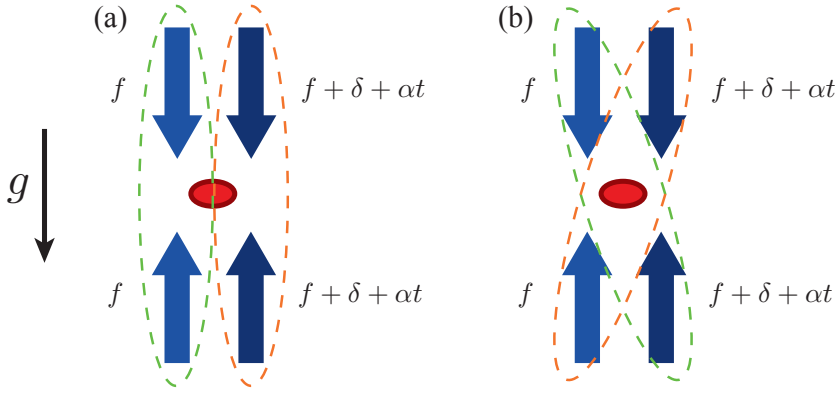

Figure 5.2: Standing wave interaction possibilities for a retro-reflected two-frequency beam. (a) Pairs of beams forming steady lattices. (b) By using orthogonal polarization rotated after reflection by 90°, the formation of standing waves is avoided. The interaction with two opposite-traveling standing waves is still possible, and double Bragg diffraction may occur.

lattice induced by the external gravity force (see sec. 2.2.2). For first-order Bragg transitions on strontium, this time corresponds to about 2 ms of free fall. At twice this time, the atom will be on resonance with a second-order transition, and so on. Therefore, the configuration of a single two-frequency beam with the same polarization is inconvenient.

In order to only produce traveling standing waves in the laboratory frame, we prepare the two-frequency beam with orthogonal polarizations and then a quarter-wave plate placed before the retro-reflection mirror rotates the polarizations of the returning light by 90°. This avoids the formation of standing waves by pairs of beams with the same frequency. On the other hand, the remaining system still contains two traveling waves with the same velocity given by the frequency difference $\Delta\omega = \omega_1 - \omega_2$, but opposite propagation direction. Both lattices can interact with an atom at rest, producing a *double Bragg diffraction*. To understand this situation let's consider the resonance conditions for the pairs of beams with different frequencies:

$$\mp\hbar[f - (f + \delta + \alpha t)] = \pm k_{\text{eff}} g t + \hbar\delta_n, \tag{5.4}$$

$$\mp\hbar[(f + \delta + \alpha t) - f] = \pm k_{\text{eff}} g t + \hbar\delta_n \tag{5.5}$$

where the first equation corresponds to the resonance condition for the pair of frequencies marked by the green ellipse in fig. 5.2(b) and to an upward and downward diffraction, according to the sign of k_{eff}; the second corresponds to the resonance condition for the pair marked by the orange ellipse. By tuning the values of δ and α we can decide which pair will be on resonance. If we want the atom to be diffracted upwards by $2n$-photon recoils we will choose $\Delta\omega = \delta_n$ and $\alpha = -k_{\text{eff}} g$ in order to keep the upward traveling standing wave on resonance along the free fall, while the downward traveling one will quickly be out of resonance because the chirping αt and the Doppler shift $k_{\text{eff}} g t$ will grow with opposite sign.

The double Bragg diffraction will always occur whenever the atoms reach a stationary point of their trajectory, i.e. the apogee of the parabolic flight. Therefore, while running the interferometer we avoid sending pulses at the apogee time. Since the atomic ensemble has a finite momentum width, the double diffraction resonance condition can be fulfilled for a certain time range. For a typical momentum width of $\sigma \sim 10$ kHz we can avoid double diffraction by not sending pulses for 1 ms around the apogee time.

Even though, in our experimental configuration double diffraction is unwanted, it is worth mentioning that double Bragg diffraction was proposed as a possible tool for symmetric large-area atom interferometer schemes where some common-mode noise sources cancel out [222, 223].

In conclusion, the final configuration we chose involves the use of a retro-reflection mirror placed on top of the cell. This mirror will be our main limitation

to the sensitivity of the interferometer. Indeed, it acts as a reference frame for the traveling standing wave with respect to the freely falling atoms. The vibration noise of the mirror can be seen as an induced inertial acceleration in the reference frame of the atoms, and it can be measured by the interferometer. In order to suppress this noise, we mounted the mirror on a suspended isolation platform. The noise spectra and the possible solutions to overcome the vibration noise limitation will be discussed later in this chapter.

5.1.3 Bragg pulses production

The Bragg beams' frequency, phase and amplitude are controlled by two independent 80 MHz AOMs. The RF scheme we used is shown in fig. 5.3(a).

The carrier frequency of the pulses is generated by a two-channel arbitrary waveform generator (Agilent 33622A), referenced to a rubidium clock standard. This generator has very high phase coherence between the two channel: less then 1 ps of rms jitter for a bandwidth up to 40 MHz, which is a negligible contribution to the interferometer phase noise. One channel delivers a continuous

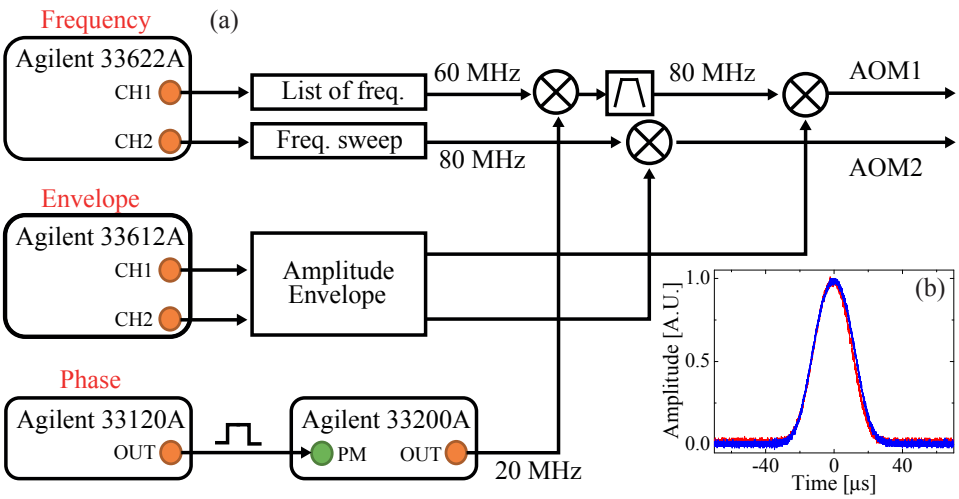

Figure 5.3: (a) RF scheme for Bragg pulse production. The carrier frequency is generated by a two-channel arbitrary waveform generator (Agilent 33622A). Channel 1 is programmed with a list of frequencies centered at 60 MHz and accounting for the detuning $\Delta\omega$ needed to produce arbitrary n-oder Bragg transitions. Channel 2 delivers a continuous frequency sweep α (centered at 80 MHz) to compensate for the varying Doppler shift of the falling atoms. The relative phase is controlled by mixing the channel 1 output with 20 MHz delivered by an Agilent 33200A phase-modulated by an Agilent 33120A. The amplitudes are shaped by an Agilent 33612A. (b) Gaussian envelope signal (red) and corresponding optical signal (blue) for a $\sigma = 10$ μs pulse.

frequency sweep α triggered when the red MOT is switched off and the atoms start to fall. The frequency chirping for blue Bragg transitions on strontium atoms is $\alpha = k_{\text{eff}} g \simeq 2\pi \times 42.55$ kHz/ms. The second channel is used to control the frequency shift $\Delta\omega$ needed to produce arbitrary n-order Bragg transitions. The frequency states are saved in a list inside the generator and triggered by the experimental control system.

The pulse amplitude is programmed in a second arbitrary waveform generator (Agilent 33612A) with 1 GSa/s sample rate. We have programmed the generator to produce Gaussian envelopes truncated at 8σ, but it can be easily modified to get every kind of desired envelope. The amplitude of the carriers is shaped with the envelope signal by means of two mixers (ZAY-1). Figure 5.3(b) shows a Gaussian envelope signal (red line) and the corresponding optical signal (blue line) for a pulse with $\sigma = 10$ μs duration.

The relative phase of the two Bragg beams has to be controlled in order to scan an interferometer fringe. Unfortunately, we can not directly trigger a phase shift in the carrier frequency generator, therefore we use a third signal generator (Agilent 33200A) that is phase modulated. The main frequency $f = 80$ MHz of the swept channel is reduced to 60 MHz and mixed with a phase-modulated 20 MHz signal. The output is filtered by a band-pass filter centered at 80 MHz. The modulation signal is a 5 V square pulse which induces a phase shift whose sensitivity is set by the 33200A generator. Since the amplitude noise of the modulating signal is transfered to phase noise, to produce the 5 V signal we used a good generator (Agilent 33120A) triggered by our TTL control system. The phase noise spectrum for the overall RF chain is reported later in this chapter as comparison to the optical phase noise.

I implemented a high-level LabView interface that simultaneously programs all these generators in order to produce an arbitrary number of pulses with arbitrary frequency, amplitude and phase. The pulse timing table is simultaneously written into the main control program that sends TTL signals to the generators in order to trigger the desired states at the right time.

5.2 Manipulation of ultra-cold ^{88}Sr with Bragg pulses

5.2.1 Velocity selection of the red MOT

As we discussed in sec. 2.4.3, as an effect of the interaction between a thermal atomic ensemble and a Bragg pulse is velocity selection. The cold atomic sample that we can initially interrogate is an ultra-cold thermal cloud of ^{88}Sr atoms, cooled and trapped in the red MOT (see sec. 3.2.2 for details). The cloud contains about 5×10^6 atoms at a temperature $T = 1.2$ μK. The expected 1-σ momentum width is $\Delta p = \sqrt{M k_B T} = 1.08\ \hbar k_L$. This temperature is not low enough to get efficient

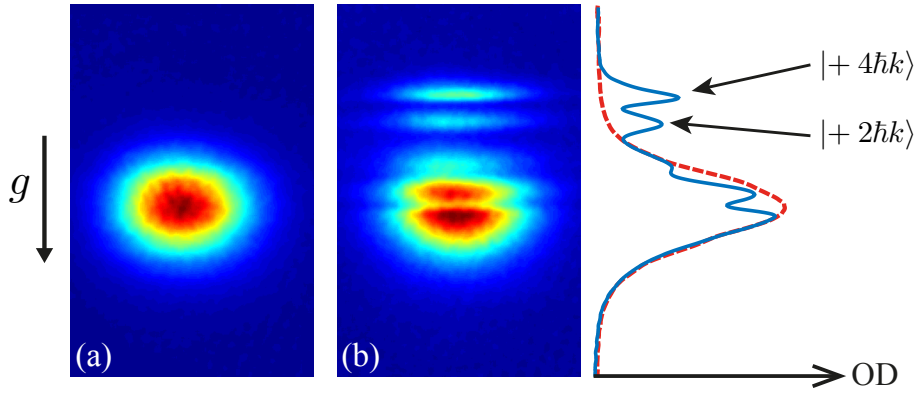

Figure 5.4: Velocity selection of the red MOT with a second-order Bragg transition. TOF image of the released red MOT not diffracted (a) and diffracted (b) by a 30 μs pulse. On the right, the two integrated profiles are shown. The center of the cloud is depleted and transfered to the on-resonance $|4\hbar k\rangle$ state. Residual off-resonance $|2\hbar k\rangle$ state is populated because of the large momentum distribution of the red MOT.

Bragg diffraction, therefore a velocity selection is required.

Figure 5.4 shows the effect of a second-order Bragg transition on the red MOT. A 30 μs pulse is applied just after the release of the trap and an absorption image is taken after a TOF of 13 ms. The images of the cloud without (a) and with (b) Bragg diffraction are compared. The on-resonance interaction depletes the center of the cloud, transferring a narrower sample to the $|4\hbar k\rangle$ state. Because the released red MOT ensemble is largely spread in momentum, a fraction of the distribution tail is resonant with the first-order transition, therefore another portion of the Gaussian profile is depleted and transfered into the $|2\hbar k\rangle$ state. Since some losses in unwanted momentum states are always present after the selection pulse, we typically apply at least three consecutive pulses in order to spatially separate the selected cloud from the red MOT.

By increasing the pulse duration a narrower momentum distribution can be obtained, although this results in a lower number of atoms in the desired momentum state. We verified that an acceptable compromise between atom number and momentum width for low-order Bragg diffractions is obtained for pulse duration between 20 and 40 μs. We characterized the selected atomic sample by measuring the momentum distribution with Bragg spectroscopy.

Bragg spectroscopy of the atomic sample

Bragg spectroscopy consists in measuring the excited state population as a function of the Bragg beams' frequency difference $\Delta\omega$ from the Bragg resonance. Because the Bragg transition is Doppler shift sensitive, the excited state will have maximum

population on resonance, and it will decrease as long as $\Delta\omega$ is tuned out of resonance. Scanning the $\Delta\omega$ around the resonance is thus a spectroscopy of the momentum distribution of the interrogated atomic cloud. Because the Bragg resonance is Fourier-limited, the interaction duration sets the resolution of the spectroscopy probe.

Figure 5.5 shows Bragg spectroscopy signal of the red MOT (red circles) and of a velocity selected cloud (blue diamonds). For the first measurement we applied second-order Bragg pulses 100 μs after releasing the trap. We chose a pulse duration of $\sigma = 50$ μs. The corresponding Fourier-limited linewidth is $\gamma_F = 2\pi/\pi\sigma = 2\pi \times 6.3$ kHz and sets the resolution for the Bragg spectroscopy. Scanning the frequency difference $\Delta\omega$ across the resonance gives a Gaussian momentum distribution with a width of $\sigma_{\Delta\omega} = 2\pi \times 37.8$ kHz.

We can extract a temperature estimation from the Bragg spectroscopy. The energy equipartition for a velocity distribution with width σ_v tell us that $T = M\sigma_v^2/2k_B$. The Doppler effect relates the Bragg detuning to the atoms' velocity, so that $\sigma_v = \sigma_{\Delta\omega}/k_L$. Thus, the temperature of the cloud along the vertical direction can be estimated by

$$T = \frac{M}{2k_B}\frac{\sigma_{\Delta\omega}^2}{k_L^2}. \tag{5.6}$$

In the case of the red MOT, the result is $T = 1.5$ μK, which is consistent with the temperature measured in TOF.

We then studied the momentum distribution of a velocity selected cloud by a 20 μs second-order pulse. After the selection we applied a second pulse, 140 μs

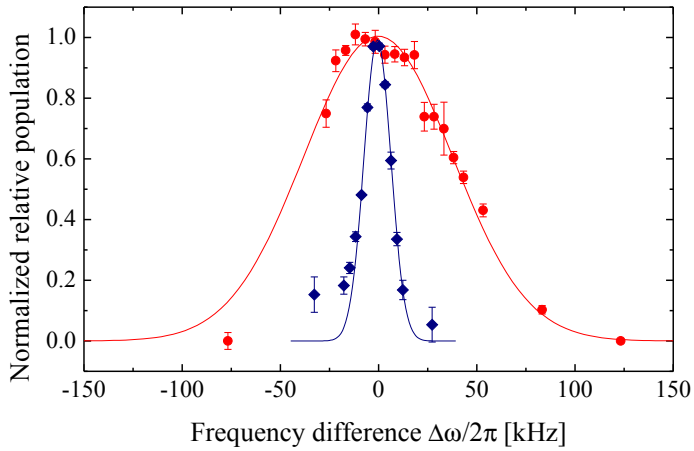

Figure 5.5: Bragg spectroscopy of the red MOT (red circles) and of a velocity selected cloud (blue diamonds). The velocity selected cloud was excited by a 2nd Bragg pulse of 20 μs duration. The measured momentum widths are $1.3\hbar k_L$ and $0.2\hbar k_L$.

long, the frequency of which was scanned across the resonance. The long duration ensures a resolution of 2 kHz due to the Fourier linewidth. The measured momentum distribution width is $\sigma_{\Delta\omega} = 2\pi \times 6.9$ kHz, which corresponds to a temperature $T = 50$ nK and a momentum spread $\Delta p = 0.2\hbar k_L$.

5.2.2 Rabi oscillations between momentum states

The Mach-Zehnder interferometer requires the population of two momentum states to be equally split, inverted after a certain time and then recombined. The population splitting ratio can be tuned by varying the interaction strength of a Bragg pulse, in terms of its intensity and duration. By keeping the intensity fixed and by varying the pulse duration, for example, Rabi oscillations between momentum states can be observed, as explained in sec. 2.4.1.

The velocity-selected atomic cloud is now taken as the initial state that we want to analyze, and we will label it as $|0\hbar k\rangle$. A Bragg pulse with a frequency difference that compensates for the Doppler shift of the falling cloud and covers enough frequency recoils ω_r for an n-order Bragg transition will produce Rabi oscillations mainly between $|0\hbar k\rangle$ and $|2n\hbar k\rangle$, while some losses into other momentum states may be present. The states' population is measured by a Gaussian least-squares fit of the atomic cloud signals, spatially separated by an adjustable TOF.

First we will consider the effect of the pulse shape on the diffraction efficiency of a first-order Bragg transition. We will then investigate the diffraction at higher orders and their main limitations.

Gaussian pulses vs square pulses

Figure 5.6 shows the Rabi oscillation measurements for a first-order Bragg transition driven by a square pulse (a) and a Gaussian pulse (b). We used the same parameters for both measurements. The peak intensity was set to $I = 400$ W/m^2 ($\bar{\Omega} = 1.3\omega_r$), which correspond to about 5 mW per beam. The detuning from resonance was set to $\delta = +2.77$ GHz $= 86 \times \gamma$. The initial momentum state was prepared by a 20 μs velocity selection pulse from the red MOT, and then separated from the red MOT tails by other two pulses. The main momentum states driven by a first-order Bragg pulse are shown: the initial state $|0\hbar k\rangle$ (black squares), the first diffraction order $|2\hbar k\rangle$ (red circles) and the losses in $|-2\hbar k\rangle$ (blue diamonds).

From these measurements we can qualitatively discuss a few considerations we have presented in sec. 2.4.1 about the theoretical analysis of Rabi oscillations for Bragg pulses. For instance, at short pulse times, non-negligible losses in the $|-2\hbar k\rangle$ states are present. This situation corresponds to the Raman-Nath regime, which occurs for time $t < 1/\sqrt{\Omega\omega_r}$ when the kinetic energy contribution can be neglected. For the parameters we have used, the Raman-Nath regime occurs for

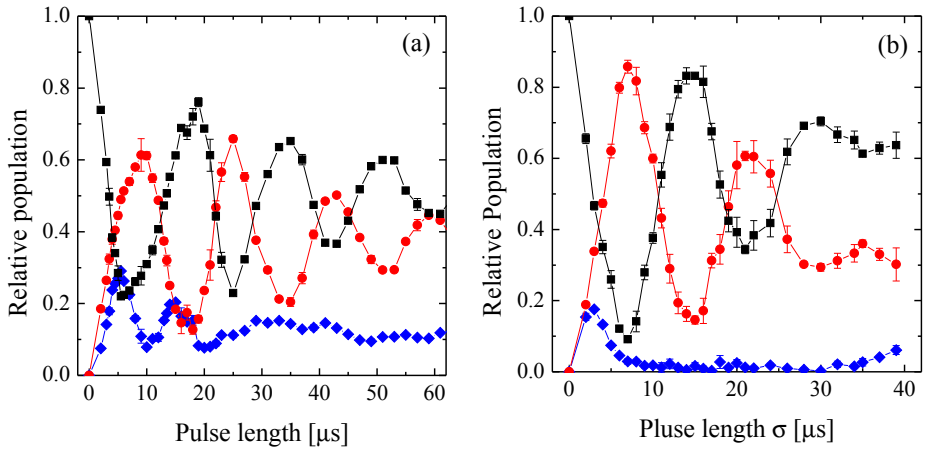

Figure 5.6: Rabi oscillations measurements for a 1st order Bragg transition driven by a square pulse (a) and a Gaussian pulse (b). We plotted the relative population of the relevant momentum states $|0\hbar k\rangle$ (black squares), $|2\hbar k\rangle$ (red circles) and $|-2\hbar k\rangle$ (blue diamonds). Parameters used: intensity per beam $I = 40$ mW/cm^2 ($\bar{\Omega} = 1.3\omega_r$), $\delta = +2.77$ GHz ($86 \times \gamma$), initial momentum width $\sigma_p = 0.2\hbar k_L$. The error bar is the statistical error over at least three consecutive measurements. The lines are just a visual guide.

$t < 13$ μs, in accordance with what we have measured in the Gaussian pulse case. For square pulses instead, the fast oscillation of the losses is larger and does not end with the Raman-Nath regime. Indeed, as we have pointed out in sec. 2.4.1, the quasi-Bragg regime lasts much longer for square pulses than for Gaussian pulses.

From now on, we will only use Gaussian pulses in our applications.

High-order Bragg diffraction

In sec. 2.4.3, we have discussed the importance of momentum width and we have pointed out that the higher the Bragg order one wants to use, the more stringent the constraint on the momentum width. As we already stated, it is not possible to reduce the momentum width without losing atoms in the selection process. Therefore, a drop of efficiency in higher order Bragg transitions is expected.

It was observed by Szigeti *et al.* [135] that, in order to keep high transfer efficiencies while moving to higher orders, an increase of the effective Rabi frequency Ω_{eff} for n-order Bragg transitions is required, expressed by eq. (2.123) and reported here as quick reference:

$$\Omega_{\text{eff}} = \frac{\Omega^n}{(8\omega_r)^{n-1}} \frac{1}{(n-1)!^2} \tag{5.7}$$

where $\Omega = \Omega_0^2/2\delta$ is the two-photon Rabi frequency and ω_r is the recoil frequency.

To increase Ω_{eff}, one has to increase the two-photon Rabi frequency, which is related to the single-photon Rabi frequency Ω_0 and therefore depends on the intensity, and also depends on the detuning δ from the internal excited state. As can easily be seen by looking at eq. (5.7), for fixed Ω the effective Rabi frequency drops dramatically for $n > 2$, because of the presence of the factorial in the denominator which is much "faster" than the n-power in the numerator. Therefore, Ω needs to be increased more and more, for a larger order n.

Since the available optical power is limited by the laser source in a real experiment, at fixed beam diameter and at full power, Ω can only be increased by reducing the detuning δ. On the other hand, approaching the resonance causes an increase of the losses due to resonant scattering, whose probability is expressed by eq. (2.30). In practice, according to the available laser power, we choose the detuning δ in order to maximize the π-pulse efficiency, which eventually determines the contrast of the interferometer.

Figure 5.7 shows some of the best Rabi oscillations we obtained according to the previous considerations, for first (a), second (b) and third (c) order Bragg transitions. We have measured the relative population of the main states involved in the oscillations and the losses in the nearby states, where present. In each plot the momentum states are marked by the same symbols: $|0\hbar k\rangle$ (black squares), $|2\hbar k\rangle$ (red circles), $|4\hbar k\rangle$ (blue diamonds) and $|6\hbar k\rangle$ (green triangles). The clouds were initially velocity selected by a 40 μs pulse which gives a momentum width $\sigma_p \simeq 0.2\hbar k_L$. The parameters we have used are: (a) intensity per beam $I = 150$ mW/cm^2, $\delta = +8$ GHz; (b) $I = 200$ mW/cm^2, $\delta = +8$ GHz; (c) $I = 230$ mW/cm^2, $\delta = +3$ GHz. The population was measured by Gaussian fit of the fluorescence signals in TOF.

For the first-order transition, we are limited by the frequency locking system to $\delta = 8$ GHz. Therefore, we need to reduce the intensity of the Bragg beams with respect to the present maximum available $I = 230$ mW/cm^2 per beam. A further increase of Ω_{eff} would simply take the dynamics too close to the Raman-Nath regime, increasing the losses and reducing the π-pulse efficiency. For the second-order transition, we typically work around the extremes of our current experimental availability in terms of intensity and detuning. For the third-order transition, we are currently limited by the available intensity and we need to stay closer to resonance ($\delta < 5$ GHz).

Figure 5.7(d) shows the typical fluorescence signals obtained for π-pulses at the first four Bragg orders. We are able to get an almost perfect diffraction (98% of efficiency) for a first-order transition and we observed up to 50% of atoms diffracted into the $|8\hbar k\rangle$ state with a fourth-order pulse at full power and at a detuning $\delta = +2.77$ GHz.

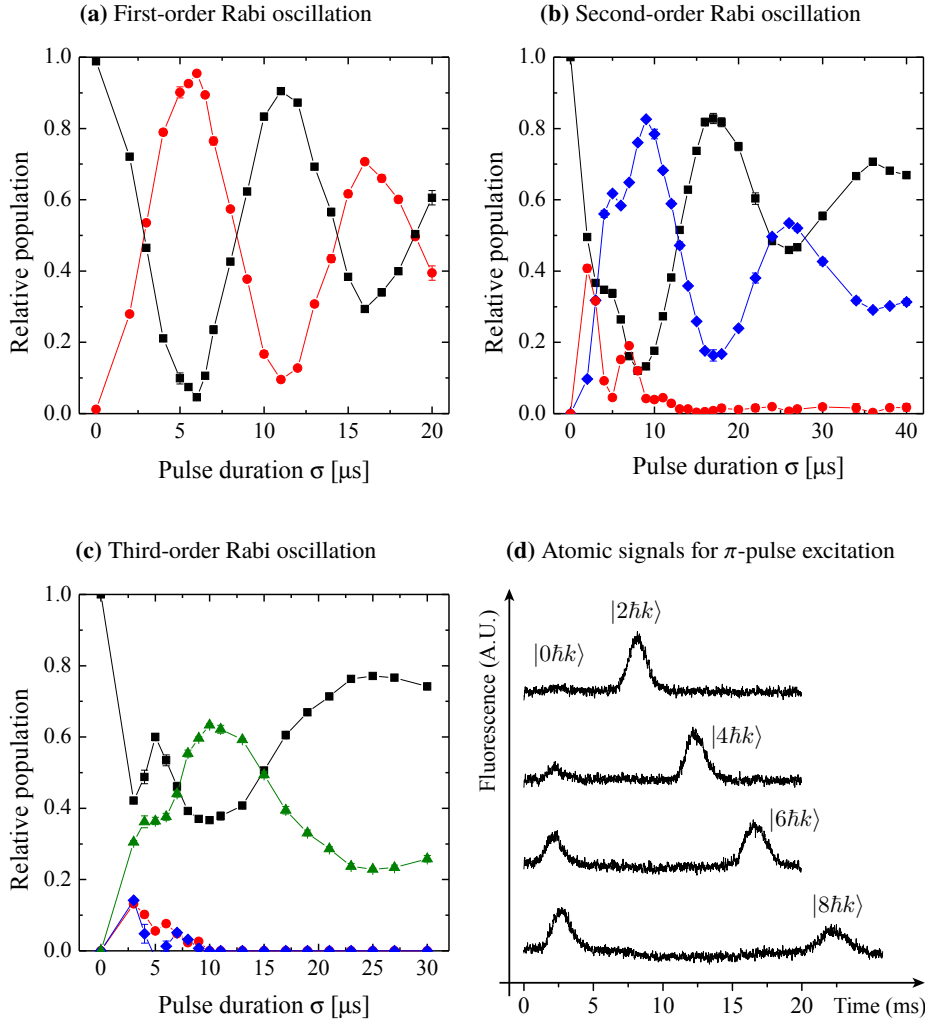

Figure 5.7: Rabi oscillations measurements for a first (a), second (b) and third (c) order Bragg transition driven by Gaussian pulses. In each plot the momentum states are marked by the same symbols: $|0\hbar k\rangle$ (black squares), $|2\hbar k\rangle$ (red circles), $|4\hbar k\rangle$ (blue diamonds) and $|6\hbar k\rangle$ (green triangles). Parameters used: (a) intensity per beam $I = 150$ mW/cm^2, $\delta = +8$ GHz; (b) $I = 200$ mW/cm^2, $\delta = +8$ GHz; (c) $I = 230$ mW/cm^2, $\delta = +3$ GHz. Initial momentum width $\sigma_p \simeq 0.2\hbar k_L$. The error bar is the statistical error over at least three consecutive measurements. The lines are just a visual guide. (d) TOF fluorescence signals of the atomic cloud excited by a π-pulse for the first four Bragg orders. From top to bottom, the transfer efficiencies are: 98%, 85%, 65%, 50%.

5.3 Mach-Zehnder interferometer with Bragg pulses

A Mach-Zehnder interferometer is composed by a three pulse sequence $\pi/2-\pi-\pi/2$. The first $\pi/2$ coherently splits the atomic cloud in two different momentum states $|p_0\rangle$ and $|p_0 + 2n\hbar k\rangle$, which are reflected after a time T by a π-pulse and then recombined by a $\pi/2$-pulse after a time $2T$. As we discussed in sec. 2.5, a Mach-Zehnder interferometer is sensitive to inertial accelerations. The phase shift between the two arms of the interferometer was derived in eq. (2.147) and takes the general form:

$$\Delta\Phi = 2nk_L T^2 a + n(\phi_{\mathrm{I}} - 2\phi_{\mathrm{II}} + \phi_{\mathrm{III}}), \tag{5.8}$$

where n is the Bragg order with wave vector k_L, T is the time separation between the interferometer pulses, a is the sum over all the participating inertial accelerations, and ϕ_i is the phase of the ith pulse. The sensitivity to acceleration measurements depends on the interferometer space-time area $2nk_L T^2$. Because of this reason we want to use high n-order Bragg diffractions and let the atomic wave packets evolve freely in the gravitational field for the longest time T possible. To increase this time we want to exploit all the available space in the MOT cell. Therefore, we implemented a pulse sequence to launch the atoms in a fountain, increasing the free-falling time.

5.3.1 Experimental sequence

The experimental sequence is depicted in fig. 5.8(a). An atomic sample of ^{88}Sr is cooled in the two-stage MOT, reaching a final temperature of 1.2 μK, with a spatial radial (vertical) size of 300 μm (50 μm) FWHM. The sequence produces about 2×10^6 trapped atoms in 1.5 s. A small fraction of the atoms ($\sim 10^5$) is selected from the MOT and launched upwards with a 40 μs π-pulse. The selection reduces the momentum distribution width to $\sigma_P \simeq 0.2\hbar k_L$ along the vertical direction. The cloud is spatially separated by the red MOT and launched in a fountain with several π-pulses up to a total momentum transfer of $40\hbar k_L$. Even though a single π-pulse would be sufficient to isolate the selected atoms from the freely falling cloud after the release from the red MOT, a larger number of pulses is applied to increase the total time of flight up to 150 ms. After the launch of the atoms in the fountain, a Mach-Zehnder interferometer is realized by applying three Bragg pulses in a $\pi/2 - \pi - \pi/2$ configuration.

The effective Rabi frequency for the Bragg pulses is set in order to get the highest π-pulse efficiency, according to the considerations we discussed in sec. 5.2.2. The pulse duration is then fixed and the $\pi/2$-pulse is realized by decreasing the amplitude in order to equally split the population over two paths separated by $2n\hbar k_L$. Fig. 5.8(b) shows an absorption image of the atoms in the two arms of the interferometer after

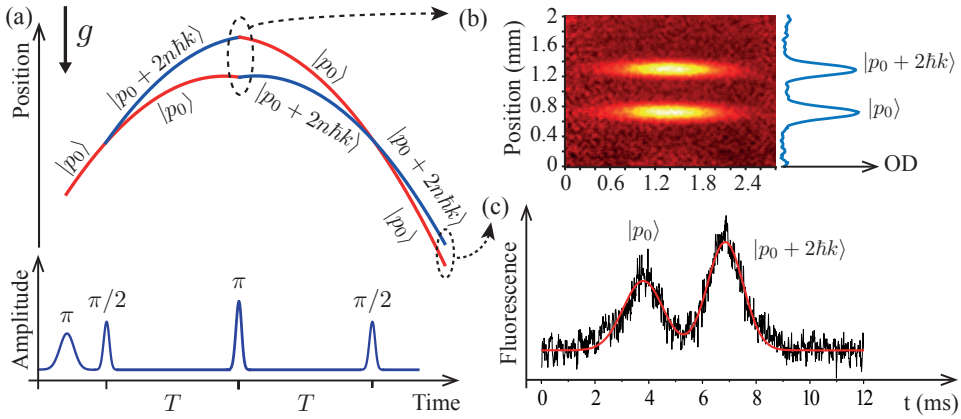

Figure 5.8: Free-falling Mach-Zehnder interferometer sequence and atom detection signals. (a) The atoms are coherently split, reflected and recombined by a $\pi/2-\pi-\pi/2$ pulse sequence. In the free-evolution time the two paths undergo ballistic trajectories. Before the interferometric sequence the atoms are velocity selected and launched by a sequence of π-pulses. (b) Absorption image of the two interferometer arms split by a first-order $\pi/2$-pulse, at the maximum space separation for a $T = 30$ ms interferometer. (c) Fluorescence signal acquired 40 ms after the last $\pi/2$-pulse. The momentum states' population is extrapolated by a double-Gaussian least-squares fit to the data.

30 ms for a first-order pulse. We notice that the spatial separation between the two interferometer arms is 600 μm, which is about two times larger than the separation induced by near-infrared light in alkali atom interferometers for the same separation time T. The two paths in the interferometer are recombined after a time $2T$.

Unlike Raman interferometry where the two paths correspond to different atomic hyperfine states and a selective detection can be used, in Bragg interferometry the internal state is the same, therefore the output arms needs to be spatially separated and detected simultaneously. The population at the two output ports is detected by either absorption imaging or fluorescence collection about 40 ms after the last pulse is applied, when the two momentum states are sufficiently separated in space. A fluorescence image of the interferometer output ports for a first-order Bragg transition and a total interferometer time $2T = 60$ ms is shown in fig. 5.8(c). The atoms are detected by a narrow probe beam passing 3 cm below the MOT position, as described in sec. 3.3.6.

5.3.2 Launching atoms in a fountain

As stated, we want to launch the atoms upwards as high as possible in order to increase the available free-falling time and so increase the interferometer area. We realize the launch in two different ways. The method that we practically

implemented in our gravimeter consists in a fast sequence of π-pulses. A second promising method consists in loading the atoms in a far-detuned accelerated optical lattice. The preliminary results of such a technique will be discussed.

Launch with a high-efficient Bragg pulse sequence

The launching method with several Bragg pulses takes advantage of the high efficiency of first-order Bragg transitions that we can achieve in our setup. Indeed, after velocity selection from the red MOT, a single π-pulse has an efficiency of approximately 98% (see sec. 5.2.2). Therefore, if a fast sequence of N pulses is applied just after the selection and before the cloud significantly expands transversely, $2N$-photon recoils can be transfered to the atoms with an overall efficiency of about $(98\%)^N$.

The typical π-pulse length for the launch is $\sigma = 6$ μs. The Gaussian envelope is truncated at 8σ, therefore a single pulse requires about 100 μs. With 20 such pulses for example, we can transfer $40\hbar k_L$ in 2 ms, with an efficiency of $(98\%)^{20} \simeq 67\%$. This launch almost doubles the total TOF from the release of the trap to the detection (placed 3 cm below the MOT position), from 75 ms to 130 ms.

Obviously, when the atoms interact with the Bragg beams and receive a kick of $2n\hbar k_L$, their frequency will be Doppler shifted. Therefore, the Bragg beams' frequency needs to be adjusted for each subsequent pulse. For an atom initially occupying the momentum state $|2m\hbar k_L\rangle$, the frequency difference $\Delta\omega$ to get an n-order Bragg diffraction to the state $|2(m+n)\hbar k_L\rangle$ needs to be increased, according to eq. (2.65): $\Delta\omega = 4(2m+n)\omega_r$.

Launch with a far-detuned accelerated lattice

Another method we began to investigate is the possibility to launch atoms confined in an accelerated optical lattice. This method might be more favorable because the Bloch oscillation process involved in the acceleration is potentially immune to losses. As it was pointed out in sec. 2.2.2, as long as the atoms initially occupy the first band, i.e. if their momentum spread is smaller than $2\hbar k_L$, the efficiency of the process is independent of the initial velocity. This is a great difference between Bloch oscillations and Bragg diffractions.

The only possible losses come from the Landau-Zener tunneling to excited bands. As long as the acceleration is adiabatic ($\dot{\Delta\omega} \ll \Omega^2$), the losses can be kept very low. We could accelerate the Bragg laser beams to perform the launch, but in the present configuration it is too close to resonance to keep the atoms trapped for a time longer than few μs. Indeed, a reasonable lattice depth $U_0 = 7E_r$ can be obtained with $I = 5$ mW/cm^2 per beam and a maximum detuning $\delta = -8$ GHz $= 250\gamma$, but the resonant scattering rate $\Gamma_s = 2\pi \times 300$ kHz is still too large.

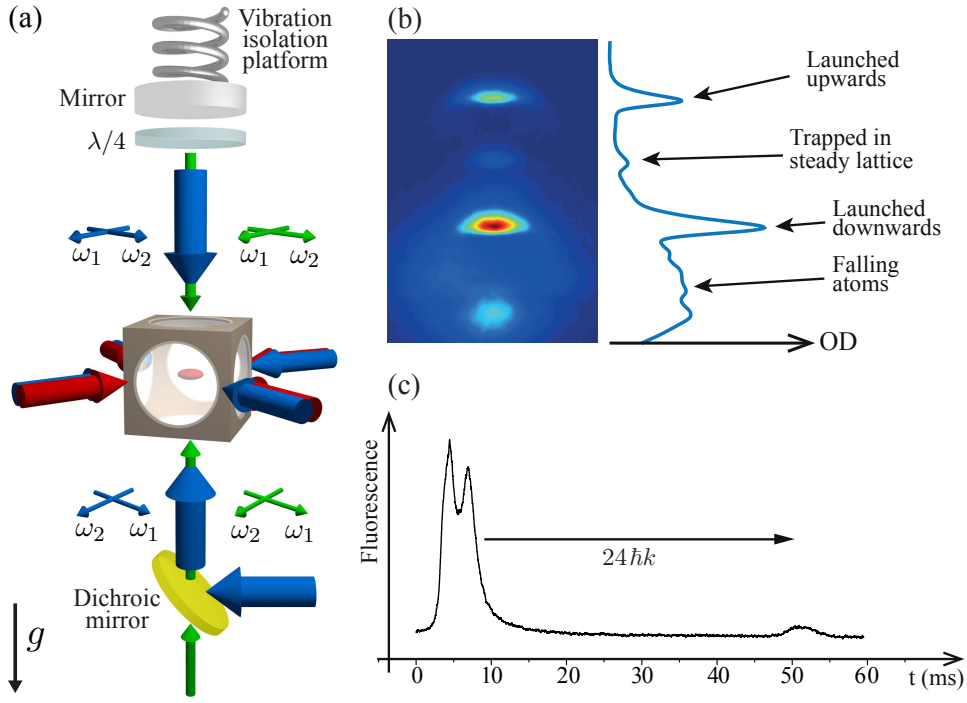

Figure 5.9: (a) Experimental configuration for combining the blue Bragg laser and the green lattice laser. The green beams are combined with the blue beams on a dichroic mirror. The polarizations are matched in order to be rotated by 90° by the same quarter-wave plate. (b) Absorption imaging of the launched clouds by two accelerated green lattices propagating in opposite directions. The lattice imparted $4\hbar k_L$. Atoms confined in a residual steady lattice and falling atoms not captured are also visible. (c) Fluorescence signal of a cloud launched by $24\hbar k_L$. The residual falling atoms and the downward accelerated cloud are also shown.

On the other hand, we can use the far-off resonance green lattice that we used for the Bloch oscillation experiment. The detuning from the ${}^1S_0$–${}^1P_1$ transition is $\delta \sim 2.7 \times 10^6 \gamma$. With our laser we can have a power of 600 mW per beam and a radius of 300 μm, so we have an intensity of 4×10^5 W/cm^2 that guarantees a lattice depth $U_0 = 7E_r$, the same lattice trapping conditions we discussed for the Bragg laser. Here the difference is the scattering rate, which is 10^4 times smaller and allows atoms to be trapped for more than 10 s (see sec. 4.2.4). Moreover, since the waist is comparable to the atomic radial dimension after the release from the red MOT, this lattice also guarantees a transversal confinement during the launch sequence.

The experimental configuration is sketched in fig. 5.9(a). The green laser optical

setup was modified in order to be compatible with the Bragg laser system. The green AOM outputs were combined with orthogonal polarizations in a PBS, and injected into a PM fiber. The fiber output is expanded in a telescope and then combined with the Bragg laser light on a dichroic mirror to be sent vertically and centered on the atoms. The polarization is rotated by the same broadband quarter-wave plate and the light is reflected by the suspended mirror. In this way, the formation of steady lattices is avoided, as described in sec. 5.1.2, unless the frequency difference between the two beams is intentionally tuned to zero. The interference only occurs for two stationary waves moving in opposite directions.

The launch sequence with the green lattice is realized as follows: the atoms are adiabatically loaded into the steady lattice from the red MOT in $\sim$ 100 μs. After 20 ms of evaporation the frequency difference between the two beams is swept at a rate $\dot{\Delta\omega} \sim 2\pi \times 50$ kHz/ms, which is small enough to maintain the adiabatic condition. The final frequency difference $\Delta\omega_{\mathrm{f}}$ obtained after a sweep Δt long, sets the number m of 2-photon recoils imparted to the atoms, according to the Bragg resonance condition $\Delta\omega_{\mathrm{f}} = 4m\omega_r$. For the green laser $\omega_r = 2\pi \times 8$ kHz. Figure 5.9(b) shows an absorption image of the launched atomic cloud after the frequency ramp. The lattice was swept for 2.5 ms up to a final frequency difference of $\Delta\omega_{\mathrm{f}} = 2\pi \times 128$ kHz, imparting $4\hbar k_L$ to the atoms in two opposite directions. Atoms confined in a residual steady lattice and falling atoms not captured are also visible. Figure 5.9(b) shows the fluorescence signal of a launch with $\Delta\omega_{\mathrm{f}} = 2\pi \times 768$ kHz that imparted $24\hbar k_L$ to the atoms. The residual falling atoms and the downwards accelerated cloud are also shown.

5.3.3 Interference fringes

The interference occurring at the recombining pulse produces complementary probability amplitudes in the two output channels, where the detection probability $P(\Delta\Phi)$ oscillates sinusoidally as a function of the total phase difference:

$$P(\Delta\Phi) = \frac{N_{|p_0\rangle}}{N_{|p_0\rangle} + N_{|p_0+2n\hbar k\rangle}} = P_0 + \frac{A}{2}\cos(\Delta\Phi), \tag{5.9}$$

where $N_{|p_0\rangle}$ and $N_{|p_0+2n\hbar k\rangle}$ are the number of atoms in the two outputs, $P_0 \sim 0.5$ is the offset probability and A is the amplitude of the fringe pattern.

The atomic interference phase $\Delta\Phi$, given by eq. (5.8), can be scanned by varying the phase of one the three Bragg pulses. Figure 5.10 shows the measured fringe patterns for first (black squares), second (red circles) and third (blue diamonds) order Bragg pulses and for an interferometer time $T = 0.5$ ms. The phase of the last $\pi/2$-pulse, ϕ_{III}, is scanned by a phase-modulated RF generator controlling one of the two AOMs' frequency, as described in sec. 5.1.3. The lines are sinusoidal

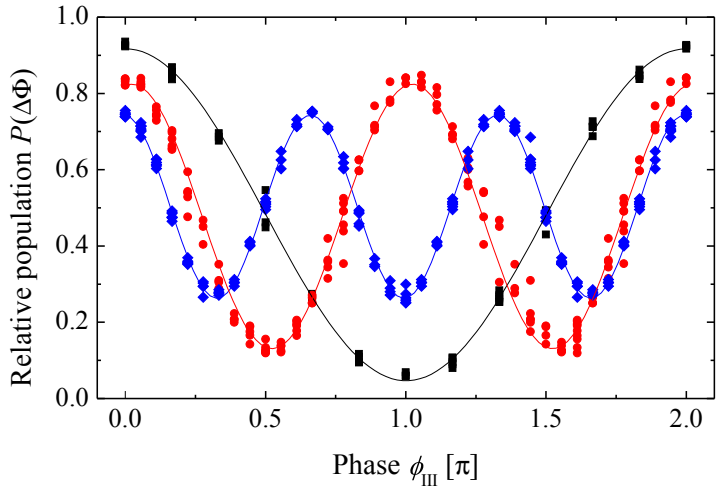

Figure 5.10: Interference fringes for first (black squares), second (red circles) and third (blue diamonds) order Bragg pulses for $T = 0.5$ ms. The interference phase $\Delta\Phi$ was scanned by varying the phase of the last Bragg pulse ϕ_{III}. The lines are sinusoidal fits of eq. (5.10).

least-squares fits of the form

$$P(\phi_{III}) = P_0 + \frac{V}{2}\cos(n\phi_{III}), \tag{5.10}$$

where P_0 and V are free parameters and n is the order of the Bragg transition. Here the amplitude is called V, that stands for *visibility*. The visibility of the interferometer is defined as the amplitude of the sinusoidal fit to the interference fringe, which has to be distinguished by the *contrast* C of the interferometer, defined as the peak-to-peak of the fringe amplitude. We determine the contrast from the measured values of $P(\Delta\Phi)$ between the 2nd and the 98th percentile (following the approach introduced in ref. [224]).

While the contrast depends only on coherence preservation during the interferometer, the visibility also takes into account the phase noise. As an example, in fig. 5.11 two interference fringes for first-order Bragg transitions and $T = 20$ ms with different phase noises are compared. While the contrast is similar for the red and blue fringes (75% against 70% respectively), the visibility of the red fringe is much smaller (45% against 64%) because of a larger phase noise.

Both the fringe contrast and the phase noise are limiting factors for the interferometer sensitivity, but they depend on different parameters. Therefore, we will study them independently.

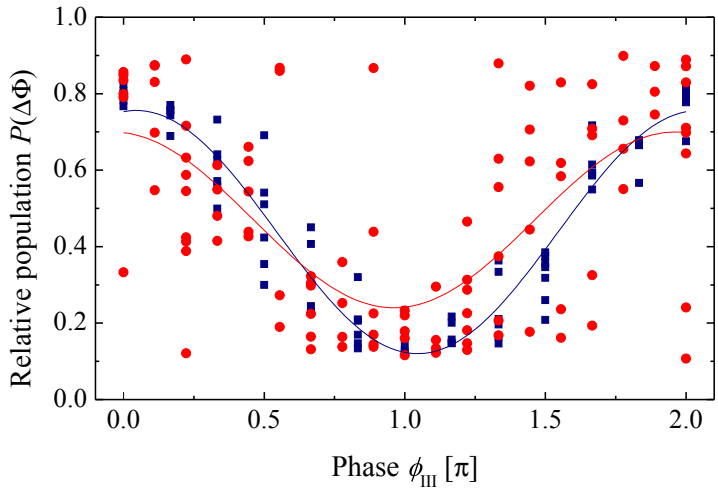

Figure 5.11: Interference fringes for first-order Bragg transitions and $T = 20$ ms with different configurations of the mirror suspension. While the contrast is similar for the red and blue fringes (75% against 70% respectively), the visibility (given by the amplitude of a sinusoidal least-squares fit) of the red fringe is much smaller (45% against 64%), indicating a higher phase noise.

5.3.4 Chirping the Bragg beams' frequency: absolute gravimetry

Since the atoms are falling during the interferometer sequence, they will see the Bragg beams' frequency shifted by the Doppler effect: $\mathbf{k}_{\text{eff}} \cdot \mathbf{v} = -2k_L g t$, if the Bragg beams are oriented along the gravity direction. To compensate for this and allow all the Bragg pulses to be on resonance along the whole ballistic trajectory, we chirp one of the Bragg beams at a rate $\alpha = k_{\text{eff}} g \simeq 2\pi \times 42.55$ kHz/ms. The chirp α induces an additional phase shift, therefore the interferometer phase $\Delta\Phi$ defined by eq. (5.8) has to be modified accordingly:

$$\Delta\Phi = n(2k_L g - \alpha)T^2 + n(\phi_{\text{I}} - 2\phi_{\text{II}} + \phi_{\text{III}}). \tag{5.11}$$

From this expression it is clear that another way to scan an interference fringe is obtained by varying the chirp α. The value of α that exactly compensates for the gravity-induced Doppler shift is determined by the relation:

$$\Delta\Phi_g = n(2k_L g - \alpha)T^2 = 0 \tag{5.12}$$

once the laser phases are set to be $\phi_j = \phi(t_j) = -\alpha t_j^2/2$, where t_j is the time of each pulse.

The interferometer transition probability $P(\Delta\Phi)$ oscillates sinusoidally as a function of α, but a central fringe can be identified: the one for which $\Delta\Phi_g = 0$.

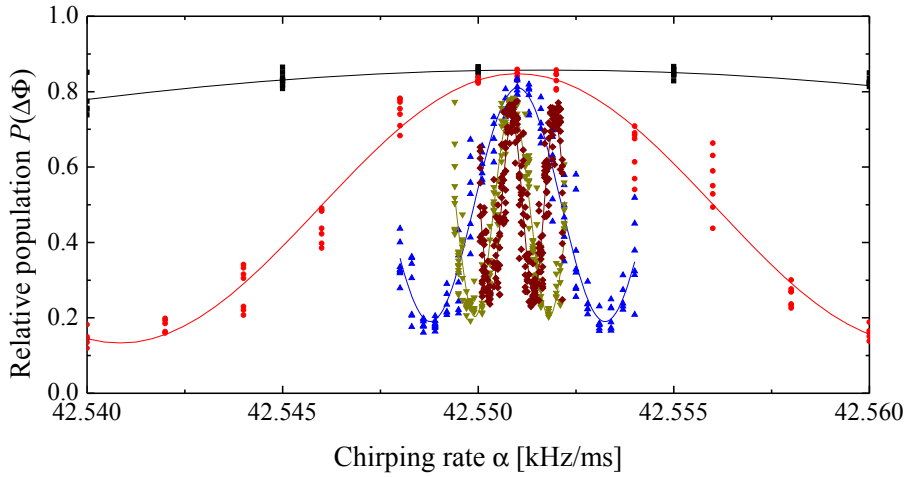

Figure 5.12: Central fringe measurements by varying the chirping rate α for first-order Bragg pulses and different interferometer times. $T = 3$ ms (black squares), 7 ms (red circles), 15 ms (blue up triangles), 23 ms (olive down triangles), 30 ms (maroon diamonds).

As expressed by eq. (5.12), this fringe does not depend on the interferometer time T, not on the Bragg order n. A measurement of the central fringe chirping gives an absolute measurement of the gravitational acceleration g. Figure 5.12 shows central fringe measurements obtained by varying the chirping rate α for first-order Bragg pulses and different interferometer times. The sensitivity to central fringe determination increases for longer interferometer times, according to eq. (5.12).

5.3.5 Gravity gradiometry

With a small change in the pulsed launch sequence, we can easily convert our system to a gravity gradiometer. Since the first pulse of the sequence velocity select about 1/10 of the atoms from the broad red MOT distribution, the residual falling cloud can be used as reservoir for a second interferometer.

To realize a gradiometer, we just add a second pulsed launch sequence before the beam splitter (see fig. 5.13). The two clouds cannot be accelerated to the same velocity, otherwise the last pulse of the second launch sequence would also interact with the upper cloud. Therefore, if we launch the first cloud with N π-pulses at order n, and we want to realize a gradiometer with n-order Bragg pulses, the second launch sequence has to be composed of $N-1$ pulses. In this way, the input velocities of the two interferometers will be separated by $2n\hbar k$, and the first $\pi/2$-pulse will act as a beam splitter for both arms, diffracting the upper arm downwards, and the lower arm upwards.

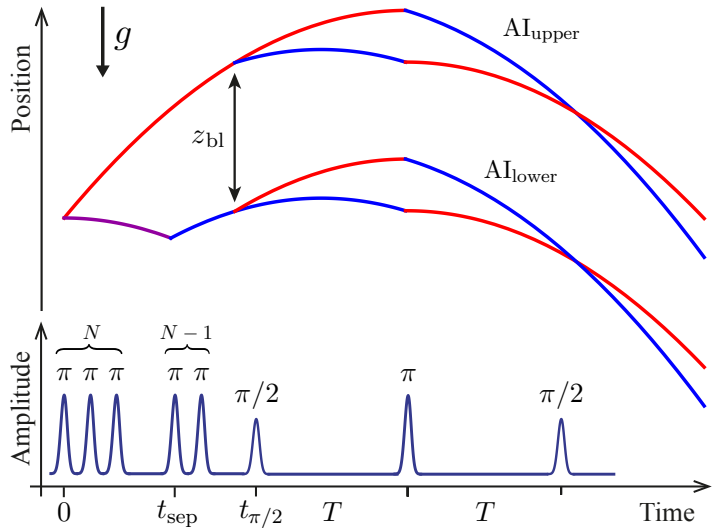

Figure 5.13: Atomic trajectories and pulse sequence for a gravity gradiometer. Two pulsed launch sequences separated by a time t_{sep} generate two traveling clouds separated spatially by z_{sep} at the beam splitter position. The two clouds are launched by one pulse difference, in order to avoid diffraction on the last pulse. The red paths correspond to $|2Nn\hbar k\rangle$, the blue to $|2n(N-1)\hbar k\rangle$.

The time separation t_{sep} between the pulsed launch sequences determine the baseline of the gradiometer, i.e. the spatial separation z_{bl} between the two interferometers at the beam splitter time. This can be easily calculated by the classical trajectories:

$$z_{bl} = \frac{2n\hbar k}{M} t_{\pi/2} + \left(t_{\pi/2} + \frac{1}{2}t_{sep}\right) g t_{sep}. \tag{5.13}$$

The gravity gradient is determined by the differential acceleration divided by the baseline.

A preliminary realization of a gravity gradiometer with this method is reported in fig. 5.14. Because the four outputs need to be detected simultaneously, particular care has to be taken for the pulse timing. Two clouds were launched from the red MOT with two launch sequences separated by 10 ms. The first cloud was launched with 8 pulses at first order, the second cloud with 7 pulses. The procedure creates two free-falling clouds spatially separated at the beam splitter position by $z_{bl} \simeq 0.5$ mm. The interferometer time was set to $T = 1$ ms. The output ports are detected 40 ms after the interferometer closure and the paths of the two interferometers cross, as shown in fig. 5.14(a). The population ratios between the output momentum states $|1\rangle = |p_0\rangle$ and $|2\rangle = |p_0 + 2\hbar k\rangle$ for the upper and lower interferometer are plotted in fig. 5.14(b). By scanning the phase of the third interferometer pulse ϕ_{III}, two

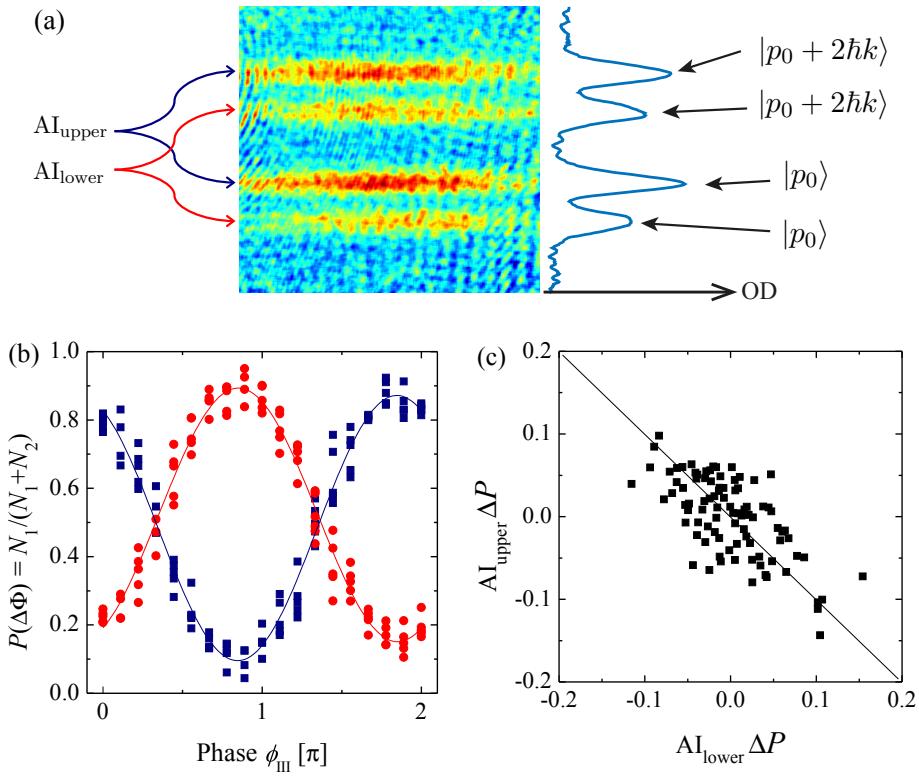

Figure 5.14: Gravity gradiometer results for two interferometers separated by a baseline of 0.5 mm. Parameters: first-order Bragg transitions and $T = 1$ ms. (a) Absorption image of the crossed outputs of the upper and lower AI. (b) Complementary interference fringes obtained by scanning the phase of the last $\pi/2$-pulse. The lines are least-squares fit to the data. (c) Residual noise of the fringes, plotted one versus the other. The correlation shows that the main phase noise is in common. Residual noise comes from the detection.

complementary fringes can be recorded.

The phase difference between the two gravimeters can be used to determine the local gravity gradient. In our case the sensitivity is limited by the small separation distance, and is not high enough to measure the Earth's gravity gradient. However, the differential-phase signal is insensitive to many noise sources such as the Bragg laser phase noise and the mirror vibrations, which are in common between the two interferometers. An evidence of this is given by the correlation between the noises on the two fringes shown in fig. 5.14(c). The residuals of the sinusoidal least-squares fits are plotted for the two fringes one versus the other. Residual uncorrelated noise is caused by detection noise.

The main limiting factor to our gravity gradiometer setup is the finite size of

the vacuum cell, which limits the maximum TOF. Because Bragg interferometers require a simultaneous detection of the output ports, avoiding spatial overlapping constrains our gradiometer parameters, and a high sensitivity configuration cannot be realized yet. A future improvement of the device will require a longer interferometer region, as in proper atomic fountains.

5.4 Current performance of the interferometer

5.4.1 Contrast

Figure 5.15 shows the values of the observed contrast for first, second and third Bragg order as a function of the interferometer time T. For different orders, the Bragg laser detuning δ was chosen in order to maintain a high Rabi frequency and a low rate of light scattering, according to the available laser power.

For short interferometer times, the contrast is mainly limited by the velocity spread along the vertical direction and by residual light scattering, which limits the π-pulse efficiency as already discussed in the Rabi oscillations analysis (see sec. 5.2.2). For long interferometer times, the contrast is mainly limited by the Rabi frequency inhomogeneity which is due to both the radial expansion of the atomic cloud and the intensity profile imperfections of the Bragg beams. The sensitivity to

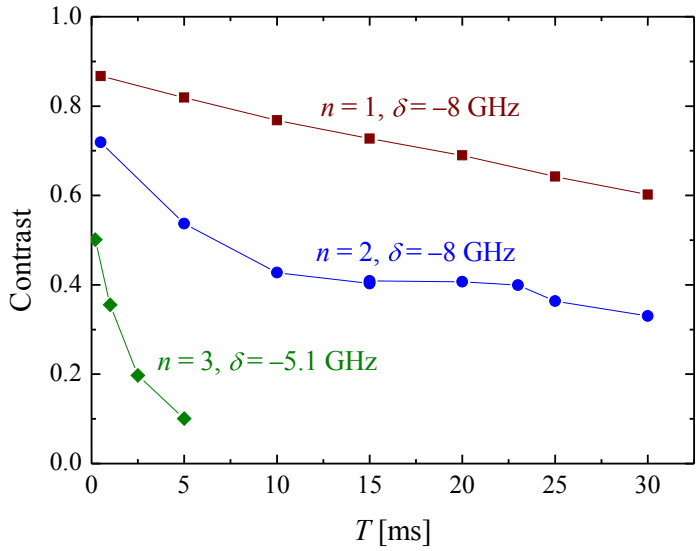

Figure 5.15: Contrast of the interference fringes as a function of time T for first (red squares), second (blue circles) and third (green diamonds) order Bragg diffraction. The detuning δ was adjusted for each order to maximize the π-pulse efficiency.

this inhomogeneity becomes more critical as the Bragg order n increases because the effective Rabi frequency scales as the nth power of the two-photon Rabi frequency (see eq. 5.7). This shows that the small sample size and the ultra-low temperatures achievable with strontium atoms can lead to a high contrast for long interferometer times even with relatively narrow Bragg beams.

Surprisingly, we observed a big difference in contrast for positive and negative detuning δ. For $T = 30$ ms, the interferometer contrast for first order Bragg diffraction is about 1.5 times larger by keeping the Bragg laser detuned to red frequencies with respect to blue. This effect is not explained by any heating mechanism, and further investigation will be required.

A technically feasible improvement by an order of magnitude in the Bragg laser power would allow us to move further from resonance ($\delta \sim 600\ \gamma$) maintaining a sufficiently high Rabi frequency and therefore realize a higher-order interferometer as demonstrated for Cs [68].

Further improvement in the contrast can be obtained by reducing the probe beam size in order to only detect the central atoms, for which the Rabi frequency inhomogeneities due to the transverse expansion are smaller. However, in doing this the effect on the sensitivity has to be taken into account. Reducing the interrogation area will reduce the number of interrogated atoms, leading to an increase of the shot noise limit and of detection noise. Therefore, there is a trade-off between contrast gain and noise suppression which has to be optimized in order to really improve the sensitivity of the gravimeter. Conversely, it is possible to explore geometries where the atoms are guided by a dipole trap along the falling axis [159]. In this scenario the atoms could be forced to remain in the region of maximum intensity of the Bragg beams, ensuring that they all contribute to the interferometer signal.

Another possible improvement resides on a further cooling of the atomic source. In this direction, a Bose-Einstein condensate would allow higher π-pulse efficiencies, thanks to its large coherence length [225]. Moreover, atomic sources at 50 nK temperature were already demonstrated with delta-kick cooling technique [226], opening interesting future perspectives.

5.4.2 Sensitivity

The sensitivity $\delta g/g$ of the interferometer as a gravimeter is determined by measuring the phase fluctuations $\delta\Phi$ at the slope of the central fringe:

$$\frac{\delta g}{g} = \frac{\delta\Phi}{2nkgT^2}. \tag{5.14}$$

The short and long-term sensitivities are characterized with the Allan deviation. The results for a first-order interferometer with a time $T = 30$ ms and the estimated effect of the main noise sources are shown in fig. 5.16. The Allan deviation scales

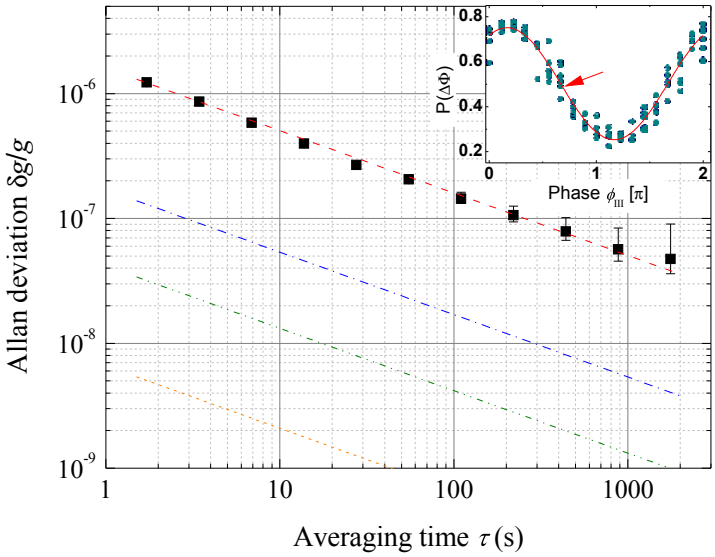

Figure 5.16: Allan deviation of the gravity acceleration measurements for a first-order interferometer with a time $T = 30$ ms (black squares). The inset shows the corresponding fringe and the point at which the phase fluctuations are measured. Also shown are the estimated effects due to the residual acceleration noise of the retro-reflection mirror (dash red line), the optical phase noise of the Bragg beams (dash dot blue line), the intensity noise of the Bragg beams (short-dash orange line) and the shot noise (1×10^5 atoms, dash dot dot green line).

as the inverse-root of the integration time with $\delta g/g = 1.5 \times 10^{-6}$ at 1 s, reaching 4×10^{-8} at 2000 s.

The sensitivity of our interferometer is presently limited by the residual acceleration of the suspended retro-reflection mirror. The estimated phase noise due to the mirror vibrations is 380 mrad/$\sqrt{\tau}$, where τ is the averaging time. The second major noise contribution comes from the optical phase noise of the Bragg beams which is estimated to be 20 mrad/$\sqrt{\tau}$, more than one order of magnitude smaller than the vibration noise. The calculated phase noise arising from intensity fluctuations of the Bragg laser is 1 mrad/$\sqrt{\tau}$, while other noise sources such as AC Stark shift effects and Bragg frequency noise are estimated to give contributions below the μrad/$\sqrt{\tau}$ level. Finally, the shot noise limit for 10^5 atoms is 10 mrad/$\sqrt{\tau}$.

In the following section we will show how these noise contributions are estimated.

5.5 Main noise sources in the Sr Bragg interferometer

Here we provide an evaluation of the main noise sources limiting the sensitivity of the Sr interferometer, using theoretical analysis as well as experimental measurements of the typical power spectral noise densities (PSD). Note that all the equations for the noise estimation are written for first order Bragg diffraction, $n = 1$. Also note that, while the estimated phase noise is proportional to n, the sensitivity of the interferometer ($\delta g/g$, as given by eq. (5.14)) does not depend on n. For the evaluations, we will consider the following typical interferometer parameter values: interferometer time $T = 30$ ms, cycle time $T_c = 1.7$ s and $\pi/2$-pulse duration $\tau_{BS} = 10$ μs. In order to maintain simplicity in the calculations we consider Bragg pulses with a square profile, although a Gaussian profile is used in the experiment. What is important for the evaluation of the noise contributions is actually the pulse area $\tau_{BS}\Omega_R$ and therefore, for $\tau_{BS} \ll T$, using different pulse shapes has a negligible effect on the result.

5.5.1 Bragg laser intensity noise

Intensity fluctuations of the Bragg beams cause fluctuations of the Rabi frequency, which affect the interferometer signal. To reduce the intensity noise coming from our laser source, we stabilized the optical amplitude by means of an AOM, as described in sec. 5.1.1. Figure 5.17 shows the PSD measurement of the Bragg laser intensity noise $S_I(f)$ with and without the active stabilization. The AOM feedback allows the relative intensity noise below 1 kHz to be reduced by almost five orders of magnitude. The low frequency peaks are a combination of a residual 50 Hz signal and harmonics of the residual amplitude modulation at 10 MHz for the PDH locking of the doubling cavity. The servo bump is visible at 30 kHz.

The estimation of phase shift induced on the interferometer by this noise follows the analysis done for Raman interferometers (see for example ref. [227]). The phase noise, written in terms of its Allan variance, is given by the following equation:

$$\sigma^2_{\Phi,I}(\tau) = \frac{T_c}{\tau}\int_0^{+\infty} S_I(f)|H_I(f)|^2 \mathrm{d}f, \tag{5.15}$$

where the transfer function $H_I(f)$, under the assumption that the intensity fluctuations for all the three pulses are uncorrelated, is given by

$$|H_I(f)|^2 = \frac{\sqrt{3}\pi}{C}\frac{\sin^4(2\pi fT)}{(2\pi fT)^2}, \tag{5.16}$$

where C is the contrast of the interferometer. For our selected values we estimate a $\sigma_{\Phi,I}(\tau) = 1\ \mathrm{mrad}/\sqrt{\tau}$.

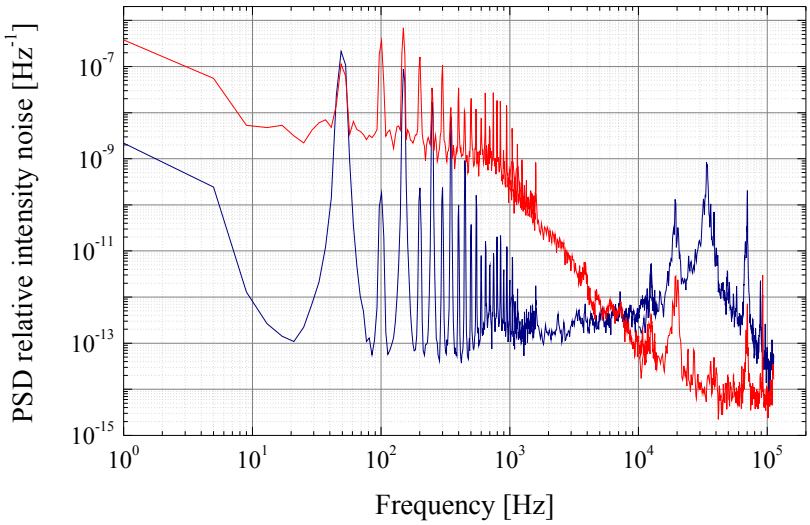

Figure 5.17: Power spectral density of the Bragg laser relative intensity noise, with (blue line) and without (red line) active stabilization.

Intensity fluctuations of the Bragg laser could, in principle, induce phase noise through the a.c. Stark shift effect. However, for Bragg diffraction this effect is reduced in comparison to Raman interactions, since atoms remain in the same internal state and only their momentum changes. A residual differential shift comes from the different detunings for the two momentum states through the Doppler shift effect. One should therefore still expect a small contribution to phase noise proportional to the intensity fluctuation

$$\Delta\phi_{ac} = \frac{4\Delta\omega}{\delta}\frac{\delta I}{I}, \tag{5.17}$$

where $\Delta\omega$ and δ are the Bragg resonance frequency and the Bragg laser detuning respectively, and δI the intensity fluctuation over the interferometer time. With our typical parameters, we estimate an induced phase noise of 4 μrad per shot, which is negligible compared to other noise sources.

5.5.2 Bragg laser frequency noise

The influence of fluctuations of the absolute Bragg laser wave vector has also been estimated. For this, the frequency stability of the 461 nm Bragg laser has been characterized through the beat note of the Bragg laser against the master cooling laser at 461 nm. The relative frequency instability at 1 s is 7×10^{-10}, indicating a

relative uncertainty of 7×10^{-10} on g, based on the relation:

$$\frac{\Delta g}{g} = \frac{\Delta k_{\text{eff}}}{k_{\text{eff}}} = \frac{\Delta \nu}{\nu}. \tag{5.18}$$

Therefore, the absolute frequency noise of the Bragg laser is not currently limiting the performance of the interferometer.

5.5.3 Bragg laser phase noise

Sensitivity function

The behavior of the interferometer phase, in presence of fluctuations in the phase difference ϕ between Bragg beams, is characterized by the sensitivity function $g(t)$. It was initially developed in the context of atomic clocks [228], and then it found application in pulsed atom interferometry for characterization of laser phase noise [229] and for vibration noise [230] contributions.

The sensitivity function is a unit-less quantity defined as the relative probability amplitude variation $\delta P(\Phi)$ due to the instantaneous phase jump $\delta\phi$ at time t in the Bragg pulse sequence:

$$g(t) = 2 \lim_{\delta\phi \to 0} \frac{\delta P(\delta\phi, t)}{\delta\phi}. \tag{5.19}$$

For a Mach-Zehnder pulse sequence τ_{BS}–T–$2\tau_{BS}$–T–τ_{BS}, $g(t)$ can be calculated in separated pieces. The transition probability for an ideal contrast $C = 1$ is $P(\Phi) = (1 - \cos\Phi)/2$, where $\Phi = \phi_I - 2\phi_{II} + \phi_{III}$ is the total phase of the interferometer due to the Bragg pulses. For phase jumps occurring between the first and the second pulse, the phases can be written as: $\phi_I = \phi$, $\phi_{II} = \phi + \delta\phi$ and $\phi_{III} = \phi + \delta\phi + \pi/2$, so the transition probability becomes $P(\delta\Phi) = (1 - \cos(\pi/2 - \delta\phi))/2$. For small $\delta\phi$, $\delta P = \partial P/\partial(\delta\phi)\delta\phi$, and if we apply the definition in eq. (5.19) we get $g(t) = -1$. In the same way, we find $g(t) = +1$ for phase jumps occurring between the second and the third pulse. To calculate $g(t)$ for phase jumps occurring during a pulse, one has to take into account the time-dependent state amplitudes of the atomic wave function. It can be seen that these terms depend on the Rabi frequency Ω_R of the driving Bragg transition. We find the total sensitivity function to be (see fig. 5.18):

$$g(t) = \begin{cases} 0 & \text{for } -T_c/2 < t < -T \\ \sin[\Omega_R(t+T)] & \text{for } -T < t < -T + \tau_{BS} \\ 1 & \text{for } -T + \tau_{BS} < t < -\tau_{BS} \\ -\sin[\Omega_R t] & \text{for } -\tau_{BS} < t < \tau_{BS} \\ -1 & \text{for } \tau_{BS} < t < T - \tau_{BS} \\ \sin[\Omega_R(t-T)] & \text{for } T - \tau_{BS} < t < T \\ 0 & \text{for } T < t < T_c/2. \end{cases} \tag{5.20}$$

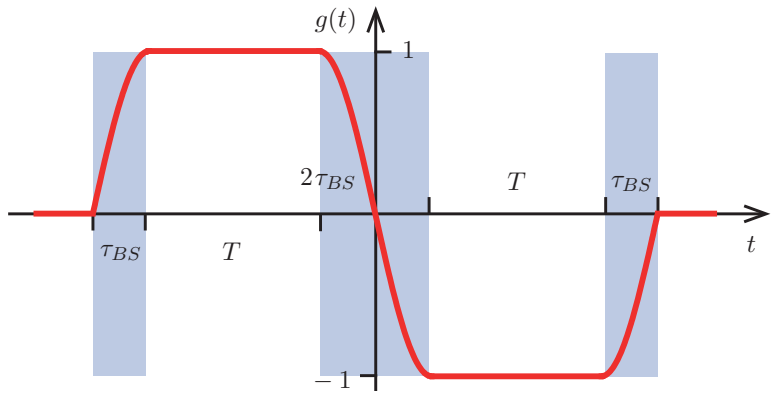

Figure 5.18: Sensitivity function $g(t)$ for a Mach-Zehnder pulse interferometer.

We defined $g(t)$ between $-T_c$ and T_c since the interferometer sequence will be repeated with a frequency $1/T_c$.

Transfer function

To understand the link between the time-dependent phase fluctuation $\delta\phi$ and the interferometer phase $\delta\Phi$, let's integrate eq. (5.19) at mid-fringe, where $\delta P \sim \delta\Phi/2$:

$$\delta\Phi = \int g(t)\mathrm{d}t = \int g(t)\frac{\mathrm{d}\phi}{\mathrm{d}t}\mathrm{d}t. \tag{5.21}$$

For a phase modulated at frequency ω_ϕ and amplitude A_ϕ, from eq. (5.21) we find $\delta\Phi = A_\phi\omega_\phi \,\mathrm{Im}[G(\omega_\phi)]$, where $G(\omega)$ is the Fourier transform of the sensitivity function. If we consider a wide distribution of frequencies over which the phase jumps can occur, we can define the transfer function in the frequency domain (also called weighting function):

$$H(\omega) = \omega G(\omega) \quad \Leftrightarrow \quad H_\phi(f) = 2\pi f \int_{-\infty}^{+\infty} \mathrm{e}^{i2\pi f t} g(t)\mathrm{d}t. \tag{5.22}$$

The transfer function $|H_\phi(2\pi f)|^2$ for our typical interferometer parameters is shown in fig. 5.19(a). We can distinguish two features. Firstly, an oscillation at frequency $1/(T + 2\tau_{BS})$ leads to zeros at harmonics of this frequency. Secondly, there is a low-pass filter due to the finite duration of the Bragg pulses, with an effective cut-off frequency $f_0 = (\Omega_R/2\pi)/\sqrt{3}$, about 15 kHz in our case.

Phase noise measurements

The PSD measurements of the phase noise $S_\phi(f)$ on the Bragg beams is presented in fig. 5.19(a). This has been characterized through the use of a digital PFD by

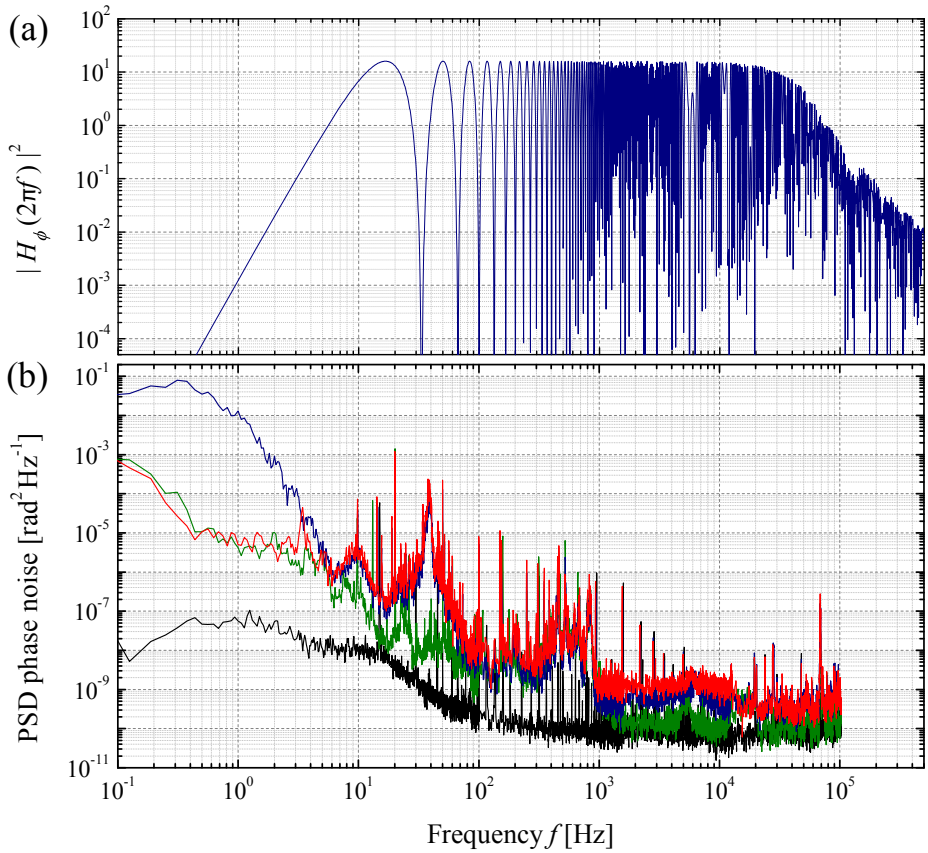

Figure 5.19: (a) Calculated transfer function for the Bragg phase noise for our typical interferometer parameters. (b) Phase noise PSD $S_\phi(f)$ for different experimental conditions: optical interferometer covered by box (red line), not covered (blue line), optical table floating (green line), RF phase noise before AOMs (black line).

comparing the beat note of the two Bragg frequency components, ω_1 and ω_2, to a reference RF synthesizer. The beat note is detected on a photodiode placed after the polarization maintaining fiber (just before the atomic sample). In the plot we also compare the spectra taken in different conditions. As described in sec. 5.1.1, we built a plastic box to cover the optical Bragg laser setup. This reduced the noise at low frequency (blue curve is without box). Floating the optical table reduced the noise around 40 Hz (green line). Unfortunately, the Bragg laser is placed on the same table as the vacuum system, therefore we need to unsuspend the table to avoid tilt drifting (red curve). For comparison we also show the RF phase noise recorded just before the AOMs (black curve). This is responsible for the base noise above 1 kHz and for the lines between 100 Hz and 1 kHz. In this region the optical noise

is larger, mainly due to vibration resonances in the optical mounts.

The rms standard deviation of the interferometer phase noise due to a Bragg laser phase noise with PSD $S_\phi(f)$ can be written as

$$\sigma^2_{\Phi,\phi} = (2\pi f)^2 \int_0^{+\infty} |H(f)|^2 S_\phi(f) \mathrm{d}f. \tag{5.23}$$

Our interferometer phase measurement consists of many measurements with a repetition rate $1/T_c$, in order to average out noise. This pulsed operation introduces an aliasing effect, widely studied in atomic clocks [231, 232], called the *Dick effect*. The one sample variance of eq. (5.23) has to be corrected as follows:

$$\sigma^2_{\Phi,\phi}(\tau) = \frac{T_c^2}{\tau^2} \int_0^{+\infty} \frac{4\sin^4(\pi f \tau)}{\sin^2(\pi f T_c)} |H_\phi(f)|^2 S_\phi(f) \mathrm{d}f. \tag{5.24}$$

Under our typical conditions we estimate $\sigma_{\Phi,\phi}(\tau) = 20\ \mathrm{mrad}/\sqrt{\tau}$, which is still one order of magnitude lower with respect to the vibration noise of the retro-reflection mirror.

5.5.4 Vibration noise

Transfer function

Another important contribution to the interferometer noise is the vibration noise, which is directly coupled to the upper retro-reflecting mirror for the Bragg beams. The degradation to the Sr interferometer sensitivity due to vibrations coupled to the retro-reflecting Bragg mirror can be easily derived from eq. (5.23), by replacing the $S_\phi(\omega)$ by $k^2_{\mathrm{eff}} S_z(\omega) = k^2_{\mathrm{eff}} S_a(\omega)/\omega^4$, where $S_z(\omega)$ and $S_a(\omega)$ are the PSD of position and acceleration noise respectively. The transfer function (shown in fig. 5.20a) acts as a second-order low pass filter, with a frequency cut-off $1/T$, which drastically suppresses the high frequency noise contribution. For large averaging time τ and a repetition rate $f_c = 1/T_c$, the sensitivity to vibration noise can be expressed by:

$$\sigma^2_{\Phi,a}(\tau) = \frac{k^2_{\mathrm{eff}}}{\tau} \sum_{n=1}^{\infty} \frac{|H(2\pi n f_c)|^2}{(2\pi n f_c)^4} S_a(2\pi n f_c). \tag{5.25}$$

Here $k_{\mathrm{eff}} = 2k_L = 4\pi/\lambda_L$ is the effective wave vector of the first-order Bragg diffraction with $\lambda_L = 461$ nm.

Vibration noise measurements

The amplitude spectral density of acceleration noise $S_a(f)$, measured on top of the supporting MinusK platform by a triaxial accelerometer (Episensor ES-T), is shown

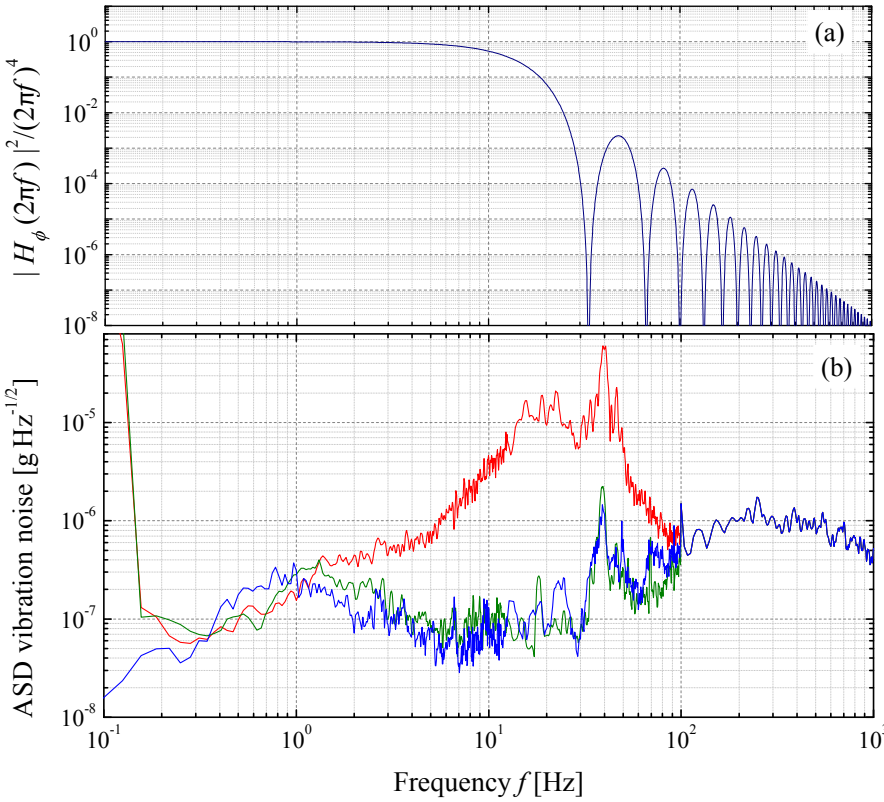

Figure 5.20: (a) Calculated transfer function for the vibration noise for our typical interferometer parameters. (b) Amplitude spectral density $S_a(f)$ measured on top of the suspension platform for different experimental conditions: platform not suspended (red line), suspended (green line), enclosed in acoustic isolation box (blue line).

in fig. 5.20(b). Here we report the spectra for the vertical acceleration only, which gives the main contribution to the interferometer noise once the Bragg beam is set vertically and the retro-reflection mirror is properly aligned. For comparison we show spectra for different experimental conditions. The red line represents the noise measured with the unsuspended platform, our ground noise. When the platform is properly tuned the typical spectrum is represented by the green line. We further improved the low frequency noise attenuation by enclosing the whole the platform in a 2 mm thick plastic box covered by a layer of foam (blue line). The noise above 100 Hz is dominated by the internal electrical noise of the accelerometer and it is not used for the transfer function calculation.

For our typical vibration noise, we estimated an Allan deviation of $\sigma_{\Phi,a}(\tau) = 380\ \text{mrad}/\sqrt{\tau}$. This contribution sets the actual limit on our interferometer sensitivity.

5.5.5 Preliminary attempts of vibration compensation

A possible solution to overcome the residual vibrational noise limitation is based on a feedback correction to the interferometer phase by using the a.c. acceleration signal measured by a low noise seismometer [230, 233].

The sensitivity function $g(t)$ expressed by eq. (5.20) can also be used to extrapolate information on the retro-reflecting mirror vibrations. By considering a mirror displacement $\mathbf{r}(t)$, the induced vibration phase noise is $\phi(t) = \mathbf{k}_{\text{eff}} \cdot \mathbf{r}(t)$. The interferometer phase shift due to the mirror motion can be calculated by applying eq. (5.21):

$$\delta\Phi_v = \int_{-\infty}^{+\infty} g(t)\mathbf{k}_{\text{eff}} \cdot \mathbf{v}(t)\mathrm{d}t, \tag{5.26}$$

where $\mathbf{v}(t) = \dot{\mathbf{r}}(t)$ is the velocity of the mirror. Using the chain rule, the previous equation can be written in terms of the mirror acceleration $\mathbf{a}(t) = \dot{\mathbf{v}}(t)$:

$$\delta\Phi_a = -\mathbf{k}_{\text{eff}} \cdot \left[f(t)\mathbf{v}(t)\mathrm{d}t\right]_{-\infty}^{+\infty} + \mathbf{k}_{\text{eff}} \cdot \int_{-\infty}^{+\infty} f(t)\mathbf{a}(t)\mathrm{d}t, \tag{5.27}$$

where $f(t)$ is the response function to acceleration noise of the mirror, and it is defined as the integral of the sensitivity function:

$$f(t) = -\int_0^t g(t')\mathrm{d}t'. \tag{5.28}$$

Figure 5.21 shows the response function corresponding to the integral of the $g(t)$ in fig. 5.18 for a Mach-Zehnder pulse interferometer. Since the $f(t)$ is zero outside

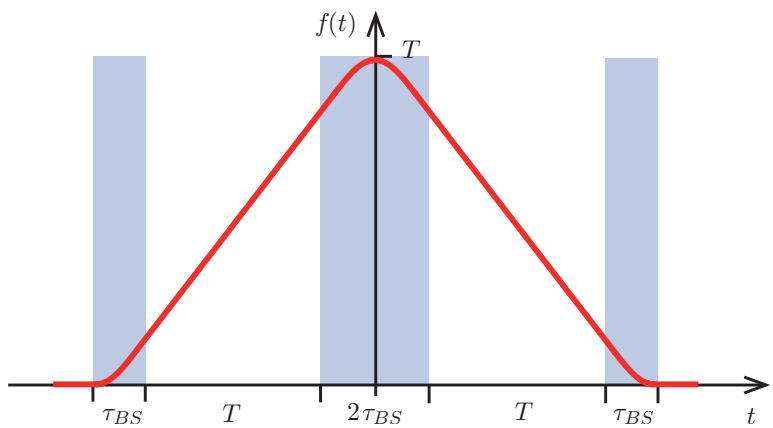

Figure 5.21: Response function $f(t)$ to acceleration of the retro-reflection mirror.

of the interferometer interval time, the first term in eq. (5.27) vanishes and the resulting interferometer phase due to acceleration of the mirror is:

$$\delta\Phi_a = +\mathbf{k}_{\text{eff}} \cdot \int_{-\infty}^{+\infty} f(t)\mathbf{a}(t)\mathrm{d}t. \tag{5.29}$$

The $f(t)$ represents a weighting function for the acceleration noise of the mirror, and the eq. (5.29) can be used to correct the atomic phase once the acceleration $\mathbf{a}(t)$ is precisely measured.

The accelerometer signal is acquired during the interferometer cycle by a digital card (NI PCI-4472B) with 24 bit resolution and 100 kHz sampling rate. As a preliminary attempt to characterize the correlation between acceleration noise and interferometer phase noise, we induced a strong acceleration modulation with a loud speaker placed on top of the isolation platform. Figure 5.22 displays the phase correction results for a 5 ms interferometer with an induced acceleration noise at 100 Hz. A typical noise acquisition is shown in fig. 5.22(a). The time origin was set to the first pulse time with an optimized delay of 2 ms. Figure 5.22(b) shows a set of 220 interferometer measurements. The noise destroys the fringe visibility, while the contrast is preserved, demonstrated by a histogram of the measured probabilities, which behaves as $\cos^{-1}(\Phi)$. Figure 5.22(c) shows the measured transition probability as a function of the phase shift calculated from the accelerometer output signal. The good correlation between the acceleration signal and the interferometer phase allows reconstruction of the fringe.

An efficient rejection requires that the accelerometer measures the vibrations of the retro-reflecting mirror as accurately as possible. This was not probably the case for us, since in a low noise environment the noise detected by the accelerometer was not correlated enough to the interferometer phase noise to produce a significant improvement of the gravimeter sensitivity. This was probably due to two reasons. Firstly, the mirror was not solidly mounted on the accelerometer but, rather was suspended from a side of the isolation platform, while the accelerometer was placed at the center of the platform itself. This could result in a significant difference in the acceleration measured by the instrument and the real one present on the mirror, which could also be due to unwanted correlations between the accelerations on different axes. This configuration was unavoidable for the present setup, which required the placement of the isolation platform on top of the experiment, and by the dimensions of the accelerometer, which did not allow it to be placed it on top of the mirror without unbalancing the isolation platform. Secondly, our accelerometer presents a huge electrical noise floor above 100 kHz, which can be mistaken for acceleration noise in the evaluation of the correction.

An improvement of this technique will require a better positioning of the accelerometer with respect to the mirror and the reduction of the noise floor of the instrument. The best configuration would be placing the isolation platform on the

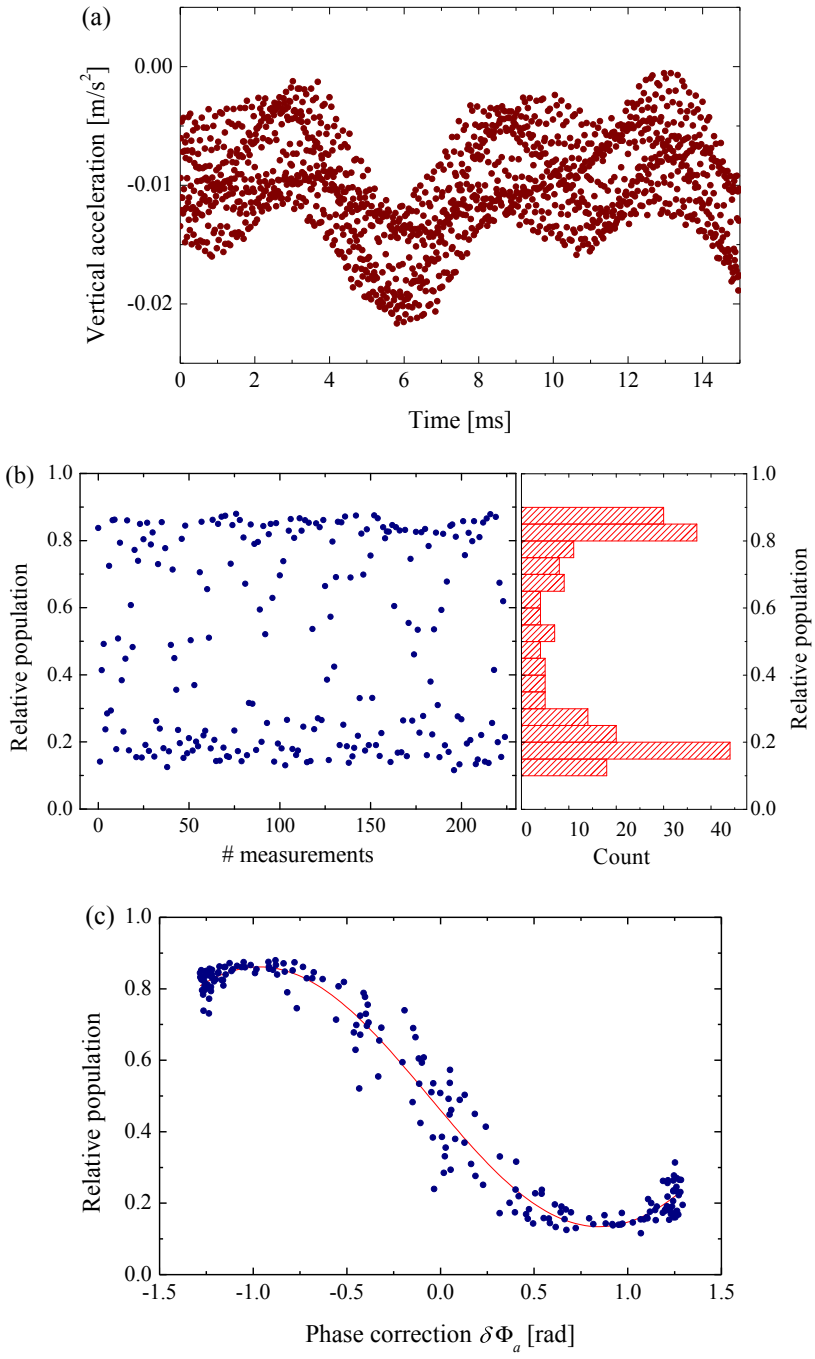

Figure 5.22: Phase correction for a 5 ms interferometer with induced acceleration noise at 100 Hz. (a) Typical accelerometer acquisition during the interferometer cycle. (b) Transition probability measurements. (c) Same data as in (b) plotted as a function of the acceleration-induced phase $\delta\Phi_a$.

ground with the accelerometer at the center and the mirror on top of it. This would require a drastic modification of the current setup since the vacuum chamber is placed on an optical table and not enough room is available in between.

Chapter 6

Conclusions and perspectives

The aim of this thesis was the demonstration of high precision gravimetry based on atom interferometry of ultra-cold strontium isotopes and the realization of fundamental tests of general relativity. In particular, during the first year I completed an experiment started in 2012. The work was successfully published in Physical Review Letters in July 2014. The aim of the experiment was testing the Einstein Equivalence Principle in its weak formulation and the spin-gravity coupling. In the second part of my Ph.D. fellowship I started a new experiment which demonstrated the potentiality of a new generation of interferometers based on strontium atoms, for future gravitational tests. The results were published in Physical Review A.

We performed a quantum test of Einstein Equivalence Principle for the bosonic ^{88}Sr isotope which has no spin versus the fermionic ^{87}Sr isotope which has a half-integer spin by coherent control of the atomic motion in an optical lattice under the effect of gravity. Gravity acceleration was measured by means of a genuine quantum effect, namely, the coherent delocalization of matter waves in an optical lattice. To compare gravity acceleration for the two Sr isotopes, we confined atomic wave packets in a vertical off-resonant laser standing wave and induced a dynamical delocalization by amplitude modulation of the lattice potential at a frequency corresponding to a multiple of the Bloch frequency ω_B, which is directly related to the gravity acceleration g. The Bloch frequency corresponds to the site-to-site energy difference induced by the gravitational force, and according to the Equivalence Principle, the frequency difference $\delta_{87,88} = \omega_{B,87} - \omega_{B,87}$ for the two isotopes must depend only on the atomic mass ratio.

In our work, we also demonstrated a new method to improve the precision of the measurement of ω_B and consequently of gravity acceleration by locking the AM oscillator frequency to the Bloch frequency. With this technique we were able to reach a sensitivity at 1 s of $\sigma_{\nu_{B,88}} = 1.5 \times 10^{-6} \nu_{B,88}$ and $\sigma_{\nu_{B,87}} = 9.8 \times 10^{-6} \nu_{B,87}$.

This new method allowed us to improve the sensitivity in the determination of the frequency of Bloch oscillations (and of gravity acceleration) by more than one order of magnitude for ^{88}Sr with respect to our previous results, achieving a precision of 5×10^{-8} for a single acquisition of about 700 s, while for ^{87}Sr we obtained a precision of 4×10^{-7}.

Each pair of Bloch frequency measurements was used to determine the Eötvös ratio η, defined as the relative differential acceleration between two test masses. The Eötvös ratio η accounts for violations of the Equivalence Principle due to a nonzero difference between gravitational and inertial mass. In the case of our experiment, η depends only on the Bloch frequencies of the two isotopes and their mass ratio. After 68 measurements of η and the evaluation of the systematic effects we were able to obtain the final result $\eta = (0.2 \pm 1.6) \times 10^{-7}$. By measuring the Bloch frequency separation of the 10 spin components of ^{87}Sr we were also able to set a limit on the spin-gravity coupling violation. We measured the coupling strength to be $k = (0.5 \pm 1.1) \times 10^{-7}$.

The present results can set bounds for previously unmeasured parameters of the standard model extension [203], can be interpreted in terms of the violation parameters for the fundamental constituents of the two atoms [218], and it sets a 10^{-7} direct bound on the boson-to-fermion gravitational constant ratio from being different from 1 [58]. Further enhancements in sensitivity with this experimental method will require simultaneous probing of the two isotopes [234] and spin-polarization of ^{87}Sr. Short-distance measurements ($r \leq 1$ cm) with $10^{-8}\omega_B$ precision can lower the limit of monopole-dipole interaction constants $g_p g_s$ by 9 orders of magnitude [56].

The second part of my work was focused on the development of a new interferometric scheme with strontium atoms based on Bragg pulses, with the aim of increasing the sensitivity of gravity measurements and the demonstration of interferometry with atomic species other than alkali-metal atoms, which are most commonly used. We demonstrated the first atom interferometer based on large-momentum-transfer Bragg diffraction in a fountain of strontium atoms, and its use for the measurement of gravity acceleration. In particular, the ^{88}Sr isotope that we used in this work has specific favorable characteristics: it is insensitive to external magnetic field because of its total null spin in the ground state and its small scattering length results in reduced decoherence due to cold collisions. These unique properties makes this atom of superior interest for the highest precision gravimetric devices.

We have studied Bragg diffraction by a 461 nm laser standing wave up to eight photon recoils and we realized a vertical Mach-Zehnder interferometer of up to 60 ms of free fall time. We studied the contrast degradation and we demonstrated its performance as a gravimeter with a sensitivity $\delta g/g = 4 \times 10^{-8}$. The results are mainly limited by technical aspects such as the available laser power, the size of

the vacuum cell and residual vibrations; therefore we anticipate a dramatic increase in performance with the increasing power of available lasers, a larger chamber to increase the interferometer time and improved isolation from vibrational noise. A variation on our scheme is the possibility to induce the Bragg transitions using the narrow intercombination line at 689 nm where stable lasers with a higher output power are already available. Moreover, schemes based on the combination of Bragg diffraction and Bloch oscillations [161, 221, 235] might allow superior performances in terms of precision and accuracy thanks to the specific properties of strontium. Other relevant prospects are the use of ultra-cold Sr sources [236] and high sensitivity detection schemes beyond the classical limit [237].

Bibliography

[1] G. M. Tino and M. A. Kasevich, eds., *Atom interferometry*, Proceedings of the International School of Physics “Enrico Fermi", Course CLXXXVIII, Varenna 2013 (Società Italiana di Fisica and IOS Press, Amsterdam, 2014).

[2] A. D. Cronin, J. Schmiedmayer, and D. E. Pritchard, “Optics and interferometry with atoms and molecules”, Rev. Mod. Phys. **81**, 1051 (2009).

[3] A. Peters, K. Y. Chung, and S. Chu, “Measurement of gravitational acceleration by dropping atoms”, Nature **400**, 849 (1999).

[4] Z.-K. Hu, B.-L. Sun, X.-C. Duan, M.-K. Zhou, L.-L. Chen, S. Zhan, Q.-Z. Zhang, and J. Luo, “Demonstration of an ultrahigh-sensitivity atom-interferometry absolute gravimeter”, Phys. Rev. A **88**, 043610 (2013).

[5] P. Gillot, O. Francis, A. Landragin, F. Pereira Dos Santos, and S. Merlet, “Stability comparison of two absolute gravimeters: optical versus atomic interferometers”, Metrologia **51**, L15 (2014).

[6] J. M. McGuirk, G. T. Foster, J. B. Fixler, M. J. Snadden, and M. A. Kasevich, “Sensitive absolute-gravity gradiometry using atom interferometry”, Phys. Rev. A **65**, 033608 (2002).

[7] F. Sorrentino, Q. Bodart, L. Cacciapuoti, Y.-H. Lien, M. Prevedelli, G. Rosi, L. Salvi, and G. M. Tino, “Sensitivity limits of a Raman atom interferometer as a gravity gradiometer”, Phys. Rev. A **89**, 023607 (2014).

[8] G. Rosi, L. Cacciapuoti, F. Sorrentino, M. Menchetti, M. Prevedelli, and G. M. Tino, “Measurement of the gravity-field curvature by atom interferometry”, Phys. Rev. Lett. **114**, 013001 (2015).

[9] F. Riehle, T. Kisters, A. Witte, J. Helmcke, and C. J. Bordé, “Optical Ramsey spectroscopy in a rotating frame: Sagnac effect in a matter-wave interferometer”, Phys. Rev. Lett. **67**, 177 (1991).

[10] T. L. Gustavson, P. Bouyer, and M. A. Kasevich, "Precision rotation measurements with an atom interferometer gyroscope", Phys. Rev. Lett. **78**, 2046 (1997).

[11] M. A. Kasevich and B. Dubetsky, "Kinematic sensors employing atom interferometer phases", US Patent 7317184 (2008).

[12] D. S. Weiss, B. C. Young, and S. Chu, "Precision measurement of the photon recoil of an atom using atomic interferometry", Phys. Rev. Lett. **70**, 2706 (1993).

[13] A. Wicht, J. M. Hensley, E. Sarajlic, and S. Chu, "A preliminary measurement of the fine structure constant based on atom interferometry", Phys. Scripta **2002**, 82 (2002).

[14] R. Bouchendira, P. Cladé, S. Guellati-Khélifa, F. Nez, and F. Biraben, "State of the art in the determination of the fine structure constant: test of quantum electrodynamics and determination of h/m_u", Ann. Phys. **525**, 484 (2013).

[15] G. Rosi, F. Sorrentino, L. Cacciapuoti, M. Prevedelli, and G. M. Tino, "Precision measurement of the Newtonian gravitational constant using cold atoms", Nature **510**, 518 (2014).

[16] M. Prevedelli, L. Cacciapuoti, G. Rosi, F. Sorrentino, and G. M. Tino, "Measuring the Newtonian constant of gravitation G with an atomic interferometer", Philos. T. Roy. Soc. A **372**, 20140030 (2014).

[17] J. B. Fixler, G. T. Foster, J. M. McGuirk, and M. A. Kasevich, "Atom interferometer measurement of the Newtonian constant of gravity", Science **315**, 74 (2007).

[18] C. W. Misner, K. S. Thorne, and J. A. Wheeler, *Gravitation* (Freeman, San Francisco, 1973).

[19] L. Randall, "Extra dimensions and warped geometries", Science **296**, 1422 (2002).

[20] R. Mathevet, R. Delhuille, and C. Rizzo, "Computation of the phase induced by non-Newtonian gravitational potentials in atom interferometry", Classical Quant. Grav. **19**, L37 (2002).

[21] S. Dimopoulos, P. W. Graham, J. M. Hogan, and M. A. Kasevich, "Testing general relativity with atom interferometry", Phys. Rev. Lett. **98**, 111102 (2007).

[22] S. Dimopoulos and A. A. Geraci, "Probing submicron forces by interferometry of Bose-Einstein condensed atoms", Phys. Rev. D **68**, 124021 (2003).

[23] D. M. Harber, J. M. Obrecht, J. M. McGuirk, and E. A. Cornell, "Measurement of the Casimir-Polder force through center-of-mass oscillations of a Bose-Einstein condensate", Phys. Rev. A **72**, 033610 (2005).

[24] G. Ferrari, N. Poli, F. Sorrentino, and G. M. Tino, "Long-lived Bloch oscillations with bosonic Sr atoms and application to gravity measurement at the micrometer scale", Phys. Rev. Lett. **97**, 060402 (2006).

[25] C. Jentsch, T. Müller, E. M. Rasel, and W. Ertmer, "HYPER: A satellite mission in fundamental physics based on high precision atom interferometry", Gen. Rel. Grav. **36**, 2197 (2004).

[26] G. M. Tino, F. Vetrano, and C. Lämmerzahl, "Editorial on the GRG special issue on "Gravitational waves detection with atom interferometry"", Gen. Rel. Grav. **43**, 1901 (2011).

[27] J. M. Hogan, D. M. S. Johnson, S. Dickerson, T. Kovachy, A. Sugarbaker, S.-w. Chiow, P. W. Graham, M. A. Kasevich, B. Saif, S. Rajendran, et al., "An atomic gravitational wave interferometric sensor in low earth orbit (AGIS-LEO)", Gen. Rel. Grav. **43**, 1953 (2011).

[28] R. Y. Chiao and A. D. Speliotopoulos, "Towards MIGO, the matter-wave interferometric gravitational-wave observatory, and the intersection of quantum mechanics with general relativity", J. Mod. Optics **51**, 861 (2004).

[29] B. Canuel, L. Amand, A. Bertoldi, W. Chaibi, R. Geiger, J. Gillot, A. Landragin, M. Merzougui, I. Riou, S. P. Schmid, et al., "The matter-wave laser interferometer gravitation antenna (MIGA): New perspectives for fundamental physics and geosciences", in E3S Web of Conferences, Vol. 4 (EDP Sciences, 2014), p. 01004.

[30] D. Colladay and V. A. Kostelecký, "CPT violation and the standard model", Phys. Rev. D **55**, 6760 (1997).

[31] T. Damour, F. Piazza, and G. Veneziano, "Runaway dilaton and equivalence principle violations", Phys. Rev. Lett. **89**, 081601 (2002).

[32] S. Capozziello and M. De Laurentis, "Extended theories of gravity", Phys. Rep. **509**, 167 (2011).

[33] C. M. Will, "The confrontation between general relativity and experiment", Living Rev. Relativity **9** (2006).

[34] J. G. Williams, S. G. Turyshev, and D. H. Boggs, "Lunar laser ranging tests of the equivalence principle", Classical Quant. Grav. **29**, 184004 (2012).

[35] S. Schlamminger, K.-Y. Choi, T. A. Wagner, J. H. Gundlach, and E. G. Adelberger, "Test of the equivalence principle using a rotating torsion balance", Phys. Rev. Lett. **100**, 041101 (2008).

[36] S. Fray, C. A. Diez, T. W. Hänsch, and M. Weitz, "Atomic interferometer with amplitude gratings of light and its applications to atom based tests of the equivalence principle", Phys. Rev. Lett. **93**, 240404 (2004).

[37] A. Bonnin, N. Zahzam, Y. Bidel, and A. Bresson, "Simultaneous dual-species matter-wave accelerometer", Phys. Rev. A **88**, 043615 (2013).

[38] D. Schlippert, J. Hartwig, H. Albers, L. L. Richardson, C. Schubert, A. Roura, W. P. Schleich, W. Ertmer, and E. M.-. Rasel, "Quantum test of the universality of free fall", Phys. Rev. Lett. **112**, 203002 (2014).

[39] M. G. Tarallo, T. Mazzoni, N. Poli, D. V. Sutyrin, X. Zhang, and G. M. Tino, "Test of Einstein Equivalence Principle for 0-spin and half-integer-spin atoms: Search for spin-gravity coupling effects", Phys. Rev. Lett. **113**, 023005 (2014).

[40] L. Zhou, S. Long, B. Tang, X. Chen, F. Gao, W. Peng, W. Duan, J. Zhong, Z. Xiong, J. Wang, et al., "Test of equivalence principle at 10^{-8} level by a dual-species double-diffraction raman atom interferometer", Phys. Rev. Lett. **115**, 013004 (2015).

[41] N. Poli, F.-Y. Wang, M. G. Tarallo, A. Alberti, M. Prevedelli, and G. M. Tino, "Precision measurement of gravity with cold atoms in an optical lattice and comparison with a classical gravimeter", Phys, Rev. Lett. **106**, 038501 (2011).

[42] J. Hartwig, S. Abend, C. Schubert, D. Schlippert, H. Ahlers, K. Posso-Trujillo, N. Gaaloul, W. Ertmer, and E. M. Rasel, "Testing the universality of free fall with rubidium and ytterbium in a very large baseline atom interferometer", New J. Phys. **17**, 035011 (2015).

[43] G. M. Tino, F. Sorrentino, D. Aguilera, B. Battelier, A. Bertoldi, Q. Bodart, K. Bongs, P. Bouyer, C. Braxmaier, L. Cacciapuoti, et al., "Precision gravity tests with atom interferometry in space", Nucl. Phys. B, Proc. Suppl. **243**, 203 (2013).

[44] B. Altschul, Q. G. Bailey, L. Blanchet, K. Bongs, P. Bouyer, L. Cacciapuoti, S. Capozziello, N. Gaaloul, D. Giulini, J. Hartwig, et al., "Quantum tests of the Einstein Equivalence Principle with the STE–QUEST space mission", Adv. Space Res. **55**, 501 (2015).

[45] A. Kellerbauer, M. Amoretti, A. S. Belov, G. Bonomi, I. Boscolo, R. S. Brusa, M. Büchner, V. M. Byakov, L. Cabaret, C. Canali, et al., "Proposed antimatter gravity measurement with an antihydrogen beam", Nucl. Phys. B, Proc. Suppl. **266**, 351 (2008).

[46] P. Hamilton, A. Zhmoginov, F. Robicheaux, J. Fajans, J. S. Wurtele, and H. Müller, "Antimatter interferometry for gravity measurements", Phys. Rev. Lett. **112**, 121102 (2014).

[47] F. W. Hehl, P. Von der Heyde, G. D. Kerlick, and J. M. Nester, "General relativity with spin and torsion: Foundations and prospects", Rev. Mod. Phys. **48**, 393 (1976).

[48] A. Peres, "Test of equivalence principle for particles with spin", Phys. Rev. D **18**, 2739 (1978).

[49] B. Mashhoon, "Gravitational couplings of intrinsic spin", Classical Quant. Grav. **17**, 2399 (2000).

[50] Y. N. Obukhov, "Spin, gravity, and inertia", Phys. Rev. Lett. **86**, 192 (2001).

[51] D. Bini, C. Cherubini, and B. Mashhoon, "Spin, acceleration and gravity", Classical Quant. Grav. **21**, 3893 (2004).

[52] S. Capozziello, G. Lambiase, and C. Stornaioloi, "Geometric classification of the torsion tensor of space-time", Ann. Phys. **513**, 713 (2001).

[53] W.-T. Ni, "Searches for the role of spin and polarization in gravity", Rep. Prog. Phys. **73**, 056901 (2010).

[54] B. R. Heckel, E. G. Adelberger, C. E. Cramer, T. S. Cook, S. Schlamminger, and U. Schmidt, "Preferred-frame and CP-violation tests with polarized electrons", Phys. Rev. D **78**, 092006 (2008).

[55] B. J. Venema, P. K. Majumder, S. K. Lamoreaux, B. R. Heckel, and E. N. Fortson, "Search for a coupling of the Earth's gravitational field to nuclear spins in atomic mercury", Phys. Rev. Lett. **68**, 135 (1992).

[56] D. F. J. Kimball, I. Lacey, J. Valdez, J. Swiatlowski, C. Rios, R. Peregrina-Ramirez, C. Montcrieffe, J. Kremer, J. Dudley, and C. Sanchez, "A dual-isotope rubidium comagnetometer to search for anomalous long-range spin-mass (spin-gravity) couplings of the proton", Ann. Phys. **525**, 514 (2013).

[57] D. J. Wineland, J. J. Bollinger, D. J. Heinzen, W. M. Itano, and M. G. Raizen, "Search for anomalous spin-dependent forces using stored-ion spectroscopy", Phys. Rev. Lett. **67**, 1735 (1991).

[58] J. D. Barrow and R. J. Scherrer, "Do fermions and bosons produce the same gravitational field?", Phys. Rev. D **70**, 103515 (2004).

[59] S. Herrmann, H. Dittus, and C. Lämmerzahl, "Testing the equivalence principle with atomic interferometry", Classical Quant. Grav. **29**, 184003 (2012).

[60] G. Varoquaux, R. A. Nyman, R. Geiger, P. Cheinet, A. Landragin, and P. Bouyer, "How to estimate the differential acceleration in a two-species atom interferometer to test the equivalence principle", New J. Phys. **11**, 113010 (2009).

[61] M. G. Tarallo, N. Poli, M. Schioppo, D. Sutyrin, and G. M. Tino, "A high-stability semiconductor laser system for a ^{88}Sr-based optical lattice clock", Appl.Phys. B **103**, 17 (2011).

[62] P. W. Graham, J. M. Hogan, M. A. Kasevich, and S. Rajendran, "New method for gravitational wave detection with atomic sensors", Phys. Rev. Lett. **110**, 171102 (2013).

[63] A. O. Jamison, B. Plotkin-Swing, and S. Gupta, "Advances in precision contrast interferometry with Yb Bose-Einstein condensates", Phys. Rev. A **90**, 063606 (2014).

[64] N. Hinkley, J. A. Sherman, N. B. Phillips, M. Schioppo, N. D. Lemke, K. Beloy, M. Pizzocaro, C. W. Oates, and A. D. Ludlow, "An atomic clock with 10^{-18} instability", Science **341**, 1215 (2013).

[65] I. Ushijima, M. Takamoto, M. Das, T. Ohkubo, and H. Katori, "Cryogenic optical lattice clocks", Nat. Photonics **9**, 185 (2015).

[66] B. J. Bloom, T. L. Nicholson, J. R. Williams, S. L. Campbell, M. Bishof, X. Zhang, W. Zhang, S. L. Bromley, and J. Ye, "An optical lattice clock with accuracy and stability at the 10^{-18} level", Nature **506**, 71 (2014).

[67] D. M. Giltner, R. W. McGowan, and S. A. Lee, "Atom interferometer based on bragg scattering from standing light waves", Phys. Rev. Lett. **75**, 2638 (1995).

[68] H. Müller, S.-w. Chiow, Q. Long, S. Herrmann, and S. Chu, "Atom interferometry with up to 24-photon-momentum-transfer beam splitters", Phys. Rev. Lett. **100**, 180405 (2008).

[69] P. A. Altin, M. T. Johnsson, V. Negnevitsky, G. R. Dennis, R. P. Anderson, J. E. Debs, S. S. Szigeti, K. S. Hardman, S. Bennetts, G. D. McDonald, et al., "Precision atomic gravimeter based on bragg diffraction", New J. Phys. **15**, 023009 (2013).

[70] N. Yu and M. Tinto, "Gravitational wave detection with single-laser atom interferometers", Gen. Rel. Grav. **43**, 1943 (2011).

[71] T. Mazzoni, X. Zhang, R. Del Aguila, L. Salvi, N. Poli, and G. M. Tino, "Large-momentum-transfer Bragg interferometer with strontium atoms", Phys. Rev. A **92**, 053619 (2015).

[72] C. Cohen-Tannoudji, *Atoms in electromagnetic fields*, Vol. 3 (World Scientific, 2004).

[73] C. Cohen-Tannoudji and J. Dupont-Roc, *Atom-photon interactions: basic processes and applications* (Wiley Online Library, 1992).

[74] C. Cohen-Tannoudji, "Atomic motion in laser light", in Les Houches, Session LII: Fundamental systems in quantum optics (Elsvier, 1992).

[75] S. H. Autler and C. H. Townes, "Stark effect in rapidly varying fields", Phys. Rev. **100**, 703 (1955).

[76] R. Grimm, M. Weidemüller, and Y. N. Ovchinnikov, "Optical dipole traps for neutral atoms", Adv. At. Mol. Opt. Phys. **42**, 170 (2000).

[77] C. Cohen-Tannoudji and S. Reynaud, "Dressed-atom description of resonance fluorescence and absorption spectra of a multi-level atom in an intense laser beam", J. Phys. B **10**, 345 (1977).

[78] P. R. Berman and R. Salomaa, "Comparison between dressed-atom and bare-atom pictures in laser spectroscopy", Phys. Rev. A **25**, 2667 (1982).

[79] J. Dalibard and C. Cohen-Tannoudji, "Dressed-atom approach to atomic motion in laser light: the dipole force revisited", J. Opt. Soc. Am. B **2**, 1707 (1985).

[80] F. Bloch, "Über die quantenmechanik der elektronen in kristallgittern", Z. Phys. **52**, 555 (1929).

[81] N. W. Ashcroft and N. D. Mermin, *Solid state physics*, Science: Physics (Saunders College, 1976).

[82] C. Kittel, *Introduction to solid state physics* (Wiley, 2005).

[83] R. Kronig and W. G. Penney, "Quantum mechanics of electrons in crystal lattices", in Proc. R. Soc. London A, Vol. 130, 814 (The Royal Society, 1931), p. 499.

[84] G. H. Wannier, "The structure of electronic excitation levels in insulating crystals", Phys. Rev. **52**, 191 (1937).

[85] P. M. Visser and G. Nienhuis, "Quantum transport of atoms in an optical lattice", Phys. Rev. A **56**, 3950 (1997).

[86] L. D. Landau and E. M. Lifshitz, *Quantum mechanics: non-relativistic theory*, Vol. 3 (Elsevier, 2013).

[87] C. Pierre, "Bloch oscillations in atom interferometry", in Proceedings of the International School of Physics "Enrico Fermi", Course CLXXXVIII, Varenna 2013 (Società Italiana di Fisica and IOS Press, 2014), p. 419.

[88] M. A. Kasevich, D. S. Weiss, E. Riis, K. Moler, S. Kasapi, and S. Chu, "Atomic velocity selection using stimulated Raman transitions", Phys. Rev. Lett. **66**, 2297 (1991).

[89] K. Moler, D. S. Weiss, M. A. Kasevich, and S. Chu, "Theoretical analysis of velocity-selective Raman transitions", Phys. Rev. A **45**, 342 (1992).

[90] C. Zener, "Non-adiabatic crossing of energy levels", in Proc. R. Soc. London A, Vol. 137, 833 (The Royal Society, 1932), p. 696.

[91] H. Jones and C. Zener, "A general proof of certain fundamental equations in the theory of metallic conduction", in Proc. R. Soc. London A (The Royal Society, 1934), p. 101.

[92] M. B. Dahan, E. Peik, J. Reichel, Y. Castin, and C. Salomon, "Bloch oscillations of atoms in an optical potential", Phys. Rev. Lett. **76**, 4508 (1996).

[93] E. Peik, M. B. Dahan, I. Bouchoule, Y. Castin, and C. Salomon, "Bloch oscillations of atoms, adiabatic rapid passage, and monokinetic atomic beams", Phys. Rev. A **55**, 2989 (1997).

[94] Q. Niu, X.-G. Zhao, G. A. Georgakis, and M. G. Raizen, "Atomic Landau-Zener tunneling and Wannier-Stark ladders in optical potentials", Phys. Rev. Lett. **76**, 4504 (1996).

[95] S. R. Wilkinson, C. F. Bharucha, M. C. Fischer, K. W. Madison, P. R. Morrow, Q. Niu, B. Sundaram, and M. G. Raizen, "Experimental evidence for non-exponential decay in quantum tunnelling", Nature **387**, 575 (1997).

[96] A. R. Kolovsky and H. J. Korsch, "Bloch oscillations of cold atoms in optical lattices", Int. J. Mod. Phys. B **18**, 1235 (2004).

[97] A. Abragam, *The principles of nuclear magnetism*, 32 (Oxford university Press, 1961).

[98] L. D. Landau, "Zur theorie der energieübertragung bei stössen", Phys. Z. Sowjetunion **1**, 88 (1932).

[99] M. Glück, A. R. Kolovsky, and H. J. Korsch, "Wannier-Stark resonances in optical and semiconductor superlattices", Phys. Rep. **366**, 103 (2002).

[100] M. Glück, A. R. Kolovsky, and H.-J. Korsch, "Lifetime of Wannier-Stark States", Phys. Rev. Lett. **83**, 891 (1999).

[101] G. H. Wannier, "Wave functions and effective Hamiltonian for Bloch electrons in an electric field", Phys. Rev. **117**, 432 (1960).

[102] V. V. Ivanov, A. Alberti, M. Schioppo, G. Ferrari, M. L. C. M. Artoni, M. L. Chiofalo, and G. M. Tino, "Coherent delocalization of atomic wave packets in driven lattice potentials", Phys. Rev. Lett. **100**, 043602 (2008).

[103] C. Sias, H. Lignier, Y. P. Singh, A. Zenesini, D. Ciampini, O. Morsch, and E. Arimondo, "Observation of photon-assisted tunneling in optical lattices", Phys. Rev. Lett. **100**, 040404 (2008).

[104] A. Alberti, V. V. Ivanov, G. M. Tino, and G. Ferrari, "Engineering the quantum transport of atomic wavefunctions over macroscopic distances", Nat. Phys. **5**, 547 (2009).

[105] A. Alberti, G. Ferrari, V. V. Ivanov, M. L. Chiofalo, and G. M. Tino, "Atomic wave packets in amplitude-modulated vertical optical lattices", New J. Phys. **12**, 065037 (2010).

[106] M. G. Tarallo, A. Alberti, N. Poli, M. L. Chiofalo, F.-Y. Wang, and G. M. Tino, "Delocalization-enhanced Bloch oscillations and driven resonant tunneling in optical lattices for precision force measurements", Phys. Rev. A **86**, 033615 (2012).

[107] J. H. Denschlag, J. E. Simsarian, H. Häffner, C. McKenzie, A. Browaeys, D. Cho, K. Helmerson, S. L. Rolston, and W. D. Phillips, "A Bose-Einstein condensate in an optical lattice", J. Phys. B **35**, 3095 (2002).

[108] A. Alberti, "Coherent transport in driven optical lattices and applications to force measurements", Ph.D Thesis (LENS - University of Florence, 2010).

[109] M. Grifoni and P. Hänggi, "Driven quantum tunneling", Phys. Rep. **304**, 229 (1998).

[110] A. R. Kolovsky, A. V. Ponomarev, and H. J. Korsch, "Damped Bloch oscillations of cold atoms in optical lattices", Phys. Rev. A **66**, 053405 (2002).

[111] V. M. Kenkre and D. W. Brown, "Exact solution of the stochastic Liouville equation and application to an evaluation of the neutron scattering function", Phys. Rev. B **31**, 2479 (1985).

[112] P. Goetsch and R. Graham, "Decoherence by spontaneous emission in atomic-momentum transfer experiments", Phys. Rev. A **54**, 5345 (1996).

[113] H. B. G. Casimir and D. Polder, "The influence of retardation on the London-van der Waals forces", Phys. Rev. **73**, 360 (1948).

[114] I. Carusotto, L. Pitaevskii, S. Stringari, G. Modugno, and M. Inguscio, "Sensitive measurement of forces at the micron scale using bloch oscillations of ultracold atoms", Phys. Rev. Lett. **95**, 093202 (2005).

[115] N. W. McLachlan, *Theory and application of Mathieu functions* (Clarendon Press, 1951).

[116] M. Horne, I. Jex, and A. Zeilinger, "Schrödinger wave functions in strong periodic potentials with applications to atom optics", Phys. Rev. A **59**, 2190 (1999).

[117] E. M. Wright and P. Meystre, "Theory of an atomic interferometer in the Raman-Nath regime", Opt. Commun. **75**, 388 (1990).

[118] S. Gupta, K. Dieckmann, Z. Hadzibabic, and D. E. Pritchard, "Contrast interferometry using Bose-Einstein condensates to measure h/m and α", Phys. Rev. Lett. **89**, 140401 (2002).

[119] R. E. Sapiro, R. Zhang, and G. Raithel, "Atom interferometry using Kapitza-Dirac scattering in a magnetic trap", Phys. Rev. A **79**, 043630 (2009).

[120] W. Li, T. He, and A. Smerzi, "Multimode Kapitza-Dirac interferometry with trapped cold atoms", Phys. Rev. Lett. **113**, 023003 (2014).

[121] C. Keller, J. Schmiedmayer, A. Zeilinger, T. Nonn, S. Dürr, and G. Rempe, "Adiabatic following in standing-wave diffraction of atoms", Appl. Phys. B **69**, 303 (1999).

[122] H. Müller, S.-w. Chiow, and S. Chu, "Atom-wave diffraction between the Raman-Nath and the Bragg regime: Effective Rabi frequency, losses, and phase shifts", Phys. Rev. A **77**, 023609 (2008).

[123] P. L. Kapitza and P. A. M. Dirac, "The reflection of electrons from standing light waves", in Math. Proc. Cambridge, Vol. 29, 02 (Cambridge Univerity Press, 1933), p. 297.

[124] S. Altshuler, L. M. Frantz, and R. Braunstein, "Reflection of atoms from standing light waves", Phys. Rev. Lett. **17**, 231 (1966).

[125] P. L. Gould, G. A. Ruff, and D. E. Pritchard, "Diffraction of atoms by light: The near-resonant Kapitza-Dirac effect", Phys. Rev. Lett. **56**, 827 (1986).

[126] P. J. Martin, B. G. Oldaker, A. H. Miklich, and D. E. Pritchard, "Bragg scattering of atoms from a standing light wave", Phys. Rev. Lett. **60**, 515 (1988).

[127] H. Batelaan, "The Kapitza-Dirac effect", Contemp. Phys. **41**, 369 (2000).

[128] S. Gupta, A. E. Leanhardt, A. D. Cronin, and D. E. Pritchard, "Coherent manipulation of atoms with standing light waves", C. R. Acad. Sci. Paris, Série IV **2**, 479 (2001).

[129] D. M. Giltner, R. W. McGowan, and S. A. Lee, "Theoretical and experimental study of the Bragg scattering of atoms from a standing light wave", Phys. Rev. A **52**, 3966 (1995).

[130] P. P. Ewald, "Zur begründung der kristalloptik", Ann. Phys. **359**, 557 (1917).

[131] J. Mathews and R. L. Walker, *Mathematical methods of physics*, Addison-Wesley World Student Series (W. A. Benjamin, 1970).

[132] D. L. Butts, K. Kotru, J. M. Kinast, A. M. Radojevic, B. P. Timmons, and R. E. Stoner, "Efficient broadband Raman pulses for large-area atom interferometry", J. Opt. Soc. Am. B **30**, 922 (2013).

[133] A. Dunning, R. Gregory, J. Bateman, N. Cooper, M. Himsworth, J. A. Jones, and T. Freegarde, "Composite pulses for interferometry in a thermal cold atom cloud", Phys. Rev. A **90**, 033608 (2014).

[134] T. Kovachy, S.-w. Chiow, and M. A. Kasevich, "Adiabatic-rapid-passage multiphoton Bragg atom optics", Phys. Rev. A **86**, 011606 (2012).

[135] S. S. Szigeti, J. E. Debs, J. J. Hope, N. P. Robins, and J. D. Close, "Why momentum width matters for atom interferometry with Bragg pulses", New J. Phys. **14**, 023009 (2012).

[136] P. R. Berman and B. Bian, "Pump-probe spectroscopy approach to Bragg scattering", Phys. Rev. A **55**, 4382 (1997).

[137] J. Stenger, S. Inouye, A. P. Chikkatur, D. M. Stamper-Kurn, D. E. Pritchard, and W. Ketterle, "Bragg spectroscopy of a Bose-Einstein condensate", Phys. Rev. Lett. **82**, 4569 (1999).

[138] M. Kozuma, L. Deng, E. W. Hagley, J. Wen, R. Lutwak, K. Helmerson, S. L. Rolston, and W. D. Phillips, "Coherent splitting of Bose-Einstein condensed atoms with optically induced Bragg diffraction", Phys. Rev. Lett. **82**, 871 (1999).

[139] Y. V. Baklanov, B. Y. Dubetsky, and V. P. Chebotayev, "Non-linear Ramsey resonance in the optical region", Appl. Phys. **9**, 171 (1976).

[140] J. C. Bergquist, S. A. Lee, and J. L. Hall, "Saturated absorption with spatially separated laser fields: Observation of optical Ramsey fringes", Phys. Rev. Lett. **38**, 159 (1977).

[141] C. J. Bordé, "Atomic interferometry with internal state labelling", Phys. Lett. A **140**, 10 (1989).

[142] C. J. Bordé, C. Salomon, S. Avrillier, A. Van Lerberghe, C. Bréant, D. Bassi, and G. Scoles, "Optical Ramsey fringes with traveling waves", Phys. Rev. A **30**, 1836 (1984).

[143] D. S. Weiss, B. C. Young, and S. Chu, "Precision measurement of $\hbar/m$ Cs based on photon recoil using laser-cooled atoms and atomic interferometry", Appl. Phys. B **59**, 217 (1994).

[144] R. P. Feynman and A. R. Hibbs, *Quantum mechanics and path integrals*, Vol. 2 (McGraw-Hill New York, 1965).

[145] M. A. Kasevich and S. Chu, "Measurement of the gravitational acceleration of an atom with a light-pulse atom interferometer", Appl. Phys. B **54**, 321 (1992).

[146] C. J. Bordé, "Atomic clocks and inertial sensors", Metrologia **39**, 435 (2002).

[147] P. Storey and C. Cohen-Tannoudji, "The Feynman path integral approach to atomic interferometry. A tutorial", J. Phys. II **4**, 1999 (1994).

[148] A. Peters, K. Y. Chung, and S. Chu, "High-precision gravity measurements using atom interferometry", Metrologia **38**, 25 (2001).

[149] T. L. Gustavson, A. Landragin, and M. A. Kasevich, "Rotation sensing with a dual atom-interferometer Sagnac gyroscope", Classical Quant. Grav. **17**, 2385 (2000).

[150] M. A. Kasevich, E. Riis, S. Chu, and R. G. DeVoe, "RF spectroscopy in an atomic fountain", Phys. Rev. Lett. **63**, 612 (1989).

[151] A. Clairon, C. Salomon, S. Guellati, and W. D. Phillips, "Ramsey resonance in a Zacharias fountain", Europhys. Lett. **16**, 165 (1991).

[152] H. Müntinga, H. Ahlers, M. Krutzik, A. Wenzlawski, S. Arnold, D. Becker, K. Bongs, H. Dittus, H. Duncker, N. Gaaloul, et al., "Interferometry with Bose-Einstein condensates in microgravity", Phys. Rev. Lett. **110**, 093602 (2013).

[153] G. Stern, B. Battelier, R. Geiger, G. Varoquaux, A. Villing, F. Moron, O. Carraz, N. Zahzam, Y. Bidel, W. Chaibi, et al., "Light-pulse atom interferometry in microgravity", Eur. Phys. J. D **53**, 353 (2009).

[154] R. Geiger, V. Ménoret, G. Stern, N. Zahzam, P. Cheinet, B. Battelier, A. Villing, F. Moron, M. Lours, Y. Bidel, et al., "Detecting inertial effects with airborne matter-wave interferometry", Nat. Commun. **2**, 474 (2011).

[155] F. Sorrentino, K. Bongs, P. Bouyer, L. Cacciapuoti, M. De Angelis, H. Dittus, W. Ertmer, A. Giorgini, J. Hartwig, M. Hauth, et al., "A compact atom interferometer for future space missions", Microgravity Sci. Tech. **22**, 551 (2010).

[156] J. M. McGuirk, M. J. Snadden, and M. A. Kasevich, "Large area light-pulse atom interferometry", Phys. Rev. Lett. **85**, 4498 (2000).

[157] S.-w. Chiow, T. Kovachy, H.-C. Chien, and M. A. Kasevich, "102$\hbar k$ large area atom interferometers", Phys. Rev. Lett. **107**, 130403 (2011).

[158] P. Cladé, S. Guellati-Khélifa, F. Nez, and F. Biraben, "Large momentum beam splitter using Bloch oscillations", Phys. Rev. Lett. **102**, 240402 (2009).

[159] C. C. N. McDonald, Gordon D. nd Kuhn, S. Bennetts, J. E. Debs, K. S. Hardman, M. Johnsson, J. D. Close, and N. P. Robins, "80$\hbar k$ momentum separation with Bloch oscillations in an optically guided atom interferometer", Phys. Rev. A **88**, 053620 (2013).

[160] G. D. McDonald, C. C. N. Kuhn, S. Bennetts, J. E. Debs, K. S. Hardman, J. D. Close, and N. P. Robins, "A faster scaling in acceleration-sensitive atom interferometers", Eur. Phys. J. **105**, 63001 (2014).

[161] R. Charriere, M. Cadoret, N. Zahzam, Y. Bidel, and A. Bresson, "Local gravity measurement with the combination of atom interferometry and Bloch oscillations", Phys. Rev. A **85**, 013639 (2012).

[162] G. Audi, A. H. Wapstra, and C. Thibault, "The AME2003 atomic mass evaluation:(II). Tables, graphs and references", Nucl. Phys. A **729**, 337 (2003).

[163] R. Rana, M. Höcker, and E. G. Myers, "Atomic masses of strontium and ytterbium", Phys. Rev. A **86**, 050502 (2012).

[164] D. R. Lide, *CRC handbook of chemistry and physics* (Taylor & Francis, New York, 2008).

[165] Y. N. Martinez De Escobar, P. G. Mickelson, P. Pellegrini, S. B. Nagel, A. Traverso, M. Yan, R. Côté, and T. C. Killian, "Two-photon photoassociative spectroscopy of ultracold ^{88}Sr", Phys. Rev. A **78**, 062708 (2008).

[166] A. Stein, H. Knöckel, and E. Tiemann, "The ^{1}S+^{1}S asymptote of Sr_2 studied by Fourier-transform spectroscopy", Eur. Phys. J. D **57**, 171 (2010).

[167] P. Raghavan, "Table of nuclear moments", At. Data Nucl. Data Tables **42**, 189 (1989).

[168] D.-I. Choi and Q. Niu, "Bose-Einstein condensates in an optical lattice", Phys. Rev. Lett. **82**, 2022 (1999).

[169] A. Buchleitner and A. R. Kolovsky, "Interaction-induced decoherence of atomic Bloch oscillations", Phys. Rev. Lett. **91**, 253002 (2003).

[170] G. Roati, E. De Mirandes, F. Ferlaino, H. Ott, G. Modugno, and M. Inguscio, "Atom interferometry with trapped Fermi gases", Phys. Rev. Lett. **92**, 230402 (2004).

[171] M. Fattori, C. D'Errico, G. Roati, M. Zaccanti, M. Jona-Lasinio, M. Modugno, M. Inguscio., and G. Modugno, "Atom interferometry with a weakly interacting Bose-Einstein condensate", Phys. Rev. Lett. **100**, 080405 (2008).

[172] M. Gustavsson, E. Haller, M. J. Mark, J. G. Danzl, G. Rojas-Kopeinig, and H.-C. Nägerl, "Control of interaction-induced dephasing of Bloch oscillations", Phys. Rev. Lett. **100**, 080404 (2008).

[173] S. Stellmer, M. K. Tey, B. Huang, R. Grimm, and F. Schreck, "Bose-Einstein condensation of strontium", Phys. Rev. Lett. **103**, 200401 (2009).

[174] P. G. Mickelson, Y. N. Martinez De Escobar, M. Yan, B. J. DeSalvo, and T. C. Killian, "Bose-Einstein condensation of ^{88}Sr through sympathetic cooling with ^{87}Sr", Phys. Rev. A **81**, 051601 (2010).

[175] S. Stellmer, B. Pasquiou, R. Grimm, and F. Schreck, "Laser cooling to quantum degeneracy", Phys. Rev. Lett. **110**, 263003 (2013).

[176] T. L. Nicholson, S. L. Campbell, R. B. Hutson, G. E. Marti, B. J. Bloom, R. L. McNally, W. Zhang, M. D. Barrett, M. S. Safronova, G. F. Strouse, et al., "Systematic evaluation of an atomic clock at 2×10^{-18} total uncertainty", Nat. Commun. **6** (2015).

[177] S. Chu, L. Hollberg, J. E. Bjorkholm, A. Cable, and A. Ashkin, "Three-dimensional viscous confinement and cooling of atoms by resonance radiation pressure", Phys. Rev. Lett. **55**, 48 (1985).

[178] W. D. Phillips, J. V. Prodan, and H. J. Metcalf, "Laser cooling and electromagnetic trapping of neutral atoms", J. Opt. Soc. Am. B **2**, 1751 (1985).

[179] A. Ashkin, "Trapping of atoms by resonance radiation pressure", Phys. Rev. Lett. **40**, 729 (1978).

[180] H. J. Metcalf and P. Van der Straten, *Laser cooling and trapping* (Springer Science & Business Media, 2012).

[181] C. J. Foot, *Atomic physics* (Oxford University Press, 2004).

[182] G. K. Woodgate, *Elementary atomic structure* (Clarendon Press, 1980).

[183] W. D. Phillips and H. J. Metcalf, "Laser deceleration of an atomic beam", Phys. Rev. Lett. **48**, 596 (1982).

[184] H. Katori, T. Ido, Y. Isoya, and M. Kuwata-Gonokami, "Magneto-optical trapping and cooling of strontium atoms down to the photon recoil temperature", Phys. Rev. Lett. **82**, 1116 (1999).

[185] T. Chaneliere, L. He, R. Kaiser, and D. Wilkowski, "Three dimensional cooling and trapping with a narrow line", Eur. Phys. J. D **46**, 507 (2008).

[186] T. H. Loftus, T. Ido, A. D. Ludlow, M. M. Boyd, and J. Ye, "Narrow line cooling: finite photon recoil dynamics", Phys. Rev. Lett. **93**, 073003 (2004).

[187] C. J. Dedman, J. Nes, T. M. Hanna, R. G. Dall, K. G. H. Baldwin, and A. G. Truscott, "Optimum design and construction of a Zeeman slower for use with a magneto-optic trap", Rev. Sci. Instrum. **75**, 5136 (2004).

[188] H. J. Kluge and H. Sauter, "Levelcrossing experiments in the first excited $^1P_1$ states of the alkaline earths", Z. Phys. A **270**, 295 (1974).

[189] G. Zu Putlitz, "Bestimmung des elektrischen Kernquadrupolmomentes des ungeraden stabilen Strontium-87-Kerns", Z. Phys. A **175**, 543 (1963).

[190] S. M. Heider and G. O. Brink, "Hyperfine structure of ^{87}Sr in the $^3P_2$ metastable state", Phys. Rev. A **16**, 1371 (1977).

[191] I. Courtillot, "Premiere observation de la transition fortement interdite $^1S_0$–$^3P_0$ du strontium, pour une horloge optique a atomes pieges", Ph.D thesis (Université de Paris VI, 2003).

[192] A. Brusch, R. Le Targat, X. Baillard, M. Fouché, and P. Lemonde, "Hyperpolarizability effects in a Sr optical lattice clock", Phys. Rev. Lett. **96**, 103003 (2006).

[193] P. Bouyer, P. Lemonde, M. B. Dahan, A. Michaud, C. Salomon, and J. Dalibard, "An atom trap relying on optical pumping", Eur. Phys. Lett. **27**, 569 (1994).

[194] T. Mukaiyama, H. Katori, T. Ido, Y. Li, and M. Kuwata-Gonokami, "Recoil-limited laser cooling of ^{87}Sr atoms near the Fermi temperature", Phys. Rev. Lett. **90**, 113002 (2003).

[195] M. Schioppo, N. Poli, M. Prevedelli, C. Lisdat, U. Sterr, G. M. Tino, et al., "A compact and efficient strontium oven for laser-cooling experiments", Rev. Sci. Instrum. **83**, 103101 (2012).

[196] R. J. Cook, "Theory of resonance-radiation pressure", Phys. Rev. A **22**, 1078 (1980).

[197] T. E. Barrett, S. W. Dapore-Schwartz, M. D. Ray, and G. P. Lafyatis, "Slowing atoms with σ^- polarized light", Phys. Rev. Lett. **67**, 3483 (1991).

[198] N. Poli, G. Ferrari, M. Prevedelli, F. Sorrentino, R. E. Drullinger, and G. M. Tino, "Laser sources for precision spectroscopy on atomic strontium", Spectrochim. Acta A **63**, 981 (2006).

[199] M. Schioppo, "Development of a transportable strontium optical clock", Ph.D Thesis (University of Florence, 2010).

[200] R. Le Targat, J.-J. Zondy, and P. Lemonde, "75%-efficiency blue generation from an intracavity PPKTP frequency doubler", Opt. Commun. **247**, 471 (2005).

[201] M. M. Fejer, G. A. Magel, D. H. Jundt, and R. L. Byer, "Quasi-phase-matched second harmonic generation: tuning and tolerances", Quantum Electron. **28**, 2631 (1992).

[202] M. A. Hohensee, H. Müller, and R. B. Wiringa, "Equivalence Principle and bound kinetic energy", Phys. Rev. Lett. **111**, 151102 (2013).

[203] V. A. Kostelecký and J. D. Tasson, "Matter-gravity couplings and lorentz violation", Phys. Rev. D **83**, 016013 (2011).

[204] C. Lämmerzahl, "Quantum tests of the foundations of general relativity", Classical Quant. Grav. **15**, 13 (1998).

[205] J. D. Tasson, (private communication), 2014.

[206] N. Beverini, N. Poli, D. Sutyrin, F.-Y. Wang, M. Schioppo, M. G. Tarallo, and G. M. Tino, "Absolute frequency measurement of unstable lasers with optical frequency combs", in Proc. SPIE 7993, ICONO 2010 (International Society for Optics and Photonics, 2011), p. 79931I.

[207] T. A. Savard, K. M. O'hara, and J. E. Thomas, "Laser-noise-induced heating in far-off resonance optical traps", Phys. Rev. A **56**, R1095 (1997).

[208] R. Holzwarth, A. Y. Nevsky, M. Zimmermann, T. Udem, T. W. Hänsch, J. Von Zanthier, H. Walther, J. C. Knight, W. J. Wadsworth, P. S. J. Russell, et al., "Absolute frequency measurement of iodine lines with a femtosecond optical synthesizer", Appl. Phys. B **73**, 269 (2001).

[209] J. D. Simmons and J. T. Hougen, "Atlas of the I_2 Spectrum from 19 000 to 18 000 cm^{-1}", J. Res. Natl. Inst. Stan. **81A**, 25 (1977).

[210] J. Ye, L. Robertsson, S. Picard, L.-S. Ma, and J. L. Hall, "Absolute frequency atlas of molecular I_2 lines at 532 nm", IEEE T. Instrum. Meas. **48**, 544 (1999).

[211] R. Holzwarth, T. Udem, T. W. Hänsch, J. C. Knight, W. J. Wadsworth, and P. S. J. Russell, "Optical frequency synthesizer for precision spectroscopy", Phys. Rev. Lett. **85**, 2264 (2000).

[212] L. I. Schiff, "Quantum mechanics", New York: Mc Graw-Hill (1968).

[213] S. L. Winoto, M. T. DePue, N. E. Bramall, and D. S. Weiss, "Laser cooling at high density in deep far-detuned optical lattices", Phys. Rev. A **59**, R19 (1999).

[214] N. Poli, C. W. Oates, P. Gill, and G. M. Tino, "Optical atomic clocks", Riv. Nuovo Cimento **36**, 555 (2013).

[215] A. D. Ludlow, M. M. Boyd, J. Ye, E. Peik, and P. O. Schmidt, "Optical atomic clocks", Rev. Mod. Phys. **87**, 637 (2015).

[216] D. W. Allan, "Statistics of atomic frequency standards", Proc. IEEE **54**, 221 (1966).

[217] M. Andia, R. Jannin, F. Nez, F. Biraben, S. Guellati-Khélifa, and P. Cladé, "Compact atomic gravimeter based on a pulsed and accelerated optical lattice", Phys. Rev. A **88**, 031605 (2013).

[218] T. Damour, "Testing the equivalence principle: why and how?", Classical Quant. Grav. **13**, A33 (1996).

[219] A. Wicht, E. Sarajlic, J. M. Hensley, and S. Chu, "Phase shifts in precision atom interferometry due to the localization of atoms and optical fields", Phys. Rev. A **72**, 023602 (2005).

[220] T. Middelmann, S. Falke, C. Lisdat, and U. Sterr, "High accuracy correction of blackbody radiation shift in an optical lattice clock", Phys. Rev. Lett. **109**, 263004 (2012).

[221] T. Kovachy, J. M. Hogan, D. M. S. Johnson, and M. A. Kasevich, "Optical lattices as waveguides and beam splitters for atom interferometry: An analytical treatment and proposal of applications", Phys. Rev. A **82**, 013638 (2010).

[222] E. Giese, A. Roura, G. Tackmann, E. M. Rasel, and W. P. Schleich, "Double Bragg diffraction: A tool for atom optics", Phys. Rev. A **88**, 053608 (2013).

[223] E. Giese, "Mechanisms of matter-wave diffraction and their application to interferometers", Fortschr. Phys. **63**, 337 (2015).

[224] G. D. McDonald, H. Keal, P. A. Altin, J. E. Debs, S. Bennetts, C. C. N. Kuhn, K. S. Hardman, M. T. Johnsson, J. D. Close, and N. P. Robins, "Optically guided linear Mach-Zehnder atom interferometer", Phys. Rev. A **87**, 013632 (2013).

[225] K. S. Hardman, C. C. N. Kuhn, G. D. McDonald, J. E. Debs, S. Bennetts, J. D. Close, and N. P. Robins, "Role of source coherence in atom interferometery", Phys. Rev. A **89**, 023626 (2014).

[226] T. Kovachy, J. M. Hogan, A. Sugarbaker, S. M. Dickerson, C. A. Donnelly, C. Overstreet, and M. A. Kasevich, "Matter wave lensing to picokelvin temperatures", Phys. Rev. Lett. **114**, 143004 (2015).

[227] A. Peters, "High precision gravity measurements using atom interferometry", Ph.D Thesis (Standford University, 1998).

[228] G. J. Dick, "Local oscillator induced instabilities in trapped ion frequency standards", in Proc. 19th Annu. Precise Time and Time Interval (U.S. Naval Observatory, 1987), p. 133.

[229] P. Cheinet, B. Canuel, F. Pereira Dos Santos, A. Gauguet, F. Yver-Leduc, and A. Landragin, "Measurement of the sensitivity function in a time-domain atomic interferometer", IEEE T. Instrum. Meas. **57**, 1141 (2008).

[230] J. Le Gouët, T. E. Mehlstäubler, J. Kim, S. Merlet, A. Clairon, A. Landragin, and F. Pereira Dos Santos, "Limits to the sensitivity of a low noise compact atomic gravimeter", Appl. Phys. B **92**, 133 (2008).

[231] L. L. Presti, D. Rovera, and A. De Marchi, "A simple analysis of the Dick effect in terms of phase noise spectral densities", IEEE T. Ultrason. Ferr. **45**, 899 (1998).

[232] G. Santarelli, C. Audoin, A. Makdissi, P. Laurent, G. J. Dick, and A. Clairon, "Frequency stability degradation of an oscillator slaved to a periodically interrogated atomic resonator", IEEE T. Ultrason. Ferr. **45**, 887 (1998).

[233] F. Yver-Leduc, P. Cheinet, J. Fils, A. Clairon, N. Dimarcq, D. Holleville, P. Bouyer, and A. Landragin, "Reaching the quantum noise limit in a high-sensitivity cold-atom inertial sensor", J. Opt. B **5**, S136 (2003).

[234] N. Poli, R. E. Drullinger, G. Ferrari, J. Léonard, F. Sorrentino, and G. M. Tino, "Cooling and trapping of ultracold strontium isotopic mixtures", Phys. Rev. A **71**, 061403 (2005).

[235] H. Müller, S.-w. Chiow, S. Herrmann, and S. Chu, "Atom interferometers with scalable enclosed area", Phys. Rev. Lett. **102**, 240403 (2009).

[236] S. Stellmer, R. Grimm, and F. Schreck, "Production of quantum-degenerate strontium gases", Phys. Rev. A **87**, 013611 (2013).

[237] M. A. Norcia and J. K. Thompson, "Strong coupling on a forbidden transition in strontium and nondestructive atom counting", arXiv:1506.02297 (2015).